Max-Planck-Institut für Astrophysik

The Presupernova Evolution of Rotating Massive Stars

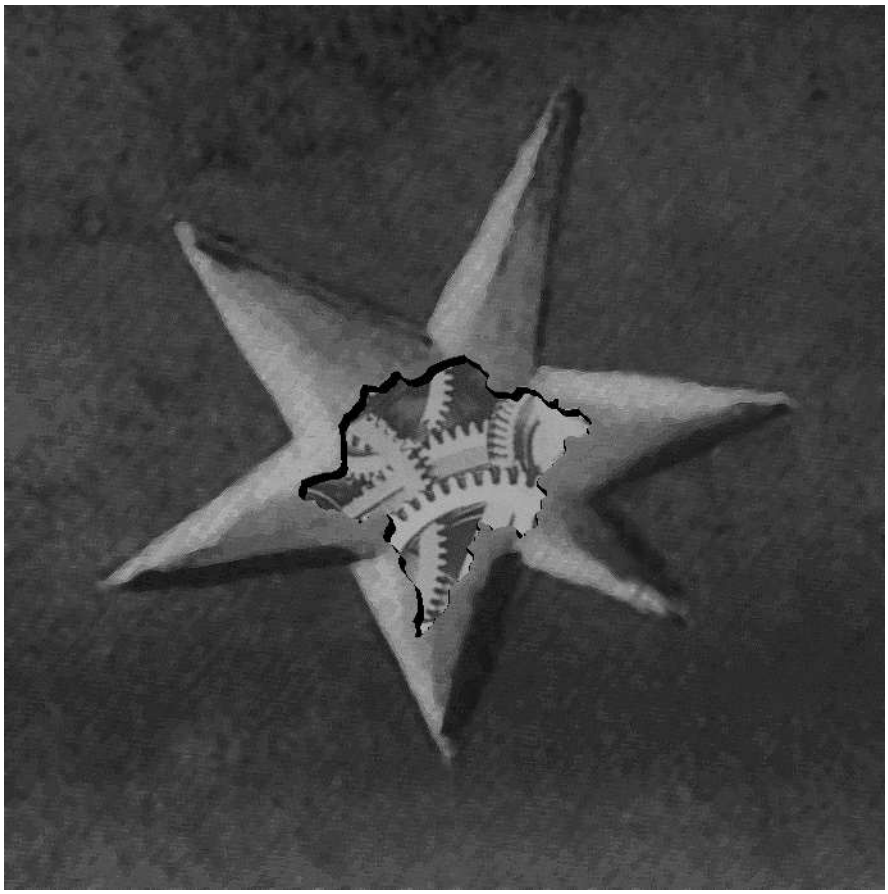

Alexander Heger

Max-Planck-Institut für Astrophysik

The Presupernova Evolution of Rotating Massive Stars

Alexander Heger

Vollständiger Abdruck der von der Fakultät für Physik der Technischen Universität München zur Erlangung des akademischen Grades eines

Doktors der Naturwissenschaften

genehmigten Dissertation.

Vorsitzender: Univ.-Prof. Dr. P. Kienle

Prüfer der Dissertation:

1. Hon.-Prof. Dr. W. Hillebrandt
2. Univ.-Prof. Dr. H. Friedrich

Die Dissertation wurde am 27.08.1998 bei der Technischen Universität München eingereicht und durch die Fakultät für Physik am 20.10.1998 angenommen.

Contents

1 Introduction **1**
1.1 Massive star models with rotation 1
1.2 Observational evidence for stellar rotation 2
1.2.1 Rotation rates 2
1.2.2 Stellar winds 3
1.2.3 Surface abundance patterns 4
1.2.4 Internal stellar structure 5
1.3 Type II supernovae and nucleosynthesis 5
1.4 Organization of this work 8

2 Numerical method and input physics **9**
2.1 Basic equations 9
2.1.1 Hydrodynamic stellar structure equations 9
2.1.2 Modification to the equations in rotating stars 10
2.1.3 Boundary conditions 12
2.1.4 Initial conditions 13
2.1.5 Thermonuclear reactions 15
2.1.6 Numerical solution 17
2.1.6.1 STERN 17
2.1.6.2 KEPLER 18
2.1.6.3 Survey of the computed model sequences 19
2.2 Mixing due to instabilities 21
2.2.1 Mixing in non-rotating stars 21
2.2.1.1 Convection and overshooting 21
2.2.1.2 Semiconvection 23
2.2.1.3 Thermohaline convection 24
2.2.2 Rotationally induced mixing 25
2.2.2.1 Dynamical shear instability 25
2.2.2.2 Solberg-Høiland instability 26
2.2.2.3 Secular shear instability 27
2.2.2.4 Eddington-Sweet circulation 30
2.2.2.5 Goldreich-Schubert-Fricke instability 31
2.2.3 Other instabilities 33
2.2.4 Angular momentum transport 34
2.2.5 Parameterization of the mixing efficiencies 35

2.3 Calibration of the mixing efficiencies 36
2.4 Mass loss 39
2.4.1 The Eddington-Limit 39
2.4.2 The Ω-limit 40
2.4.3 Angular momentum loss 42

3 Evolution of the stellar interior 43
3.1 Central hydrogen burning 43
3.1.1 Chemical mixing: the example of 20 $M_\odot$ stars 44
3.1.2 Transport of angular momentum 49
3.1.3 The influence of the initial rotation rate 52
3.2 Central helium burning 54
3.2.1 Chemical mixing 54
3.2.2 Transport of angular momentum 59
3.3 Late evolution until core collapse 61
3.3.1 Chemical mixing in the helium shell 62
3.3.2 Chemical mixing inside the C/O core 65
3.3.3 Transport of angular momentum 65
3.3.4 Stability to triaxial deformations 66
3.4 Angular momentum prior to core collapse 67
3.5 Implications for young pulsars and supernovae 74
3.5.1 Comparison with observed young pulsars 74
3.5.2 Formation of Kerr black holes? 75
3.6 Comparison with other work 77

4 Evolution of the surface properties 81
4.1 Central hydrogen burning 81
4.1.1 Evolution in the HR diagram 81
4.1.2 Rotational velocities 84
4.1.3 Surface abundances 85
4.2 Post-central hydrogen burning 91
4.2.1 Evolution in the HR diagram 91
4.2.2 First dredge-up abundances 95
4.2.3 Second dredge-up abundances 98
4.2.4 Rotational velocities 99
4.3 Spin-up of contracting red supergiants 100
4.3.1 The spin-up mechanism 101
4.3.1.1 Assumptions 101
4.3.1.2 The spin-down of convective envelopes 102
4.3.1.3 The spin-up of convective envelopes 105
4.3.2 Numerical simulation 106
4.3.3 Discussion and different scenarios 111
4.3.3.1 Blue loops during or after core helium burning 112
4.3.3.2 Red supergiant → Wolf-Rayet star transition 112
4.3.3.3 Pre-main sequence evolution 113

4.3.3.4 Post-AGB evolution . . . 114
4.4 Pulsations . . . 114
4.4.1 Model properties . . . 115
4.4.2 Linear stability analysis . . . 117
4.4.3 Non-linear computation of the pulsations . . . 120
4.4.4 Discussion . . . 121

5 Effects of rotation on the nucleosynthesis 125
5.1 Presupernova yields resulting from large network calculations . . . 125
5.2 Nucleosynthesis during hydrogen burning . . . 132
5.2.1 Depletion of light elements . . . 132
5.2.2 Production of ^{14}N . . . 133
5.2.3 Production of the radioactive isotope ^{26}Al . . . 133
5.2.4 Revised reaction rates and ^{17}O production . . . 134
5.3 Nucleosynthesis during helium burning and beyond . . . 135
5.3.1 Sodium . . . 135
5.3.2 ^{26}Al content in the presupernova models . . . 135
5.3.3 Neutron-rich isotopes of magnesium, silicon, and sulfur . . . 136
5.3.4 The s-process . . . 137
5.4 Nucleosynthesis in the growing helium shell . . . 138
5.4.1 Conversion of ^{14}N into ^{14}C and ^{18}O . . . 141
5.4.2 Fluorine . . . 142
5.4.3 Production of ^{15}N . . . 142
5.4.4 X-grains . . . 143
5.5 The influence of μ-barriers . . . 143
5.5.1 Nucleosynthesis in the envelope . . . 144
5.5.2 Core sizes and late nucleosynthesis . . . 144

6 Summary 147

A An improved treatment of nuclear burning in the STERN code 153
A.1 Simple reactions . . . 153
A.2 Self reactions . . . 156
A.3 Application . . . 158

B Improvement of hydrogen burning in the KEPLER code 159
B.1 Binding energy versus released energy . . . 159
B.2 Neutrino losses . . . 159
B.3 Implications . . . 160

C Nuclear reactions in STERN 161

D Surface abundance changes during the main sequence evolution 165

E Diagrams for the evolution of the internal stellar structure **169**
E.1 Explanation of the diagrams 169
E.2 Brief description of the evolutionary phases 170
E.3 Nuclear energy generation and neutrino losses 171

F Presupernova structure of the stars **195**

Bibliography **211**

Acknowledgements **219**

Curriculum vitae **221**

Chapter 1

Introduction

1.1 Massive star models with rotation

The quantitative theory of stellar structure is more than 100 years old (see Emden 1907) and our understanding of the stellar interior has improved dramatically during this time, especially since it became possible to construct detailed stellar models with the help of computers in the 1950's. Although many fundamental questions still remain in the field of low- and intermediate mass stars, their evolutionary path — i.e., their way from the main sequence through the red giant and asymptotic giant branch to the white dwarf stage — has been known in detail for several decades (see, for example, Iben 1974). Also, the principles of the evolution of massive stars' cores through the major nuclear fusion stages from hydrogen through silicon burning have been known for that long (e.g., Weaver, Zimmerman & Woosley 1978).

However, even today, our understanding of many observable properties of massive stars ($M_{\rm ZAMS} \gtrsim 8{\rm M}_\odot$, $\log L/{\rm L}_\odot \gtrsim 4$) remains rudimentary. For example, when in 1987 a blue supergiant exploded as a supernova in the Large Magellanic Cloud (Arnett et al. 1989) it was a surprise to the community. Another example: the observed dependence of the blue-to-red supergiant ratio on metallicity contradicts all existing stellar evolution calculations (Langer & Maeder 1995). Uncertainty surrounds not only the post-main sequence phase of massive stars. Many aspects of the core hydrogen burning evolution are still poorly understood. In the following it will be shown that much of the present uncertain state may be a consequence of the neglected effects of rotation.

The first to recognize the importance of rotation for celestial bodies was Sir Isaac Newton. Early studies of rotating, self-gravitating, incompressible fluids were carried out by McLaurin, Jakobi, Poincaré, and Schwarzschild. Important contributions for the numerical treatment of rotating stars were provided by Kippenhahn & Thomas (1970). Kippenhahn, Meyer-Hofmeister & Thomas (1970) performed calculations taking these effects into account and used a simple model for angular momentum transport. Studies with artificial rotation laws were carried out by Endal & Sofia (1976). In their pioneering work, Endal & Sofia (1978) considered several rotationally induced instabilities, made order-of-magnitude estimates for their efficiencies, and performed time-dependent stellar evolution calculations of rotating

massive stars up to the ignition of carbon burning. Later, Pinsonneault et al. (1989) introduced a parameterization of the poorly known efficiencies of the rotationally induced transport processes of Endal & Sofia (1978) and gauged them to solar models. The simulations of the present work are based largely on these two works.

A prescription for the turbulent mixing due to differential rotation by Zahn (1983); Maeder (1987) has been used by, e.g., Langer (1992), Denissenkov (1994) and Eryurt et al. (1994) for evolutionary models for O and B stars in the Milky Way and the Large Magellanic Cloud (LMC). Chaboyer & Zahn (1992), Zahn (1992), and Urpin, Shalybkov & Spruit (1996) developed a model for the interaction of meridional circulation and shear instabilities, resulting in a fourth order differential equation for the angular momentum transport. However, even this theory still contains free parameters to be gauged through observations. Model calculations of the main sequence evolution of massive stars with this prescription and modifications of it have been performed by, e.g., Talon et al. (1997) and Meynet (1997). More recently, Maeder & Zahn (1998) developed a model which also includes the effect of semiconvection. The model which will be presented here lacks some of the physical details of those very recent works but is simpler, easier to understand, and more easily extrapolable to the late stages of stellar evolution.

1.2 Observational evidence for stellar rotation

1.2.1 Rotation rates

The most direct method to determine the rotation rate of stars is the spectroscopic measurement of the widening of line profiles (e.g., Slettebak & Howard 1955; Slettebak et al. 1975). This is due to the Doppler shift of light emanating from different regions of the stellar surface. Because of the rotational motion some parts of the stellar surface move towards us (spectral line is blue shifted) while others recede from us (spectral line is red shifted). In a similar way the orbital motion of binary stars is measured, but in that case the the Doppler shift of the lines affects the whole surface of the star and the result is a variation of the Doppler shift with time. In the case of stellar rotation light with different amounts of Doppler shift reaches us at the same time and therefore the spectral line appears broadened. In both cases only that part of the motion which is parallel to the line of sight causes a measurable Doppler shift, while the movement perpendicular to the line of sight only causes the *quadratic* Doppler shift and is not measurable for "normal" stars. That is, only the fraction $v \sin \phi$ of the rotational velocity, v, parallel to the line of sight can be measured, where ϕ is the inclination angle of the rotation axis relative to the "plane" of the sky. Only in the exceptional case of eclipsing binaries is the inclination angle known. Unfortunately, these are mostly close binary systems and the rotation rate might be affected by their interaction (e.g., tidal forces, mass exchange). Binary stars are not considered in the present work. Thus, the true equatorial rotational velocities must be deconvolved from a sample of stars using a statistical model to get approximate mean values (Fukuda 1982).

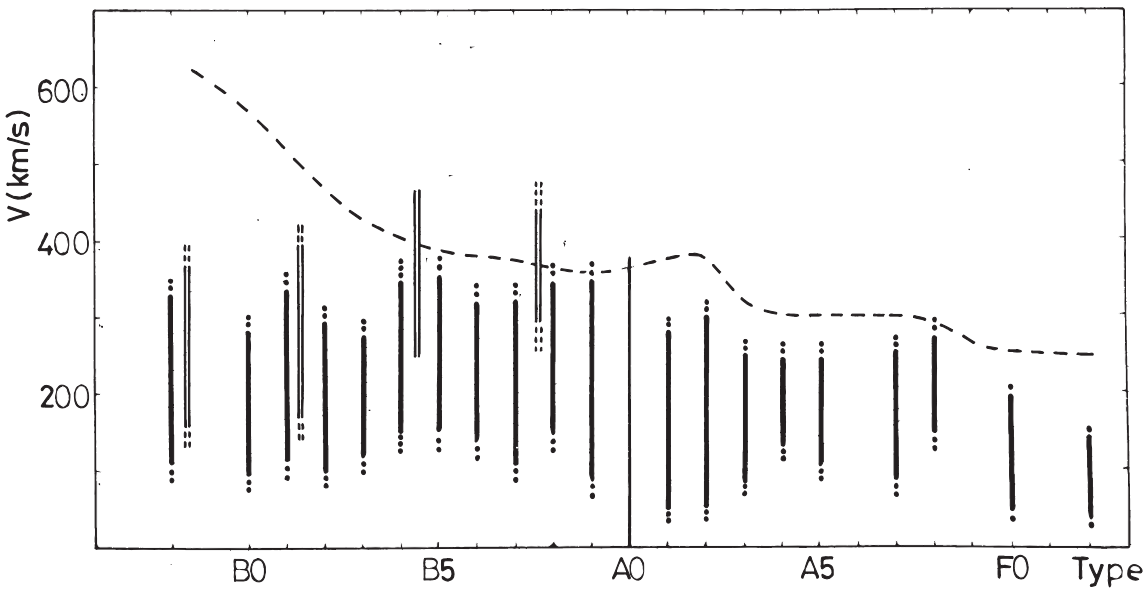

Figure 1.1: (from Fukuda 1982) Characteristic ranges of equatorial rotational velocities for normal field stars (thick lines) and for emission-line stars (double lines) as a function of spectral type. The dashes line approximates the breakup velocity, as calculated by Collins II (1974).

One finds typical mean rotation rates for dwarf single late B and early O stars, the kind of stars considered in the present work, of around $200\,\mathrm{km\,s^{-1}}$ (see Fig. 1.1; Slettebak 1970; Fukuda 1982; Halbedel 1996; Penny 1996; Howarth et al. 1997). This is about 30 % to 40 % of their break-up velocity (Sect. 2.4.2). Some of the stars actually rotate close to their break-up velocity (Fukuda 1982; Halbedel 1996). The emission line Be stars in general show higher mean rotation rates. The typical average equatorial rotation rates can reach as high as $400\,\mathrm{km\,s^{-1}}$ (Fukuda 1982).

1.2.2 Stellar winds

Other indications for stellar rotation are the deviation of the stellar mass loss from spherical symmetry. One example are the non-spherical winds observed for O and B stars, Be and B[e] stars. This asphericity can be reflected in the line profiles, e.g., the P-Cygni profiles, for mass losing hot stars (Fullerton 1997), in a polarization of the light (Bjorkman 1997) and an excess in the infra-red and radio flux (Fullerton 1997). The combined effects of a stellar wind and non-negligible rotation can range from a small density contrast between equator and pole, to the formation of a wind compressed region in the equator, or even to a wind compressed disk (Bjorkman & Cassinelli 1993). Be and B[e] stars show emission lines, an indication of high densities, as expected from the confinement of a large fraction of the stellar mass loss to the small opening angle of a disk. This can also be an indication of comparably high mass loss rates. However, the details of the processes which may or may not lead to disk-like structures in stellar winds are still not too well understood (Owocki & Gayley 1997).

A second type of phenomena where the effect of rotation becomes apparent

is the occurrence of circumstellar rings and deformed circumstellar shells (Langer, Heger & García-Segura 1998c). These shells and rings result from the interactions of the winds from different evolutionary phases of the stars and, occasionally, the ionizing radiation emanating from the star (García-Segura, Langer & Mac Low 1997; Meyer 1997). Many of these structures show a remarkable rotational symmetry and might be best explained by stellar rotation. An example is the ring system around Supernova 1987A (Fig. 1.2; Burrows 1994) or the ring found around the blue supergiant Sher 25 (Brandner et al. 1997). Examples of rotationally symmetric structures around stars with higher or lower mass than those considered in the present work are the "hour glass" nebula around Eta Carinae (Weis et al. 1997; Nota et al. 1997; Langer, García-Segura & Mac Low 1998b) or the bipolar shape of many planetary nebulae (García-Segura et al. 1998).

1.2.3 Surface abundance patterns

A more indirect, but nevertheless powerful, demonstration of the importance of stellar rotation are "peculiar" observed, i.e., deviations from the abundances found in the interstellar medium from which these stars formed. Thermonuclear reactions in the stellar interior may destroy or produce some isotopes at the expense of others, but since the thermonuclear processing depends sensitively on the temperature, below a specific threshold temperature no processing occurs during the lifetime of the star. Therefore, the surfaces of these stars are not expected to show processed material.

Striking surface abundance anomalies of massive stars comprise an enrichment of nitrogen, accompanied by low values of carbon and oxygen (Gies & Lambert 1992; Herrero 1994). In some of the more massive stars a notable enrichment of helium is also observed (Herrero et al. 1992). These abundance patterns are typical for hydrogen burning, and the corresponding processes take place only several solar masses below the surface — too deep to be uncovered by stellar winds during the main sequence evolution. An interesting feature is the depletion of boron, which is found to occur in most B-type stars (Venn, Lambert & Lemke 1996). It was in particular the observed boron versus nitrogen pattern in B-type stars which lead Fliegner, Langer & Venn (1996) to the conclusion that the surface abundance anomalies of massive main sequence stars could not, in general, be a consequence of close binary interaction.

All the above surface abundance peculiarities, which lead to discrepancies with standard evolutionary models of massive stars can be recovered by introducing one major effect of stellar rotation: the mixing of matter in the envelopes of massive main sequence stars (e.g., Langer et al. 1997a; Langer, Heger & Fliegner 1997b). It explains the enrichment of species produced deep inside the stars, and the depletion of fragile species, by transporting processed matter to the stellar surface.

An issue closely related to the surface enrichment is the so-called mass discrepancy for massive main sequence stars found by Herrero et al. (1992). They find that masses derived from the effective gravitational acceleration, as deduced from the spectrum, are much lower than those derived from standard stellar evolution

calculations (see also Vrancken et al. 1998). As will be shown, also this might be accounted for by additional internal mixing in rotating stars.

1.2.4 Internal stellar structure

Unlike its surface properties, the internal structure of a star, including its internal rotation, is not directly accessible to observations. An exception is the sun, where recent helioseismological data allows to derive the density profile and the rotation profile in the deep interior (Thompson et al. 1996). For other stars such extensive data is not available, and therefore only very little is known *from observations*.

Slowly pulsating B-type stars (SPBs; Waelkens 1987, 1991) might offer a possibility to learn about the internal structure of rotating stars in the future, when better pulsation data will become available. The slow pulsations of these stars are interpreted as g-modes (e.g., Gautschy & Saio 1993) which penetrate, and therefore probe, the deep stellar interior. Interestingly, observations (Waelkens et al. 1998) show that most of the SPBs are slow rotators. Ushomirsky & Bildsten (1998) find that rotational effects become important for the pulsations only for rotational periods comparable or higher than the pulsation period, while the observed SPBs mostly show much lower projected rotational velocities. Ushomirsky & Bildsten (1998) do not expect the centrifugal forces being responsible for the suppression of these pulsations. They conclude that this might be an observational selection effect. However, the g-mode excitation depends on the chemical composition[1] and therefore may be affected by rotationally induced mixing in the radiative envelope of the star (Bildsten 1998).

However, today the determination of the internal structure and rotation rate of main sequence stars other than our sun from stellar seismology is not yet possible. This problem gets even worse when it comes to the internal rotation of massive post-main sequence stars and their evolution until core collapse. Only the predictions of theoretical models for nucleosynthesis, supernovae explosions and their remnants can to be compared to the corresponding observational data.

1.3 Type II supernovae and nucleosynthesis

Single massive stars born with a mass of eight times the mass of our sun or more, develop a collapsing core, consisting mostly of elements of the iron group ("iron core") at the end of their evolution and terminate their lives as spectacular explosions known as supernovae. The remnant of such a supernova is either a neutron star or a black hole. Less massive stars become asymptotic giant branch stars, and lose their hydrogen-rich envelopes in a strong stellar wind, leaving behind a degenerate core,

[1] More precisely, it depends on the Brunt-Väisälä frequency N with $N^2 := \frac{g\delta}{H_P}\left(\nabla_{ad} - \nabla + \frac{\varphi}{\delta}\nabla_\mu\right)$ (Sect. 2.2.1.1; Kippenhahn & Weigert 1991) and thereby changes in the presence of composition *gradients*. This may change the excitation pattern of g-modes inside the star and by that suppress them. Since the composition gradients take some time to build up, one would expect to see pulsations in some, the youngest, of the fast rotators, too.

a white dwarf consisting of helium, carbon and heavier elements up to magnesium. For solitary white dwarfs no additional thermonuclear burning occurs and the star ends its life as a cooling ember.

Different types of supernovae are classified by their observational properties. The major classes are Type I supernovae, which do not show hydrogen lines in their spectra, and Type II supernovae where hydrogen lines are clearly present (Minkowski 1941). Type I supernovae are subclassified spectroscopically (Harkness & Wheeler 1990) as Type Ia (about 80 %; Filippenko 1997), which do show a particular silicon feature in their spectra and are thought to be thermonuclear detonations of white dwarfs (Hoyle & Fowler 1960; Nomoto, Thielemann & Yoki 1984; Woosley & Weaver 1986), and Type Ib/Ic supernovae, which are thought to be core-collapse events occurring in massive stars which have lost their hydrogen-rich envelope. The absence of a helium feature in the spectrum distinguishes Type Ic supernovae from Type Ib (Harkness & Wheeler 1990). The loss of the envelope can be due to extensive mass loss or interactions with binary companion stars (Woosley 1990). The two major groups of Type II supernovae are subclassified photometrically for different shapes of their light curves, i.e., the evolution of the luminosity as a function of time. Depending on whether the luminosity drops linearly after the maximum or shows a marked plateau they are classified as Type II-L or II-P supernovae, respectively (Harkness & Wheeler 1990; Leibundgut 1995; Filippenko 1997). From theoretical models the main ingredients affecting the display of Type II supernovae are differences in the structure of the stellar envelope at the time of explosion (Leibundgut 1996), i.e., e.g., how much mass the hydrogen-rich envelope contains and how extended it is.

The famous example of a Type II supernovae event is the supernova which occurred on February 23, 1987 in the Large Magellanic Cloud, a companion galaxy of the Milky Way, and was cataloged as SN 1987A. It was the by far closest supernova since centuries and opened unprecedented possibilities for observation and the testing of theoretical models. However, to the surprise of the scientific community, the stellar progenitor of this supernovae was a blue supergiant (Gilmozzi et al. 1987) with an effective surface temperature of more than 15 000 K and a radius of several tens times that of our sun. In contrast, according to theoretical models and analyses of many Type II supernova light curves most of the Type II supernovae progenitor stars are expected to be red supergiants, which have effective surface temperatures of 3 000 K to 4 000 K and radii of several hundreds to thousands times that of our sun at the instant of explosion (Eastman et al. 1994). Therefore SN 1987A might be an exception than a normal case. One important influence on the properties of the star at the end of its evolution is its initial composition, i.e., the matter the star forms from, which is different in the less evolved LMC than in the vicinity of our sun.

A completely unexpected, spectacular feature of SN 1987A was a nebulae system of three rings around it (Fig. 1.2; Plait et al. 1995; Burrows et al. 1995), which originates from the presupernova star and was ionized by the flash of the supernova explosion. The "inner" ring surrounds the supernova and is bright and small. The two "outer" rings are larger but fainter and of about equal size. They are located above and below the plane defined by the inner ring. All three rings share the

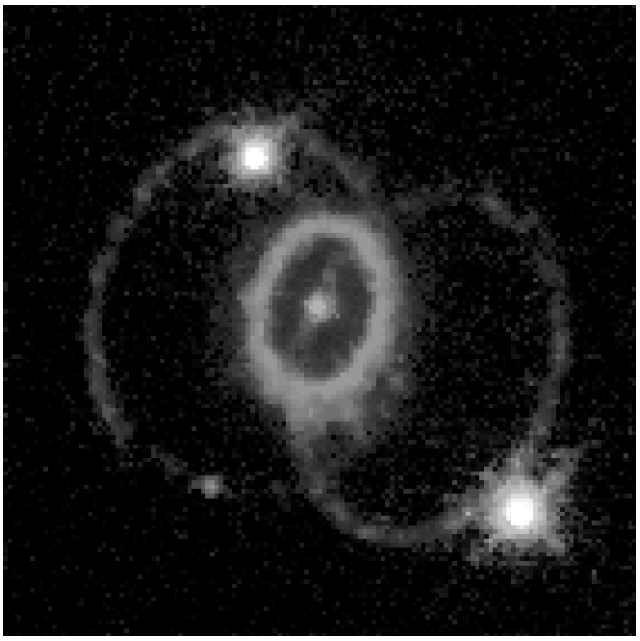

Figure 1.2: Triple ring structure around supernova SN 1987A observed by the Hubble Space Telescope on February 1994 (Burrows 1994). The supernova is located in the center of the inner ring. The two bright spots below the upper edge of the left ring and in the bottom right corner are foreground stars and not associated with the supernova.

same axis of rotational symmetry, which passes through the supernova itself. This symmetry may be a hint that rotation played an important role in the evolution of the progenitor star of this supernova — and be interference maybe in the evolution of most of the massive stars. However, it is not yet clear whether the progenitor star of SN 1987A was a rotating single star or the result of the interaction with a close binary companion (Podsiadlowski 1998; Woosley et al. 1998).

The massive stars which become core-collapse supernovae are the principal agents of nucleosynthesis and chemical evolution of galaxies (Timmes, Woosley & Weaver 1995). They are responsible for the production of most of the elements between oxygen and calcium in the periodic system of elements (Timmes et al. 1995; Woosley & Weaver 1995; Thielemann, Nomoto & Hashimoto 1996), and maybe half of the iron (Tsujimoto et al. 1995). Most of the nuclei produced by the slow neutron capture process (s-process; Mathews & Ward 1985) up to a mass number of $A = 90$ (Langer, Arcoragi & Arnould 1989; Arcoragi, Langer & Arnould 1991) and probably those produced by the rapid neutron capture process (r-process; Mathews & Ward 1985) nuclei (Burbidge et al. 1957) originate from these stars.

An interesting question related to the internal rotation rate of massive stars is the rotation rate of the newly born neutron stars which form from the collapsing core of the star. In the present work, for the first time, the evolution of rotating stars is followed from the main sequence up to onset of core collapse in consistent stellar evolutionary models. A challenge to the present work is the study by Spruit & Phinney (1998) who claim that the transport of angular momentum is dominated by magnetic fields during the late stages of stellar evolution. However, their result is based upon simplifying assumptions on the behavior of the magnetic field inside stars — which are even less understood and investigated than those of plain rotation. In the present work, magnetic fields are ignored.

1.4 Organization of this work

In the present work models of rotating stars with approximately solar composition in the mass range from $8\,M_\odot$ up to $25\,M_\odot$ are investigated. These stars evolve to core collapse but keep a hydrogen-rich envelope until the supernova explosion. Thus they are the typical progenitor stars of Type II supernovae.

In Chapter 2 the basic equations governing stellar evolution, the input physics used, the treatment of rotating stars and a brief description of the numerical method is given. Transport processes in the stellar interior induced by rotation and its influence on the mass loss rate are discussed. In Chapter 3 the evolution the internal structure of rotating stars from central hydrogen ignition until core collapse, to about 1 s before core bounce, is investigated for various initial masses. Stellar models with different initial rotational velocities and different assumptions about the rotationally induced mixing processes are compared. Implications for the supernovae and their remnants are discussed. Features of the rotating stars accessible to observations are studied in Chapter 4. That is, e.g., the evolution of luminosity, surface rotational velocity and chemical composition is investigated. A mechanism which spins up stars during the transition from red to blue supergiants is discussed. It can lead to critical rotation at the surface of the star during that phase, and may even explain the inner ring of SN 1987A. Pulsational properties of the stars with high luminosity-to-mass ratio, caused by the rotationally induced mixing, are examined and implications for the circumstellar matter around Type II supernova progenitors are surveyed. A detailed study of the nucleosynthesis in rotating stars until core collapse is given in Chapter 5, where a 200 isotope network is used to follow the evolution of rotating $12\,M_\odot$ and $15\,M_\odot$ stars. The results are compared with calculations of Weaver & Woosley (1995) and observational constraints.

Appendices A and B list improvements included in the two different stellar evolution codes used, STERN and KEPLER, respectively, and Appendix C lists all nuclear reactions included in STERN. Appendix D compiles figures of the evolution of surface abundances and surface isotope ratios. In Appendix E, plots of the temporal evolution of the internal stellar structure of the models, from the birth of the star until core collapse, are shown. Appendix F gives the pre-collapse structure of stellar models.

Chapter 2

Numerical method and input physics

2.1 Basic equations

2.1.1 Hydrodynamic stellar structure equations

The structure and evolution of stars is governed by a set of partial differential equations, the so-called *stellar structure equations*. In this work, the *hydrodynamic* version, which includes inertia terms, is used. In case of a non-rotating, spherically symmetric star these equations take the following form:

$$\left(\frac{\partial r}{\partial m}\right)_t = \frac{1}{4\pi r^2 \rho} \tag{2.1}$$

$$\left(\frac{\partial r}{\partial t}\right)_m = u \tag{2.2}$$

$$\left(\frac{\partial P}{\partial m}\right)_t = \frac{Gm}{4\pi r^4} - \frac{1}{4\pi r^2}\left(\frac{\partial u}{\partial t}\right)_m \tag{2.3}$$

$$\left(\frac{\partial l}{\partial m}\right)_t = \varepsilon_{\mathrm{n}} + \varepsilon_\nu + \frac{P}{\rho^2}\left(\frac{\partial \rho}{\partial t}\right)_m - \left(\frac{\partial \epsilon}{\partial t}\right)_m \tag{2.4}$$

$$\left(\frac{\partial T}{\partial m}\right)_t = -\nabla \frac{GmT}{4\pi r^4 P}\left[1 + \frac{r^2}{Gm}\left(\frac{\partial u}{\partial t}\right)_m\right] \tag{2.5}$$

(Langer et al. 1988). A detailed discussion and derivation of these equations can be found, e.g., in Cox & Giuli (1968); Kippenhahn & Weigert (1991). Here r is the radial distance from the center of the star, ρ, the density, u, the radial velocity, P, the pressure, T, the temperature, l, the local luminosity, ϵ, the internal energy per unit

mass, and G, the gravitational constant. The energy release due to thermonuclear burning is denoted $\varepsilon_{\rm n}$ and the contribution of local heat losses due to neutrinos is ε_ν (inherently negative). The two independent variables are the time t and the mass coordinate $m(r) = \int_0^r 4\pi r^2 \rho \, {\rm d}r$, as defined by Eq. (2.1). The latter ranges from $m = 0$ at the center to the total mass of the star, $m = M$, at the stellar "surface". The total mass of the star is actually a function of time, $M = M(t)$ due to mass accretion and mass loss from the surface (Sect. 2.4).

In radiative zones the temperature gradient

$$\nabla := \frac{{\rm d}\ln T}{{\rm d}\ln P} := \left(\frac{\partial \ln T}{\partial \ln P}\right)_t \tag{2.6}$$

is given by the radiative temperature gradient

$$\nabla_{\rm rad} = \frac{3}{16\pi acG}\frac{\kappa l P}{m T^4}\left[1 + \frac{r^2}{Gm}\left(\frac{\partial u}{\partial t}\right)_m\right]^{-1} , \tag{2.7}$$

where a is the radiation constant, c, the velocity of light, and κ, the Rosseland mean opacity. In this work the opacities are taken from the recent OPAL tables (Iglesias & Rogers 1996) and from Alexander (1994) and Alexander & Fergusson (1994) for low temperatures. For high temperatures and metallicities $Z > 0.1$ the Los Alamos opacities (Huebener et al. 1964) are used. In convective regions ∇ is determined from the mixing-length theory (MLT; Prantl 1925; Vitense 1953; Böhm-Vitense 1958).

2.1.2 Modification to the equations in rotating stars

In rotating stars, centrifugal forces act on the matter and lead to deviations from spherical symmetry. For slow to moderate rotation these deformations remain rotationally symmetric (Tassoul 1978). Only if the rotational energy exceeds a notable fraction of the binding energy of the star is genuine triaxial deformation energetically favorable. The case of rigidly rotating, self-gravitating, incompressible, and inviscid fluids was already studied by McLaurin in the 18th century. More general studies are, e.g., that of polytropic gaseous spheres performed by Ostriker & Bodenheimer (1973) (see also Eriguchi & Müller 1985).

In this work, however, only the case of "slow" rotation is considered, i.e., where no triaxial deformations are expected. Some stars may reach "critical" rotation (Sect. 2.4.2) at the surface during some short stages of their evolution (Sect. 4.3). However, this affects only the very outermost layers of the stars and is not expected to have any major influence on the vast inner part of the stars.

Even for the case of slow rotation, the shapes of equipotential surfaces are affected by the centrifugal potential and therefore deviate from spherical symmetry. The momentum equation and the energy transport equation for spherically symmetric stars have to be modified in order to take this effect into account.

In this work, the centrifugal force is included according to the method described by Kippenhahn & Thomas (1970) in the approximation of Endal & Sofia (1976) and applied to the hydrodynamic stellar structure equations (Fliegner 1993). In this

approach, mass shells correspond to equipotential surfaces of the effective potential ψ which includes gravity and rotation, instead of spherical shells. Corrections are applied to the acceleration and the radiative temperature gradient. According to Zahn (1975), Chaboyer & Zahn (1992), and Zahn (1992), anisotropic turbulence acts much stronger on isobars, which coincide with the equipotential surfaces, than in the perpendicular direction. This enforces "shellular" rotation rather than cylindrical rotation (see also Meynet & Maeder 1997), and it sweeps out compositional differences on equipotential surfaces. Therefore it can be assumed that the matter on equipotential surfaces is chemically homogeneous. Together with the shellular rotation this allows one to retain the one-dimensional approximation. The specific angular momentum, j, of such a mass shell is treated as a local variable and the angular velocity, ω, is computed from the specific moment of inertia, i. The time-dependent redistribution of j is described in Sect. 2.2.4, its influence on transport processes in Sect. 2.2.2, and the modification to the stellar structure equations of non-rotating stars are outlined in the following.

Let V_ψ be the volume enclosed by an equipotential surface of the potential ψ and $S_\psi := \partial V_\psi$ its surface area. Then its "radius" r_ψ is defined as the radius of a sphere of the same volume by $V_\psi = 4\pi {r_\psi}^3/3$, and the basic form of the equation of continuity, Eq. (2.1), does not change:

$$\left(\frac{\partial m_\psi}{\partial r_\psi}\right)_t = 4\pi {r_\psi}^2 \rho \ . \tag{2.8}$$

For quantities varying on equipotential surfaces, a mean value is defined by

$$\langle \cdot \rangle := \frac{1}{S_\psi} \oint_{S_\psi} \cdot \ \mathrm{d}o \ , \tag{2.9}$$

where $\mathrm{d}o$ is an element of surface area. The effective gravitational acceleration is defined by the gradient of the potential, $\mathbf{g} := \nabla\psi$, which is normal to S_ψ. For the equation of momentum balance, Eq. (2.3), one finds (Endal & Sofia 1976)

$$\left(\frac{\partial P}{\partial m_\psi}\right)_t = -\frac{G m_\psi}{4\pi {r_\psi}^4} f_\mathrm{P} - \frac{1}{4\pi {r_\psi}^2}\left(\frac{\partial^2 r_\psi}{\partial t^2}\right)_{m_\psi} \ , \tag{2.10}$$

where the inertia term (last term) is added here. The influence of rotation is described by f_P, which is defined as

$$f_\mathrm{P} := \frac{4\pi {r_\psi}^4}{G m_\psi S_\psi} \langle g^{-1} \rangle^{-1} \ , \tag{2.11}$$

where $g = |\mathbf{g}|$. The radiative temperature gradient in Eq. (2.5) is replaced by

$$\left(\frac{\partial \ln T}{\partial \ln P}\right)_t = \frac{3\kappa}{16\pi acG}\frac{P}{T^4}\frac{L_\psi}{m_\psi}\frac{f_\mathrm{T}}{f_\mathrm{P}}\left[1 + \frac{{r_\psi}^2}{G m_\psi f_\mathrm{P}}\left(\frac{\partial^2 r_\psi}{\partial t^2}\right)_{m_\psi}\right]^{-1} \ . \tag{2.12}$$

The last factor on the right hand side is included to account for inertia as it follows from the momentum equation (Fliegner 1993), and

$$f_{\mathrm{T}} := \left(\frac{4\pi {r_\psi}^2}{S_\psi}\right)^2 \left(\langle g\rangle\langle g^{-1}\rangle\right)^{-1} . \tag{2.13}$$

For a derivation of these formulae and for the numerical evaluation of f_{T} and f_{P} see Endal & Sofia (1976). The equations for f_{T} and f_{P} are solved iteratively with the stellar structure equations (Sect. 2.1.6) in order to obtain consistent models (Endal & Sofia 1976; Fliegner 1993). In the rest of this work the index ψ is skipped.

Note that there is, in principle, an inconsistency between the assumption of shellular rotation and the method described by Kippenhahn & Thomas (1970), i.e., the assumption of shellular rotation does not generally lead to a conservative potential as it were the case for constant rotation rate on cylinders, which is used by Kippenhahn & Thomas (1970). However, Meynet & Maeder (1997) show that replacing the average $\langle \cdot \rangle$ by "appropriate mean values", i.e., reinterpreting the quantities describing the stellar structure as the mean values over the isobars, allows one to keep the formalism of Kippenhahn & Thomas (1970) as a good approximation.

2.1.3 Boundary conditions

For the system of first order partial differential equations, Eqs. (2.1-2.5), five boundary condition have to be satisfied.

At mass coordinate $m = 0$, the center of the star, the three natural boundary conditions are: $l = u = r = 0$.

The two remaining conditions are outer boundary conditions. These are chosen at the photosphere, i.e., at an optical depth $\tau(r) = \int_r^\infty \kappa\rho \,\mathrm{d}r = 2/3$, except for Wolf-Rayet stars, where an analytic, optically thick, grey, spherical wind model is used (Langer 1989a; Heger & Langer 1996). At the outer boundary the mass coordinate is set to $m = M$; the mass of the atmosphere is neglected.

The first outer boundary condition is given by Stefan-Boltzmann's law:

$$L = 4\pi R^2 \sigma {T_{\mathrm{eff}}}^4 . \tag{2.14}$$

It relates the stellar luminosity $L := l(M)$, the stellar radius $R := r(M)$ and the temperature $T_{\mathrm{eff}} := T(M)$.

The second condition assumes a plane-parallel static grey atmosphere and is approximated similar to Appenzeller (1970). It gives the density at $\tau = 2/3$:

$$\rho(M) \approx \frac{2\mu}{3\kappa\Re T_{\mathrm{eff}}}\left(1 - \frac{\kappa L}{4\pi c G M}\right)\left[\frac{GM}{R^2} + \left(\frac{\partial u}{\partial t}\right)_{m=M}\right] . \tag{2.15}$$

Here $\Re$ is the gas constant and μ is the mean molecular weight, defined by

$$\mu := \left(\sum_i \frac{X_i(1+Z_i)}{\mu_i}\right)^{-1} , \tag{2.16}$$

isotope	mass fraction	isotope	mass fraction	isotope	mass fraction
^{1}H	$7.00{\cdot}10^{-1}$	^{14}N	$1.07{\cdot}10^{-3}$	^{24}Mg	$5.60{\cdot}10^{-4}$
^{3}He	$3.78{\cdot}10^{-5}$	^{15}N	$3.92{\cdot}10^{-6}$	^{25}Mg	$7.09{\cdot}10^{-5}$
^{4}He	$2.80{\cdot}10^{-1}$	^{16}O	$1.04{\cdot}10^{-3}$	^{26}Mg	$7.81{\cdot}10^{-5}$
^{6}Li	$6.69{\cdot}10^{-10}$	^{17}O	$3.95{\cdot}10^{-6}$	^{27}Al	$6.24{\cdot}10^{-5}$
^{7}Li	$9.63{\cdot}10^{-9}$	^{18}O	$2.08{\cdot}10^{-5}$	^{28}Si	$7.08{\cdot}10^{-4}$
^{9}Be	$1.72{\cdot}10^{-10}$	^{19}F	$3.89{\cdot}10^{-7}$	^{29}Si	$3.58{\cdot}10^{-5}$
^{10}B	$1.04{\cdot}10^{-9}$	^{20}Ne	$1.77{\cdot}10^{-3}$	^{30}Si	$2.37{\cdot}10^{-5}$
^{11}B	$4.92{\cdot}10^{-9}$	^{21}Ne	$4.31{\cdot}10^{-6}$	^{56}Fe	$1.37{\cdot}10^{-3}$
^{12}C	$3.62{\cdot}10^{-3}$	^{22}Ne	$1.29{\cdot}10^{-4}$		
^{13}C	$4.03{\cdot}10^{-5}$	^{23}Na	$3.60{\cdot}10^{-5}$		

Table 2.1: Initial isotopic mass fractions for the models computed with the STERN code (Sect. 2.1.6.1). They are taken from Grevesse & Noels (1993). The initial abundances of the radioactive isotopes ^{7}Be, ^{8}B, ^{11}C, ^{12}N, and ^{26}Al, and that of ^{2}H are set to zero.

where the sum runs over all species i, and X_i, Z_i and μ_i are the mass fraction, number of free electrons, and molecular weight of species i, respectively (Kippenhahn & Weigert 1991)[1]. In rotating stars the surface temperature is also a function of latitude (von Zeipel 1924a; Owocki & Gayley 1997; Meynet & Maeder 1997). In the above approach, the mean effective temperature of the star is considered; rotation enters only by its influence on the stellar radius ($R = r_\psi(m)$).

2.1.4 Initial conditions

The initial model for the calculations presented in this work is that of a fully convective, rigidly rotating pre-main sequence star. In the Hertzsprung-Russell (HR) diagram such stars are located on their Hayashi line. These models are constructed from the Lane-Emden equation (Kippenhahn & Weigert 1991) with a polytropic index of $n = 3/2$. Typically, initial stellar radii around $1\,000\,\mathrm{R}_\odot$ are used. This kind of initial condition is for computational convenience only and does not intend to reproduce the true pre-main sequence evolution (see also Beech & Mitalas 1994; Bernasconi & Maeder 1996).

The influence of rotation on the stellar structure is negligible in the initial models; it becomes more important when the stars contract towards central hydrogen ignition. The initial rotation rate is adjusted such that the stars settle at the desired equatorial rotation rate on the main sequence, where close-to rigid rotation establishes throughout the star, mainly by the action of Eddington-Sweet circulation (Sect. 2.2.2.4) and the Goldreich-Schubert-Fricke instability (Sect. 2.2.2.5). Almost none of the star's initial angular momentum is lost before it reaches the main sequence.

All models in this work use an approximately solar initial chemical composition

[1] A rough estimate of the mean molecular weight μ at typical compositions for hydrogen burning is given by $\mu \approx 4/(2 + 6X_{\mathrm{H}} + X_{\mathrm{He}})$, where X_{H} and X_{He} are the mass fractions of hydrogen and helium, respectively.

isotope	mass fraction	isotope	mass fraction	isotope	mass fraction
^{1}H	$7.0000{\cdot}10^{-1}$	^{16}O	$1.0175{\cdot}10^{-2}$	^{36}Ar	$1.0176{\cdot}10^{-4}$
^{3}He	$2.9798{\cdot}10^{-5}$	^{20}Ne	$1.8545{\cdot}10^{-3}$	^{40}Ca	$6.9515{\cdot}10^{-5}$
^{4}He	$2.7997{\cdot}10^{-1}$	^{24}Mg	$7.3366{\cdot}10^{-4}$	^{48}Cr	$3.1177{\cdot}10^{-6}$
^{12}C	$3.2467{\cdot}10^{-3}$	^{28}Si	$8.1332{\cdot}10^{-4}$	^{52}Fe	$1.9180{\cdot}10^{-5}$
^{14}N	$1.1732{\cdot}10^{-3}$	^{32}S	$4.5056{\cdot}10^{-4}$	^{54}Fe	$1.3594{\cdot}10^{-3}$

Table 2.2: Initial isotopic mass fractions for the models computed with the KEPLER code (Sect. 2.1.6.2). The initial abundances of the radioactive isotopes ^{44}Ti and ^{56}Ni are set to zero.

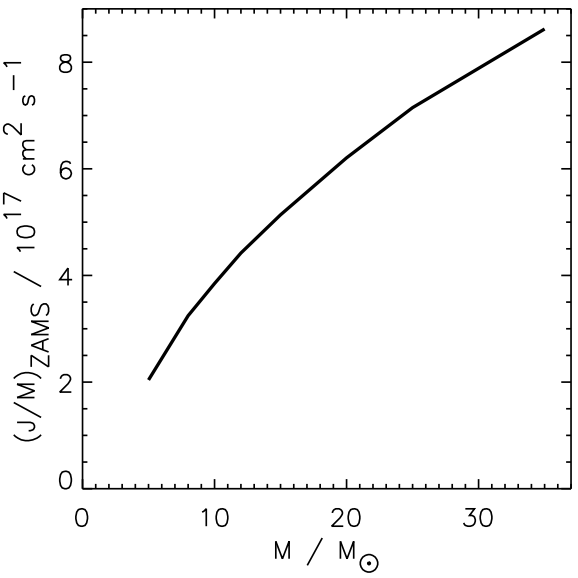

Figure 2.1: Specific angular momentum J/M of ZAMS models with an equatorial rotation rate of $200\,\mathrm{km\,s^{-1}}$ as a function of mass for stars of solar composition.

with a mass fraction of all elements heavier than helium ("metals") of $Z = 0.02$. The mass fractions of hydrogen and helium are set to $X = 0.7$ and $Y = 1 - X - Z = 0.28$, respectively. In STERN (Sect. 2.1.6.1), the abundance ratios of the isotopes within each of these groups are chosen to have the solar system meteoritic abundance ratios according to Grevesse & Noels (1993) (see Table 2.1). Calculations performed with the KEPLER code (Sect. 2.1.6.2) start on the pre-main sequence with a relative distribution of the metals according to Anders & Grevesse (1989) as given in Table 2.2.

For the main set of models in this work the initial angular momentum is determined such that the stars reach a rotational velocity of $\sim 200\,\mathrm{km\,s^{-1}}$ on the zero-age main sequence (ZAMS). This is a typical empirical value for the stars considered in the present work, i.e., for the mass range $8\,\mathrm{M_\odot} \ldots 25\,\mathrm{M_\odot}$ (Slettebak 1970; Fukuda 1982; Halbedel 1996; Penny 1996; Howarth et al. 1997). This corresponds to $\sim 35\,\%$ of their "critical" rotation speed (Sect. 2.4.2). Also models with different rotation rates are computed, in order to investigate the influence of this parameter on the evolution of massive stars.

Since the radius and density structure of stars change with their initial mass, the total angular momentum needed for a given rotation rate on the zero-age main sequence is not strictly proportional to the total mass. In Fig. 2.1 the average

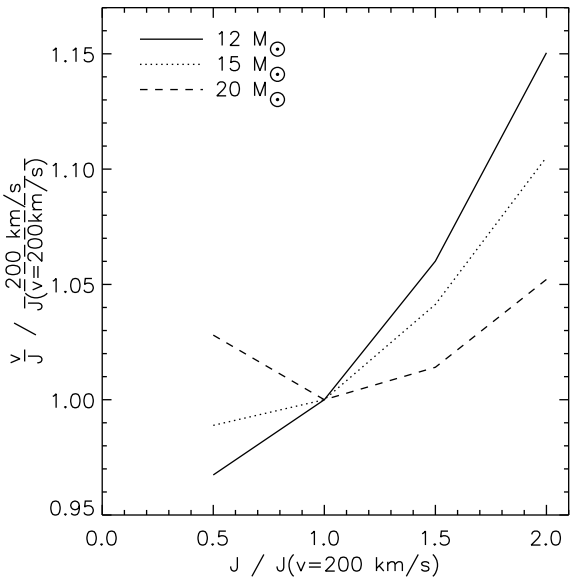

Figure 2.2: Ratio v/J of the equatorial rotational velocity at the surface, v, to the initial angular momentum, J, as a function of the initial angular momentum for three different masses, $12\,M_\odot$, $15\,M_\odot$, and $20\,M_\odot$. Both v and J are given in units of the corresponding model with $v \approx 200\,\mathrm{km\,s^{-1}}$.

specific angular momenta, J/M, of models with a rotational velocity of $200\,\mathrm{km\,s^{-1}}$ at core hydrogen ignition are shown as a function of total mass. The increase of J/M is due to the lower density of more massive main sequence stars.

Also, the rotational velocity of the stars does not change linearly with their initial angular momentum. In Fig. 2.2, the ratio of rotational velocity to angular momentum is shown as a function of the initial angular momentum of the stars for different initial masses. If there were a linear relation between the angular momentum and the rotation rate, all curves in this diagram would be horizontal. But due to the reduction of the effective gravity by centrifugal forces, the stars expand (Fig. 2.3C). Since the stellar radius increases faster than the total momentum of inertia of the star, the surface rotation increases more rapidly than the initial angular momentum. The opposite trend occurs for the slowest rotating $20\,M_\odot$ model in Fig. 2.2 occurs because the opacity, which strongly affects the structure of the outer layers of the stars, is a sensitive function of temperature and density. At the same time the effective temperature and the luminosity of the stars drop as the rotation rate increases (Fig. 2.3A and B), and therefore the star is not at the position of a non-rotating zero-age main sequence star of the same effective temperature in the HR diagram, but instead has a larger radius and higher luminosity. Both effects are more important for the lower masses because they are closer to their critical rotation rate (Sect. 2.4.2).

2.1.5 Thermonuclear reactions

Thermonuclear burning constitutes the main energy source of stars during most of their lifetime. However, this process also alters the chemical composition of the star. The changes in composition due to burning are given by

$$\left(\frac{\mathrm{d}Y_i}{\mathrm{d}t}\right)_{\mathrm{nuc}} = \sum_{\substack{\alpha_k,\alpha_l,\ldots,\alpha_i,\ldots \\ \beta_k,\beta_l,\ldots,\beta_i,\ldots}} \lambda_{\alpha_k k+\alpha_l l+\ldots\rightarrow\beta_k k+\beta_l l+\ldots} \frac{\beta_i-\alpha_i}{\alpha_k!\alpha_l!\ldots} Y_k^{\alpha_k} Y_l^{\alpha_l} \ldots \tag{2.17}$$

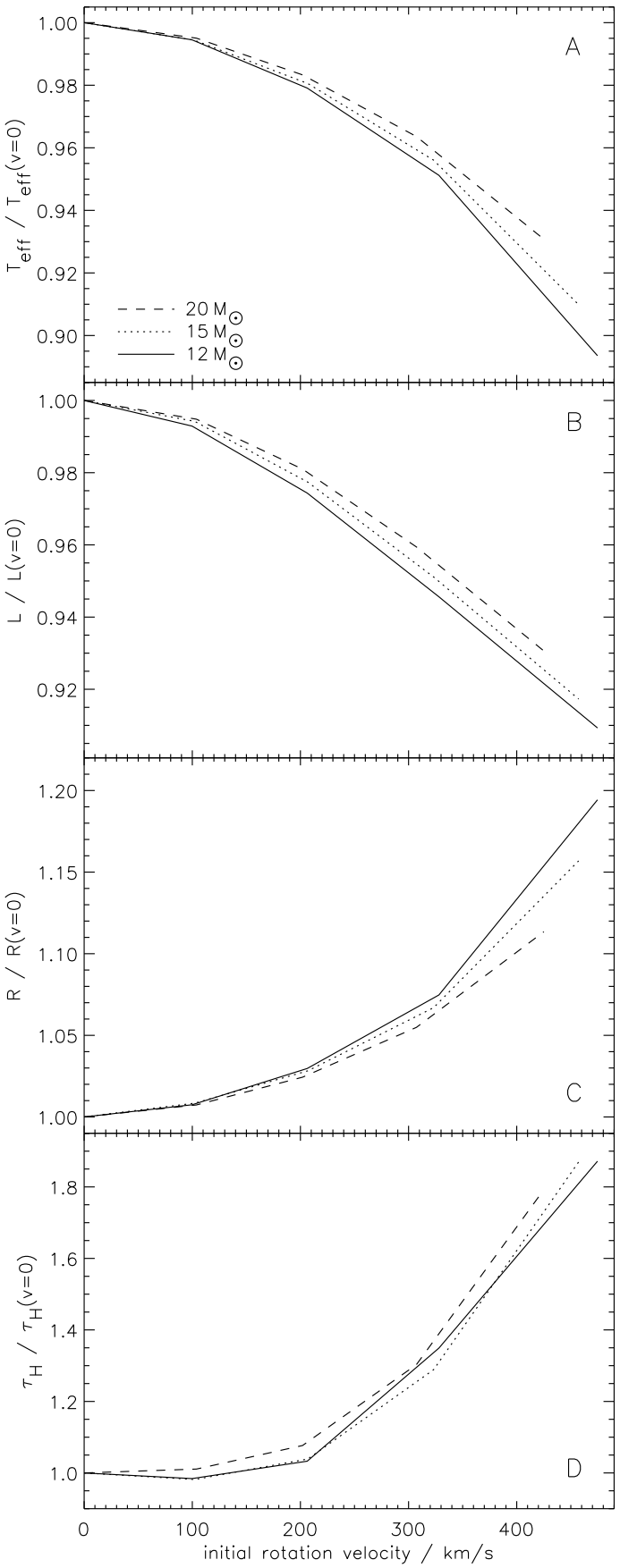

Figure 2.3: Effective temperature $T_{\rm eff}$ (Panel **A**), luminosity L (Panel **B**), stellar radius R (Panel **C**), and main sequence lifetime $\tau_{\rm MS}$ (Panel **D**) in units of the corresponding values for non-rotating stars, as a function of the equatorial surface rotation rate at hydrogen ignition for three different stellar masses, 12, 15, and 20 $\rm M_\odot$.

with

$$Y_i = \frac{X_i}{A_i} \,, \qquad \left(\frac{\mathrm{d}Y_i}{\mathrm{d}t}\right)_{\mathrm{nuc}} = \frac{1}{A_i}\left(\frac{\mathrm{d}X_i}{\mathrm{d}t}\right)_{\mathrm{nuc}} \tag{2.18}$$

(Arnett 1996), where A_i is the mass number of the isotope i and Y_i its abundance (in moles per gram). The reaction rates, λ, mostly depend on density and temperature only, except for, e.g., electron screening effects, which are treated according to Itoh, Kuwashima & Munakata (1990). The summation runs over the number of particles of all species $k, l, \ldots$ of reactants ($\alpha_k, \alpha_l, \ldots \in \mathbb{N}_0$) and products ($\beta_k, \beta_l, \ldots \in \mathbb{N}_0$) involved in a reaction such that every possible reaction $\alpha_k k + \alpha_l l + \ldots \rightarrow \beta_k k + \beta_l l + \ldots$ is included in Eq. (2.17). For practical purposes, the numerical solution of this equation, however, takes into account only a fraction of all species and possible reactions (see Sect. 2.1.6). A more detailed description of thermonuclear reactions and nuclear networks is given, e.g., in Clayton (1968). The dominant reactions in stars are simple binary reactions like proton, neutron, and α captures, the triple α process during helium burning, heavy ion reaction like $^{12}\mathrm{C}+^{12}\mathrm{C}$ and $^{16}\mathrm{O}+^{16}\mathrm{O}$, photo-disintegration, and weak interactions like β^+ decay, β^- decay, and electron capture.

The energy release due to thermonuclear burning ε_{n} can be determined from the reaction rates and the energy release per reaction (Sect. 2.1.6.1), or from the changes in the sum of rest masses of all isotopes (Sect. 2.1.6.2).

2.1.6 Numerical solution

The stellar structure equations are a system of partial differential equations containing five independent unknown functions (r, u, l, T, and ρ) which depend on the two independent variables t and m. For numerical solution the problem is discretized in space (i.e., in the mass coordinate m in the Lagrangian codes used in this work) and time. Starting from an initial model (Sect. 2.1.4), subsequent (in time) models are obtained by solving this system of equations and its boundary conditions iteratively by a multi-dimensional Newton-Raphson solver. This method usually is referred to as the Henyey method (Hofmeister, Kippenhahn & Weigert 1964).

Two different numerical stellar evolution codes are used in this work. They are briefly described in the following.

2.1.6.1 STERN

One of the codes used in this work is a pseudo-Lagrangian, hydrodynamic code (Langer et al. 1988), based on the "Göttinger stellar evolution code". For numerical solution, the mass coordinate m is replaced by the relative mass coordinate $q := m/M$. If the stellar mass remains constant, the stellar structure equations displayed in Sect. 2.1.1 remain unchanged except for a constant positive factor $1/M$. In case the stellar mass changes with time, e.g., by mass loss, additional advection terms

arise and the time derivative has to be replaced by

$$\left(\frac{\partial}{\partial t}\right)_m = \left(\frac{\partial}{\partial t}\right)_q - q\frac{\dot{M}}{M}\left(\frac{\partial}{\partial q}\right)_t , \tag{2.19}$$

where

$$\dot{M} := -\frac{\mathrm{d}M}{\mathrm{d}t} \tag{2.20}$$

is the mass loss rate. With this replacement the stellar structure equations displayed in Sect. 2.1.1 are solved, including the modifications due to rotation (Sect. 2.1.2; Fliegner 1993), together with the boundary conditions from Sect. 2.1.3. This code will be referred to as "STERN".

The equation of state includes radiation, ionization, relativistic electron degeneracy, and electron-positron pairs. Ions are treated as a Boltzmann gas (El Eid & Langer 1986).

The chemical evolution due to thermonuclear burning is traced by 35 isotopes: ^{0}n, ^{1}H, ^{2}H, ^{3}He, ^{4}He, ^{6}Li, ^{7}Li, ^{7}Be, ^{9}Be, ^{8}B, ^{10}B, ^{11}B, ^{11}C, ^{12}C, ^{13}C, ^{12}N, ^{14}N, ^{15}N, ^{16}O, ^{17}O, ^{18}O, ^{19}F, ^{20}Ne, ^{21}Ne, ^{22}Ne, ^{23}Na, ^{24}Mg, ^{25}Mg, ^{26}Mg, ^{26}Al, ^{27}Al, ^{28}Si, ^{29}Si, ^{30}Si, and ^{56}Fe. Except for ^{19}F, ^{26}Al, and ^{56}Fe, reactions between them are solved in a 32 isotope network. These reaction rates are also used to determine the nuclear energy generation rate ε_n used in Eq. (2.4). The neutrino losses are determined according to (Munakata, Kohyama & Itoh 1985).

Additionally, the Ne/Na and Mg/Al hydrogen-burning cycles are solved separately using a 13 isotope network including ^{1}H, ^{18}O, ^{19}F, ^{20}Ne, ^{21}Ne, ^{22}Ne, ^{23}Na, ^{24}Mg, ^{25}Mg, ^{26}Mg, ^{26}Al, ^{27}Al, ^{28}Si, and ^{16}O (Braun 1997). The contribution of these reaction cycles to the energy generation of the star is neglected.

The reaction networks are solved separately for each zone between the individual stellar structure integration time-steps. This allows for subcycling of the reaction network with fine time-steps wherever needed, without having to employ these small time-steps for the evolution of the stellar structure.

Small inconsistencies between the determination of ε_n and the amount of burned of matter arise within this method, since ε_n is only computed from the composition at the beginning of a stellar structure integration time-step. A method to improve the consistency between the nuclear energy generation rate ε_n and the abundance changes due to burning is presented in Appendix A.

2.1.6.2 KEPLER

In the KEPLER code (Weaver et al. 1978; Weaver, Woosley & Fuller 1984; Woosley & Weaver 1988) the hydrodynamic equations are cast in a different form and also include a viscosity term which is important only when sonic or supersonic motion is present. The equation of state includes a crude treatment of Coulomb corrections, additional to what is used in STERN (Weaver et al. 1978). A 19-isotope network, including the elements ^{1}H, ^{3}He, ^{4}He, ^{12}C, ^{14}N, ^{16}O, ^{20}Ne, ^{24}Mg, ^{28}Si, ^{32}S, ^{36}Ar, ^{40}Ca, ^{44}Ti, ^{48}Cr, ^{52}Fe, ^{54}Fe, ^{56}Ni and additionally neutrons and protons from

photodisintegration, is used (Woosley 1986). Though not explicitly included in the network, flows proceeding through the isotopes ^{27}Al, ^{31}P, ^{35}Cl, ^{39}K, ^{43}Sc, ^{47}V, ^{51}Mn, ^{35}Co, ^{53}Fe, and ^{2}H are included implicitly by assuming their abundances are in steady state with their neighboring nuclei (Weaver et al. 1978). Silicon burning is followed using a quasi-equilibrium network of 137 isotopes, in which subgroups of elements are treated in nuclear statistical equilibrium while reactions between these subgroups are considered explicitly. Beyond silicon burning full nuclear statistical equilibrium is assumed. A more detailed description of the reaction networks in KEPLER can be found in Weaver et al. (1978). These networks allow the accurate computation of the nuclear energy generation rate ε_{n} from hydrogen burning until core collapse by computing the changes in the total binding energy of all isotopes. They are solved simultaneously with the hydrodynamic stellar structure equations with compositional changes coupled implicitly to the equation of state. However, an improvement of the treatment of hydrogen burning, which has been implemented in the frame of this work, is presented in Appendix B.

In this work, angular momentum is added to KEPLER as a new local variable, and rotationally induced mixing processes according to Sect. 2.2.2 are added in the same way as in STERN (actually the same FORTRAN module is used in both codes). However, the modifications to the momentum balance and the energy transport (Sect. 2.1.2) applied in STERN are not included into KEPLER. The same opacities used in STERN are also included in KEPLER, which allows for more consistency between the two codes. For temperatures above 10^9 K the opacities used in KEPLER are chiefly due to electron scattering with corrections due to relativity and degeneracy (Weaver et al. 1978). Convection is treated essentially the same way in both codes. The different formulations of semiconvection are given in Sect. 2.2.1.2.

As outer boundary conditions a finite (or zero) boundary pressure and temperature is utilized in KEPLER. The radius of the photosphere is determined as the location where an optical depth of 2/3 is reached. This treatment of the outer boundary condition, but also the mass loss, is less accurate than that implemented in STERN (Sect. 2.1.3). For this reason, the stellar evolution from the pre-main sequence until a central temperature of 10^9 K, i.e., before central neon ignition, is followed by STERN, and the rest of the evolution until core collapse by KEPLER. At this stage of evolution, the total mass lost in its remaining lifetime (about 100 yr) prior to core-collapse is negligible. The stellar envelope, and therefore the outer appearance of the star, hardly changes.

2.1.6.3 Survey of the computed model sequences

Table 2.3 lists those models which are analyzed in detail in Chapters 3 and 4. Here, the naming convention of the models shall be briefly explained: The models with names starting with "`E`" are adjusted to have a rotational velocity of $\sim 200\,\mathrm{km\,s^{-1}}$ on the zero-age main sequence. Those with names starting with "`G`" initially carry half as much total angular momentum and correspond to rather slow rotators, those with "`F`" have initially 1.5 times the total angular momentum of the "`E`" models, corresponding to fast rotators, and those with "`H`" have initially twice as much total

model	$M_{\rm initial}$ $M_\odot$	$J_{\rm initial}$ 10^{52} erg s	$v_{\rm ZAMS}$ km s^{-1}	f_c	f_μ	evolution followed until
D10	10	0	0	–	–	carbon shell burning
D12	12	0	0	–	–	off-center neon burning
D15	15	0	0	–	–	core collapse
D20	20	0	0	–	–	core collapse
D25	25	0	0	–	–	core collapse
E08	8	0.53	205	0.01	0	carbon shell burning
E10	10	0.80	207	0.01	0	core collapse
E12	12	1.10	206	0.01	0	core collapse
E15	15	1.60	206	0.01	0	core collapse
E20	20	2.50	201	0.01	0	core collapse
E25	25	3.50	205	0.01	0	core collapse
G12	12	0.55	100	0.01	0	core hydrogen exhaustion
F12	12	1.65	327	0.01	0	core hydrogen exhaustion
E12B	12	1.10	206	1/30	0.05	off-center neon burning
E15B	15	1.60	206	1/30	0.05	core collapse
E20B	20	2.50	201	1/30	0.05	core collapse
F12B	12	1.65	328	1/30	0.05	carbon shell burning
F15B	15	2.40	323	1/30	0.05	core collapse
F20B	20	3.75	307	1/30	0.05	core collapse
G12B	12	0.55	99	1/30	0.05	carbon shell burning
G15B	15	0.80	102	1/30	0.05	core collapse
G20B	20	1.25	103	1/30	0.05	core collapse
H12B	12	2.20	474	1/30	0.05	carbon shell burning
H15B	15	3.20	457	1/30	0.05	core hydrogen exhaustion
H20B	20	5.00	425	1/30	0.05	core helium burning

Table 2.3: Parameters of the model sequences. Shown are the model name (left column), the initial mass $M_{\rm initial}$, the initial angular momentum $J_{\rm initial}$, the equatorial rotational velocity at the surface at central hydrogen ignition $v_{\rm ZAMS}$, and two parameters of rotationally induced mixing, f_c and f_μ. The last column gives the final evolutionary stage to which the models are evolved.

angular momentum, and are extremely rapid rotators. An initial "D" designates non-rotating models. In models with a terminal "B" in their name, different parameters governing the rotationally induced mixing processes have been adopted (Sect. 2.3). The evolution until a central temperature of 10^9 K is followed with STERN, the remaining evolution until core collapse is followed with KEPLER.

Two further model are investigated in Chapter 5, Models KE12 and KE15B, and evolved until core collapse. They have the same initial angular momentum and use the same input physics as Models E12 and E15B, only the entire evolution is followed with KEPLER using an extended nuclear network.

For the parameter study in Sect. 2.2.5, 48 models in the mass range from 4 $M_\odot$ to 60 $M_\odot$ are followed with KEPLER from hydrogen ignition to core hydrogen exhaustion. All models have an equatorial rotational velocity at the surface of ~ 200 km s^{-1}.

2.2 Mixing due to instabilities

Mixing inside stars plays a very important rôle in their evolution. For example, they can replenish the fuel in the hot burning regions and prolong the lifetime of that burning phase, or transport matter from the deep interior to the surface of the star where it can be observed.

In this work, compositional mixing is treated as diffusive process and is implemented by solving the diffusion equation

$$\left(\frac{\partial X_i}{\partial t}\right)_m = \left(\frac{\partial}{\partial m}\right)_t \left[(4\pi r^2 \rho)^2 D \left(\frac{\partial X_i}{\partial m}\right)_t\right] + \left(\frac{\mathrm{d}X_i}{\mathrm{d}t}\right)_{\mathrm{nuc}} , \tag{2.21}$$

where D is the diffusion coefficient constructed from the sum of individual mixing processes. The first term on the right hand side conserves the mass of each species, k, the second accounts for nuclear transreaction within a zone (Sect. 2.1.5). At the inner and outer boundary reflecting conditions are used:

$$\left(\frac{\partial X_i}{\partial m}\right)_t \Bigg|_{m=0} = 0 = \left(\frac{\partial X_i}{\partial m}\right)_t \Bigg|_{m=M(t)} . \tag{2.22}$$

Mixing and burning are treated as separate and sequential operations. The different contributions to the diffusion coefficient D are discussed in the following sections. Mass loss is also treated as a separate operation. In practice this imposes severe restrictions on the time step. However, to date exist no computations where this is solved as a whole for a sufficiently large nuclear reaction network to follow stellar evolution beyond the first one or two burning phases.

2.2.1 Mixing in non-rotating stars

2.2.1.1 Convection and overshooting

Convection is *the* classical case of an instability considered in stellar evolution calculations. It occurs when the temperature gradient gets larger than the stabilizing contributions of adiabatic temperature gradient and the gradient in the mean molecular weight μ (Fig. 2.4). That is, a stratification is stable against convection if

$$\nabla_{\mathrm{ad}} - \nabla + \frac{\varphi}{\delta}\nabla_\mu \geq 0 \tag{2.23}$$

(e.g., Kippenhahn & Weigert 1991). This is the so-called Ledoux criterion for convection. Here the common definitions are used:

$$\nabla_{\mathrm{ad}} := \left(\frac{\partial \ln T}{\partial \ln P}\right)_{\mathrm{ad}} , \qquad \nabla_\mu := \frac{\mathrm{d}\ln \mu}{\mathrm{d}\ln P} , \qquad \nabla := \frac{\mathrm{d}\ln T}{\mathrm{d}\ln P} , \tag{2.24}$$

$$\delta := -\left(\frac{\partial \ln \rho}{\partial \ln T}\right)_{\mu,P} , \qquad \varphi := \left(\frac{\partial \ln \rho}{\partial \ln \mu}\right)_{P,T} . \tag{2.25}$$

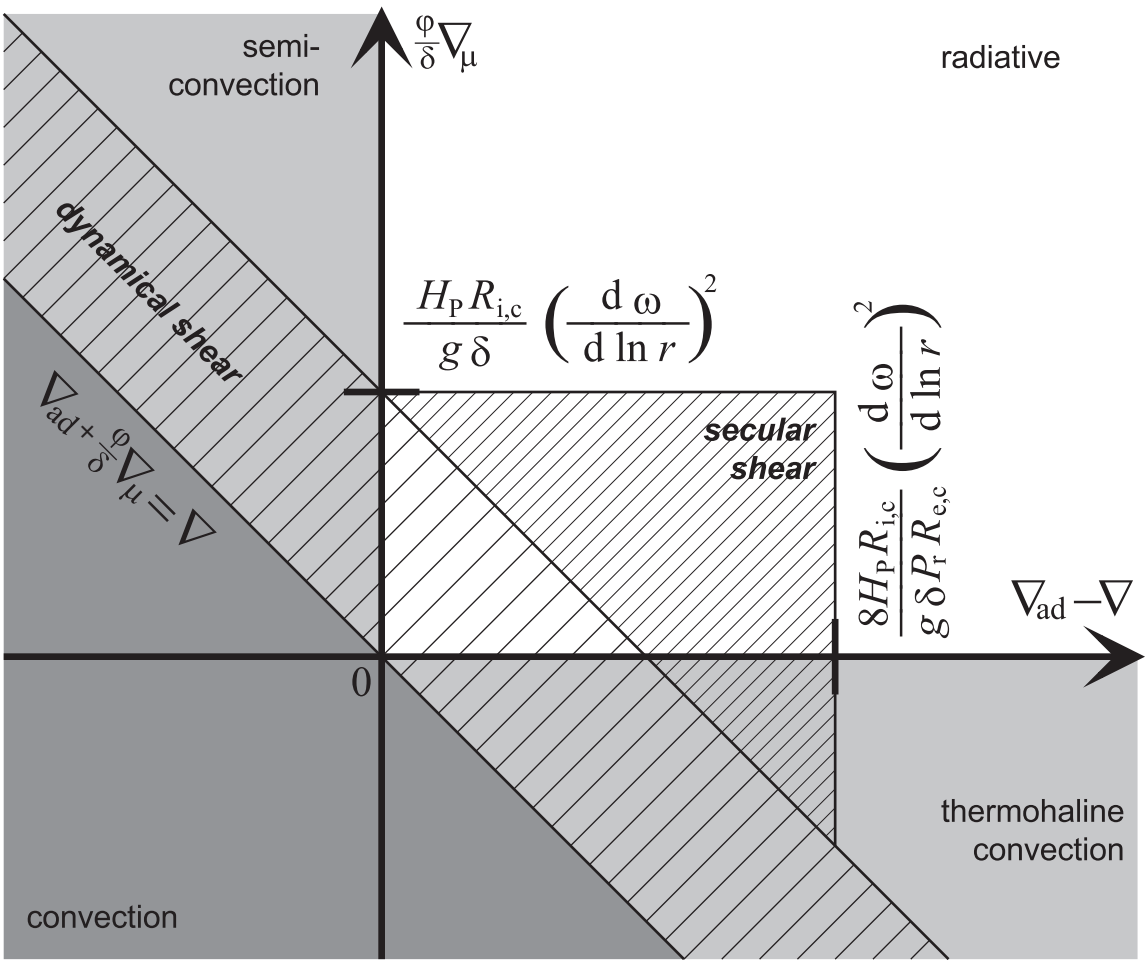

Figure 2.4: Regions of different instabilities that can lead to mixing. The horizontal axis is the stabilizing temperature gradient, and the vertical axis is the stabilizing gradient in the mean molecular weight ∇_μ (vertical axis) according to the local and linear stability analysis. Both axes have identical units. Convection is indicated by dark grey, semiconvection (at positive mean molecular weight gradients) and thermohaline convection (at negative μ-gradients) are displayed in light grey, and the radiative regime is shown in white. In this plane the dynamical shear instability (wide thick hatching) can act only up to a certain distance to the Ledoux-unstable region, which is determined by the amount of shear (Fig. 2.5). The secular shear instability (narrow fine hatching) can penetrate in regions further away from convection, because it is slow enough to allow for thermal adjustment of displaced mass elements; however the composition cannot adjusted that fast (the ratio of those two time-scales is given by the Prandtl-number Pr). Note that in stars usually $8/(\mathrm{Pr}\,R_{e,c}) \gg 1$ ($R_{e,c}$ is the critical Reynolds number), and therefore the secular shear unstable region reaches much further to the right than sketched here, i.e., it can exist in region much more distant from convection than the dynamical shear instability, but it can penetrate only little into regions stabilized by μ-gradients. The shear instabilities are described in Sections 2.2.2.1 and 2.2.2.3

The index "ad" stands here for "at constant entropy and composition".

The diffusion coefficient for composition mixing is treated according to the mixing-length theory (Vitense 1953; Böhm-Vitense 1958):

$$D_{\rm conv} := \alpha_{\rm MLT} H_{\rm P} v_{\rm conv}/3 \ , \tag{2.26}$$

where $v_{\rm conv}$ is the convective velocity. The pressure scale-height is defined for the hydrostatic case by

$$H_{\rm P} := -\frac{{\rm d}r}{{\rm dln}\, P} = \frac{P}{\rho g} \ . \tag{2.27}$$

The local gravitational acceleration is given by $g = Gm/r^2$. In this work a mixing-length parameter of $\alpha_{\rm MLT} = 1.5$ is used (Langer 1991a).

The mixing performed by convection is fast in comparison to most of the other time-scales relevant for the stellar evolution. It operates on the local dynamical time-scale and usually manages to smooth out any compositional inhomogeneities in the regions where it is active. Only when the time-scale of thermonuclear burning becomes comparable to that of convection, as, e.g., during central silicon and shell oxygen burning, can notable gradients persist.

A process closely related to convection is the so called "overshooting". The convective motion does not immediately stop at the edge of a convective region, some penetration into the stably stratified layers beyond ("overshooting") occurs. There is, however, no conclusive theory available which derives the magnitude of this effect. Therefore it is mostly parameterized, using the assumption that the overshooting distance is some fraction of a pressure scale-height (e.g., Chin & Stothers 1991; Schaller et al. 1992). In the present work overshooting is neglected. It will be shown that rotation leads to mixing above the convective core of massive stars during central hydrogen burning and thereby to the formation of more massive helium cores later in the evolution. In order to obtain such mixing, overshooting was originally introduced.

2.2.1.2 Semiconvection

Semiconvection is a secular instability which can occur in non-rotating stars. According to a stability analysis by Kato (1966), it is an oscillatory instability which appears in regions where an unstable temperature gradient is stabilized against convection by a sufficiently large gradient in the mean molecular weight (μ-gradient), i.e., it lives in the regime

$$\frac{\varphi}{\delta}\nabla_\mu \geq \nabla - \nabla_{\rm ad} \geq 0 \tag{2.28}$$

(Kippenhahn & Weigert 1991; and Fig. 2.4). Heat transfer between a displaced mass element and its surrounding causes the growth of the instability on the local thermal time-scale.

Often in the literature the so-called "Schwarzschild criterion" for convection is used for stellar evolution calculations (e.g., Schaller et al. 1992), where the gradient in the mean molecular weight in Eq. (2.23) is not taken into account, and

therefore semiconvective regions are treated as convective. In the present work this simplifications is not made; the Ledoux criterion Eq. (2.23) is used for convection, Eq. (2.28) as criterion for semiconvection and all mixing processes are treated in a time-dependent fashion.

In STERN, semiconvection is treated following Langer, Sugimoto & Fricke (1983). The diffusion coefficient for this process is computed from

$$D_{\rm sem} = \frac{\alpha_{\rm sem} K}{6 c_{\rm P} \rho} \frac{\nabla - \nabla_{\rm ad}}{\nabla_{\rm ad} - \nabla + \frac{\varphi}{\delta}\nabla_\mu} , \qquad K = \frac{4acT^3}{3\kappa\rho} , \tag{2.29}$$

where K is the thermal conductivity and $c_{\rm P}$ the specific heat at constant pressure. As proposed by Langer (1991a), an efficiency parameter of $\alpha_{\rm sem} = 0.04$ is adopted here.

In KEPLER semiconvection is computed from

$$D'_{\rm sem} = \frac{1}{6}{\alpha_{\rm MLT}}^2 v_{\rm sem} H_{\rm P} , \tag{2.30}$$

where the velocity $v_{\rm sem}$ is determined through

$$v_{\rm sem} = \sqrt{(\nabla - \nabla_{\rm ad}) \frac{P\delta}{g\rho^2} \frac{{\rm d}P}{{\rm d}r}} . \tag{2.31}$$

The diffusion coefficient is limited to a fraction $\alpha_{\rm sem}$ of the radiative diffusion coefficient

$$D_{\rm rad} = \frac{K}{\rho c_{\rm V}} \tag{2.32}$$

by means of

$$D_{\rm sem} = \frac{\alpha_{\rm sem} D_{\rm rad} D'_{\rm sem}}{D'_{\rm sem} + \alpha_{\rm sem} D_{\rm rad}} . \tag{2.33}$$

In this work a value of $\alpha_{\rm sem} = 10^{-4}$ is used in KEPLER, which results in a comparable efficiency for semiconvection as the value used for STERN (Woosley 1997).

2.2.1.3 Thermohaline convection

Thermohaline convection ("salt finger instability") occurs in regions with inversions of the mean molecular weight ($\nabla_\mu < 0$), i.e., matter with higher mean molecular weight lying above matter with lower mean molecular weight, which are stabilized by a temperature gradient ($\nabla - \nabla_{\rm ad}$). The condition for its occurrence is

$$\frac{\varphi}{\delta}\nabla_\mu \leq \nabla - \nabla_{\rm ad} \leq 0 \tag{2.34}$$

(Kippenhahn & Weigert 1991; Braun 1997; and Fig. 2.4). Similar to semiconvection, it can occur in the absence of rotation. The Rayleigh-Taylor instability which

would operate on a dynamical time-scale cannot occur because the temperature gradient suppresses the growth of adiabatic perturbations, so that an instability can occur only if heat transport becomes important, i.e., on a thermal time-scale. This instability is important in binary stars, where, e.g., helium-rich matter from the companion star can be accreted to the surface of a hydrogen-rich star. In massive single stars such inversions are rare, and if they occur they are usually rather weak. As an example, helium remaining above the center of the star after core helium exhaustion burns at higher temperatures and results in a higher oxygen-to-carbon ratio than what resulted from the central helium burning below. Thus a tiny inversion in the mean molecular weight arises. Another example is the off-center ignition of carbon, neon, or oxygen in degenerate cores. However, thermohaline mixing is unimportant in the present work and is therefore ignored.

Nevertheless it shall be noted that strong enough inversions of the mean molecular weight lead to convection (i.e., Rayleigh-Taylor instability; Braun 1997) or, in the case of differential rotation, to the dynamical shear instability (Fig. 2.4) even before convection can occur. If the stabilizing temperature gradient $(\nabla_{\rm ad} - \nabla)$ is not too strong, the secular shear instability sets in (Fig. 2.4).

2.2.2 Rotationally induced mixing

Even more important than the alteration of the momentum balance and the energy transport equation are the mixing processes induced by rotation inside the star. In this work, mixing processes according to Endal & Sofia (1978) are included in a parametric way, following the work of Pinsonneault et al. (1989). Five different mixing processes induced by rotation are considered here. To account for the uncertain efficiency of the processes in mixing of matter they are weighed by efficiency factors (Pinsonneault et al. 1989; Sect. 2.3) and then added to the diffusion coefficient D in the diffusion equation (2.21).

2.2.2.1 Dynamical shear instability

The dynamical shear instability sets in where the energy that can be gained from the shear flow becomes comparable to the work which has to be done against the potential for an adiabatic turn-over of a mass element ("eddy"). This means that it is stabilized by density gradients. Since there is no potential work required on equipotential surfaces, this instability can work very efficiently on those (baroclinic instability) and thus enforce rigid rotation (Endal & Sofia 1978; Pinsonneault et al. 1989) and the removal of chemical inhomogeneities on equipotential surfaces. This is the major justification for the assumption of a shellular rotation law and the approximation that the composition is only a function of the mass coordinate (Sect. 2.1.2).

The linear condition for stability is given by

$$R_{\rm i} := \frac{\rho\delta}{P}\left(\nabla_{\rm ad} - \nabla + \frac{\varphi}{\delta}\nabla_{\mu}\right)\left(g\frac{{\rm d}\ln r}{{\rm d}\omega}\right)^2 > R_{\rm i,c} \approx \frac{1}{4} \tag{2.35}$$

for the case of a rotating fluid (Zahn 1974). Here ω is the angular velocity, $R_{\rm i}$ is the Richardson number, and $R_{\rm i,c}$, its critical value which is about 1/4, which is also

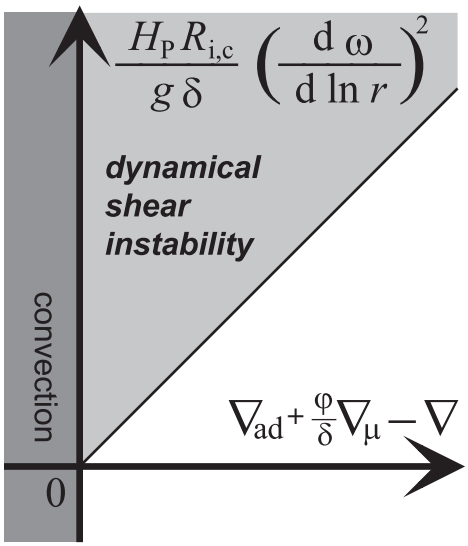

Figure 2.5: Unstable region against dynamical shear (light grey) in the plane of stabilizing temperature and composition stratification (horizontal axis) and destabilizing shear (vertical axis). Both axes have the same units. The region unstable against convection is indicated in dark grey. See also Fig. 2.4.

is used in the present work. Note that the term for ∇_μ was omitted in the original work by Endal & Sofia (1978) and Pinsonneault et al. (1989). The corresponding diffusion coefficient is computed from the spatial extent of the unstable region $d_{\rm inst}$, limited to a pressure scale-height, and the local dynamical time-scale (see also Endal & Sofia 1978):

$$D_{\rm DSI} = \left[\min\left\{d_{\rm inst}, H_{\rm P}\right\}\left(1 - \max\left\{\frac{R_{\rm i}}{R_{\rm i,c}}, 0\right\}\right)\right]^2 / \tau_{\rm dyn}\ , \tag{2.36}$$

where the dynamical time-scale is defined by

$$\tau_{\rm dyn} := \sqrt{r^3/(G\,m)}\ . \tag{2.37}$$

Furthermore, it is assumed that the instability is weaker when the deviation from the Richardson criterion is smaller. This is accounted for by a factor $(1 - R_{\rm i,c}/R_{\rm i})^2$, which is limited to the range $[0, 1]$. For $R_{\rm i} > R_{\rm i,c}$, the flow is assumed to be stable against the dynamical shear instability and thus $D_{\rm DSI}$ is set to 0.

2.2.2.2 Solberg-Høiland instability

The Solberg-Høiland instability arises if an adiabatically displaced mass element experiences a net force (the sum of gravity, buoyancy and centrifugal force) that has components in the direction of the displacement only. Wasiutyński (1946) gives a condition for the stability against axisymmetric adiabatic perturbations of this kind. It decays into two scalar conditions; at the equator the condition for stability in the vertical direction is given by

$$R_{\rm SH} := \frac{g}{\rho}\left[\left(\frac{{\rm d}\rho}{{\rm d}r}\right)_{\rm ad} - \frac{{\rm d}\rho}{{\rm d}r}\right] + \frac{1}{r^3}\frac{\rm d}{{\rm d}r}\left(r^2\omega\right)^2 \geq 0 \tag{2.38}$$

(Tassoul 1978; Endal & Sofia 1978). If the specific angular momentum $j \sim r^2\omega$ is constant with r, the last term on the left-hand side vanishes and the Ledoux

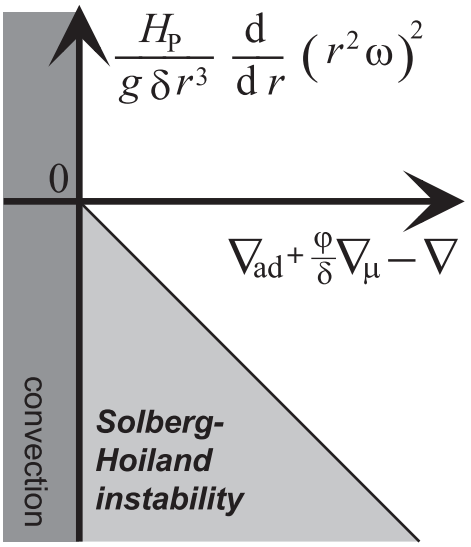

Figure 2.6: Unstable regions against the Solberg-Høiland instability (light grey) in the plane of stabilizing temperature and composition stratification (horizontal axis) and stabilizing increasing specific angular momentum ($j \sim r^2\omega$) (vertical axis). Both axes have identical units. The region unstable against convection is indicated in dark grey. Only in regions of decreasing j the Solberg-Høiland instability can act; however it is strongly suppressed by a stable stratification.

criterion results (not the Schwarzschild criterion as stated by Endal & Sofia (1978)). This can be seen by rewriting the condition for stability into

$$R_{\rm SH} := \frac{g\delta}{H_{\rm P}}\left[\nabla_{\rm ad} - \nabla + \frac{\varphi}{\delta}\nabla_\mu\right] + \frac{1}{r^3}\frac{\rm d}{{\rm d}r}\left(r^2\omega\right)^2 \geq 0 \tag{2.39}$$

and comparing it with Eq. (2.23). If, on the other hand, the medium is marginally stable to convection, the first term on the right hand side vanishes and the Rayleigh criterion results (Tassoul 1978; Kippenhahn & Weigert 1991). Notably, this instability only contributes in in regions of *decreasing* specific angular momentum (Fig. 2.6) and is strongly suppressed in stable stratifications ($\nabla < \nabla_{\rm ad}\frac{\varphi}{\delta}\nabla_\mu$). In unstably stratified regions convection operates.

The diffusion coefficient induced by the Solberg-Høiland instability is estimated in a way similar to that for the dynamical shear instability. The extent of the unstable region $d_{\rm inst}$, limited to the pressure scale-height, is used as the characteristic length-scale, and the dynamical time-scale is used as characteristic time-scale:

$$D_{\rm SHI} = \left[\min\left\{d_{\rm inst}, H_{\rm P}\right\}\left(\frac{r\,R_{\rm SH}}{g}\right)\right]^2 / \tau_{\rm dyn}\ . \tag{2.40}$$

Again, as for the dynamical shear instability, a factor of order unity ($r\,R_{\rm SH}/g$) was introduced to smoothly turn on the instability as the criterion for stability gets increasingly violated, and $D_{\rm SHI}$ is set to 0 wherever the stability criterion is fulfilled.

2.2.2.3 Secular shear instability

The strict criterion for dynamical shear instability can be relaxed considerably by allowing for thermal adjustment of radial perturbations. However, this process then operates on the thermal time-scale only, and therefore is a secular process. Gradients in the mean molecular weight, which may inhibit the occurrence of the instability, also have to be taken into account.

According to Endal & Sofia (1978), the following two conditions have to be violated simultaneously for the instability to set in (Fig. 2.4):

$$R_{\mathrm{is},1} := \frac{\mathcal{P}_{\mathrm{r}}\, R_{\mathrm{e,c}}}{8}\frac{\rho\delta}{P}(\nabla_{\mathrm{ad}} - \nabla)\left(g\frac{\mathrm{d}\ln r}{\mathrm{d}\omega}\right)^2 > R_{\mathrm{i,c}} \tag{2.41}$$

(Townsend 1958; Zahn 1975) because of the relaxed condition for the temperature gradient and

$$R_{\mathrm{is},2} := \frac{\rho\varphi\nabla_{\mu}}{P}\left(g\frac{\mathrm{d}\ln r}{\mathrm{d}\omega}\right)^2 > R_{\mathrm{i,c}} \tag{2.42}$$

because the condition for μ-gradient is not relaxed. The latter formula follows from the physical idea of Endal & Sofia (1978) but corrects error in their Eq. (10). For the critical Reynolds number, $R_{\mathrm{e,c}}$, a value of 2 500 is assumed in this work. The Prandtl number, $\mathcal{P}_{\mathrm{r}}$, is defined as the ratio of the thermal diffusion time-scale to the angular momentum diffusion time-scale, and is estimated according to Tassoul (1978):

$$\mathcal{P}_{\mathrm{r}} = \frac{c_{\mathrm{V}}(\mu_{\mathrm{p}} + \mu_{\mathrm{r}})}{\chi}\ , \tag{2.43}$$

where the coefficients of shear viscosity of the plasma and by the radiation are computed according to

$$\mu_{\mathrm{p}} \approx 0.406\,\frac{\sqrt{m_{\mathrm{i}}(k_{\mathrm{B}}T)^5}}{(Z_{\mathrm{i}}e)^4\ln\Lambda}\ , \qquad \mu_{\mathrm{r}} = \frac{4aT^4}{15c\kappa\rho}\ , \tag{2.44}$$

(Spitzer 1962; Tassoul 1978), respectively. The quantity Λ is the ratio of the cut-off length for ion collisions, which is taken as the ratio of the Debye length to the impact parameter for a $\pi/2$ deflection for Rutherford scattering of the ions, i.e.,

$$\Lambda = \frac{2}{3e^3}\sqrt{\frac{m_{\mathrm{i}}(k_{\mathrm{B}}T)^3}{\pi\rho {Z_{\mathrm{i}}}^5}} \tag{2.45}$$

(for details see Spitzer 1962). Here e is the charge of the electron in e.s.u., Z_{i} is the charge number of the ion, and m_{i}, its mass. It has to be noted that for the burning phases beyond hydrogen burning as well as for He/C/O stars it is important to take the Z_{i}-dependence of the plasma viscosity into account. The quantity Λ enters only logarithmically and $\ln\Lambda$ is of the order of 25. A more recent determination of the ion and the electron contribution to the shear viscosity can be found in Itoh, Kohyama & Takeuchi (1987) and references given therein. At temperatures below the Fermi temperature, depending somewhat on the chemical composition, the ion viscosity dominates over the electron contribution. For the evaluation of the formulae above, partial ionization, as exists in the surface layers of star, is not taken into account, but for computational ease total ionization is assumed everywhere.

If magnetic fields and neutrinos are neglected, the thermal conductivity is given by $\chi \approx K$ (Tassoul 1978). The opacity κ used in this work takes the energy transport by radiation as well as heat conduction by the degenerate electron gas into account. Following Endal & Sofia (1978), the circulation velocity associated with this process is computed from the time-scale and the length-scale of the turbulent elements,

$$v_{\rm SSI} = \sqrt{\frac{\nu}{R_{\rm e,c}} \frac{{\rm d}\omega}{{\rm dln}\, r}} \ , \tag{2.46}$$

limited to the adiabatic sound velocity $c_{\rm s}$. The kinematic viscosity, ν, is given by (Tassoul 1978)

$$\nu = (\mu_{\rm p} + \mu_{\rm r})/\rho \ . \tag{2.47}$$

For the typical length-scale the velocity scale height of the flow is assumed,

$$H_{\rm v,SSI} := \left| \frac{{\rm d}r}{{\rm dln}\, v_{\rm SSI}} \right| , \tag{2.48}$$

limited to the pressure scale height. The resulting diffusion coefficient is given by

$$D_{\rm SSI} = \min\{v_{\rm SSI}, c_{\rm s}\} \min\{H_{\rm v,SSI}, H_{\rm P}\} \left(1 - \frac{\max\{R_{\rm is,1}, R_{\rm is,2}\}}{R_{\rm i,c}}\right)^2 \ . \tag{2.49}$$

Again the instability is smoothly turned on with increasing violation of the stability criteria (term in the last bracket).

Note that the $R_{\rm is,1}$ criterion might be weakened at high temperatures by allowing for a faster thermal adjustment of mass elements to their surrounding due to neutrino losses. If a mass element is moved downward by a radial perturbation within a region with $\nabla < \nabla_{\rm ad}$ and if nuclear burning can be neglected, it would be hotter than its surrounding and thus experience stronger neutrino losses. The diameter, d_ν, for which such a perturbation (assuming a spherical blob) has an adjustment time-scale by radiation/heat conduction equal to that of neutrino losses is given by

$$d_\nu = \sqrt{\frac{16acT^4}{K_\nu \varepsilon_\nu \kappa \rho^2}} \ , \tag{2.50}$$

where

$$K_\nu := \left(\frac{\partial {\rm ln}\, \varepsilon_\nu}{\partial {\rm ln}\, T}\right)_{ad} = \left(\frac{\partial {\rm ln}\, \varepsilon_\nu}{\partial {\rm ln}\, T}\right)_\rho + \frac{1}{\Gamma_3 - 1} \left(\frac{\partial {\rm ln}\, \varepsilon_\nu}{\partial {\rm ln}\, \rho}\right)_T \approx 12 \tag{2.51}$$

and

$$\Gamma_3 := \left(\frac{{\rm dln}\, T}{{\rm dln}\, \rho}\right)_{\rm ad} + 1 \ . \tag{2.52}$$

The effective Prandtl number is thus smaller in those regions than that computed from the formulae given above. However, it turns out that this effect becomes

important only in the iron core – if anywhere at all. There, a d_ν of the order of 100 cm is found; elsewhere d_ν becomes a notable fraction of the stellar radius ($\gtrsim 10^{-3}$); therefore the contribution of neutrino cooling to the Prandtl number is neglected in this work.

By a similar mechanism, thermonuclear burning can stabilize or destabilize the flow, depending on whether it is exothermal or endothermal, respectively, and also ionization affects the stability of the stratification. However, this also affects the mean molecular weight of the gas and thus has additional effects. Furthermore, thermonuclear burning in non-convective regions usually is associated with non-negligible μ-gradients, which usually dominate the stability criteria. Therefore, this effect is also neglected in the present work.

In recent work, Maeder & Meynet (1996); Maeder (1997a); Maeder & Zahn (1998) reconsidered the interaction of thermal diffusivity, horizontal turbulence (due to the baroclinic instability) and vertical shear. An important conclusion that can be drawn from their work is that μ-gradients might not completely suppress the occurrence of the shear instability, since the medium is already turbulent due to the baroclinic instability. Consequently, some mixing can occur (Maeder 1997a). In the present work, a parameterization of the efficiency of the secular shear instability for chemical mixing, and of the μ-gradients in suppressing its occurrence is used (Sect. 2.2.5).

2.2.2.4 Eddington-Sweet circulation

As first shown by von Zeipel (1924b,a) for rigid rotation, and later by Baker & Kippenhahn (1959) for a general rotation law, a rotating star cannot be in hydrostatic and radiative thermal equilibrium at the same time. This is because surfaces of constant density, constant temperature and constant pressure (i.e., constant potential) do not coincide. For example, the deviation from spherical symmetry causes the radiative gradient to be different at the equator and the pole. In order to balance this effect, a large-scale meridional circulation develops (Eddington 1925, 1929; Vogt 1925). Since baroclinic instabilities smooth out inhomogeneities efficiently on equipotential surfaces on short time-scales, only the perpendicular ($\approx$ radial) component of the circulation velocity is considered here, and the process is approximated by diffusion along the radial coordinate.

Kippenhahn (1974) estimated the circulation velocity as

$$v_\mathrm{e} := \frac{\nabla_\mathrm{ad}}{\delta\,(\nabla_\mathrm{ad}-\nabla)}\frac{\omega^2 r^3 l}{(Gm)^2}\left(\frac{2(\varepsilon_\mathrm{n}+\varepsilon_\nu)r^2}{l}-\frac{2r^2}{m}-\frac{3}{4\pi\rho r}\right). \tag{2.53}$$

In the presence of μ-gradients, the meridional circulation has to work against the potential and thus might be inhibited or suppressed (Mestel 1952, 1953). Formally, this can be written as a "stabilizing" circulation velocity, which is estimated as

$$v_\mu := \frac{H_\mathrm{P}}{\tau^*_\mathrm{KH}}\frac{\varphi\nabla_\mu}{\delta\,(\nabla-\nabla_\mathrm{ad})} \tag{2.54}$$

(Kippenhahn 1974; Pinsonneault et al. 1989), where

$$\tau^*_{\rm KH} := \frac{Gm^2}{r(l - m\varepsilon_\nu)} \tag{2.55}$$

is the local Kelvin-Helmholtz time-scale and is used as an estimate for the local thermal adjustment time-scale of the currents (Pinsonneault et al. 1989). The spatial extent of the currents is typically of the order of the radius coordinate r. Here, neutrino losses are taken into account, because they reduce the thermal time-scale in the late stages of the stellar evolution significantly. Note that ε_ν is defined as the energy *generation* rate due to neutrino losses and therefore is negative. This increases the numerator in the definition of the local Kelvin-Helmholtz time-scale and thus decreases $\tau^*_{\rm KH}$.

For the evaluation of the diffusion coefficient, the sign of the circulation velocity does not contribute, but the stabilizing "currents" due to μ-gradients always points in the direction opposite to the meridional flow, thus resulting in a reduction of the effective circulation velocity. It is then computed from

$$v_{\rm ES} := \max\{|v_{\rm e}| - |v_\mu|, 0\} \tag{2.56}$$

(Endal & Sofia 1978; and Fig. 2.7). The diffusion coefficient is calculated as the the product of the circulation velocity and a typical length-scale for the circulation. This is assumed to be the minimum of the extent $d_{\rm inst}$ of the instability and the velocity scale-height

$$H_{\rm v,ES} := \left|\frac{{\rm d}r}{{\rm dln}\, v_{\rm ES}}\right| \tag{2.57}$$

(Endal & Sofia 1978), i.e.,

$$D_{\rm ES} := \min\{d_{\rm inst}, H_{\rm v,ES}\} v_{\rm ES} \ . \tag{2.58}$$

In recent work, Chaboyer & Zahn (1992); Zahn (1992); Urpin et al. (1996); Talon et al. (1997); Maeder & Zahn (1998) have discussed several improvements to the theory of meridional circulation and their interaction with the baroclinic instability. In contrast to the present work, their method requires the solution of a fourth order differential equation in ω, which is numerically very involved. Until now this method has been used only to investigate main sequence stars. An interesting result of these work for the Eddington-Sweet circulation is that the stabilizing effect of μ-gradients, entering through $v_{\rm e}$ in $v_{\rm ES}$ (Eqs. (2.53) and (2.56)), may be reduced (Sect. 2.2.5). The second important change to the above estimate is that the interaction of the baroclinic instability and the large-scale meridional reduces the mixing by the Eddington-Sweet circulation by a factor of order 30, in agreement with the numerical studies by Pinsonneault et al. (1989) for the sun.

2.2.2.5 Goldreich-Schubert-Fricke instability

Goldreich & Schubert (1967) and Fricke (1968) performed an analysis of stability against axisymmetric perturbations (GSF instability). For the inviscid limit

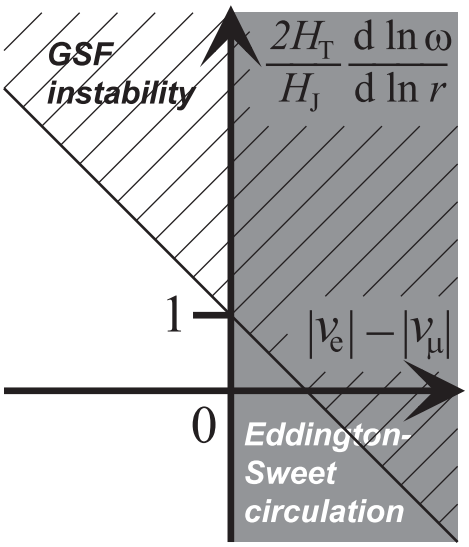

Figure 2.7: Unstable regions against Eddington-Sweet circulation (dark grey) and against Goldreich-Schubert-Fricke instability (hatching) in the plane of residual Eddington-Sweet circulation velocity (horizontal axis) and the factor v_g/v_e (vertical axis) of Goldreich-Schubert-Fricke velocity relative to Eddington-Sweet circulation velocity in the absence of μ-gradients. The boundary of the GSF-unstable region intersects the x-axis at $|v_e| - |v_\mu| = |v_e|$, i.e., where $|v_\mu| = 0$.

($\mathcal{P}_r \ll 1$), which can be well assumed in the interior of stars, they derive two conditions for stability in chemically homogeneous stars Kippenhahn (1969):

$$\frac{\partial j}{\partial r} \geq 0 \qquad \text{and} \qquad \frac{\partial \omega}{\partial z} = 0 \; . \tag{2.59}$$

The first condition is the secular analogue to the Solberg-Høiland stability criterion Eq. (2.39), where the stabilization by the temperature gradient is removed due to the acting of thermal conduction. This is very similar to the relation between the secular and the dynamical shear instability. The second condition of Eq. (2.59) is the analogue to the Taylor-Proudman theorem for slowly rotating incompressible fluids (Kippenhahn 1974; Tassoul 1978): in case the rotational velocity depends on the distance from the equatorial plane, i.e., the rotation profile is not conservative, meridional flows will be driven. Also in this case, the buoyancy force, which acts to suppress the instability, can be removed by heat conduction. However, this proceeds only on the time-scale required for thermalization. Interestingly, the typical velocities for both of the above processes are quite similar (Kippenhahn 1974).

Since the second condition of Eq. (2.59) is in general in contradiction with the shellular rotation law enforced by the baroclinic instability, except for the case of solid body rotation, the GSF instability will lead towards uniform rotation in chemically homogeneous regions (Endal & Sofia 1978).

Its dependence on differential rotation is stronger than that of the Eddington-Sweet circulation, and the large-scale circulation velocity in the equatorial plane can be estimated by

$$v_g = \frac{2H_T r}{{H_j}^2}\left(1 + 2\frac{\mathrm{dln}\, r}{\mathrm{dln}\,\omega}\right)^{-1} v_e = \frac{2H_T}{H_j}\frac{\mathrm{dln}\,\omega}{\mathrm{dln}\, r} v_e \tag{2.60}$$

(Endal & Sofia 1978; James & Kahn 1970, 1971). Here $H_T := -(\mathrm{d}r)/(\mathrm{d}\ln T)$ is the temperature scale-height and $H_j := (\mathrm{d}r)/(\mathrm{d}\ln j)$ the scale-height of the angular momentum distribution. The GSF instability has the same μ-dependence as the

the Eddington-Sweet circulation (Endal & Sofia 1978) and therefore the resulting circulation velocity is computed in the same way, taking the stabilizing effect of the μ-gradient into account:

$$v_{\rm GSF} := \max\left\{|v_{\rm g}| - |v_\mu|, 0\right\} . \tag{2.61}$$

Again, the diffusion coefficient is determined from the circulation velocity $v_{\rm GSF}$ and the minimum of the circulation velocity scale height $H_{\rm v,GSF}$ and the extent $d_{\rm inst}$ of the instability:

$$D_{\rm GSF} := \min\left\{d_{\rm inst}, H_{\rm v,GSF}\right\} v_{\rm GSF} \tag{2.62}$$

where we define in the same way as above

$$H_{\rm v,GSF} := \left| \frac{{\rm d}r}{{\rm dln}\, v_{\rm GSF}} \right| . \tag{2.63}$$

In Fig. 2.7, the parameter space in which the GSF instability and the Eddington-Sweet instability operate are compared. In regions with small gradients in the angular velocity the Eddington-Sweet circulation will dominate, while the GSF instability becomes more important as the differential rotation increases. For strong differential rotation secular and dynamic shear instability will also set in.

2.2.3 Other instabilities

The five instabilities discussed in the previous section cannot be considered as a complete list of rotationally induced instabilities of relevance for stellar evolution. However, they appear to be the most relevant ones, and are the best (though not well) understood ones. In the future, the following things might be considered.

For the ABCD-instability (Spruit, Knobloch & Roxburgh 1984) and the triply diffusive instability (Knobloch & Spruit 1983), no reliable estimates of efficiency exist. Furthermore, non-axisymmetric instabilities may also exist, but they are, poorly investigated so far.

Another important issue is that of the interaction of the different instabilities, and the interaction of rotation and rotationally induced instabilities with the instabilities listed in Sect. 2.2. The interaction of the shear instabilities and the Eddington-Sweet circulation has been investigated by, e.g., Chaboyer & Zahn (1992); Zahn (1992); Urpin et al. (1996); Meynet & Maeder (1997); Maeder (1997a); Talon & Zahn (1997); Talon et al. (1997); Maeder & Zahn (1998), and recently also semiconvection has been included by Maeder (1997a) and by Maeder & Zahn (1998). However, the effects of the interaction are not large and therefore not taken into account in the present work.

In this work, magnetic fields are also neglected. They might transport angular momentum by magnetic torques ($\sim r^3 B_r B_\phi$; Spruit 1997), or cause instabilities by magnetic buoyancy due to winding up of magnetic field lines through differential rotation. This could be effective even if the initial field strength is small (Spruit 1997; Spruit & Phinney 1998). Unfortunately the strength of the initial field is

is not known. The Velikhov-Chandrasekhar instability depends on the presence of magnetic fields only, not on their strength, but it is efficiently suppressed by μ-gradients (Acheson 1978; Spruit 1997). Detailed studies of the action of magnetic fields inside stars must be left to future investigations.

2.2.4 Angular momentum transport

Similar to the work by Endal & Sofia (1978) and Pinsonneault et al. (1989), in this work, the transport of angular momentum is formulated as a diffusive process

$$\left(\frac{\partial\omega}{\partial t}\right)_m = \frac{1}{i}\left(\frac{\partial}{\partial m}\right)_t\left[(4\pi r^2\rho)^2 i\nu\left(\frac{\partial\omega}{\partial m}\right)_t\right] - \frac{2\omega}{r}\left(\frac{\partial r}{\partial t}\right)_m\left(\frac{1}{2}\frac{\mathrm{d}\ln i}{\mathrm{d}\ln r}\right) \tag{2.64}$$

(Endal & Sofia 1978), where ν is the turbulent viscosity and i, the specific angular momentum of a shell at mass coordinate m. For a spherical shell of constant density, inner radius r_i and outer radius r_o, the specific moment of inertia, i, is given by $i = 0.4\,({r_\mathrm{o}}^5 - {r_\mathrm{i}}^5)/({r_\mathrm{o}}^3 + {r_\mathrm{i}}^3)$; for an arbitrary thin shell of radius r this simplifies to $i = 2/3\,r^2$. The last term in Eq. (2.64), an advection term, accounts for contraction or expansion of the layers at constant mass coordinate. The factor in the last bracket on the right hand side vanishes if the gyration constant $k := i/r^2$ does not depend on r, as, e.g., if all shells are moving homologously.

Eq. (2.64) is essentially a diffusion equation for ω along the "moment of inertia coordinate"

$$I(m) := \int_0^m i(m')\,\mathrm{d}m' \;, \tag{2.65}$$

defined analogously to the mass coordinate (Sect. 2.1.1). This equation conserves angular momentum and leads to rigid rotation in a region of extent ℓ whenever the diffusion time-scale, $\tau_\mathrm{D} := \ell^2/\nu$, is short enough in comparison to structural changes of the star. This is, e.g., the usually the case in convection zones.

At the inner and outer boundary reflecting conditions similar to those given for Eq. (2.21) for the compositional mixing are used. Especially, at the surface of the star, the angular momentum contained in the layers which are lost due to stellar winds gets removed from the star (Sect. 2.4.3).

The turbulent viscosity, ν, is determined as the sum of the convective and semi-convective diffusion coefficients, and those from rotationally induced instabilities (Endal & Sofia 1978; Sect. 2.3). In contrast to Endal & Sofia (1978) and Pinsonneault et al. (1989), in this work the transport equation for angular momentum is solved for the entire star as a whole.

Since the evolutionary time-scale of the star is in most cases much longer than the convective time-scale, Eq. (2.64) results in rigid rotation in those regions. Unlike composition, which can show significant gradients even inside convective regions due to burning (e.g., during central silicon burning), angular momentum is locally conserved, and therefore convective regions can more easily reach rigid rotation than chemical homogeneity during hydrostatic burning phases. This, however, does not hold if the respective layers are contracting or expanding rapidly.

The approximation that convection leads to rigid rotation rather than constant specific angular momentum seems to be justified at least if the rotational period is long in comparison to the convective time scale, and it may also hold for more rapid rotation if convective blobs can be assumed to scatter elastically (Kumar, Narayan & Loeb 1995). Latitudinal variations of the rotational velocity, as deduced from helioseismological data for the solar convective envelope (Thompson et al. 1996), are not taken into account in the one-dimensional stellar evolution calculations of the present work; however, the latitudinally averaged rotation rate of the solar convection zone deviates by less than 5 % from solid body rotation (e.g., Antia, Basu & Chitre 1997).

In recent work by, e.g., Chaboyer & Zahn (1992); Zahn (1992); Urpin et al. (1996); Maeder & Zahn (1998), the transport of angular momentum due to the Eddington-Sweet circulation has been considered as an advective processes, instead of a diffusive one, contributing an additional term to Eq. (2.64). However, there are more instabilities than taken into account in theses works, and the influence of this neglect on the late evolutionary stages is not well investigated. Moreover, the mixing due to rotationally induced instabilities and their prescription in the present work are calibrated to observation (see below), such that the uncertainties are significantly reduced here.

2.2.5 Parameterization of the mixing efficiencies

The diffusion coefficients used in this work are subject to considerable uncertainties, as they result from order-of-magnitude estimates of some of the relevant time- and length-scales. Therefore "factors of order unity" are introduced, similar to the treatment by Pinsonneault et al. (1989), in order to calibrate the diffusion coefficients with observational data. Uncertainties remain, but here for the first time this calibration is done for massive stars.

For this work, two main parameters are relevant for this calibration. The first is the ratio of turbulent viscosity to the diffusion coefficient, $f_\mathrm{c} := D/\nu$. The contribution of the rotationally induced instabilities to the diffusion coefficients is assumed to be reduced by the factor f_c, while their full value enters the turbulent viscosity,

$$D = D_\mathrm{conv} + D_\mathrm{sem} + f_\mathrm{c}(D_\mathrm{DSI} + D_\mathrm{SHI} + D_\mathrm{SSI} + D_\mathrm{ES} + D_\mathrm{GSF}) \ , \tag{2.66}$$

$$\nu = D_\mathrm{conv} + D_\mathrm{sem} + D_\mathrm{DSI} + D_\mathrm{SHI} + D_\mathrm{SSI} + D_\mathrm{ES} + D_\mathrm{GSF} \ . \tag{2.67}$$

The second factor, f_μ, describes the sensitivity of the rotationally induced mixing processes to μ-gradients, i.e., ∇_μ is replaced by $f_\mu \nabla_\mu$.

As shown by Meynet & Maeder (1997), μ-gradients can efficiently in suppress rotationally induced transport processes (see also Endal & Sofia 1978). This is in contradiction to observations of the enrichment of the surface of main sequence stars with products of the CNO (e.g., Gies & Lambert 1992; Herrero et al. 1992; Vrancken et al. 1998). This implies that the inhibiting effect of μ-gradients may not be as strong as the theory in Sect. 2.2.2 predicts. In fact, it has been shown by Talon

& Zahn (1997), Maeder (1997a), and especially by Maeder & Zahn (1998), that the interaction of vertical shear and horizontal turbulence may act to reduce the stringent criteria Eqs. (2.42) and (2.54). For this reason the parameter $f_\mu \in [0,1]$ was introduced (see also Pinsonneault et al. 1989). As expected from the strength of the inhibiting effect of ∇_μ it turns out that actually values of $f_\mu \ll 1$ are necessary.

In order to reproduces the solar surface ^{7}Li abundance, Pinsonneault et al. (1989) introduced the factor $f_c \in [0,1]$. They find a value of 0.046 for their best fit. From theoretical work Chaboyer & Zahn (1992) find a value of $f_c = 1/30$ for the combined action of shear and meridional circulation. This is also the value chosen for most of the models presented in this work (Table 2.3).

2.3 Calibration of the mixing efficiencies

The best probe of rotationally induced mixing mixing in stars, one directly accessible to observations, is the evolution of the surface composition during central hydrogen burning. While lithium and boron are depleted early during this phase (Venn et al. 1996; Fliegner et al. 1996) since they are destroyed at relatively low temperatures, nitrogen (^{14}N), the dominant species in the CNO cycle, is only produced from carbon (mainly ^{12}C) and oxygen (^{16}O) at higher temperature, i.e., much deeper inside the star. Therefore, an increase of nitrogen at the surface should be accompanied by an decrease of carbon (^{12}C) or, in the case of even deeper mixing, oxygen (^{16}O), which is destroyed at even higher temperatures.

Since stars at the zero-age main sequence do not show any processing, one needs to compare the surface abundance patterns of evolved core-hydrogen burning stars with the result of corresponding models. Typically, an enrichment of nitrogen of the order of $2-3$ is observed for evolved stars of about 10 to 20 $M_\odot$ (Vrancken et al. 1998; Gies & Lambert 1992; Herrero 1994). This is thought to reflect rotationally induced mixing. It has to be kept in mind that the amount of mixing, and therefore the changes of the surface abundances, also depend on the initial rotation rate of the star, while observations can only give the projected rotation rate $v \sin\phi$ (where ϕ is the inclination angle). Also, observed samples are restricted to rather low (Gies & Lambert 1992) or moderate (Vrancken et al. 1998) projected rotational velocities ($v \sin\phi < 85\,\mathrm{km\,s^{-1}}$ in Gies & Lambert 1992), since strong rotational line broadening does not allow for accurate abundance determination. For this reason, fast rotators are not accessible except when they are observed pole-on. Unfortunately, also *isotopic* abundance ratios are not detectable in the atmospheres of these hot stars, but only elemental abundances.

Processing of carbon to nitrogen does not introduce large μ-gradients and therefore is insensitive to f_μ, because the atomic weight of carbon and nitrogen is not much different, and because they only constitute a small mass fraction. On the other hand, an enrichment of helium in the O stars (Herrero et al. 1992; Herrero, Villamariz & Martín 1998) to a mass fraction of 40 % or more is an interesting probe for the calibration of f_μ. For less massive stars, a much lower enrichment of helium is expected. However, helium abundances are hard to determine and therefore there

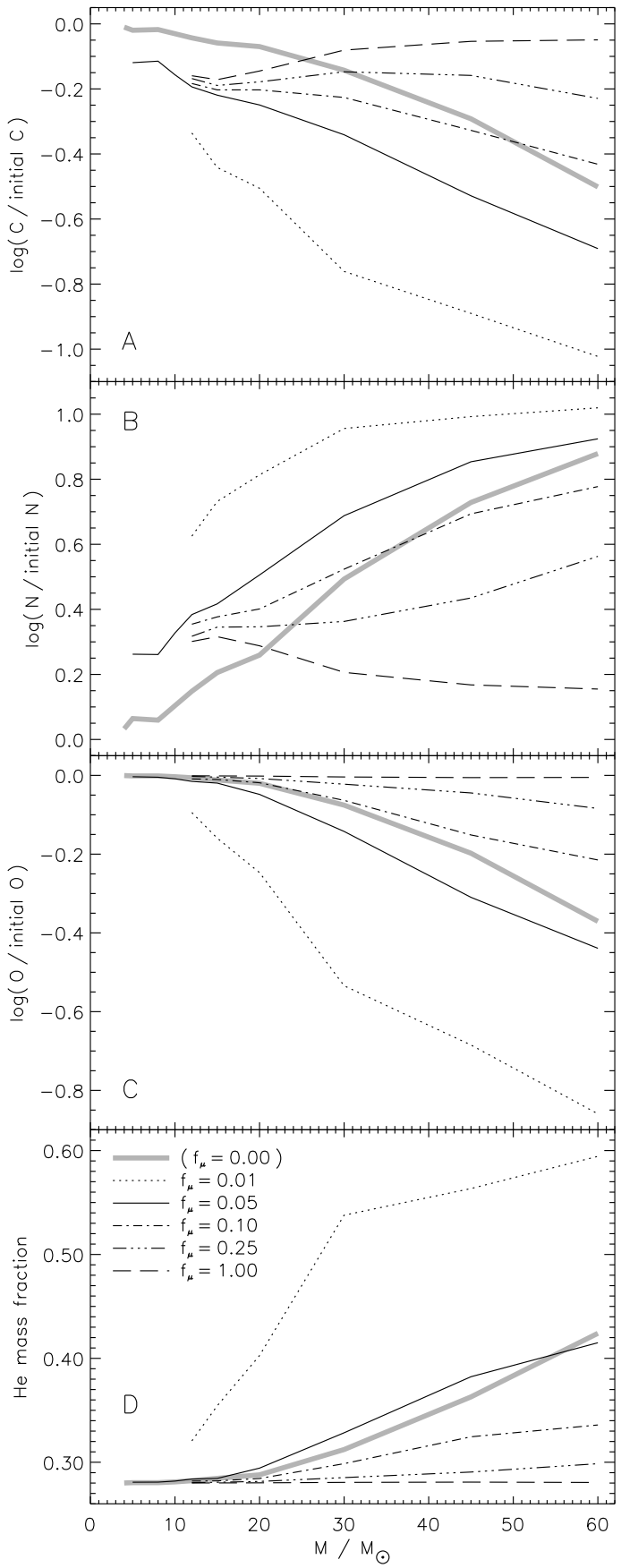

Figure 2.8: Surface abundances at core hydrogen exhaustion as a function of initial mass for models with an equatorial surface rotation rate of $\sim 200\,\mathrm{km\,s^{-1}}$ at ignition of central hydrogen burning. Black lines correspond to different values of f_μ (Sect. 2.3) for fixed $f_\mathrm{c} = 1/30$. The thick grey line corresponds to $f_\mathrm{c} = 1/100$ and $f_\mu = 0$. In Panels **A**–**C**, the change of the mass fractions of carbon, nitrogen, and oxygen, respectively, relative to the initial values are shown; Panel **D** shows the same for helium. Models with initial masses of $12\,\mathrm{M}_\odot$, $15\,\mathrm{M}_\odot$, $20\,\mathrm{M}_\odot$, $30\,\mathrm{M}_\odot$, $45\,\mathrm{M}_\odot$, and $60\,\mathrm{M}_\odot$ have been calculated with the KEPLER code exclusively for this study. For $f_\mu = 0.05$ (solid black line) and $f_\mu = 0$ (grey line) additionally $5\,\mathrm{M}_\odot$, $8\,\mathrm{M}_\odot$, and $10\,\mathrm{M}_\odot$ stars are computed and for the case $f_\mu = 0$ also a $4\,\mathrm{M}_\odot$ model is calculated.

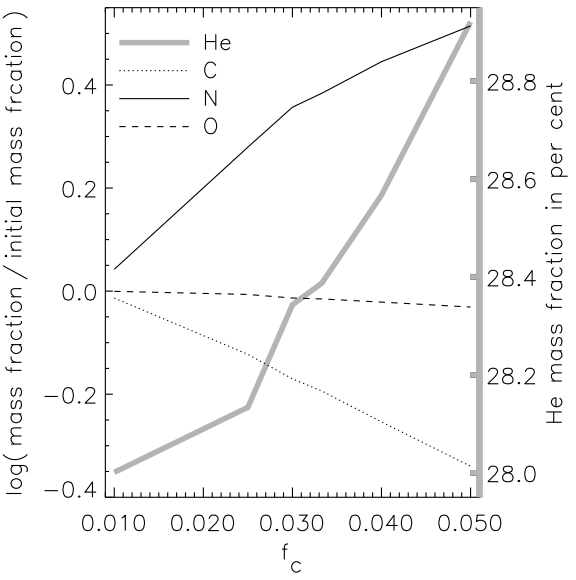

Figure 2.9: Surface abundances at core hydrogen exhaustion as a function of f_c, for $12\,M_\odot$ stars with an equatorial rotational velocity at the surface of $\sim 200\,km\,s^{-1}$ at ignition of central hydrogen burning. The thin black dotted, solid, and dashed lines give the logarithm of the mass fractions of carbon, nitrogen, and oxygen, respectively, relative to their initial values (left scale). The thick grey line shows the mass fraction of helium (right scale). Model sequences have been computed for $f_c = 0.01$, 0.025, 0.03, 1/30, 0.04 and 0.05 with the KEPLER code exclusively for this study.

exist considerable uncertainties in these values (Herrero 1994).

Due to the problems mentioned above, the calibration of f_c and f_μ using surface abundances can only be carried out for stars with typical rotation rates. Slower or faster rotators will have more or less changes in their surface abundances, respectively. Since surface abundance determinations are only available for low $v \sin\phi$, the present observational data can be expected to correspond to stars which are biased towards little mixing.

For calibration, calculations were carried out for solar metallicity stars in the mass range $4\,M_\odot$ to $60\,M_\odot$. An initial rotational velocity at the ZAMS of $\sim 200\,km\,s^{-1}$ is chosen. This is typical for most stars in this mass range (Slettebak 1970; Fukuda 1982; Lang 1991; Halbedel 1996; Penny 1996; Fig. 1.1).

In Fig. 2.8, the surface mass fractions of carbon, nitrogen, and oxygen relative to their initial values, and that of helium at central hydrogen exhaustion are shown as a function of the initial stellar mass. A value of $f_\mu = 0.05$ reproduces an enhancement of nitrogen by a factor of 2 to 3 in the mass range $10\,M_\odot$ to $20\,M_\odot$, and results in a surface helium mass fraction of $\sim 40\,\%$ for the $60\,M_\odot$ star, while the enrichment remains quite small for stars below $20\,M_\odot$. For $f_\mu = 0.01$, nitrogen and helium are clearly enriched too much for stars below $30\,M_\odot$. On the other hand, the nitrogen enrichment might be too low for values of $f_\mu \geq 0.1$. Certainly, for $f_\mu = 0.25$ and $f_\mu = 1.0$ the nitrogen abundance for the most massive stars ($30\,M_\odot \ldots 60\,M_\odot$) appears to be inconsistent with the observations. The same is true for the helium abundances.

In summary, $f_\mu = 0.05$ seems to be the best value (provided $f_c = 1/30$; Sect. 2.2.5). This set of parameters is used in the present work for the models whose name ends with "B" (Table 2.3). The consequences of a variation of f_c for fixed $f_\mu = 0.05$ is shown in Fig. 2.9 for the example of a $12\,M_\odot$ star: for small values of f_c the nitrogen abundance drops low, while for large values helium gets quite high.

As discussed above, too much surface enrichment occurs with $f_c = 1/30$ for small values of f_μ (0.01). Nevertheless, it is interesting to investigate the case where

μ-gradients are completely neglected, since the calibration of f_c and f_μ is not unambiguous, and different combinations might result in similar surface enrichments. The surface abundance, however, are the only clear observational constraint, while the degree of internal mixing is not directly observable. Therefore, a second parameter set of $f_c = 0.01$ and $f_\mu = 0$ is also used. The resulting surface abundances (displayed as thick grey line in Fig. 2.8) show quite similar enrichments. Models with this choice of f_c and f_μ do *not* carry a "`B`" at the end of their name (Table 2.3). A value of $f_c = 0.01$ for $f_\mu = 0$ is also supported by calibrations of the lithium, beryllium and boron surface abundance for the sun by Fliegner (1993).

2.4 Mass loss

Mass loss from the stellar surface ("stellar winds") significantly affects the evolution of stars in the considered mass range (Chiosi & Maeder 1986). For example, it influences the fraction of central helium burning spent in the "red" or the "blue" part of the HR diagram. For sufficiently massive stars, mass loss can remove the hydrogen-rich envelope during central helium burning or even before. This leads to the formation of Wolf-Rayet stars (Langer 1989a). Mass loss on time-scales comparable to the stellar thermal time-scale may even reduce the stellar luminosity (Heger & Langer 1996). Furthermore, mass loss causes the loss of angular momentum from the star (Langer 1998). For most evolutionary phases of massive stars, mass loss rates are still uncertain (e.g., Feast 1992; Salasnich, Bressan & Chiosi 1997).

In this work, the empirical mass loss rate of Nieuwenhuijzen & de Jager (1990) is used, but modified to account for rotation (Sect. 2.4.2). Fig. 2.10 compares this rate with previous determinations of the mass loss rates by de Jager, Nieuwenhuijzen & van der Hucht (1988) and de Jager, Nieuwenhuijzen & van der Hucht (1986). For Wolf-Rayet stars, the mass loss rate determined by Langer (1989b) is applied. The uncertainties in these mass loss rates are due to the uncertainties in the observational data and their interpretation.

2.4.1 The Eddington-Limit

Starting from the hydrostatic equation in the equatorial plane

$$-\frac{1}{\rho}\left(\frac{\partial P}{\partial r}\right)_t + \frac{v^2}{r} - \frac{Gm}{r^2} = 0 \ , \tag{2.68}$$

where v is the equatorial rotational velocity, the pressure gradient can be split into the contribution of gas pressure $P_{\rm gas}$ and radiation pressure

$$-\frac{1}{\rho}\left(\frac{\partial P}{\partial r}\right)_t = -\frac{1}{\rho}\left(\frac{\partial P_{\rm gas}}{\partial r}\right)_t + \frac{\kappa L}{4\pi c r^2} \ . \tag{2.69}$$

If both, the gas pressure and the centrifugal forces (second term on the right hand side of Eq. (2.68)) are neglected, the *Eddington Luminosity* $L_{\rm ed}$ is obtained, i.e., the maximum luminosity $L_{\rm ed}$ that can be balanced by gravity. The ratio of this

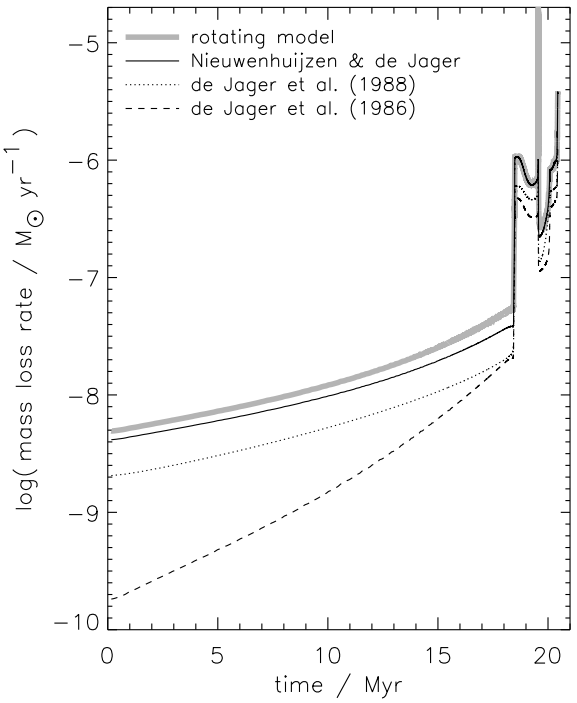

Figure 2.10: Mass loss rate as a function of time for a rotating $12\,M_\odot$ star with an initial equatorial rotation rate of $\sim 200\,\mathrm{km\,s^{-1}}$ (Model E12) during its evolution from central hydrogen ignition until core collapse. The black solid, dotted, and dashed lines show the mass loss rates given by Nieuwenhuijzen & de Jager (1990); de Jager et al. (1988, 1986), respectively, as they would result from the surface parameters of this sequence. The thick grey line gives the mass loss rate actually used for the calculation (Nieuwenhuijzen & de Jager 1990), and includes the mass loss enhancement due to rotation. The "spike" in the mass loss rate at 19.56 Myr corresponds the the onset of a blue loop (Sect. 4.3).

luminosity to the actual luminosity is usually referred to as the *Eddington Factor* Γ:

$$L_{\mathrm{ed}} := \frac{4\pi cGm}{\kappa}\,, \qquad \Gamma := \frac{L}{L_{\mathrm{ed}}} = \frac{\kappa L}{4\pi cGm}\,. \tag{2.70}$$

With this definition, the sum of the gravitational acceleration and the radiation pressure gradient can be written in the form of a reduced effective gravity:

$$\frac{Gm}{r^2} - \frac{\kappa L}{4\pi cr^2} = (1-\Gamma)\frac{Gm}{r^2}\,. \tag{2.71}$$

2.4.2 The Ω-limit

If centrifugal forces in Eq. (2.68) are considered, a rotational velocity v_{crit} can be defined, at which centrifugal forces balance gravity and radiation pressure, and the ratio of the critical velocity to the true velocity is denoted by Ω (Langer 1997):

$${v_{\mathrm{crit}}}^2 := \frac{Gm}{r}(1-\Gamma)\,, \qquad \Omega := \frac{v}{v_{\mathrm{crit}}} = v/\sqrt{\frac{Gm}{r}(1-\Gamma)}\,. \tag{2.72}$$

For the derivation of this expression, the effect of gravity darkening (von Zeipel 1924b,a) is neglected, since its order of magnitude and even its sign is still unclear for the case of realistic, non-barotropic stars (Kippenhahn 1977). In the limit $\Gamma = 0$ the critical velocity is equal to the Keplerian velocity ${v_{\mathrm{kep}}}^2 = Gm/r$ for a circular orbit. This means that a rotating star will reach a *critical rotation rate* before it reaches either the Eddington Limit or the plain Keplerian rotation limit (Langer

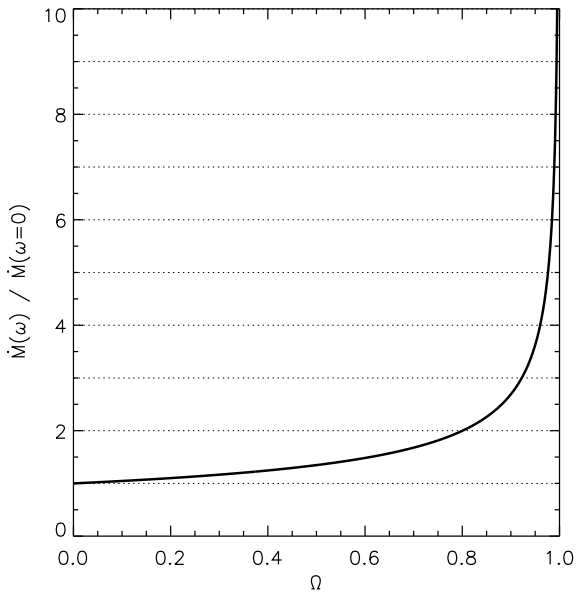

Figure 2.11: Mass loss rate $\dot{M}(\omega)$ in units of the mass loss rate of a non-rotating star $\dot{M}(\omega = 0)$ as a function of the surface rotation parameter Ω.

1997) Stars approaching the Ω-limit will be subject to a strong increase of their mass loss according to Friend & Abbott (1986)

$$\frac{\dot{M}(\omega)}{\dot{M}(\omega = 0)} = \left(\frac{1}{1-\Omega}\right)^{\xi} , \qquad \xi \approx 0.43 . \tag{2.73}$$

In the stellar interior convection will set in if the star gets close to the local Eddington Limit (Langer 1997). Density inversions can also cause the gas pressure gradient to exert a stabilizing contribution (i.e., acting in the same direction as gravity). Both effects are present in models for extended red supergiants, where a density inversion forms at the upper edge of the convective envelope where a peak in opacity is located. Therefore, in this work, the Eddington Factor, Γ, in Eq. (2.73) is evaluated only in the radiative part of the optical depth range $\tau \in [2/3, 100]$ (Lamers 1993; Langer 1997), where $\tau(r) = \int_r^\infty \kappa\rho \, \mathrm{d}r$ has the usual definition.

The quantitative result for the Ω-dependence of the mass loss rate obtained by Friend & Abbott (1986) was questioned by Owocki, Cranmer & Gayley (1996), who performed hydrodynamic simulations of winds of rotating hot stars including the effect of non-radial radiation forces and gravity-darkening in the approximation of von Zeipel (1924b,a). However, the only crucial ingredient for the model calculations, which is confirmed by Owocki & Gayley (1997), is the fact that the mass loss rate increases strongly as the star approaches the Ω-limit, so that the star cannot exceed critical rotation, but rather loses more mass and angular momentum (see also Langer 1998).

The behavior of the mass loss, Eq. (2.73) is displayed in Fig. 2.11. When $\Omega = 1$ is approached, almost arbitrarily high mass loss rates are reached, independently of the mass loss rate at $\omega = 0$. However, mass loss also causes a spin-down of the star and a decrease of the luminosity, such that an equilibrium mass loss rate results (Langer 1998). In Fig. 2.10 the mass loss rate resulting from this treatment is shown as the thick grey curve. During central hydrogen burning (the first 14.3 Myr), this

star with an initial equatorial rotation rate of $\sim 200\,\mathrm{km\,s^{-1}}$, corresponding to a value of $\Omega \approx 0.3$, the increase of the mass loss rate due to rotation is small in comparison to the uncertainty in the mass loss rate for non-rotating stars.

2.4.3 Angular momentum loss

The loss of angular momentum from the surface due to stellar winds is approximated by removing of the angular momentum along with the surface layer when they leave

$$\dot{J} = \dot{M} j_{\mathrm{surf}} \ , \tag{2.74}$$

where j_{surf} is the average specific angular momentum at the surface of the star and the mass loss is assumed independent of latitude. A latitudinal variation of the surface rotation rate, as e.g., observed for the sun, or of the mass loss rate would affect the specific angular momentum loss rate. Since these effects are presently not well investigated for massive stars, they are not included in this work.

No magnetic braking is assumed here. This approximation is justified since the massive stars considered here do not have extended convective envelopes like the sun when they are in the blue part of the HR diagram. No strong magnetic fields are expected in this case. Moreover, while they are red supergiants they are so extended that their radius becomes comparable to the Alfvén radius. In this stage, angular momentum loss due to the high mass loss rates are expected to dominate over that from the magnetic braking.

Chapter 3

Evolution of the stellar interior

The internal structure of stars is directly accessible to observations only in rare cases. The best example is the sun where detailed helioseismological data allows one to study the density structure and rotation profile almost down to the very center (Thompson et al. 1996). Other examples are observations of neutrinos which come directly from the center of the sun or the neutrinos collected from the explosion of the Supernova 1987A. However, for stars other than our sun, in particular for massive stars, such data are not available and only theoretical studies and indirect observations, like the nucleosynthesis ejected in a supernova, can aid in understanding their internal evolution.

3.1 Central hydrogen burning

During their first major burning phase, massive stars transform hydrogen into helium through the *CNO cycle* (Bethe 1939; Clayton 1968). During that process, equilibrium abundances of the CNO isotopes are established which are different from their initial abundances and which depend somewhat on temperature. Roughly, a ratio of $1 : 50 \ldots 100 : 1 \ldots 5$ (by mass fraction) for $^{12}\mathsf{C} : {}^{14}\mathsf{N} : {}^{16}\mathsf{O}$ is achieved (Arnould & Mowlavi 1993) during central hydrogen burning in the core of massive stars. This stands in contrast to the typical initial ratio for these isotopes in stars, as, for example, deduced from meteoritic abundances, of about $1 : 0.3 : 3$. Most of the initial carbon and oxygen is converted into $^{14}\mathsf{N}$. This demonstrates why nitrogen was chosen for the calibration procedure in Sect. 2.3.

One subcycle of the CNO process passes through $^{17}\mathsf{F}$ and $^{17}\mathsf{O}$ and this is responsible not only for processing $^{16}\mathsf{O}$ into $^{14}\mathsf{N}$, but also for the production of $^{17}\mathsf{O}$ during central hydrogen burning. Another characteristic property of the CNO cycle is the production of $^{13}\mathsf{C}$ and the destruction of $^{15}\mathsf{N}$. Other cycles occur during hydrogen burning, where, e.g., neon, sodium, magnesium and aluminum are involved. They do not contribute significantly to the energy generation, but they do change the abundances. Changes in abundance for the various isotopes of these elements occur in different regions of the star and give additional information about the stellar interior.

The light isotopes ^{3}He, ^{6}Li, ^{7}Li, ^{9}Be, ^{10}B, and ^{11}B are destroyed at low temperature in the envelope of the star. Therefore, they can be used to constrain mixing processes in the upper part of the envelope. For example, the surface depletion of lithium is also used to investigate models for the present sun (Talon & Charbonnel 1998).

In the layers of the stars above the convective core, only partial processing of the CNO isotopes occurs, i.e., they do not reach their equilibrium abundances. In particular, there is almost no processing of hydrogen into helium. For some isotopes of the CNO cycle the production occurs at lower temperatures than their destruction reactions (e.g., ^{13}C and ^{17}O), so that they can reach abundance maxima at some point in the envelope where the temperature is too low for the full CNO cycle to proceed.

However, none of this would be directly observable at the surface of the stars were it not for mass loss and mixing. Due to mass loss (Sect. 2.4), which strongly increases with stellar mass, outer layers are removed uncovering the layers beneath, although, even in the case of the $25\,M_\odot$ star (Model `E25`), less than 10 % of the initial mass is lost. At this point rotation comes into play. Meridional circulation (Eddington-Sweet circulation) and other rotationally induced instabilities can cause mixing in the stellar interior and transport matter to the surface. This latter is discussed in more detail in Chapter 4. In the following sections the evolution of the internal structure is emphasized.

3.1.1 Chemical mixing: the example of 20 $M_\odot$ stars

Fig. 3.1 compares the internal profiles of the main isotopes in a non-rotating star and two rotating $20\,M_\odot$ models at core hydrogen exhaustion. Convection causes flat profiles in the innermost few solar masses. Small convective and/or semiconvective regions cause a strip-like pattern in the regions above the convective core (Fig. E.5).

In the non-rotating case Fig. 3.1 also shows that there is no mixing beyond this region. This is demonstrated by the kink in the hydrogen, helium and oxygen profiles at about $m = 10\,M_\odot$. Between $m = 10$ and $m = 13\,M_\odot$, a sharp decrease in ^{12}C appears which is due to partial CNO processing "in place", i.e., without any transport. Deeper in the core, the carbon mass fraction increases again and reaches its equilibrium value. In the same region where the carbon abundance decreases, nitrogen is enhanced. Below $m = 10\,M_\odot$ ^{14}N approaches its CNO equilibrium value while oxygen is depleted. There is no thermonuclear depletion of oxygen above $m = 10\,M_\odot$. Above $m \approx 14\,M_\odot$, all isotopes still have their initial mass fractions.

In contrast, the rotating models in Fig. 3.1 show thermonuclear processed matter mixed all the way to the surface of the star. In Model `E20` (Fig. 3.1A, see also Fig. E.11), inhibiting effects of μ-gradients on the rotationally induced instabilities are *not* taken into account. In this case, an extended gradient in helium (and hydrogen) reaches from the upper edge of the convective core up to the surface. Along with helium, nitrogen is also enriched while carbon and and oxygen are depleted. Between $m = 5\,M_\odot$ and $m = 10\,M_\odot$, carbon is enhanced. Oxygen is enhanced in the convective core due to continuous supply from the envelope.

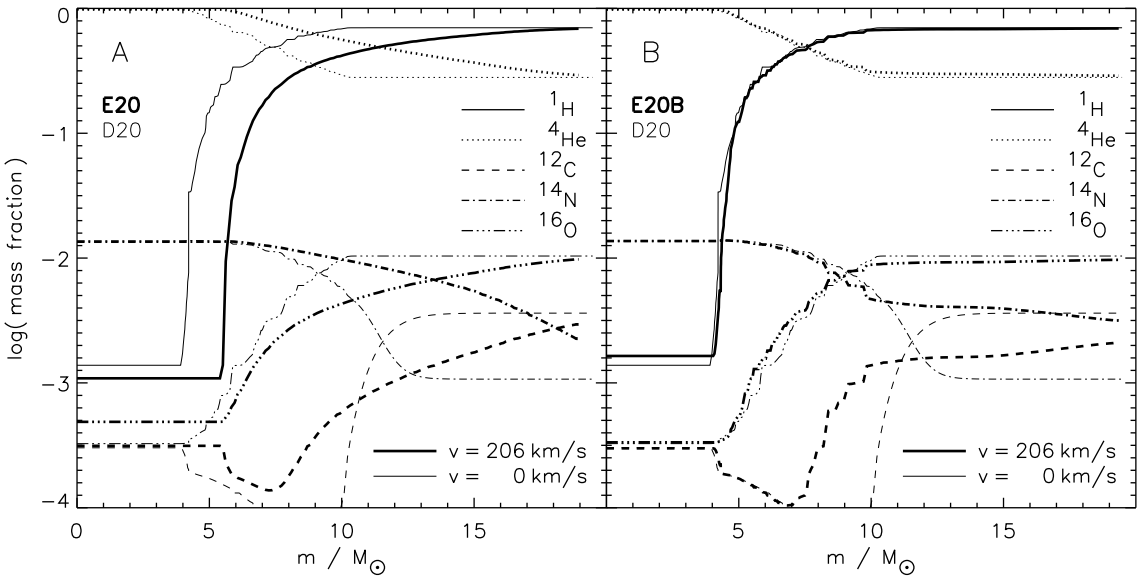

Figure 3.1: Mass fractions of different isotopes as a function of the mass coordinate m at core hydrogen exhaustion. Compared are the chemical structures of rotating (thick lines) and a non-rotating (thin lines; same in both Panels; Model `D20`) $20\,M_\odot$ models. The rotating models have a ZAMS equatorial rotational velocity of $\sim 200\,\mathrm{km\,s^{-1}}$. Panel **A**: Model `E20`, where rotationally induced mixing is *not* inhibited by μ-gradients. Panel **B**: Model `E20B`, where rotationally induced mixing is (slightly; $f_\mu = 0.05$) inhibited by μ-gradients. See also Figs. 3.2 and 3.4.

An important feature of Model `E20`, the mass of its hydrogen-depleted core, is about $1.5\,M_\odot$ larger than in the non-rotating case. This is due to the increase of the mean molecular weight in the whole envelope as a consequence of helium enrichment. For chemically homogeneous stars, $L \propto \mu^4 M^3$ (Kippenhahn & Weigert 1991), i.e., the star becomes more luminous during its evolution than a non-rotating star of the same initial mass (even though it started central hydrogen burning with lower luminosity due to the decrease of the "effective gravity" through centrifugal forces; see Sect. 2.1.4 and Fig. 4.7). Due to mixing of hydrogen from the envelope into the core and the lower luminosity at ignition of core-hydrogen burning, the star spends more time during central hydrogen burning than its non-rotating counterpart.

During central hydrogen burning, the dominant rotationally induced mixing process is the Eddington-Sweet circulation. This is fast enough to keep the whole star close to rigid rotation (Sect. 3.1.2), which renders shear instabilities unimportant. The GSF instability remains one to two orders of magnitude less efficient than the Eddington-Sweet circulation. Note that the μ-gradients built up by the rotationally induced mixing above the convective core are strong enough to suppress the occurrence of extended semiconvective structures (Fig. E.11). The secular shear instability occurs only in a small layer close to surface, and never contributes significantly to the mixing.

In contrast to Model `E20`, μ-gradients *are* taken into account in Model `E20B` (Figs. 3.1B and E.18). The μ-gradient which forms at the upper edge of the convective core is not smoothed out fast enough by the rotationally induced mixing processes in this case, but instead almost completely chokes off any mixing between

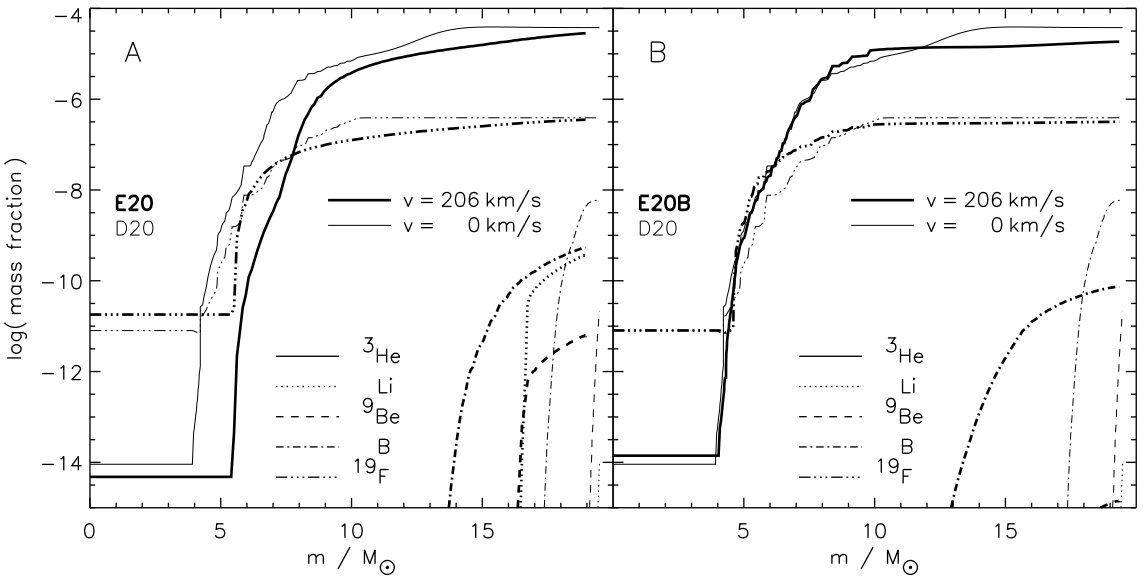

Figure 3.2: Mass fractions of ^{3}He (solid lines), lithium (dotted lines), ^{9}Be (dashed lines), boron (dash-dotted lines), and ^{19}F (dash-triple-dotted lines) as a function of the mass coordinate m at core hydrogen exhaustion for the same models as in Fig. 3.1. See also Fig. 3.4.

core and envelope quite early during the evolution. Therefore, below $m = 10\,\mathrm{M}_{\odot}$ the composition of Model `E20B` is quite similar to that of Model `D20`. Only the higher concentration of carbon in Model `E20` shows the occurrence of *some* mixing early on.

Above the "barrier" due to the μ-gradient (μ-barrier), however, mixing is quite efficient, as can be seen from the non-zero slope of the composition profiles throughout the envelope in Model `E20B`, and is stronger than for Model `E20`. This difference occurs because the efficiency for compositional mixing is assumed to be $f_{\mathrm{c}} = 1/30$ in Model `E20B` instead of $f_{\mathrm{c}} = 1/100$ for Model `E20`. Therefore, a stronger enrichment of nitrogen close to the surface results in Model `E20B`, which is mainly due to the processing of carbon into nitrogen. The abundance of ^{16}O in the envelope does not change much in Model `E20B`, because the temperature above the μ-barrier is not high enough to allow for its processing. Only a little enrichment of helium appears above the μ-barrier, because it is the cause for the μ-barrier.

The contributions of the different rotationally induced mixing processes above the μ-barrier are similar in Models `E20` and `E20B`, except that close to the μ-barrier the GSF instability becomes important in Model `E20B`. Within the μ-barrier, almost all rotationally induced mixing is suppressed and the mixing is dominated by semiconvection. The secular shear instabilities do not appear here, because they are sufficiently inhibited by the the μ-gradient. The regions at the boundaries of convective layers, where the shear flow could overcome the stabilizing effect of the μ-gradients, are too small to be resolved in the calculations.

The light elements are already destroyed at the rather low temperatures in the upper part of the envelope and therefore enable allow study the mixing close to the surface. Lithium is most fragile and destroyed first, closely followed by beryllium. At

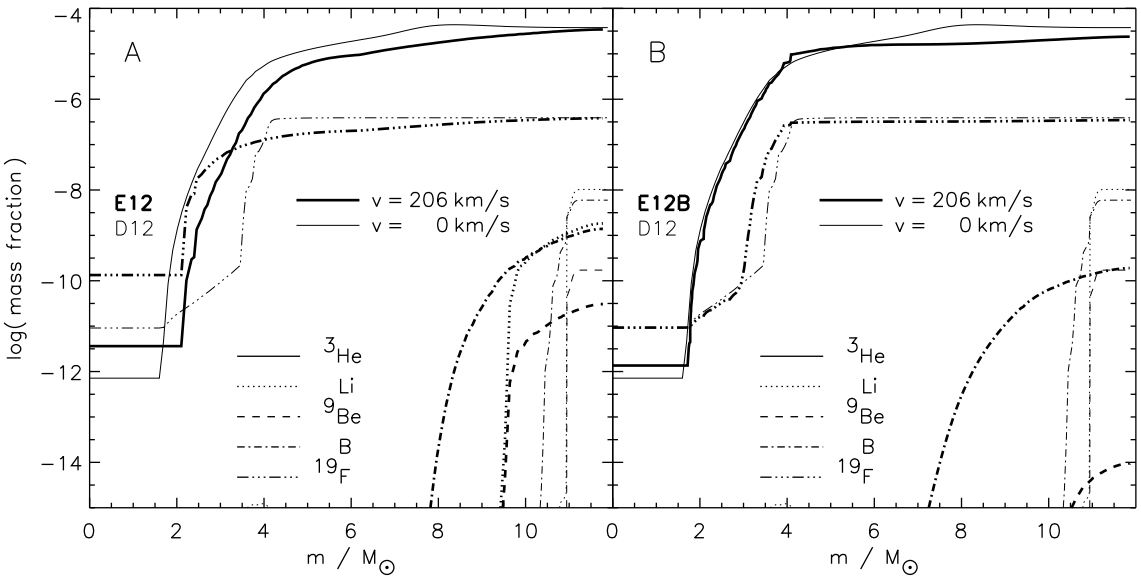

Figure 3.3: Mass fractions of ^{3}He (solid lines), lithium (dotted lines), ^{9}Be (dashed lines), boron (dash-dotted lines), and ^{19}F (dash-triple-dotted lines) as a function of the mass coordinate m at core hydrogen exhaustion. Compared are the chemical structures of rotating (thick lines) and a non-rotating (thin lines; same in both Panels; Model D20) 12 $M_\odot$ models. The rotating models have a ZAMS equatorial rotational velocity of $\sim 200\,\mathrm{km\,s^{-1}}$. Panel **A**: Model E12, where rotationally induced mixing is *not* inhibited by μ-gradients. Panel **B**: Model E12B, where rotationally induced mixing is (slightly; $f_\mu = 0.05$) inhibited by μ-gradients. See also Fig. 3.2.

somewhat higher temperatures, boron follows, and further in, more than five solar masses below the surface in 20 $M_\odot$ stars, the destruction of ^{3}He proceeds Fig. 3.2.

In non-rotating stars, the isotopes are just destroyed "in place" where the temperature gets high enough; at the lower temperatures closer to the surface they are not altered (Fig. 3.3). Thus their surface abundance changes during central hydrogen burning only when the mass loss is sufficiently strong to remove the unaltered layers. This is the case in Model D20 for lithium and beryllium, as can be seen in Fig. D.1B3,C3. Due to the strong temperature-dependence of the destruction rates, the abundance changes due to this can become quite dramatic.

In rotating stars, the rotationally induced mixing causes a (mostly) downward transport of the light elements. This has two important effects. First, the light elements are transported into regions where the temperature is sufficiently high to destroy them. This leads to a more severe depletion of these isotopes by the rotating massive stars during central hydrogen burning. The faster the mixing in the envelope, the greater this depletion is. Secondly, due to mass loss and expansion of the stars during central hydrogen burning evolution, envelope layers which have been hot enough to destroy the light elements cool down, and the rotationally induced mixing can enrich these layers again with the residual left of the light elements in the layers above. That is, some of the light isotopes are *preserved* by the rotationally induced mixing (Figs. 3.2 and 3.3).

Obviously, these two effects compete with each other. As long as the mass loss is small enough not to remove most of the unprocessed matter from the surface,

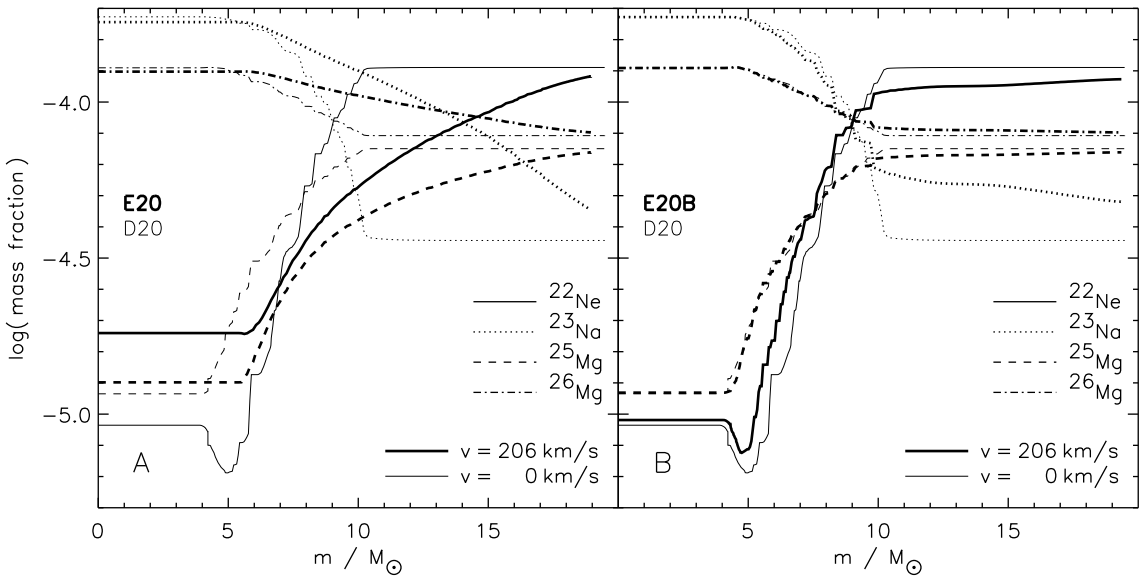

Figure 3.4: Mass fractions of ^{22}Ne (solid lines), ^{23}Na (dotted lines), ^{25}Mg (dashed lines), and ^{26}Mg (dash-dotted lines) as a function of the mass coordinate m at core hydrogen exhaustion for the same models as in Fig. 3.1. See also Fig. 3.2.

both the surface abundance and the total mass of the corresponding isotope will be higher in the non-rotating star. But when mass loss becomes strong enough to remove all the unprocessed matter of a non-rotating star, the rotating model can, for the same amount of mass loss, actually retain both a higher total mass and surface mass fraction of the fragile isotope. The magnitude of the effect depends upon the amount of mass loss and the efficiency of the mixing. An example can be seen in Fig. D.1B3 for the depletion of lithium. For non-rotating Model `D20` the depletion is about two orders of magnitude greater than in the slowly rotating Model `G20`. In a similar way, Model `E20`, where the efficiency of the mixing in the envelope is less than in Model `E20B`, experiences less destruction of beryllium and lithium than Model `D20` (Fig. 3.2A). But the destruction is also less than in Model `E20B`, where the efficient mixing would lead to a strong depletion even without mass loss (Fig. 3.2B; see also Fig. 3.3 for a model with less mass loss).

In the models of series "`B`", where the mixing in the envelope is relatively fast, the destruction due to the mixing of light elements into burning layers dominates and this effect increases with initial angular momentum. This mixing can almost completely destroy lithium, beryllium, and boron (Figs. 4.6A and D.1B,C) in the less massive stars and reduce ^{3}He by more than a factor of ten (Fig. D.1A) even at the surface. See also the discussion of surface enrichment in Sect. 4.1.3.

The abundances of the stable isotopes of neon, sodium, magnesium, and aluminum are altered only in the hot convective core of the star. Above the μ-barrier, no nuclear processing takes place. In the core ^{21}Ne and ^{22}Ne are converted to ^{23}Na by the reaction $^{21}\mathrm{Ne}(\mathrm{p},\gamma)^{22}\mathrm{Na}(\beta^+\nu_\mathrm{e})^{22}\mathrm{Ne}(\mathrm{p},\gamma)^{23}\mathrm{Na}$. Thus a depletion of ^{21}Ne and ^{22}Ne is accompanied by an enrichment of ^{23}Na. The long-lived radioactive isotope ^{26}Al is produced from ^{25}Mg by proton capture, but beta-decays back to ^{26}Mg with

a lifetime of $\sim 1\,\mathrm{Myr}$. The processing of $^{26}\mathrm{Mg}$ to $^{27}\mathrm{Al}$ leads to a slight enrichment in this aluminum isotope, but it is unimportant for $^{26}\mathrm{Mg}$. The abundances of $^{20}\mathrm{Ne}$ and $^{24}\mathrm{Mg}$ are essentially unaffected.

Due to the high temperatures required, no enrichment of sodium and $^{26}\mathrm{Al}$ is present in the envelope of the non-rotating Model `D20`, but strong gradients exist inside the envelope of the rotating Model `E20` (inefficient μ-barriers; see Fig. 3.4), and some, but not much enrichment is found at the surface (Sect. 4.1.3 and Appendix D).

In Model `E20B` the μ-gradient is weak enough to allow an efficient transport of these processed isotopes from the core into the envelope only during the early phase of hydrogen burning. In particular, the rapid conversion of $^{22}\mathrm{Ne}$ to $^{23}\mathrm{Na}$ at hydrogen ignition allows it to be mixed into the envelope before the formation of the μ-barrier. Due to the more efficient mixing inside the envelope, $^{23}\mathrm{Na}$ is even more enriched at the surface than in `E20`, even though its total mass inside the envelope is much less. This also happens for the other isotopes of the neon/sodium and the magnesium/aluminum cycles.

Note that the strength of enrichment of nuclear processed matter increases with initial mass. Fig. 2.8 shows the enrichment at the surface as a function of initial stellar mass and also for different assumptions for the inhibiting effect of μ-gradients. Several effects contribute: With increasing stellar mass the stellar interior becomes increasingly dominated by radiation pressure, and the radiative zone of the star is closer to the adiabatic stratification, which, for example, increases the velocity of the Eddington-Sweet circulation (Eq. 2.53). Additionally, the convective core comprises a larger fraction of the total stellar mass and the mass loss increases. Both helps to bring processed matter to the surface of the star.

3.1.2 Transport of angular momentum

Like chemical mixing, the transport of angular momentum depends strongly on the efficiency of the inhibition of the rotationally induced mixing processes by μ-gradients. Fig. 3.5 shows the internal angular velocity profile of two rotating $15\,\mathrm{M}_\odot$ stars (Models `E15` and `E15B`) with a ZAMS equatorial rotational velocity of $\sim 200\,\mathrm{km\,s^{-1}}$ at central hydrogen ignition and exhaustion.

Model `E15` remains close to rigid rotation, i.e., the difference between surface and core angular velocity is always less than 30 %. The over-all decrease of the rotation rate by a factor of ~ 3 is caused by two effects: mass loss from the surface carries away $\sim 40\,\%$ of the initial angular momentum and the expansion of the stellar envelope increases the total moment of inertia $I = \int i\,\mathrm{d}m \propto \int r^2\,\mathrm{d}m$ by a factor of ~ 2. At the same time, the core of the star contracts. The persistence of rigid rotation implies transport of angular momentum from the core to the surface. This effect can be seen in Fig. 3.6A from the drop of the specific angular momentum in the core, and in the integrated angular momentum in Fig. 3.7A. Because of its smaller radial extent, the core contains only a small fraction of the total angular momentum $J = \int \omega i\,\mathrm{d}m$ of the star (Fig. 3.7). For higher mass loss rates, i.e., for more massive stars, the spin-down (decrease of ω) is dominated by the mass loss, while at lower mass it is dominated by the expansion of the envelope.

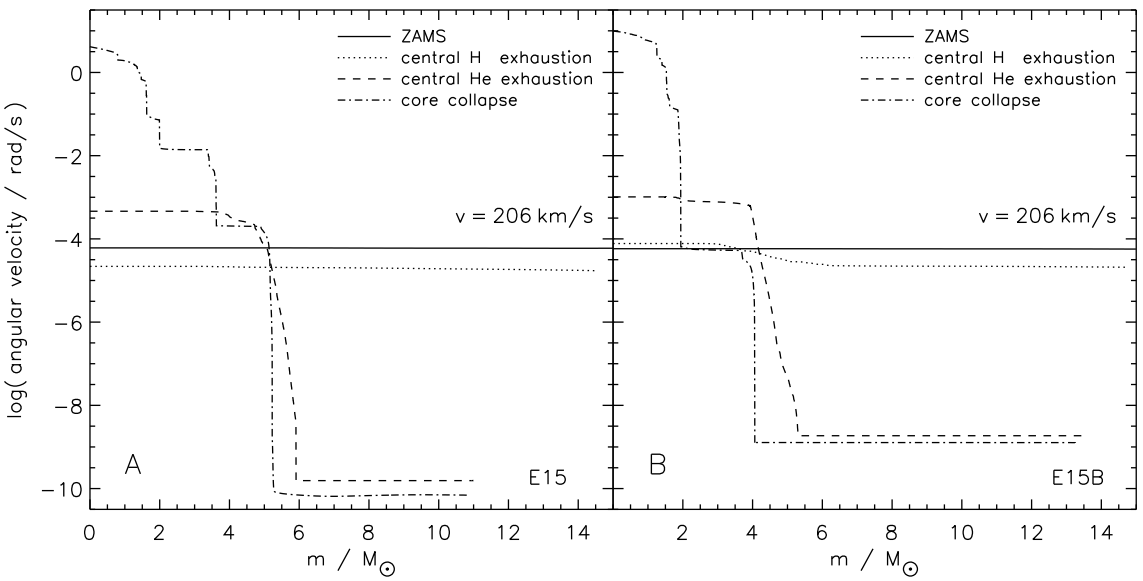

Figure 3.5: Angular velocity as a function of the mass coordinate m at different evolutionary stages for two $15\,M_\odot$ stars with a ZAMS equatorial rotational velocity of $\sim 200\,km\,s^{-1}$. Panel **A** shows Model `E15` (inefficient μ-barrier), and Panel **B** Model `E15B` (efficient μ-barrier). See also Figs. 3.6 and 3.7.

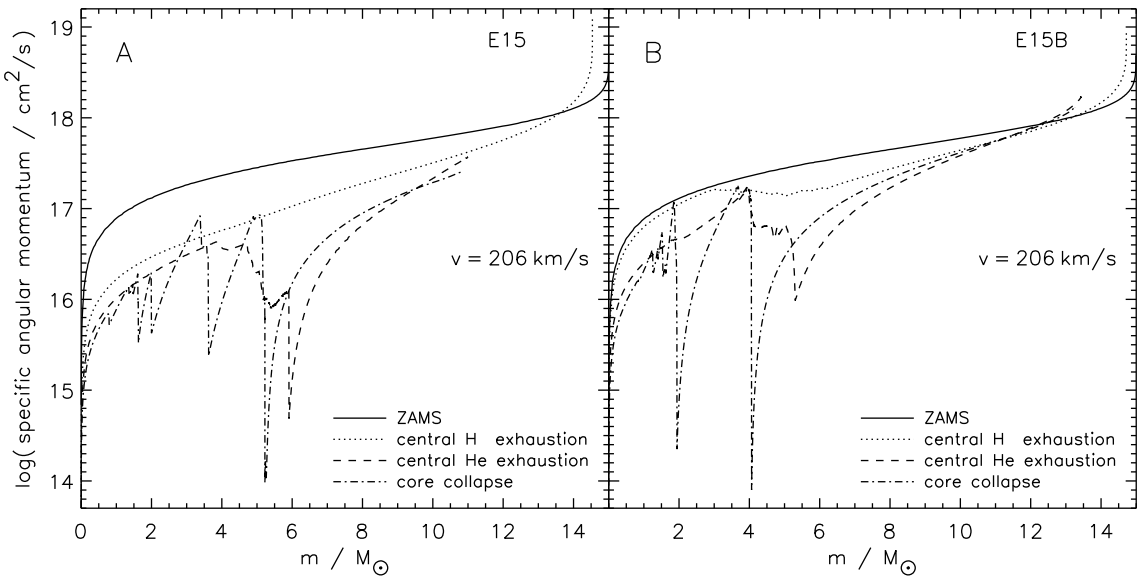

Figure 3.6: Specific angular momentum as a function of the mass coordinate m for the same models and evolutionary stages shown in Fig. 3.5. Panel **A** shows Model `E15`, and Panel **B** Model `E15B`. See also Fig. 3.7.

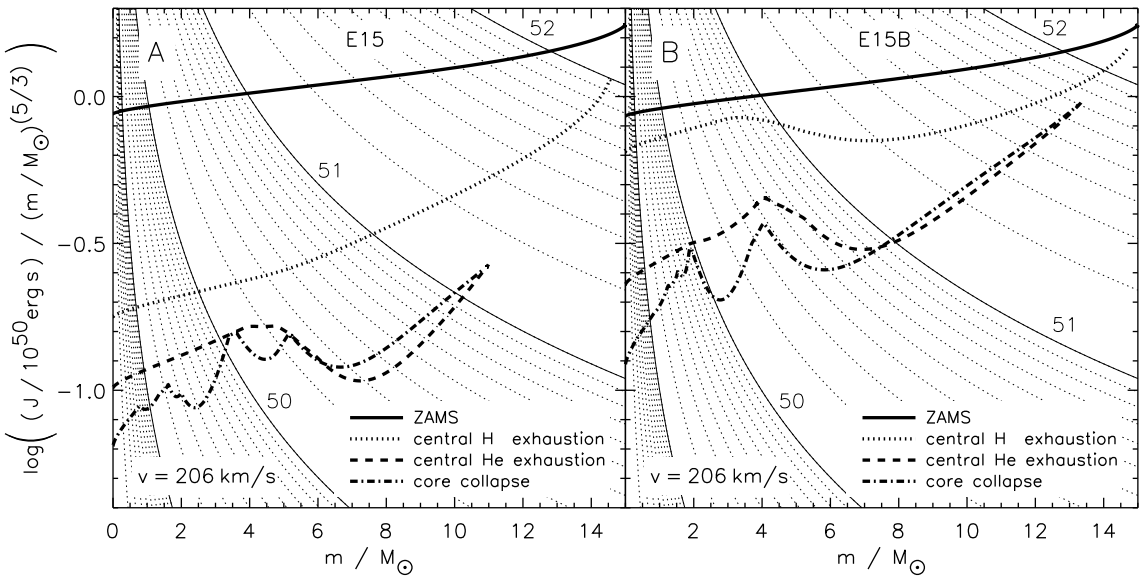

Figure 3.7: Logarithm of the integrated angular momentum $J(m) = \int_0^m j(m')\,\mathrm{d}m'$ divided by $m^{5/3}$, as a function of the mass mass coordinate m for the same models and evolutionary stages shown in Fig. 3.5 (thick lines). Panels **A** and **B** show Models `E15` and `E15B`, respectively. The thin lines give a logarithmic scale of levels of constant J, labeled with $\log(J/\mathrm{erg\,s})$. See also Figs. 3.5 and 3.6.

For a rigidly rotating body of constant density ρ_0, the total angular momentum $J(m)$ enclosed below the mass coordinate m is given by

$$J(m) := \int_0^m j(m')\,\mathrm{d}m' = \frac{3\omega k}{5}\left(\frac{3}{4\pi\rho_0}\right)^{2/3} m^{5/3} \propto m^{5/3}\ . \tag{3.1}$$

In our models, density and angular momentum vary with the mass coordinate m. However, Eq. (3.1) illustrates that the quantity $J(m)/m^{5/3}$ varies only slowly with m. Therefore this ratio is plotted in Figs. 3.7, 3.10, 3.22, 3.23, and 3.21. The evolution of $J(m)$ is useful to understand the transport of angular momentum throughout the evolution of a given stellar model. If angular momentum is transported through the surface defined by a mass coordinate m, $J(m)$ drops. If no such transport occurs, $J(m)$, and also $J(m)/m^{5/3}$, remain constant. If a line of constant J is followed from one evolutionary stage to a subsequent one, it can be seen to what mass coordinate angular momentum has been transported in the star during the time between the two evolutionary stages.

When the rotationally induced mixing processes are inhibited by μ-gradients, differential rotation between the core and the envelope results. This is shown in Fig. 3.5B for Model `E15B`. The ratio of core to envelope angular velocity evolves to ~ 4. The envelope rotates slightly faster than in Model `E15`, because the star loses only 20 % of the initial total angular momentum, i.e., about half as much as Model `E15`. This is caused by the lower luminosity of Model `E15B` towards the end of central hydrogen burning (Figs. 4.2 and 4.7 below), which results in a lower mass loss, about 60 % of that of Model `E15`. Figs. 3.6B and 3.7B also show the "trapping" of the angular momentum in the core: the specific angular momentum hardly changes

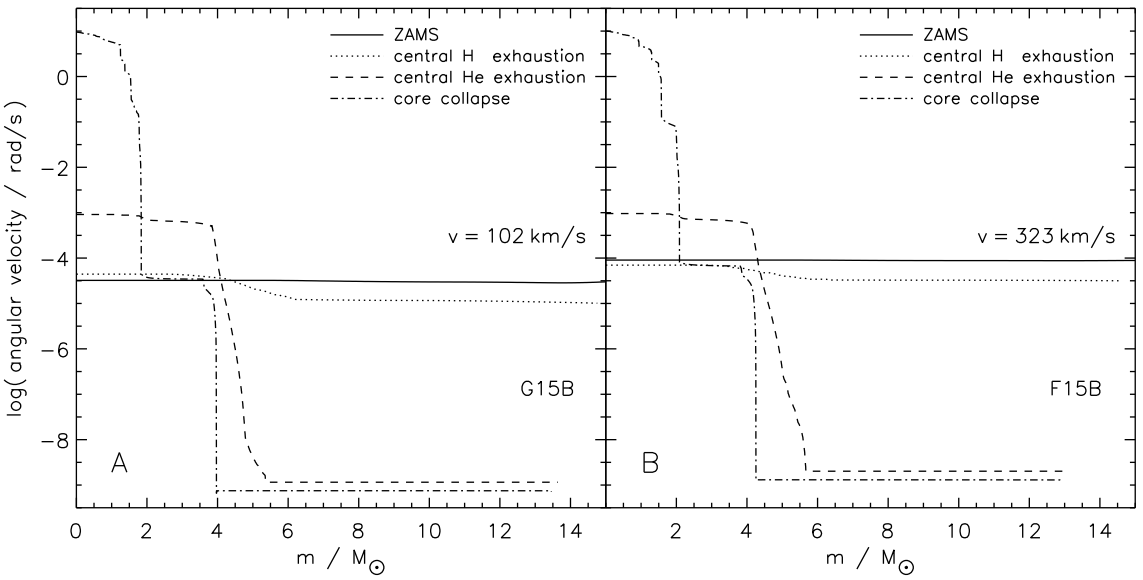

Figure 3.8: Angular velocity as function of the mass mass coordinate m at different evolutionary stages for two $15\,M_\odot$ models. In Panel **A** and **B** the evolution of stars with a ZAMS equatorial rotational velocity of $\sim 100\,km\,s^{-1}$ (Model `G15B`) and $\sim 300\,km\,s^{-1}$ (Model `F15B`), respectively, are depicted. Both models take μ-gradients into account. See also Figs. 3.9 and 3.10.

during central hydrogen burning, and $J(m)$ drops least at the location of the μ-barrier ($m \approx 3.5\,M_\odot$). The higher value of j in most parts of the envelope in comparison to Model `E15` is due to the lower angular momentum loss.

3.1.3 The influence of the initial rotation rate

Figs. 3.8, 3.9, and 3.10 show the evolution of angular velocity and specific angular momentum in Models `G15B` and `F15B`. The latter model initially has three times more angular momentum than the first, and this factor of three is conserved until central hydrogen exhaustion.

The faster rotation of Model `F15B` sustains the transport of angular momentum out of the core for a longer time than in Model `G15B`, where the core angular momentum is almost completely conserved (Figs. 3.9 and 3.10). That is, the more angular momentum initially present in the stars, the later during central hydrogen burning the rotation becomes too weak to overcome the μ-gradient.

The rotation rate of the core at central hydrogen exhaustion in Model `E15B` is much closer to that in Model `F15B` than to Model `G15B`. Accordingly, the angular momentum is less efficiently trapped in the fast rotating Model `F15B` than in the Models `G15B` and `E15B` (Figs. 3.6, 3.7, 3.9, and 3.10). This means that for the values of f_c and f_μ assumed here, the core rotation rate seems to converge to an upper limit which is close to that of Model `F15B`. In the regions with constant mean molecular weight the Eddington-Sweet circulation is efficient enough to keep the envelope close to rigid rotation even in the case of the slow rotator Model `G15B`. However, it is not fast enough to completely mix the envelope, so that different amounts of depletion of light elements occur for the different initial rotation rates (see also Sect. 4.1.3).

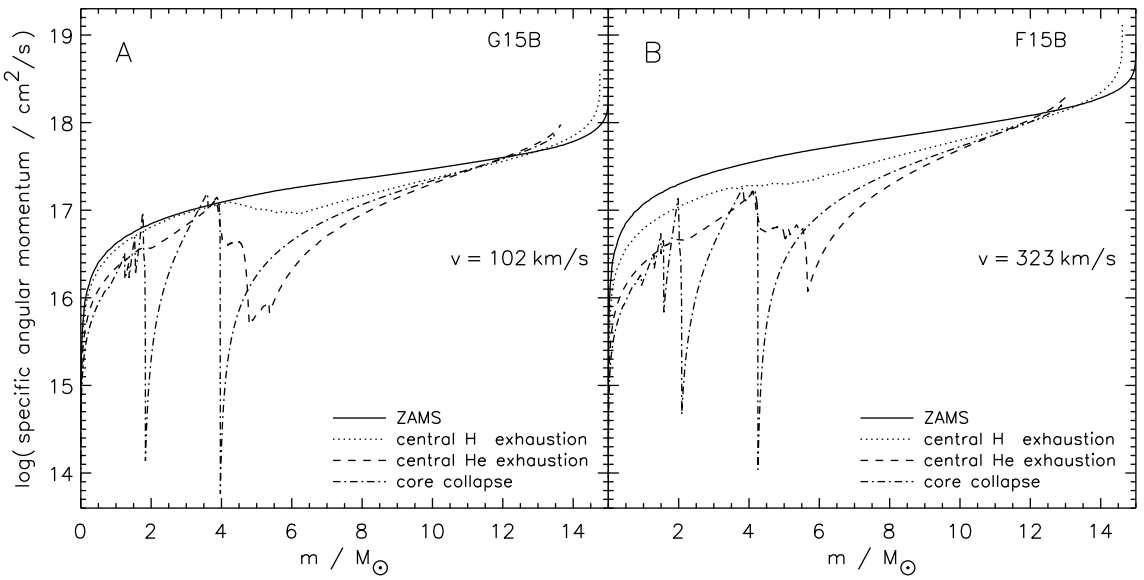

Figure 3.9: Specific angular momentum as a function of the mass mass coordinate m for the same models and evolutionary stages shown in Fig. 3.8. Panels **A** shows Model `G15B` and **B** (Model `F15B`). See also Fig. 3.10.

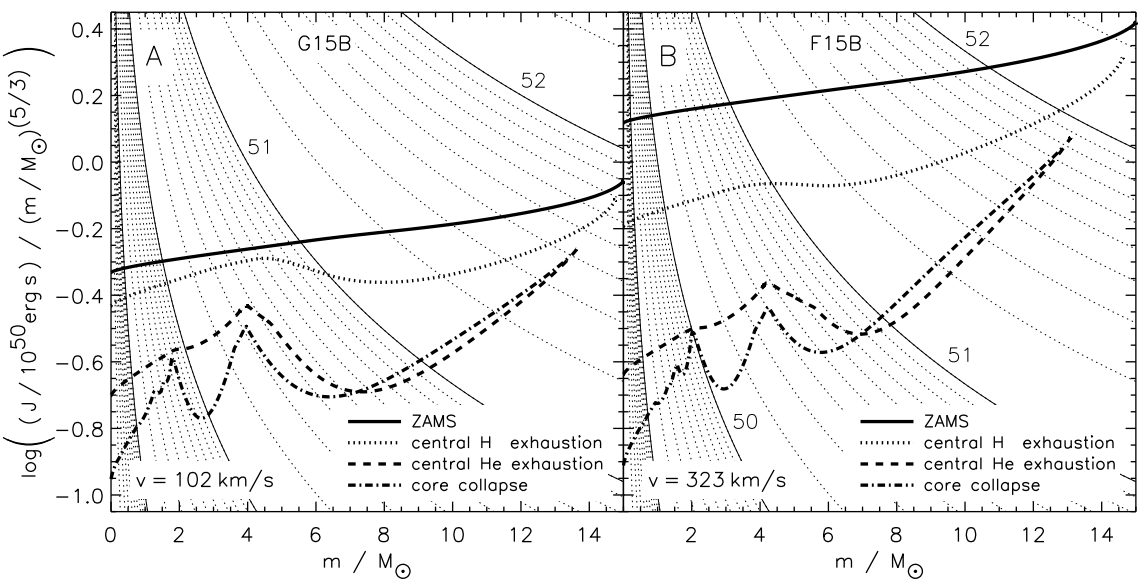

Figure 3.10: Logarithm of the integrated angular momentum $J(m) = \int_0^m j(m')\,\mathrm{d}m'$ divided by $m^{5/3}$ as a function of the mass mass coordinate m for the same models and evolutionary stages shown in Fig. 3.8 (thick lines). Panels **A** and **B** show the Model `G15B` and (Model `F15B`), respectively. The thin lines have the same meaning as in Fig. 3.7. See also Fig. 3.9.

The stronger angular momentum transport out of the core of the faster rotating models occurs simultaneously with the rotationally induced mixing across the μ-barrier: The masses of the convective cores at the end of central hydrogen burning are about $2.4\,M_\odot$, $2.5\,M_\odot$, $2.6\,M_\odot$, and $2.8\,M_\odot$ for Models `D15`, `G15B`, `E15B`, and `F15B`, respectively. For comparison, Model `E15`, where the μ-barrier is inefficient, has a core of about $3.5\,M_\odot$ at the end of central hydrogen burning. Even for the fast rotating Model `F15B`, the μ-barrier effectively limits the enlargement of the convective core as compared to Model `E15`, and thus the resultant helium core is also smaller (see also Figs. E.4, E.10, E.14, E.17, and E.20).

3.2 Central helium burning

After core hydrogen exhaustion, most of the models become red supergiants (except for Model `H12B` which first lives some time as blue supergiant) and their hydrogen-rich envelope forms an extended convection zone. The evolution of this envelope is discussed in detail in Chapter 4. In the following, the evolution of the core will be considered, mainly using the example of $15\,M_\odot$ models.

3.2.1 Chemical mixing

During core helium burning, a central convective core forms. This core rotates rigidly and remains chemically homogeneous. Above the convective core, there lies a radiative layer consisting mainly of helium. At its upper edge, hydrogen burns in a radiative shell source, causing the helium core to grow in mass (e.g., Fig. E.15). In mass coordinate, this shell source is very sharp. It contributes between about 10 % and 50 % to the total luminosity of the star.

As central helium burning proceeds, the convective core would grow if the Schwarzschild criterion for convection (Sect. 2.2.1.2) were considered. According to the Ledoux criterion for convection (Sect. 2.2.1.2), however, this is prevented by the difference in mean molecular weight between the "heavier" (i.e., higher mean molecular weight) material in the convection zone, which is partially burned to carbon and oxygen, and the "lighter", more helium-rich layers above. Typically, this leads to the formation of several small convective regions above the convective core, each separated by small semiconvective layers (e.g., Model `D15` in Figs. 3.11C and E.4). Therefore, mixing between those layers and the convective core is significantly reduced. Note that the mass of the helium-depleted carbon-oxygen core (C/O-core) determines the later evolution of the star.

As in the case of central hydrogen burning the μ-barriers are not removed by the rotationally induced mixing processes during core helium burning, if $f_\mu \gtrsim 0.05$ (e.g., Model `E15B` in Figs. 3.11B and E.17), even for the fast rotating Model `F15B` (Fig. E.20). The shear across the semiconvective layers does not become strong enough to overcome the μ-gradient, which also grows with time. This does not change much with the size of the helium core (Models `E12B`, `E15B`, and `E20B`). However, this result changes dramatically if the rotationally induced mixing is assumed

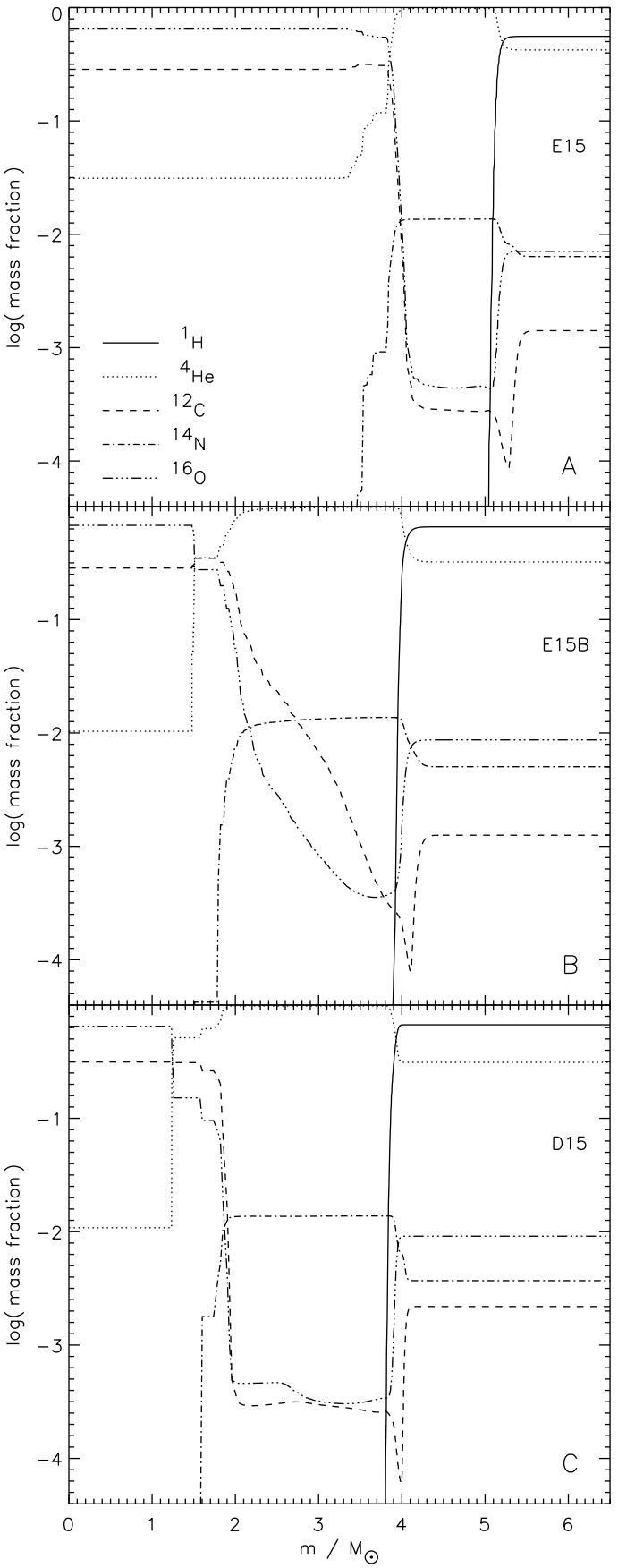

Figure 3.11: Mass fraction of the dominant species of three $15\,M_\odot$ models at the end of central helium burning as a function of the mass coordinate m. Panels **A** and **B** refer to Models `E15` and `E15B`, respectively, which have a ZAMS equatorial rotational velocity of $\sim 200\,km\,s^{-1}$, but different assumptions for the parameters of rotationally induced mixing. Panel **C** shows the non-rotating Model `D15`.

central	E15				E15B			
burning	$\tau^*_{\rm KH}$	$\omega/\omega_{\rm Kep}$	$\tau_{\rm ES}$	$\tau_{\rm burn}$	$\tau^*_{\rm KH}$	$\omega/\omega_{\rm Kep}$	$\tau_{\rm ES}$	$\tau_{\rm burn}$
phase	yr		yr	yr	yr		yr	yr
hydrogen	$5{\cdot}10^4$	$5{\cdot}10^{-2}$	$2{\cdot}10^7$	$1{\cdot}10^7$	$5{\cdot}10^4$	$5{\cdot}10^{-2}$	$2{\cdot}10^7$	$1{\cdot}10^7$
helium	$5{\cdot}10^4$	$2{\cdot}10^{-2}$	$1{\cdot}10^8$	$1{\cdot}10^6$	$7{\cdot}10^4$	$6{\cdot}10^{-2}$	$2{\cdot}10^7$	$1{\cdot}10^6$
carbon	$4{\cdot}10^4$	$3{\cdot}10^{-2}$	$4{\cdot}10^7$	$4{\cdot}10^2$	$6{\cdot}10^4$	$8{\cdot}10^{-2}$	$9{\cdot}10^6$	$4{\cdot}10^3$
oxygen	10	$5{\cdot}10^{-2}$	$3{\cdot}10^3$	1	30	0.1	$3{\cdot}10^3$	5
silicon	0.3	$8{\cdot}10^{-2}$	50	$1{\cdot}10^{-2}$	0.3	0.2	10	$3{\cdot}10^{-2}$

Table 3.1: Values of the Kelvin-Helmholtz time-scale $\tau^*_{\rm KH}$ (Eq. (2.55)), the ratio of angular velocity to the Keplerian angular velocity $\omega/\omega_{\rm Kep}$, the Eddington-Sweet circulation time-scale $\tau_{\rm ES}$ (Zahn 1992), and the burning time-scale $\tau_{\rm burn}$ for the core region during the major nuclear burning phases, for models `E15` (left) and `E15B` (right).

to be insensitive to μ-gradients (i.e., $f_\mu = 0$; Model `E15` in Figs. 3.11A and E.10). In this case, the dynamical shear instability can operate in semiconvective regions. In addition to the larger C/O core mass, the unrestricted growth of the central convective core results in a lower mass fraction of carbon in the center at core helium exhaustion. There are two reasons for that. Larger cores produce more oxygen since they evolve at higher temperatures. And second, also helium is mixed into the the convective core due to its growth, towards the end of core helium burning and this helium fuses with carbon, converting it to oxygen rather than forming new carbon. Rotationally induced mixing processes are responsible for a further supply of helium during the end of central helium burning. This may affect the production factors of carbon and oxygen, which have been used by Weaver & Woosley (1993) to gauge the experimentally uncertain $^{12}{\rm C}(\alpha,\gamma)^{16}{\rm O}$ reaction rate .

An interesting issue is the mixing in the radiative helium layer between the convective core and the hydrogen-burning shell. If the products of helium burning could be mixed upward into the hydrogen-burning shell, *primary* production of $^{14}{\rm N}$ could occur. Usually nitrogen is only produced from the "seed" CNO isotopes initially present in the star. If hydrogen were transported down into the helium-burning center, a much stronger than normal s-process could result and build up more heavy or neutron-rich elements. The dominant mixing process present in this layer is Eddington-Sweet circulation, with some contribution from the GSF instability. During the early stages of core hydrogen burning of models with $f_\mu = 0$ (e.g., Model `E15`), the secular shear instability dominates slightly over the Eddington-Sweet circulation at the upper edge of the helium core. Towards central helium exhaustion, the mixing is dominated by the GSF instability. In the case of $f_\mu = 0.05$, the secular shear instability is suppressed by the μ-gradients, and is inefficient because differential rotation is more efficiently smoothed out by the Eddington-Sweet circulation. Consequently, the GSF instability, which is sensitive to differential rotation, is weakened, too.

An estimate for the contribution of the Eddington-Sweet circulation to the rotationally induced mixing in radiative layers can be obtained from the time-scale $\tau_{\rm ES}$

of the Eddington-Sweet circulation given by (Zahn 1992)

$$\tau_{\rm ES} \sim \tau_{\rm KH} \left(\frac{\omega_{\rm Kep}}{\omega} \right)^2 , \qquad \omega_{\rm Kep} := \sqrt{Gm/r^3} \, . \tag{3.2}$$

For the amount of differential rotation in the models, this gives also the characteristic time-scale for mixing by the GSF instability (Sect. 2.2.2.5).

Table 3.1 compares the characteristic Eddington-Sweet time-scales in the radiative layers above the convective core at different burning phases with the durations of the burning phases for Models `E15` and `E15B`. Obviously, there is only sufficient time for the Eddington-Sweet circulation to perform significant mixing during central hydrogen burning. Later phases occur too rapidly. In Model `E15B` some slight mixing during central helium burning is present, but the rotation in the core of Model `E15` is too slow. Additionally, the efficiency, $f_{\rm c}$, of chemical mixing is taken to be higher in Model `E15B` than in Model `E15`. This can be seen in Fig. 3.11B. There is a gradient in ^{12}C and ^{16}O, reaching from the convective core up to the edge of the helium core. However, the increase in ^{12}C or ^{16}O is not sufficient to allow for a primary nitrogen production in the hydrogen-burning shell. A small increase in ^{15}N appears at the upper edge of the helium core, but it is not significant in comparison to the total ^{15}N in the star, or the amount destroyed during hydrogen burning. This effect is not notably more pronounced in the faster rotating Model `F15B`, or for the stars with different initial mass. In Model `E15` (Fig. 3.11A) the ^{12}C and ^{16}O gradient is much steeper and levels off to the CNO equilibrium values a few tenths of a solar mass above the convective core. As expected, no enrichment of ^{12}C and ^{16}O appear above the outermost semiconvective layer of the convective core in the non-rotating Model `D15` (Fig. 3.11C).

An energetic limit on the amount of mixing that can be performed by shear instabilities can be derived by comparing the rotational energy of the core with the potential energy required to lift processed matter from the upper edge of the convective core to the hydrogen-burning shell source, taking into account buoyancy. Note that this limit does not apply to the Eddington-Sweet circulation, which is powered by thermal imbalance. For a typical value of $\omega/\omega_{\rm Kep} = 0.05$ and a difference in the mean molecular weight of fully ionized carbon relative to helium of ~ 0.3 (oxygen would be even heavier), an enrichment of carbon by only $\lesssim 0.5\,\%$ is possible. This assumes the carbon to be homogeneously distributed throughout the radiative layer and all the rotational energy of the core is used to supply the buoyancy energy. However, there should be some dissipation and a gradient in the abundance from the center to the surface should build up, similar to Fig. 3.11B. Both reduce the amount of mixing to the surface of the helium core. A similar limit would also apply to mixing by magnetic instabilities which are caused by the winding up of magnetic fields, converting rotational energy into magnetic field energy.

Some mixing is present between the helium core and the hydrogen-burning shell, but the high rise in entropy and the small pressure scale-height at the location of the hydrogen-burning shell suppress most of it. Comparing Figs. E.10 and E.17, it can be seen that the tail of the energy generation rate at the lower bound of the hydrogen-burning shell source in Model `E15B` penetrates deeper into the helium core,

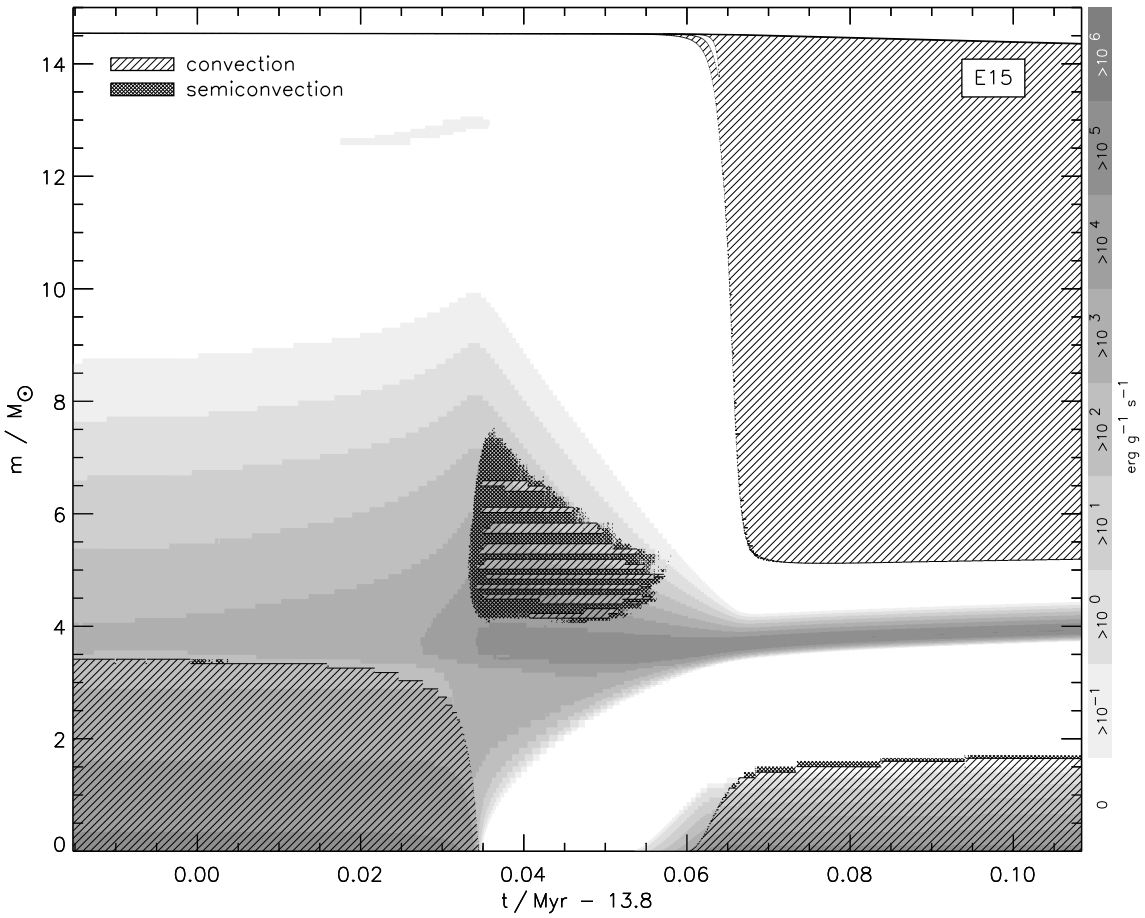

Figure 3.12: Evolution of the internal structure of Model `E15` from core hydrogen exhaustion until core helium ignition. Convection (semiconvection) is indicated as diagonal (crossed) hatching. Different shades of grey give orders of magnitude of the nuclear energy generation rate (scale on the right-hand side). The topmost solid line corresponds to the surface of the star. See Appendix E and Fig. E.10 for more details.

i.e., some small amount of hydrogen is mixed down and burned there. In Model `E15`, where the core is rotating slower, and also in the non-rotating Model `D15` (Fig. E.4), the energy generation due to the hydrogen shell burning drops off much steeper. However, the protons in Model `E15B` burn quite fast as they are mixed deeper inside the helium core. They cannot reach the central convective region. This could only happen if the mixing were much faster, like by convection. Its actual occurrence during helium shell burning is discussed in Sect. 3.3.1.

The mixing in the layers above the helium core is also dominated by the Eddington-Sweet circulation. Here, the circulation time-scale is longer than that in the helium core ($\gtrsim 10^9$ yr), mainly because of the slower rotation (relative to Keplerian rotation; see Fig. 3.5). Some minor transport of angular momentum occurs, but the chemical mixing processes are negligible.

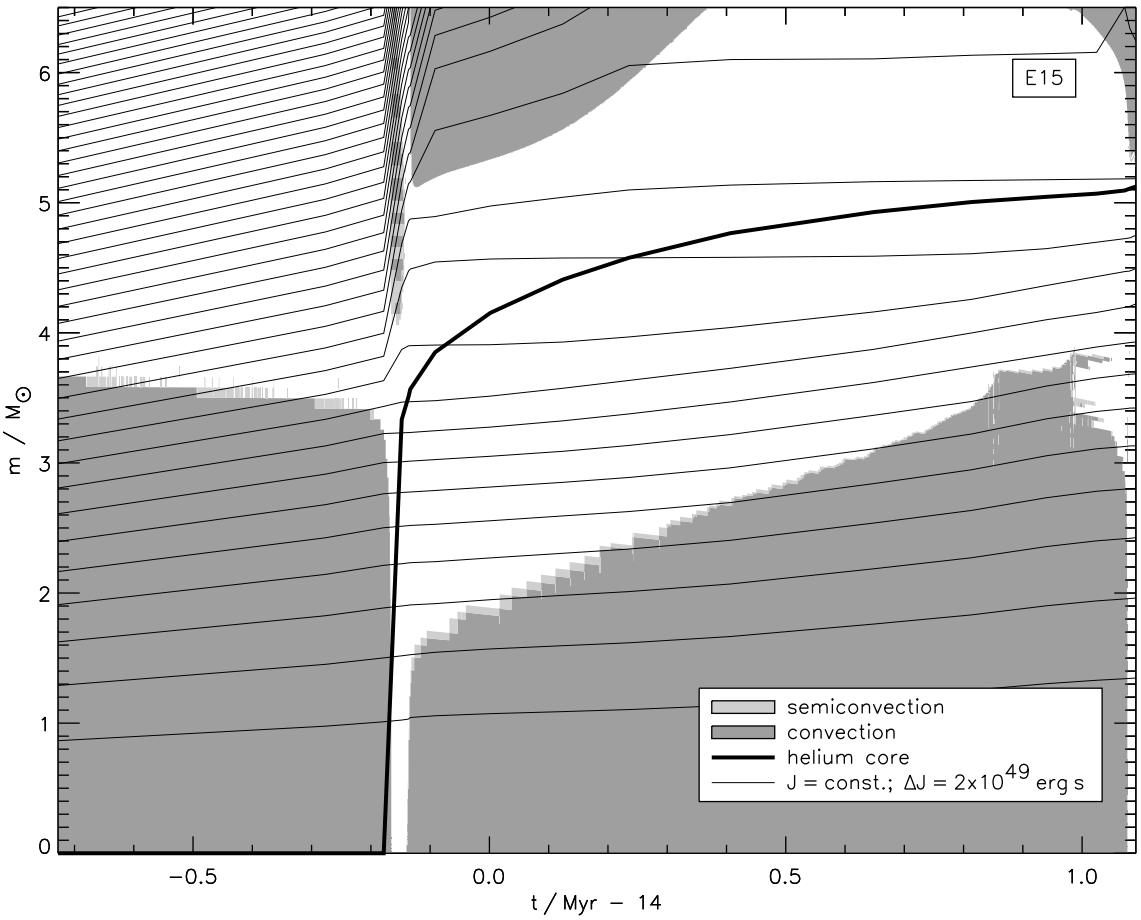

Figure 3.13: Evolution of the angular momentum from core hydrogen exhaustion until core helium exhaustion in the innermost $6.5\,M_\odot$ of Model E15. Shown are lines of constant total angular momentum $J = \int_0^m j\,dm$ (thin lines); they have a spacing of $2{\cdot}10^{49}$ erg s. The thick line indicates the upper edge of the helium core, light grey shading semiconvection, and dark grey shading convective regions. See also Fig. 3.12.

3.2.2 Transport of angular momentum

After core hydrogen exhaustion, the stars undergo a phase of major restructuring: the core contracts, while the envelope expands. This leads to a spin-up of the core (Figs. 3.5 and 3.8) and a spin-down of the envelope. At the same time, the convective envelope grows in mass and its bottom approaches the helium core. The steep gradient in angular velocity between at the lower boundary of the rigidly rotating convective envelope and the helium core (Fig. 3.5), is much shallower in the physical space coordinate r (radius) than in the mass coordinate m, because at the same position a large gradient in density appears. The rigidly rotating envelope is characterized at core helium burning and on into the collapse phase, by a steep rise in the specific angular momentum at its inner edge (Figs. 3.6 and 3.9). The whole helium core stays close to rigid rotation during central helium burning (Figs. 3.5 and 3.8). The evolution of the envelope is discussed in more detail in Chapter 4.

Until core helium exhaustion, the helium core loses appreciable amounts of an-

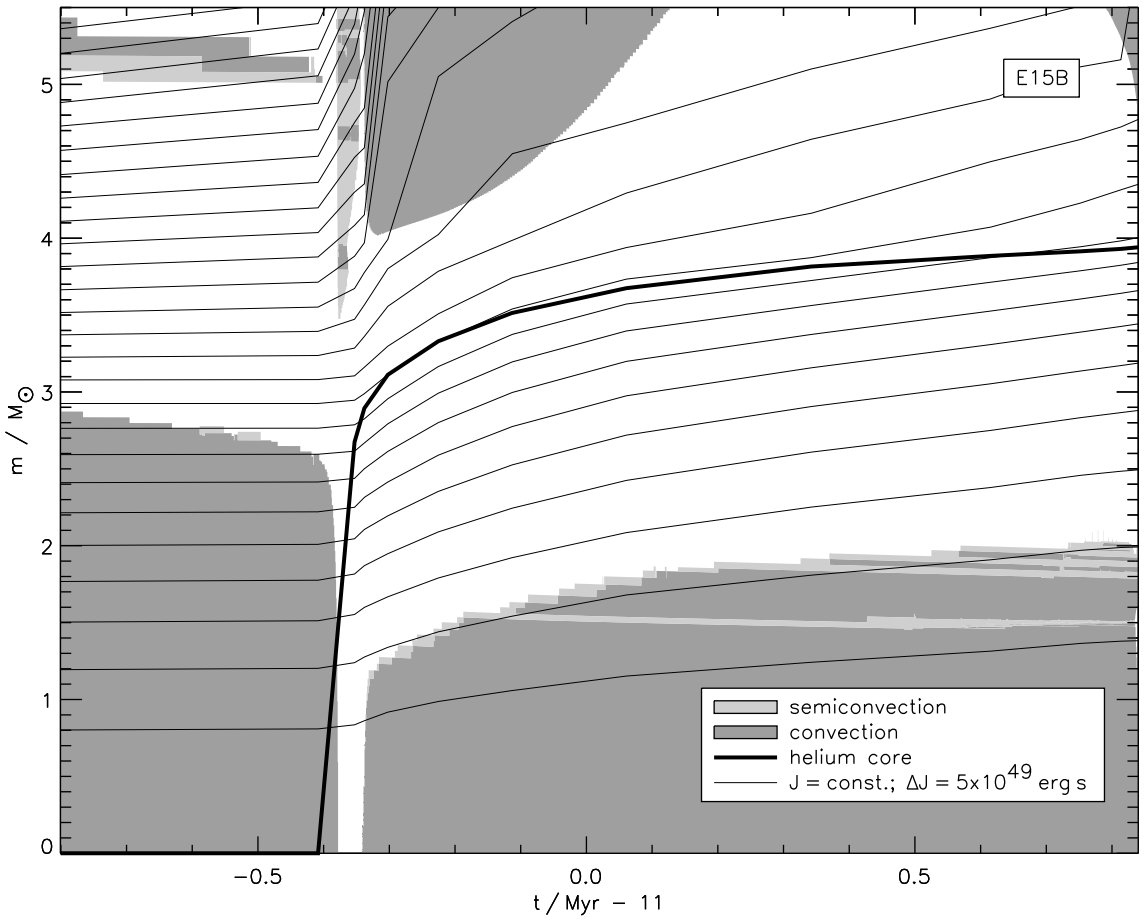

Figure 3.14: Evolution of the angular momentum from core hydrogen exhaustion until core helium exhaustion in the innermost $5.5\,M_\odot$ of Model `E15B`. Lines and shading have the same meanings as in Fig. 3.13, except that the lines of constant total angular momentum J have a spacing of $5{\cdot}10^{49}$ erg s.

gular momentum compared to the angular momentum contained in the same region at core hydrogen exhaustion (Figs. 3.6, 3.7, 3.9, and 3.10). Three major processes contribute to this effect: First, some angular momentum is lost during the star's restructuring phase between central hydrogen depletion and helium ignition. Second, the core grows in mass during its evolution due to hydrogen shell burning, and thereby engulfs regions with lower specific angular momentum, such that the core gains little angular momentum by its growth (Figs. 3.13 and 3.15). The reasons for the low specific angular momentum above the core are secular shear instabilities, the *first dredge-up*, and short-lived convective regions which temporarily extend down to mass coordinates smaller than the final helium core mass (Fig. 3.12). In the diagrams in Appendix E these short-lived convective regions appear only as a small stripe immediately preceding the formation of the extended convective envelope. During the first dredge-up, the surface convection zone penetrates deep into the star, close to the young helium core (Fig. 3.12) and in doing so mixes thermonuclear processed matter from the stellar interior to the surface (Chapter 4), and also transports angular momentum. In the present calculations, the resulting

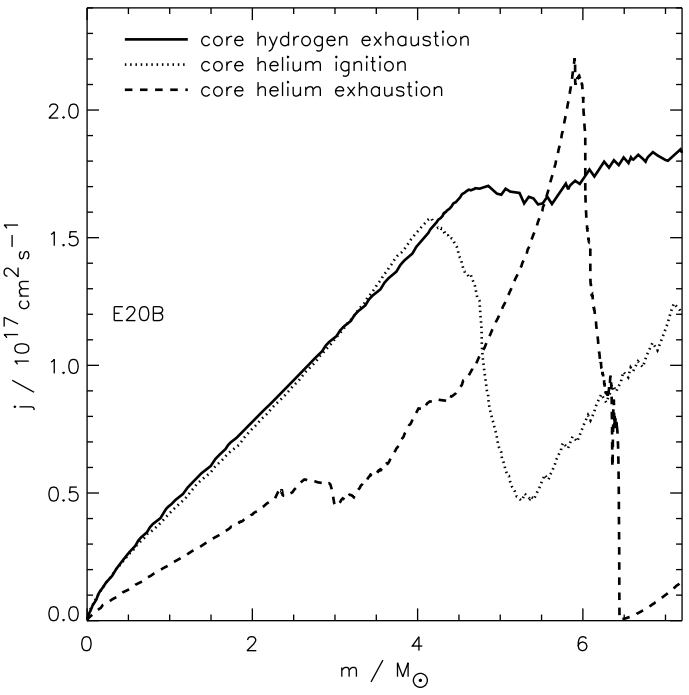

Figure 3.15: Specific angular momentum as a function of the interior mass coordinate m in Model `E20B` at core hydrogen depletion (solid line), core helium ignition (dotted line; core mass $\sim 4\,M_\odot$), and core helium depletion (dashed line; core mass $\sim 6\,M_\odot$).

regions of decreasing specific angular momentum do not become unstable to the Solberg-Høiland instability because they are stabilized by buoyancy (stable temperature stratification and μ-gradients). Third, there is angular momentum transport from the helium core into the envelope through the hydrogen-burning shell. This is much less efficient for Model `E15` (Fig. 3.13), than in the Models `G15B`, `E15B` (Fig. 3.14), and `F15B`. These models of the "`B`" series lose less angular momentum during the restructuring phase because of the inhibiting effect of the μ-gradients, but more during central helium burning, due to their considerably faster rotation. The rotation helps to overcome the inhibiting effect of buoyancy due to the stabilizing temperature stratification and μ-gradients. The operation of rotationally induced instabilities in the vicinity of the hydrogen-burning shell was also discussed in the previous section.

The relative loss of angular momentum in Models `G15B`, `E15B`, and `F15B` during helium burning increases with the initial amount of angular momentum left at the end of central hydrogen burning. Consequently they end up with very similar core angular momenta (Figs. 3.9 and 3.10) and rotation rates (Fig. 3.8), about three times that of Model `E15` (Figs. 3.5 and 3.7).

3.3 Late evolution until core collapse

After core helium exhaustion, the C/O core contracts and subsequently phases of carbon, neon, oxygen, and silicon central convective and shell burning follow inside this core. A brief description of the evolution of a typical Type II supernova progenitor model and its burning phases is given in Appendix E.2.

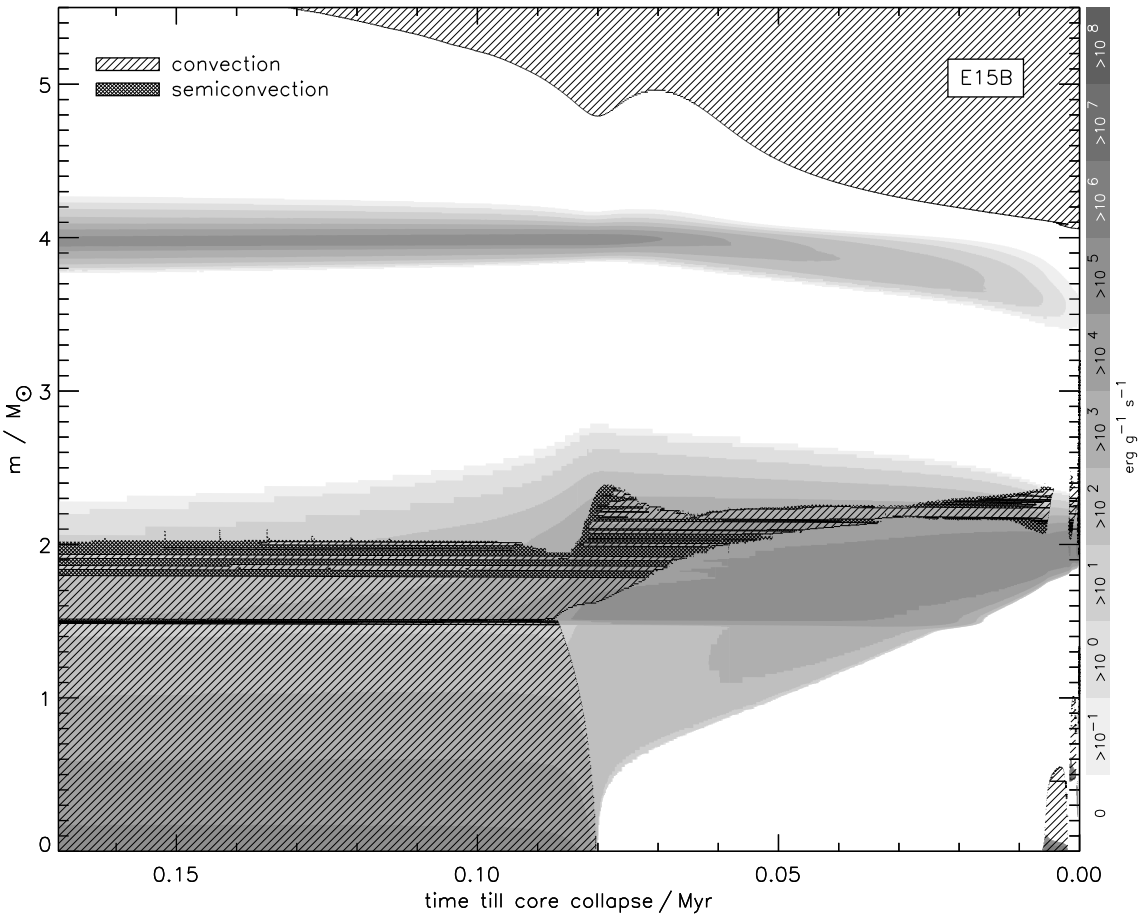

Figure 3.16: Evolution of the internal 5.5 $M_\odot$ of Model `E15B` from core helium exhaustion until core collapse. Shading and hatching has the same meaning as in Fig. 3.12. See also Fig. E.17 in Appendix E.

3.3.1 Chemical mixing in the helium shell

One of the most spectacular mixing events induced by rotation during late stages of stellar evolution is the dredge-down of protons into the helium-burning shell. After core helium exhaustion, the C/O core contracts and the burning of helium continues in a shell source. At the same time, the outer layers of the helium shell expand and energy generation in the hydrogen-burning shell decreases by several orders of magnitude (e.g., Model `E15B` in Figs. 3.16 and E.17). In many of the low-mass stars, the hydrogen shell extinguishes completely due to the decreasing temperature and density at its location. The rotationally induced mixing can now operate more efficiently because this implies a reduced entropy barrier. The two processes which are responsible for the mixing in this situation are, again, the Eddington-Sweet circulation and the GSF instability. Due to the lower temperatures, protons mixed downwards into the helium-rich layers burn slower than if the hydrogen-shell source were active and can therefore penetrate deeper into the helium-rich layers. In Fig. 3.16, this is visible as the extension of the hydrogen-burning region towards lower mass coordinate after the end of central helium burning. During this time

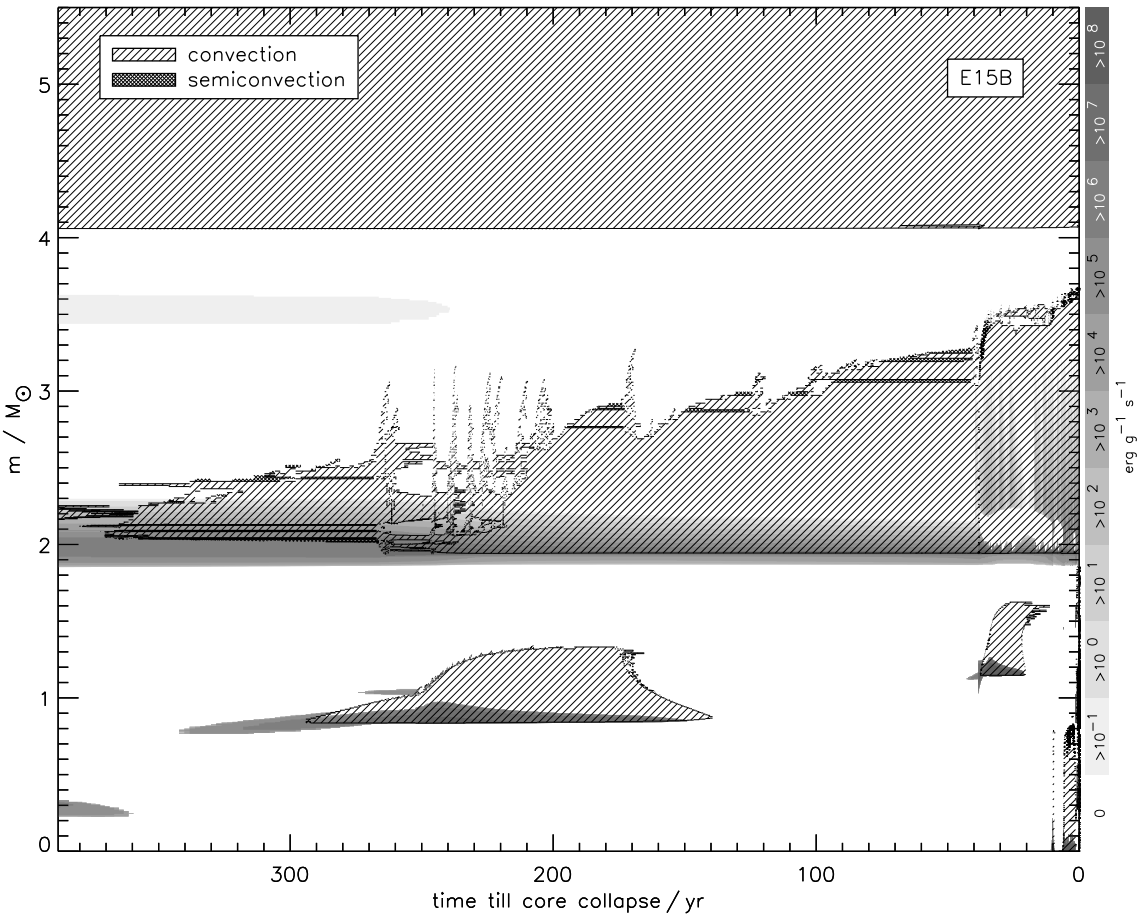

Figure 3.17: Evolution of the internal 5.5 $M_\odot$ of Model `E15B` from carbon shell burning until core collapse. Shading and hatching has the same meaning as in Fig. 3.12. The helium shell is located between $m = 2\,M_\odot$ and $4\,M_\odot$. See also Fig. E.17 in Appendix E.

the total energy generation rate in the hydrogen shell drops by orders of magnitude. Due to the continuing contraction of the C/O core, the bottom of the helium shell becomes increasingly hotter and the overlying convection zone extends towards the upper edge of the helium core. When this convection zone reaches regions where protons have been enriched by the rotationally induced mixing, they are transported into the hot helium-burning shell source and burn rapidly (Fig. 3.17). The proton-burning time-scale becomes comparable to the convective mixing time-scale, and most of the hydrogen is burned before it can reach the bottom of the convective helium shell (Fig. 5.1).

This mechanism opens new channels of nucleosynthesis which are investigated in more detail in Chapter 5. The injection of protons into the hot helium layers and their fast burning also causes a contribution to the energy generation. In Fig. 3.17 and in the figures in Appendix E this is reflected in an extended release of energy in the convective helium shell (e.g., Fig. E.17). It is usually governed by single mixing "events" because of the feedback between the expansion of the convective region in the helium shell and the energy generation by the injected protons. The longer duration of later mixing "events" in the figures in Appendix E is due to

both, the larger amount of hydrogen mixed down at later times when regions with higher hydrogen mass fractions are entered, but also due to the choice of the time-axis. It cannot be ruled out that also the temporal discretization required by the numerical solution of the stellar structure equations is responsible for the strength of the individual "events". The amount of hydrogen mixed into the helium convection zone obviously depends upon the hydrogen enrichment in the layers into which the convective helium shell penetrates. In the present work, hydrogen mass fractions up to 10^{-6} are found in those layers.

The occurrence of this kind of mixing is favored by the following two conditions. First, large core masses, i.e., larger initial stellar masses, cause a stronger growth of the convective helium shell. Second, more mixing is obtained for faster core rotation.

The dependence on the core mass can be seen by comparing Models `E15B` and `E20B` (Figs. E.17 and E.18) or Models `E15` and `E20` (Figs. E.10 and E.11). In both cases the convective helium shell reaches closer to the upper edge of the helium core for the more massive stars. The deeper in the gravitational potential the bottom of the helium shell is located, the higher energy generation rates result, and the stronger is the growth of the convective helium shell. Usually this increases for more massive cores. Due to this effect, the contraction of the C/O core during the late evolution causes the continuing growth of the convective helium shell. Factors other than the mass also determine the radial extent of the C/O core, for example, how close to its upper edge carbon burning proceeds. It is also important how deep the bottom of the convective part of the helium shell actually reaches, since the convective mixing it is responsible for the fuel supply. For example, in Model `D20` (Fig. E.5) the convective helium shell is split into three different convective regions separated by μ- and entropy barriers. There is hardly any mixing between them. The upper edge of the outer convective helium shell stays more than $1.5\,M_\odot$ below the hydrogen-rich layers. In Model `G20` (Fig. E.15), e.g., the barriers inside the convective helium shell are not present and the convection zone extends closer to the hydrogen-rich layers. Some small effect on this may also be due to rotationally induced mixing in the vicinity of the bottom of the helium shell.

The influence of the rotationally induced mixing on the hydrogen enrichment in the helium core can be seen by comparing Models `G20B` and `F20B` (Figs. E.15 and E.21). The core of Model `G20B` is rotating slower and consequently shows less mixing of hydrogen into the upper edge of the helium shell. Also Model `E20` (Fig. E.11) has less mixing, because it rotates slower (Fig. 3.22) and less efficient chemical mixing is assumed inside the chemically homogeneous helium core. In the non-rotating models (e.g., Model `D20`) this mixing of protons into the convective helium shell cannot occur because no protons are transported below the former hydrogen shell source. The transition between the hydrogen-free and the hydrogen-rich layers constitutes an efficient (μ- and entropy-) barrier which cannot be easily perforated by the convective helium shell, and it can therefore extend only into essentially hydrogen-free layers.

The sharp transitions in mean molecular weight and entropy at the upper edge of the helium core are also not significantly reduced in the rotating models (Appendix F); the traces of hydrogen mixed down into the helium layers have little effect

on these.

3.3.2 Chemical mixing inside the C/O core

Mixing due to rotationally induced instabilities inside the C/O core during the remaining burning phases is unimportant. The dominant instabilities occurring are again the Eddington-Sweet circulation and the GSF instabilities, at about same order of magnitude. From Table 3.1 it can be seen that the Eddington-Sweet circulation is not fast enough to induce significant mixing.

No important new paths of nucleosynthesis can be expected to come from mixing of *traces* of material into a neighboring burning phase inside the C/O core, because such traces are already present.

In the fast rotating cores of the models of the "`B`" series, secular shear instabilities arise above several of the central and shell convection zones for a limited time, but they do not become efficient enough to cause any noticeable mixing.

3.3.3 Transport of angular momentum

From the previous discussion of the weak mixing inside the C/O core it is clear that the rotationally induced mixing processes cannot effectively remove angular momentum from the core. In particular, they do not keep the core, or even the core and the envelope, in rigid rotation. Strong differential rotation results (Figs. 3.5 and 3.8). The only instability which is efficient enough to enforce rigid rotation in the domain of its operation at this time is convection. Since the radii of the lower boundaries of the major convection zones of carbon, oxygen, and silicon burning are much smaller than that of their upper edges, large difference in the specific angular momentum from the bottom to the top of the convection zone can exist. Thus, angular momentum is redistributed, mainly from inside out. The typical signature of such a convection zone is a steep drop of the specific angular momentum at its bottom, accompanied by a large increase at its top (Figs. 3.6, 3.9, and 3.20). The most pronounced example is that of the convective envelope. Another is the convective helium shell at a lower mass coordinate. Some smaller spikes of convective carbon, neon, and/or oxygen, and silicon shell burning are also apparent.

Convection zones that subsequently overlap can transport angular momentum efficiently over larger scales than their individual extent. This is most efficient if the lower boundary of a convective shell overlaps with the upper boundary of a preceding convection zone. For the models investigated in this work, such an overlap occurs rather infrequently (Appendix E). Subsequent shells, which are driven by nuclear burning, tend to form their lower boundary at the upper edge of a preceding shell, where the fuel for their burning is not yet depleted. The most prominent example of this is the sequence of carbon-burning shells (e.g., Fig. E.11). The only exceptions are some of the late carbon burning shells, and the oxygen burning shells in Models `G15B` and `E15B`. Most of the redistribution of angular momentum inside the C/O core happens only *inside* the individual convective regions. This results in a spiky j-profile.

Convective angular momentum transport does not operate across the boundary of the C/O core. These cores retain their angular momentum after core helium exhaustion. Some redistribution, mainly due to convection, occurs inside the cores. This can be seen in Fig. 3.7A for Model `E15`. No angular momentum is lost from below $m \approx 3.4\,\mathrm{M}_\odot$ and $m \approx 5.1\,\mathrm{M}_\odot$, i.e., the boundaries of the helium and the C/O core, respectively, after central helium exhaustion.

In models with more rapidly rotating cores, (Models `G15B`, `E15B`, and `F15B`; Figs. 3.7B and 3.10), some of the angular momentum does get lost from the helium core. Its upper boundary is located at $m \approx 3.7\,\mathrm{M}_\odot$ and remains a significant barrier for angular momentum transport. The loss of angular momentum from the helium core is correlated with the mixing of hydrogen into the helium shell described in Sect. 3.3.1. The boundary between the C/O core and the helium shell is an even better insulator for angular momentum. In none of the models, notable amounts of angular momentum are transported across it (Figs. 3.7 and 3.10). However, note that any transport of angular momentum by magnetic fields is neglected here (see Sections 2.2.3 and 3.5.1).

3.3.4 Stability to triaxial deformations

As described in Sect. 2.1.2, the approximations employed in this work are limited to slow rotation in the sense that no triaxial deformation appear. In the KEPLER code, the influence of the centrifugal forces on the structure is even completely neglected. However, when models from calculations with STERN, where centrifugal forces *are* included, are "linked" to KEPLER at a central temperature of $10^9\,\mathrm{K}$, the evolution continues usually smoothly, i.e., these forces *are not* important at this point of evolution. On the ZAMS, the rotational energy E_rot of the star is negligible in comparison to its gravitational binding energy E_pot for all model, even for those which are close to critical rotation at their surface ($E_\mathrm{rot}/|E_\mathrm{pot}| \ll 1\,\%$).

However, during their evolution the stellar models contract and — as outlined in Sect. 3.3.3 above — the transport of angular momentum out of the core is inhibited or slow, with the consequence of rapidly rotating cores (Figs. 3.5, 3.8, and Table 3.3). For local angular momentum conservation in a shell with given specific angular momentum j, the ratio of angular velocity to Keplerian angular velocity scales as

$$\frac{\omega}{\omega_\mathrm{Kep}} = \frac{j}{k\sqrt{Gmr}} \sim r^{-1/2}\,, \qquad k \approx 2/3\,. \tag{3.3}$$

The ratio of the specific rotational energy to the gravitational potential is then given by

$$\frac{e_\mathrm{rot}}{\phi_\mathrm{grav}} = \frac{1}{2}\left(\frac{\omega}{\omega_\mathrm{Kep}}\right)^2\,. \tag{3.4}$$

This ratio is displayed for several $15\,\mathrm{M}_\odot$ models in Fig. 3.19. A uniformly rotating, self-gravitating, incompressible, and inviscid fluid (McLaurin spheroid) becomes secularly unstable to triaxial deformations when the ratio of rotational to gravitational

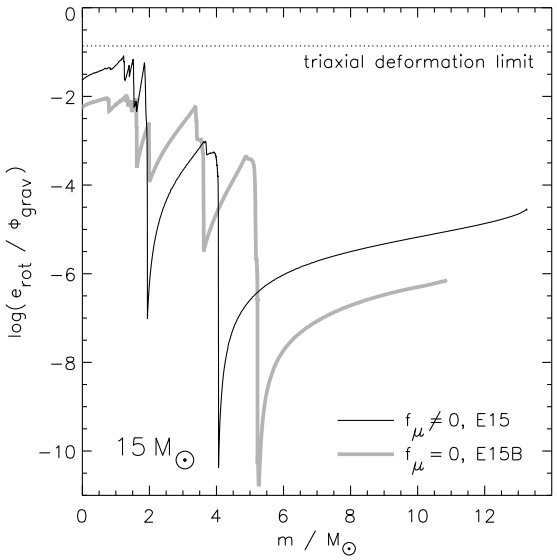

Figure 3.18: Ratio of specific rotational energy $e_{\rm rot} = \frac{1}{2}\omega j$ to the gravitational potential $\phi_{\rm grav} = Gm/r$, as function of the mass coordinate m at the onset of core collapse. Shown are two $15\,{\rm M}_\odot$ stars with a ZAMS equatorial rotational velocity of $\sim 200\,{\rm km\,s^{-1}}$. The black line shows Model `E15B` and the grey line Model `E15`. The dotted line indicates the limit for secular instability to triaxial deformations in McLaurin spheroids (Ostriker & Bodenheimer 1973).

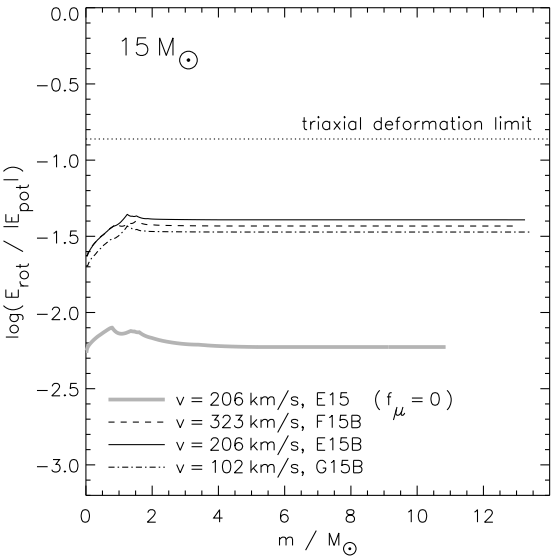

Figure 3.19: Ratio of integrated rotational energy $E_{\rm rot}(m) = \frac{1}{2}\int_0^m \omega(m')j(m')\,{\rm d}m'$ to integrated gravitational potential energy $E_{\rm pot}(m) = \int_0^m Gm'/r(m')\,{\rm d}m'$ as a function of the mass coordinate m for different $15\,{\rm M}_\odot$ stars. The dash-dotted, solid, and dashed lines correspond to Models `G15B`, `E15B`, and `F15B`. The thick grey line corresponds to Model `E15`, which uses a different assumption about the rotationally induced mixing processes. The dotted line shows the limit for secular instability to triaxial deformations in McLaurin spheroids (Ostriker & Bodenheimer 1973).

potential energy

$$\frac{E_{\rm rot}}{E_{\rm pot}} = \frac{1}{2}\int_0^m \omega^2(m')\,{\rm d}m' \Bigg/ \int_0^m {\omega_{\rm Kep}}^2(m')\,{\rm d}m' \tag{3.5}$$

exceeds ~ 0.1375 (e.g., Ostriker & Bodenheimer 1973; Tassoul 1978). If this ratio exceeds ~ 0.26, the object becomes dynamically unstable to non-axisymmetric instabilities and fission may occur (Ostriker & Tassuol 1969; Ostriker & Bodenheimer 1973). The stars simulated in the present work are well below these limits even at the pre-collapse stages ($E_{\rm rot}/E_{\rm pot} \lesssim 0.3$ of the critical value; see Fig. 3.18), and therefore no triaxial instabilities arise.

3.4 Angular momentum prior to core collapse

From the previous discussions it is clear that the distribution of angular momentum in the star at onset of core collapse strongly reflect its recent convective structure. Sharp peaks of specific angular momentum appear at the upper edges of former or still active convective regions, i.e., at the top of shells of equal composition. Fig. 3.20

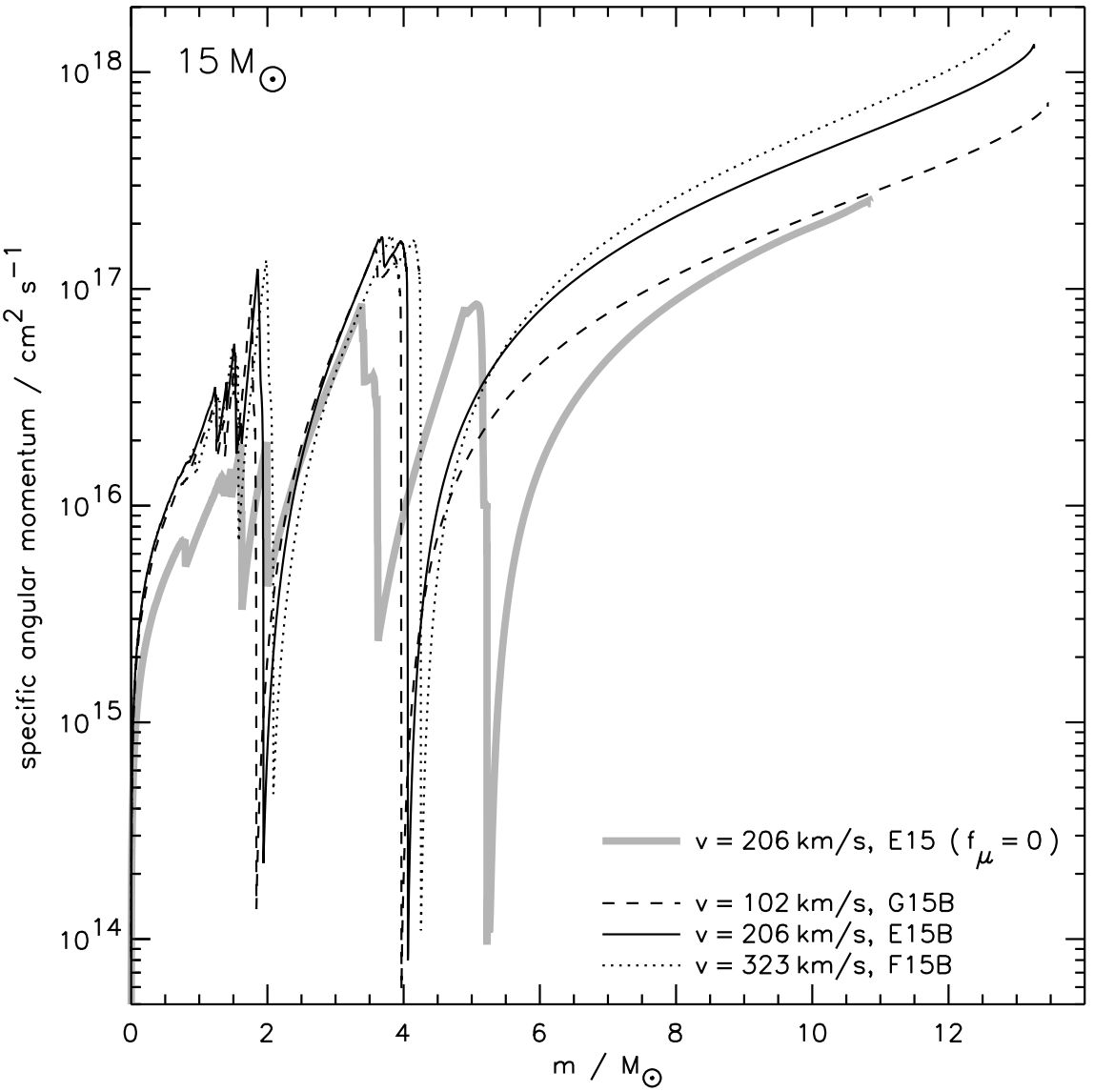

Figure 3.20: Specific angular momentum as a function of the mass coordinate m for $15\,M_\odot$ stars at the onset of core collapse. The black lines show Models `G15B`, `E15B`, and `F15B` with ZAMS rotational velocity of $\sim 100\,\mathrm{km\,s^{-1}}$ (dotted), $\sim 200\,\mathrm{km\,s^{-1}}$ (solid), and $\sim 300\,\mathrm{km\,s^{-1}}$ (dashed), respectively. The thick grey line shows the Model `E15`, for which the rotationally induced mixing-processes are assumed insensitive to μ-gradients.

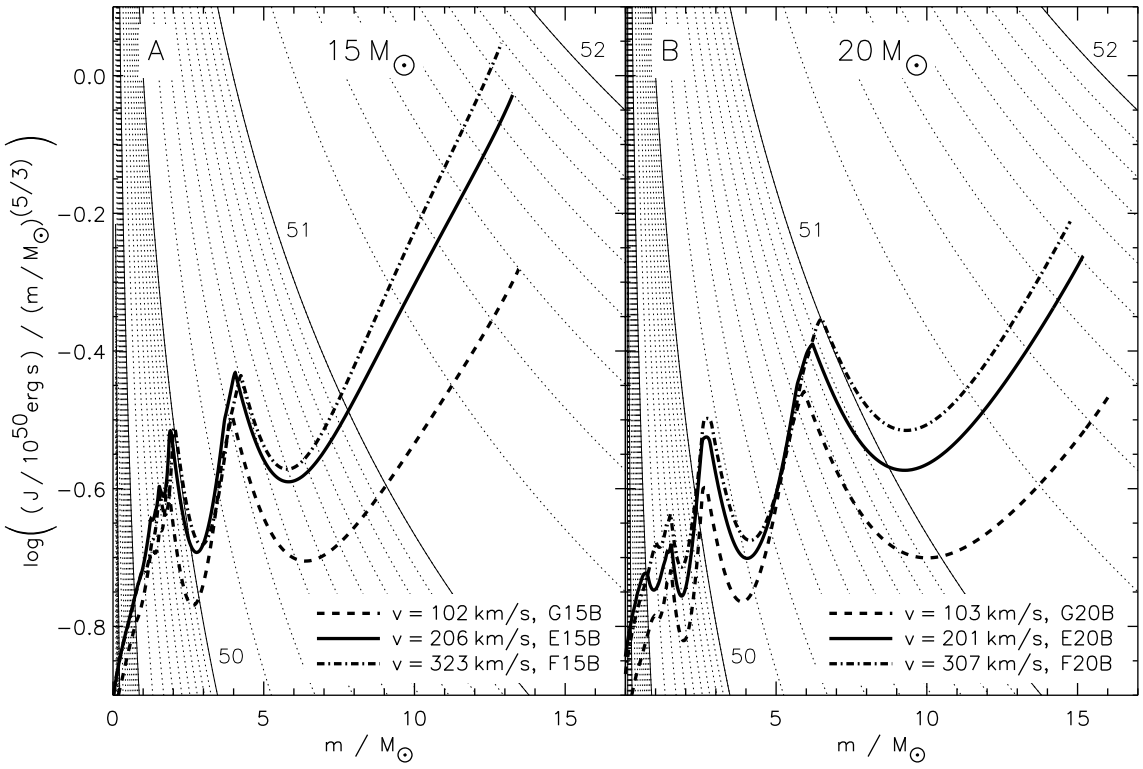

Figure 3.21: Integrated angular momentum $J(m) = \int_0^m j(m')\,\mathrm{d}m'$ divided by $m^{5/3}$ as a function of the mass mass coordinate m for different ZAMS rotational velocities (thick lines) at core collapse. The two Panels show stars of initial masses of $15\,\mathrm{M}_\odot$ (Panel **A**: Models `G15B`, `E15B`, and `F15B`) and $20\,\mathrm{M}_\odot$ (Panel **B**: Models `G20B`, `E20B`, and `F20B`). The thin lines have the same meaning as in Fig. 3.7.

shows the distribution of the specific angular momentum at the pre-collapse stage of $15\,\mathrm{M}_\odot$ stars with different initial rotation rates (Models `E15`, `G15B`, `E15B`, and `F15B`). The calculations of the present work are stopped at the onset of core collapse, defined by the infall velocity inside the iron core exceeding $9{\cdot}10^2\,\mathrm{km\,s^{-1}}$. At this stage of evolution the investigated stars typically have central densities of $\lesssim 1{\cdot}10^{10}\,\mathrm{g\,cm^{-3}}$.

Clearly, Model `E15` has much less angular momentum left in the core than the other models (see also Table 3.2). The three $15\,\mathrm{M}_\odot$ stars with different rotation rates on the ZAMS (Models `G15B`, `E15B`, and `F15B`) show a very similar distribution of angular momentum. This can also be seen from the integrated angular momenta in Fig. 3.21A. Their similarity in the angular momentum distribution is reflected in their entire structure, for example the masses of the cores Table 3.2. The reason for this is the inhibitation of rotationally induced mixing during central hydrogen burning by the μ-barrier and its relatively small effect during central helium burning. In contrast, Model `E15` grows a larger helium and C/O core due to the lack of sensitivity to μ-gradients.

Similar results are also found for the $20\,\mathrm{M}_\odot$ stars Fig. 3.21B. Here, the differences in the final angular momentum are slightly larger inside the helium core than for the $15\,\mathrm{M}_\odot$ stars, but still much smaller than the differences in the initial angular momenta of the models. The main reason for this convergence is stronger mixing

during the early evolution of the faster rotating stars. Most of this happens during core hydrogen burning, where in the faster rotators the mixing can overcome the μ-barrier for a longer time (Sect. 3.1.1) and thus transport more angular momentum out of the central region of the star (Fig. 3.9). Similarly, during core helium burning the mixing inside the helium core increases with increasing rotation (Sect. 3.2.2) such that very similar angular momenta are reached at core helium exhaustion (Fig. 3.10B).

The total angular momentum in the final models is dominated by that of the envelope (Table 3.2). Models `G15B`, `E15B`, and `F15B` show that for an initially faster rotation, a slightly larger helium core results (Table 3.2) and therefore the stars becomes more luminous. This, in turn, causes higher mass loss and by that a higher loss of angular momentum, such that the total angular momentum in the envelope decreases by a larger factor for the faster rotators — or for more massive stars, which also experience larger mass loss (Figs. 3.21B and 3.22B). This has to be distinguished from the transport of angular momentum due to rotationally induced mixing processes, which is responsible for the slow-down of the core rotation.

Table 3.2 gives some key parameters of the final models. Included are the final mass of the star, the masses of the helium, C/O, and iron cores, and the angular momenta contained in theses cores. For the iron core additionally the average specific angular momentum is given. Models `D10`, `D12`, `E08`, `G12B`, `E12B`, and `F12B` develop degenerate neon/magnesium/oxygen cores and central neon burning starts off-center. Due to the computational difficulties (and expense) these models are not followed until core collapse, but stopped during neon/oxygen shell burning or even before neon ignition. In Model `D10` even carbon burning ignites off-center. Models `D10` and `E08` experience a dredge-up of almost the entire helium shell by the convective envelope. Therefore the final helium core is small and has little angular momentum. The remaining helium shell above the C/O core at the point where the calculation is ended is only a few hundreds of a solar mass. The masses of the helium cores before the dredge-up are 2.25 and 2.1 $M_\odot$, respectively. Model `E25` loses its hydrogen-rich envelope during central helium burning and becomes a Wolf-Rayet star. Strong Wolf-Rayet mass loss sets in and further decreases the mass of the star. It ends up with only 5.45 $M_\odot$ at the time of core collapse and very little angular momentum.

Both the total and specific final angular momentum of stars with the same rotational velocity at core hydrogen ignition increases with mass Fig. 2.1. Therefore it might be expected that this is reflected in the angular momentum distribution of the pre-collapse stars. The models with inefficient μ-gradients for the rotationally induced mixing (models `E08`...`E25`) clearly show the opposite trend for their total angular momentum (Table 3.2 and Fig. 3.22A). The small break in this trend between Model `E12` and Model `E15` occurs because the former undergoes a blue loop during central helium burning, during which it loses a large portion of the angular momentum in the envelope, while the later does not (see also Sect. 4.3).

Models `G15B` and `G20B`, `E15B` and `E20B`, `F15B` and `F20B` show the same trend, but here the corresponding 12 $M_\odot$ stars (Models `G12B`, `E12B`, and `F12B`, respectively) have lower final total angular momenta. The decrease of the total angular momentum

Table 3.2: Properties of the final models of various sequences. Listed are the initial mass $M_{\rm initial}$, the final mass $M_{\rm final}$, the mass of the helium core $M_{\rm He}$, the mass of the carbon/oxygen core $M_{\rm C/O}$ and the mass of the iron core $M_{\rm Fe}$ at the onset of core collapse unless stated differently. In the same way the corresponding total angular momenta are given, and in the last column the specific angular momentum of the iron core is shown. Additionally, the rotational velocity at core hydrogen ignition, $v_{\rm ZAMS}$, is given.

model	$M_{\rm initial}$ $M_\odot$	$M_{\rm final}$ $M_\odot$	$M_{\rm He}$ $M_\odot$	$M_{\rm C/O}$ $M_\odot$	$M_{\rm Fe}$ $M_\odot$	$v_{\rm ZAMS}$ km s^{-1}	$J_{\rm initial}$ erg s	$J_{\rm final}$ erg s	$J_{\rm He}$ erg s	$J_{\rm C/O}$ erg s	$J_{\rm Fe}$ erg s	$j_{\rm Fe}$ cm^2 s^{-1}
D10	10	9.61	1.24[a]	1.22	–[b]	0	0	0	0	0	0	0
D12	12	11.42	2.85	1.42	–[b]	0	0	0	0	0	0	0
D15	15	13.55	3.82	1.77	1.33	0	0	0	0	0	0	0
D20	20	16.31	5.68	2.31	1.64	0	0	0	0	0	0	0
D25	25	18.72	7.86	3.11	1.36	0	0	0	0	0	0	0
E08	8	7.65	1.38[a]	1.35	–[b]	205	$5.30{\cdot}10^{51}$	$2.49{\cdot}10^{51}$	$2.40{\cdot}10^{49}$	$2.36{\cdot}10^{49}$	–[b]	–[b]
E10	10	9.23	2.84	1.78	1.36	207	$8.00{\cdot}10^{51}$	$2.09{\cdot}10^{51}$	$8.04{\cdot}10^{49}$	$3.89{\cdot}10^{49}$	$2.13{\cdot}10^{49}$	$7.87{\cdot}10^{15}$
E12	12	10.35	3.63	2.37	1.34	206	$1.10{\cdot}10^{52}$	$1.29{\cdot}10^{51}$	$1.20{\cdot}10^{50}$	$5.32{\cdot}10^{49}$	$1.50{\cdot}10^{49}$	$5.63{\cdot}10^{15}$
E15	15	10.86	5.10	3.40	1.46	206	$1.60{\cdot}10^{52}$	$1.38{\cdot}10^{51}$	$2.30{\cdot}10^{50}$	$1.15{\cdot}10^{50}$	$1.86{\cdot}10^{49}$	$6.40{\cdot}10^{15}$
E20	20	11.00	7.71	5.01	1.73	201	$2.50{\cdot}10^{52}$	$7.15{\cdot}10^{50}$	$3.95{\cdot}10^{50}$	$1.82{\cdot}10^{50}$	$1.92{\cdot}10^{49}$	$5.58{\cdot}10^{15}$
E25[c]	25	5.45	5.45	4.07	1.69	205	$3.50{\cdot}10^{52}$	$1.40{\cdot}10^{50}$	$1.40{\cdot}10^{50}$	$7.52{\cdot}10^{49}$	$1.05{\cdot}10^{49}$	$3.12{\cdot}10^{15}$
G12B	12	11.32	2.68	1.41	–[b]	99	$5.50{\cdot}10^{51}$	$3.07{\cdot}10^{51}$	$1.15{\cdot}10^{50}$	$4.18{\cdot}10^{49}$	–[b]	–[b]
G15B	15	13.46	3.63	1.79	1.34	102	$8.00{\cdot}10^{51}$	$3.99{\cdot}10^{51}$	$2.36{\cdot}10^{50}$	$6.80{\cdot}10^{49}$	$3.28{\cdot}10^{49}$	$1.23{\cdot}10^{16}$
G20B	20	16.03	5.55	2.61	1.38	103	$1.25{\cdot}10^{52}$	$3.49{\cdot}10^{51}$	$5.33{\cdot}10^{50}$	$1.24{\cdot}10^{50}$	$3.13{\cdot}10^{49}$	$1.14{\cdot}10^{16}$
E12B	12	11.25	2.72	1.46	–[b]	206	$1.10{\cdot}10^{52}$	$4.92{\cdot}10^{51}$	$1.29{\cdot}10^{50}$	$4.94{\cdot}10^{49}$	–[b]	–[b]
E15B	15	13.26	3.69	1.89	1.40	206	$1.60{\cdot}10^{52}$	$6.96{\cdot}10^{51}$	$2.73{\cdot}10^{50}$	$8.77{\cdot}10^{49}$	$4.07{\cdot}10^{49}$	$1.46{\cdot}10^{16}$
E20B	20	15.19	5.71	2.69	1.38	201	$2.50{\cdot}10^{52}$	$5.10{\cdot}10^{51}$	$6.36{\cdot}10^{50}$	$1.55{\cdot}10^{50}$	$3.47{\cdot}10^{49}$	$1.26{\cdot}10^{16}$
F12B	12	10.93	3.04	1.61	–[b]	328	$1.65{\cdot}10^{52}$	$3.43{\cdot}10^{51}$	$1.72{\cdot}10^{50}$	$5.98{\cdot}10^{49}$	–[b]	–[b]
F15B	15	12.89	3.88	2.01	1.38	323	$2.40{\cdot}10^{52}$	$7.90{\cdot}10^{51}$	$3.01{\cdot}10^{50}$	$9.69{\cdot}10^{49}$	$3.66{\cdot}10^{49}$	$1.33{\cdot}10^{16}$
F20B	20	14.76	5.99	2.75	1.36	307	$3.75{\cdot}10^{52}$	$5.45{\cdot}10^{51}$	$7.42{\cdot}10^{50}$	$1.71{\cdot}10^{50}$	$3.71{\cdot}10^{49}$	$1.37{\cdot}10^{16}$
H12B	12	9.77	3.81	1.78	–[b]	474	$2.20{\cdot}10^{52}$	$1.41{\cdot}10^{51}$	$2.59{\cdot}10^{50}$	$6.93{\cdot}10^{49}$	–[b]	–[b]

[a] dredge-up of helium core [b] not evolved to pre-collapse stage [c] star becomes a Wolf-Rayet star during central helium burning

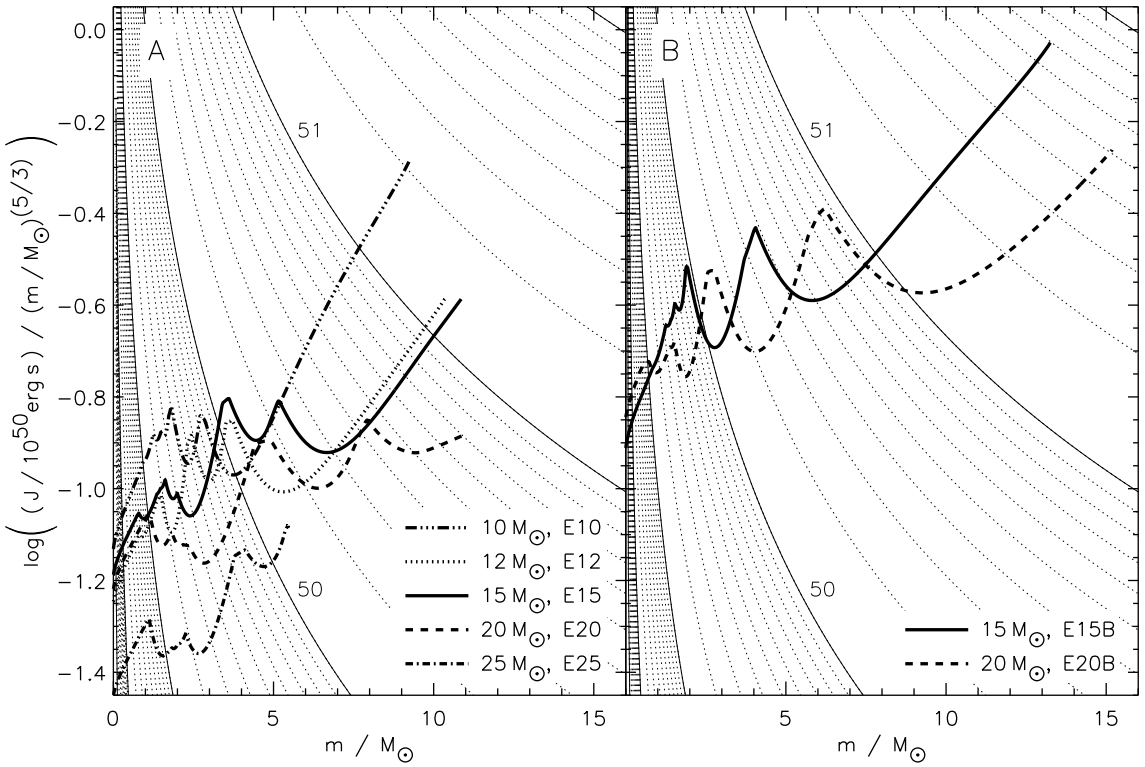

Figure 3.22: Integrated angular momentum $J(m) = \int_0^m j(m')\,\mathrm{d}m'$ divided by $m^{5/3}$ as a function of the mass mass coordinate m for different initial masses (thick lines) at core collapse. The stars have a ZAMS equatorial rotational velocity of $\sim 200\,\mathrm{km\,s^{-1}}$. Panel **A** displays the Models `E10`, `E12`, `E15`, `E20`, and `E25`. Panel **B** gives the Models `E15B` and `E20B`. The thin lines have the same meaning as in Fig. 3.10.

for the more massive stars is the result of higher mass loss. In the limit of low mass loss, as is characteristic of stars with lower mass, the angular momentum loss is also lower. In this case the final angular momentum resembles the initial angular momentum more closely and grows monotonically with mass, while for the more massive stars it does not.

A different trend is found for the angular momentum of the helium and C/O cores. The angular momentum of these cores increases with the mass of the initial model, but most of this increase is due to the larger sizes of these cores in the more massive stars. However, the specific angular momenta of the C/O core increase less than those of the helium cores, and for a given mass coordinate, on average, the specific angular momenta inside the these cores even decreases with increasing initial mass. This illustrates the increased transport of angular momentum out of the larger cores.

Furthermore, an interesting result is noted: The specific angular momentum of the iron core tends to decrease with increasing initial mass! Besides the stronger mixing in more massive stars, the reason for this trend is that the convective helium core and the C/O core masses increase more rapidly with initial mass than that of the iron core. As a result, angular momentum is transported more efficiently out of the center of the star. Therefore the lower-mass stars typically show faster rotation

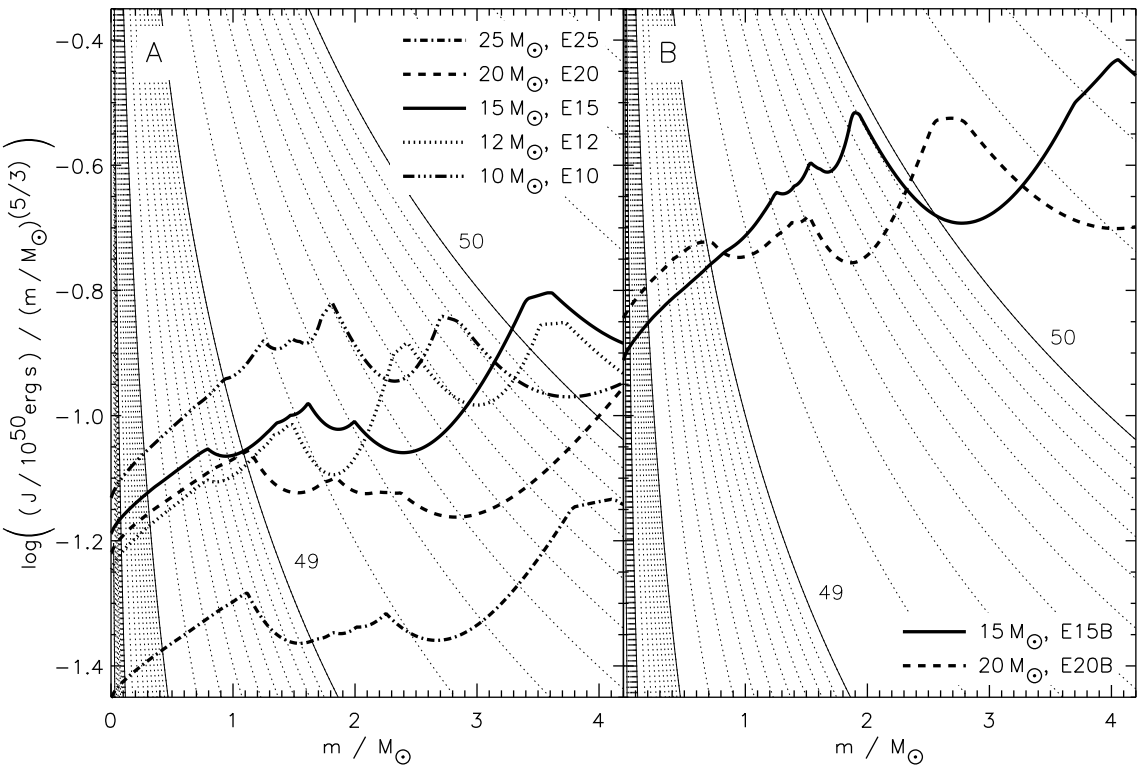

Figure 3.23: Magnification of the innermost 4.2 $M_\odot$ of Fig. 3.22.

in the iron core than the more massive ones (Table 3.2 and Fig. 3.23). This effect is also the reason for the much higher values of specific angular momentum in the iron cores of models where the growth of the convective helium core is inhibited by μ-barriers (e.g., Model `E15B` in comparison to Model `E15`).

Due to the increase in helium and C/O core masses, and the more efficient transport of angular momentum in the initially faster rotating stars, the final angular momentum of the core is not a monotonic function of the initial rotation of the star. Since, for a rigidly rotating core of constant density, $J(m)$ scales as $m^{5/3}$ (Eq. 3.1), both total and (average) specific angular momentum increase with mass. Therefore the size of the iron core has significant influence on these values. However, unless the iron core that forms after central silicon burning is already large enough to collapse, one or more subsequent phases of silicon shell burning occur until the critical iron core mass is exceeded. The sizes of these shells depend on the details of the preceding evolution. As a result, the iron core mass does not necessarily increase monotonically with initial mass or rotation. For example, the iron core of Model `D20` is larger than those of the 20 $M_\odot$ models of the "`B`" series.

Another striking feature in Table 3.2 is the apparently larger mass of some of the helium cores in the non-rotating models compared to the slow rotating models of the "`B`" series. This is due to the criterion used to determine the size of the helium core: it is defined by the mass coordinate at which the hydrogen mass fraction drops below 10^{-3}. In the rotating models of the "`B`" series the hydrogen gradient at the top of the helium core is significantly shallower. If instead a hydrogen mass fraction

evolutionary state	$J(m)/m$ $\mathrm{cm^2\,s^{-1}}$	r cm	ρ_c $\mathrm{g\,cm^{-3}}$	ω $\mathrm{rad\,s^{-1}}$	$\omega/\omega_\mathrm{Kep}$
H ignition	$5.5{\cdot}10^{16}$	$5.8{\cdot}10^{10}$	4.8	$5.0{\cdot}10^{-5}$	$4.6{\cdot}10^{-2}$
H exhaustion	$1.0{\cdot}10^{16}$	$4.3{\cdot}10^{10}$	12.5	$1.6{\cdot}10^{-5}$	$1{\cdot}10^{-2}$
He exhaustion	$6.5{\cdot}10^{15}$	$7.2{\cdot}10^{9}$	$3{\cdot}10^{3}$	$3.8{\cdot}10^{-4}$	$1.5{\cdot}10^{-2}$
pre-collapse	$5.6{\cdot}10^{15}$	$2.2{\cdot}10^{8}$	$3.9{\cdot}10^{9}$	$3.7{\cdot}10^{-1}$	0.08
neutron star	$(5{\cdot}10^{15})$	$(1.2{\cdot}10^{6})$	$\sim 4{\cdot}10^{14}$	$1{\cdot}10^{4}$	0.9

Table 3.3: Evolution of the radius, r, the angular velocity, ω, and its ratio to the Keplerian rotational velocity, $\omega_\mathrm{Kep} = \sqrt{Gm/r^3}$, all at a mass coordinate of $m = 1.7\,\mathrm{M_\odot}$, and the mass of the iron core at core collapse of Model E20. The second column gives the specific angular momentum $J(m)/m$ of the inner $1.7\,\mathrm{M_\odot}$. The central density ρ_c is given for comparison. The initial model has a mass of $20\,\mathrm{M_\odot}$ and a ZAMS rotational velocity of $\sim 200\,\mathrm{km\,s^{-1}}$. Assuming that the neutron star gets a radius of about 12 km and retains about the angular momentum of the iron core at core collapse, it evolves close to critical rotation. It is assumed that the moment of inertia of the rigidly rotating neutron star of radius R and mass M is given by $0.8\frac{2}{5}MR^2$. The geometrical factor $\frac{2}{5}$ corresponds to a solid sphere of constant density, and the numerical factor 0.8 is found from a neutron star model provided by Eberl (1997).

of 10^{-2} is chosen, the helium core masses are similar or even larger for the rotating models (e.g., Figs. F.2 and F.12). Note that the size of the C/O core is defined in a similar way: by the mass coordinate at which the helium mass fraction drops below 10^{-3}.

3.5 Implications for young pulsars and supernovae

In Table 3.3 the evolution of the specific angular momentum contained in the innermost $1.7\,\mathrm{M_\odot}$ (mass of the iron core at core collapse) is given for Model E20. Since the evolution of the star and its contraction proceeds faster than the transport of angular momentum, the core spins up and gets closer to critical rotation (Eq. 3.3). If this is extrapolated, without further transport, to a neutron star within an assumed radius of 12 km, the neutron star will rotate with 90 % of Keplerian rotation (Table 3.3). However, Model E20 chosen for this example has the largest iron core of all of the models investigated in this work (Table 3.2), as well as an unusually low specific angular momenta in the core. The the other models (except Model E25) have even more specific angular momentum in the collapsing iron core than a neutron star, can possibly carry ($\omega/\omega_\mathrm{Kep} \propto jm^{-1/2}$). This much angular momentum certainly is important in the dynamics of the whole core collapse, and it could be expected that significant deviations from spherical symmetry arise (Imshennik 1995; Aksenov et al. 1997; Zwerger & Müller 1997; Rampp, Müller & Ruffert 1998).

3.5.1 Comparison with observed young pulsars

At 90 % of Keplerian angular velocity the neutron star formed from the iron core of Model E20 would have to a rotational period of 0.6 ms. This is much faster than the periods measured for young neutron stars. In Table 3.4 the periods of

pulsar	period ms	j ($R = 12\,\mathrm{km}$) $\mathrm{cm^2\,s^{-1}}$
PSR B0531+21 (Crab)	33	$8.8{\cdot}10^{13}$
PSR B0540-69 (LMC)	50	$5.8{\cdot}10^{13}$
PSR B1509-58	150	$1.9{\cdot}10^{13}$
PSR J0537-6910 (N157B; LMC)	16	$1.8{\cdot}10^{14}$

Table 3.4: Rotational periods of known young pulsars associated with supernova remnants (Mashall et al. 1998) and their specific angular momentum $j = J/M$ for an assumed radius of $R = 12\,\mathrm{km}$, if rigid rotation and a moment of inertia of $I = 0.32MR^2$ is assumed (see Table 3.3).

the four known young neutron stars associated with supernova remnants (Mashall et al. 1998) are given along with their specific angular momentum (with the same assumption regarding moment of inertia as above). This can be compared to the specific angular momentum in the iron cores found in the pre-collapse models in Table 3.2. The models in this work have roughly ~ 20 to 100 times more specific angular momentum than found in these neutron stars. For most of the models, some angular momentum has to be lost in order to collapse to form a neutron star in any case. Triaxial deformations would result and gravitational radiation be emitted — even during the explosion. Still it might be expected that the resulting neutron stars would spin much faster than observed. However, these observed "young" neutron stars are already several hundreds of years old, and could have spun much faster immediately after their formation. In recent work it has been found that rapidly rotating young neutron stars can be spun down on a time-scale of about a year by oscillations and the emission of gravitational radiation. Periods compatible with those of the observed young neutron stars are possible (Lindblom, Owen & Morsink 1998; Owen et al. 1998).

Another possibility is that the efficiency of some rotationally induced mixing processes has been underestimated or that some important transport mechanism is missing in the models of the present work (see also Sect. 2.2.3). Spruit & Phinney (1998), for example, assumed that winding up of a weak magnetic field by differential rotation could cause enough Maxwell stress to keep the *whole* star in uniform rotation until termination of central carbon burning. This would imply neutron star periods of $\sim 100\,\mathrm{s}$, much larger than the observed ones, and now a different mechanism has to be employed in order to spin them up again (e.g., off-center "kicks" during the explosion). However, it is not clear whether magnetic fields actually operate as efficiently as suggested in their work, because the interaction of the magnetic fields with the other processes inside the stars are known. In general, the evolution of magnetic instabilities in the stellar interior have, so far, been inadequately investigated.

3.5.2 Formation of Kerr black holes?

If the large angular momentum calculated in this work is an embarrassment for pulsars, it is very favorable for the collapsar model for γ-ray bursts (Woosley 1993). If

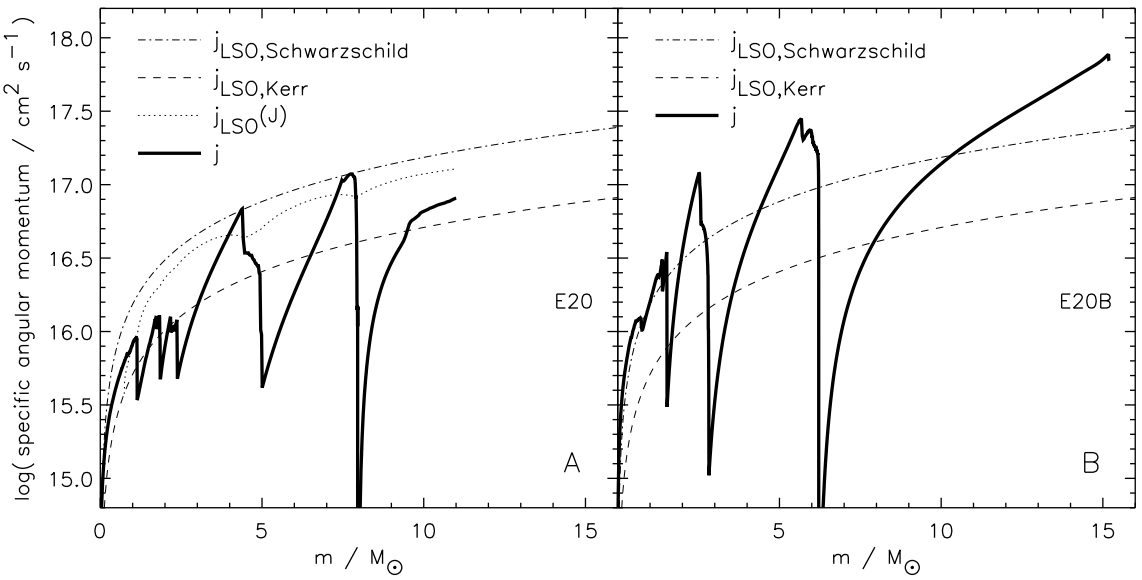

Figure 3.24: Specific angular momentum j in the star (thick line) as a function of the mass mass coordinate m at the onset of core collapse of a $20\,M_\odot$ star with a ZAMS equatorial rotational velocity of $\sim 200\,km\,s^{-1}$. Panel **A** and **B** show Models `E15` and `E15B`, respectively and compare the the resulting profiles of stars with different assumptions about the parameters of rotationally induced mixing. The dashed line gives the specific angular momentum needed to get into the last stable orbit around a non-rotating Schwarzschild black hole (dashed line) of (rest-)mass equal to the mass coordinate. The dash-dotted line give the same but for a maximum-rotating Kerr black hole (spin-parameter $a := Jc/(Gm) = m$). If assumed that all (rest-)mass below has fallen into a black hole and added its angular momentum to it, the dotted line results for the j needed to get into the last stable orbit; where this approximation would lead to values of $a > m$ the curve is truncated to the Kerr-limit. For the Model `E15B` shown in Panel **B** this is the case everywhere. A derivation of these limits can be found in Shapiro & Teukolski (1983) or Novikov (1997). It has to be noted, however, that this plot is for giving a measure of the amount of angular momentum in the pre-collapse model only. This shall not imply that these stars actually will form black holes.

the cores of the stars would collapse to a black hole, the angular momentum calculated here would be enough to support matter in a stable disk outside (Shapiro & Teukolski 1983; Novikov 1997). This is roughly sketched in Fig. 3.24, where the distribution of specific angular momentum at the pre-collapse stage of the two $20\,M_\odot$ Models `E20` and `E20B` is shown. Thin dashes and dash-dotted lines indicate the specific angular momenta of the last stable orbit around a non-rotating and a maximum rotating black hole of mass equal to the mass coordinate. If the matter in the star has more angular momentum than necessary to get into the last stable orbit, an accretion disc might form, and efficiently transform gravitational binding energy into heat, up to 42.3 % of the rest mass for a maximum rotating black hole (Shapiro & Teukolski 1983; Novikov 1997). Note that the specific angular momentum displayed in Fig. 3.24 is the average over a shell. The actual value of specific angular momentum at the equator is higher than that by 50 %, while it is zero at the pole. Therefore matter might fall in almost freely at the pole, while it hits the centrifugal barrier at the equator. In case a supernova explosion fails and a black hole results instead of a neutron star, this might be a mechanism for an efficient

energy source or even a γ-ray burst (Woosley 1993; Popham, Woosley & Fryer 1998; MacFadyen & Woosely 1998).

3.6 Comparison with other work

Kippenhahn et al. (1970) previously investigated rapidly rotating $9\,M_\odot$ stars ($v \gtrsim 400\,km\,s^{-1}$) and followed their evolution until central helium exhaustion. They did not consider mass loss or any mixing of composition due to rotation, but included the centrifugal force according to Kippenhahn & Thomas (1970). They compared two different assumption for the transport of angular momentum inside the star. In the first, angular momentum is locally conserved in all radiative regions and uniform rotation is enforced in convective regions. In the second, rigid rotation is enforced also in all radiative region which are chemically homogeneous.

Their second model has some similarities with present models of the "B" series, in the sense that a faster spinning core evolves inside a (close-to) uniformly rotating envelope at the end of central hydrogen burning. Compositional mixing from the core into the envelope is also inhibited in their work by a μ-barrier. In comparison, in the present work, some mixing still occurs across the μ-barrier. Therefore, in contrast to Kippenhahn & Thomas (1970), in the present work also angular momentum is transported out of the core during central hydrogen burning. Like in core hydrogen burning, the μ-barriers do not allow any mixing between the core and the envelope during central helium burning in the models of Kippenhahn & Thomas (1970). Therefore no angular momentum is lost from the core, and, in contrast to the present work, the models of Kippenhahn et al. (1970) end up with rapidly spinning cores which already become secularly unstable to triaxial deformations (Ostriker & Bodenheimer 1973) at the end of central helium burning.

Kippenhahn et al. (1970) found that the lifetime of the stars during core hydrogen burning increases due to the "hydrostatic" effect of centrifugal forces by only 4 % (Fig. 2.3D), and during central helium burning by 11 %. This "hydrostatic" effect by itself is already sufficient to significantly change the evolution of their models in the HR diagram during central helium burning and causes bigger loops (see also Endal & Sofia 1976). But due to the smaller transport of angular momentum out of the core, their core rotation is much faster than that found in the present work. Here, mixing inside the core is the dominant effect on the evolution.

Endal & Sofia (1978) followed the evolution of $7\,M_\odot$ and $10\,M_\odot$ stars with a ZAMS rotational velocity of $\sim 200\,km\,s^{-1}$ using essentially the same method as in the present work, except for some improvements in the input physics of the individual processes applied here (Sect. 2.2 and Endal & Sofia 1978). They used the Schwarzschild criterion for convection, however, and did not include mass loss. In their work, the μ-barrier above the convective hydrogen-burning core suppresses mixing and transport of angular momentum almost completely. Their stellar cores thus lose very little angular momentum during central hydrogen burning. Because $f_\mu < 1$ is used in the present work, the inhibiting effect of the μ-gradients is smaller here, but even so a similar μ-barrier forms during central hydrogen burning. How-

ever, in the present work, mixing between the core and the envelope occurs during the early part of central hydrogen burning. Angular momentum is lost from the convective core and helium enrichment at the surface can also result, in agreement with observation. This is not reproduced by Endal & Sofia (1978).

During central helium burning the angular momentum loss from the core is greater in Endal & Sofia (1978) than in Kippenhahn & Thomas (1970), but a great deal of angular momentum is still retained in the core at core helium exhaustion. From core helium depletion until where their model calculations end, i.e., before carbon ignition, they find a reduction of specific angular momentum by only $\sim 0.2\,\mathrm{dex}$ in the helium and C/O core relative to the specific angular momentum on the ZAMS. This is much higher specific angular momentum than found at carbon ignition in the cores of even the fastest rotating models of the present work. In models with comparable initial angular momentum to those of Endal & Sofia (1978), in the present work a reduction of $\sim 0.5\,\mathrm{dex}$ in the models of the "B" series and $\sim 1\,\mathrm{dex}$ in the models with inefficient μ-barriers are found (e.g., Fig. 3.7).

In earlier work by Endal & Sofia (1976), where no time-dependent rotationally induced angular momentum transport was taken into account, but only different rotation laws were imposed, an even more extreme result was obtained. All models reached critical rotation before carbon ignition.

Eryurt et al. (1994) considered turbulent diffusion according to Zahn (1983) in their computation of a $20\,\mathrm{M}_\odot$ stars with a metallicity of $Z = 0.008$. They found a surprisingly large enrichment of $^{14}\mathrm{N}$ — a mass fraction of more than 0.02 — at the surface of their model at the end of central hydrogen burning. Since the CNO cycle conserves the total mass of CNO isotopes, this result seems rather implausible and cannot be reproduced in the present work.

Meynet & Maeder (1997) used a prescription for the Eddington-Sweet circulation in the "asymptotic regime" according to Zahn (1992), and a Richardson criterion modified for thermal effects (Maeder 1995; Maeder & Meynet 1996). They computed the hydrogen-burning evolution of stars from $9\,\mathrm{M}_\odot$ to $60\,\mathrm{M}_\odot$. They also find a strong inhibiting effect of the μ-gradients on the rotationally induced mixing and angular momentum transport processes, and only modest effects due to the centrifugal forces. In contrast to models of the present work, their models do not reproduce the surface enrichment of helium in massive stars found by, e.g., Herrero et al. (1992). Also, they get strong differential rotation at central hydrogen exhaustion, much stronger than found in the models of the "B" series in the present work.

Talon et al. (1997) followed the main sequence evolution of $9\,\mathrm{M}_\odot$ stars with ZAMS rotation rates of $100\,\mathrm{km\,s^{-1}}$ and $300\,\mathrm{km\,s^{-1}}$ until end of central hydrogen burning, using the prescription for the Eddington-Sweet circulation by Zahn (1992). The helium enrichment in the envelope shows a smooth profile consistent with that for models E08 or E10 (which, however, have a ZAMS rotational velocity of $\sim 200\,\mathrm{km\,s^{-1}}$). Their model with low ZAMS rotational velocity shows less mixing than the Models E08 and E10, and their fast rotating model shows more mixing. Their models show steep composition gradients close to the surface of the star at central hydrogen exhaustion. This may result from the low mass loss in their calculation in combination with inefficient mixing close to the surface. At a higher mass loss rate,

their fast rotating model would have shown considerably stronger CNO processing at the surface The mixing decreases close to the surface also in the models of the present work, but mass loss and mixing are sufficiently strong to disallow the formation of significant abundance gradients at the surface. Talon et al. (1997) find a stronger differential rotation between core and surface compared to Models `E08` and `E10`, due to the downward advection of angular momentum by meridional circulation in the theory of Zahn (1992), but comparable to what is found, e.g., for Model `E12B`. That is, this downward advection is not too strong an effect, which may justify its neglect in the present work.

Meynet (1997) has computed the main sequence evolution of $20\,M_\odot$ and $40\,M_\odot$ stars, applying a further change to the physics of rotationally induced mixing discussed by Meynet & Maeder (1997), according to Maeder (1997b). The inhibiting effect of μ-gradients on shear mixing and Eddington-Sweet circulation is strongly reduced in the new formulation. His $20\,M_\odot$ star of comparable initial rotation shows a larger enrichment of helium in the envelope and the surface layers at the end of central hydrogen burning than Model `E20`, and a similar mass of the hydrogen-depleted core. However, this model still maintains significantly stronger differential rotation, again due to the downward advection of angular momentum by the Eddington-Sweet circulation. Note that the physics used in Meynet (1997) has been revised again by Maeder & Zahn (1998) for a more consistent treatment of μ-gradients. Models with this prescription are not yet available.

Summarizing, the prescription for rotationally induced mixing used in the model of Kippenhahn et al. (1970) corresponds roughly to $f_\mu = f_c = \infty$ in terms of the present formulation. Endal & Sofia (1978) used about $f_\mu = f_c = 1$. Both works failed to reproduce important aspects of the surface abundances observed in massive stars, for example the helium enrichment. This is prevented by the strong inhibiting effect of the μ-gradients (Meynet & Maeder 1997). The recent picture of interacting Eddington-Sweet circulation, anisotropic turbulence and shear instabilities (Chaboyer & Zahn 1992; Maeder & Zahn 1998) has been continuously improved in the last years (e.g., Urpin et al. 1996; Maeder 1997b; Talon & Zahn 1997; Talon et al. 1997). Unfortunately, the most recent work in this series, Maeder & Zahn (1998), which includes a more consistent treatment of compositional gradients, came to late to be considered here. But this type of description for rotationally induced mixing is numerically involved, computationally expensive, and has not been successfully tested for post-hydrogen burning stars to date. However, the results obtained in earlier work (Talon et al. 1997; Meynet 1997) for massive main sequence stars are not significantly different from the results of the present work. Here, empirical values of $f_c = 1/30$ and $f_\mu = 0.05$ have been adopted.

Chapter 4

Evolution of the surface properties

The predicted temporal evolution of the surfaces of rotating massive stars is of particular importance since it allows a direct comparison of these models with observations.

4.1 Central hydrogen burning

Core hydrogen burning takes about 90 % of the whole stellar lifetime and is therefore the evolutionary phase which can be most easily compared with observations.

At core hydrogen ignition, faster rotating stars behave in some respect like stars of lower mass. They are less luminous (Sect. 2.1.4), i.e., burn hydrogen at a lower rate, and age slower. This is due to the reduction of the effective gravity by of centrifugal forces (Kippenhahn et al. 1970). But at the same time, the radius (r_ψ) of a rotating star is larger than that of a non-rotating star of same mass. Therefore it appears in the HR diagram at a lower effective temperature. This can be seen in Figs. 4.1, 4.2, and 4.3 by comparing the starting points of the evolutionary track of stars with different initial rotation rates in the HR diagram (see also Fig. 2.3 and Bodenheimer 1971; Endal & Sofia 1976).

4.1.1 Evolution in the HR diagram

Without any rotationally induced mixing, rotating stars evolve essentially parallel to non-rotating stars in the HR diagram during core hydrogen burning, but at lower luminosity and surface temperature (Kippenhahn et al. 1970; Endal & Sofia 1976). However, rotationally induced mixing can increase the average mean molecular weight in the star by enriching the envelope in helium (Sect. 3.1.1). The temporal evolution of the internal helium profile then depends on the strength of the inhibiting effect of μ-gradients on the mixing and on the initial angular momentum of the star (Fig. 3.1). The increasing helium enrichment makes the star evolving more luminous (Sect. 3.1.1). Due to the helium enrichment in the envelope, a rotating star can exceed the luminosity of a non-rotating star of same initial mass (Fig. 4.1). The higher luminosity causes the convective core to stay larger or even grow (Fig. E.22). Due the centrifugal force, the faster rotating stars remain at lower luminosity than a

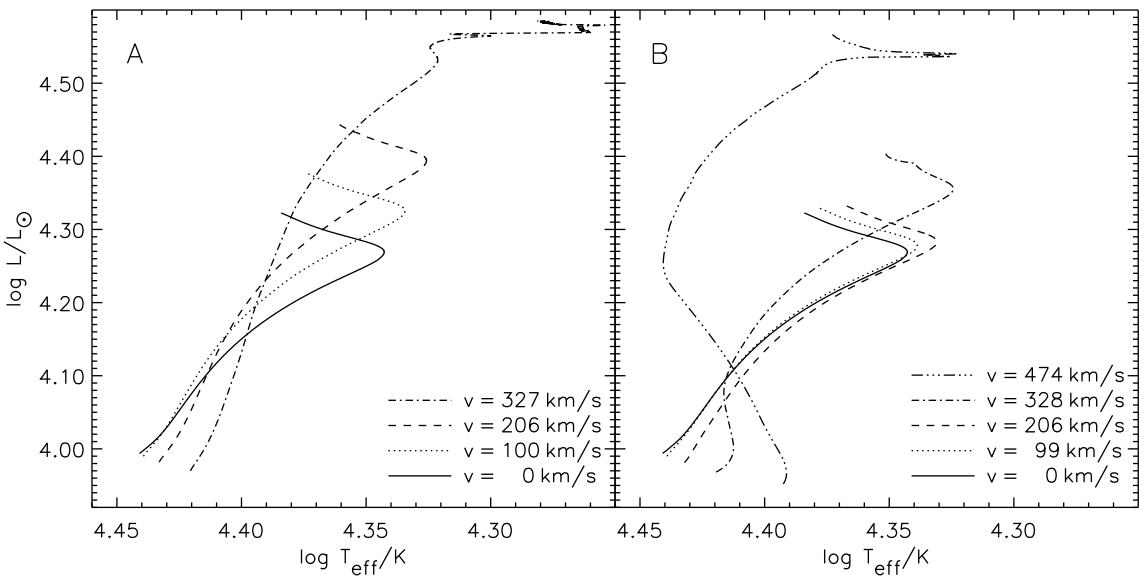

Figure 4.1: Main sequence evolution of $12\,M_\odot$ stars with different ZAMS rotational velocities in the HR diagram. Panel **A**: Models `D12`, `G12`, `E12`, and `F12`, where rotationally induced mixing is assumed insensitive to μ-gradients. Panel **B**: Models `D12`, `G12B`, `E12B`, `F12B`, and `H12B`, where rotationally induced mixing is assumed to be sensitive to μ-gradients.

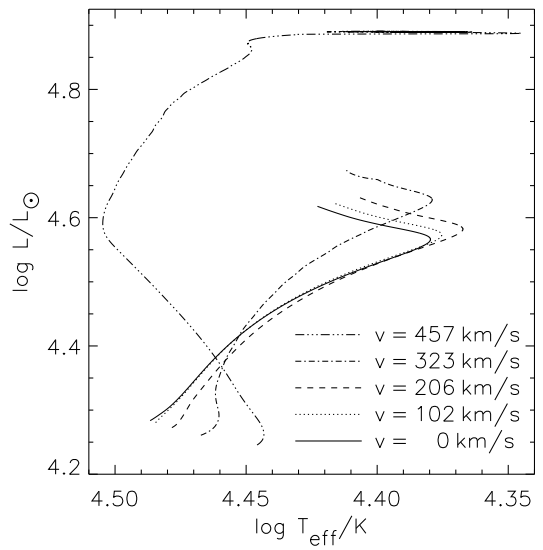

Figure 4.2: Core hydrogen burning evolution in the HR diagram of $15\,M_\odot$ models with ZAMS rotational velocities of $0\,km\,s^{-1}$ (Model `D15`; solid line), $102\,km\,s^{-1}$ (Model `G15B`; dotted line), $206\,km\,s^{-1}$ (Model `E15B`; dashed line), $323\,km\,s^{-1}$ (Model `F15B`; dash-dotted line), and $457\,km\,s^{-1}$ (Model `H15B`; dash-triple-dotted line).

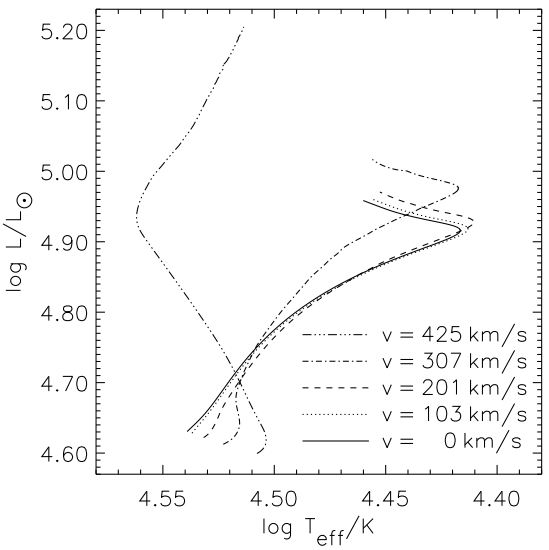

Figure 4.3: Core hydrogen burning evolution in the HR diagram of $20\,M_\odot$ models with ZAMS rotational velocities of $0\,km\,s^{-1}$ (Model `D20`; solid line), $103\,km\,s^{-1}$ (Model `G20B`; dotted line), $201\,km\,s^{-1}$ (Model `E20B`; dashed line), $307\,km\,s^{-1}$ (Model `F20B`; dash-dotted line), and $425\,km\,s^{-1}$ (Model `H20B`; dash-triple-dotted line). The fastest rotating star becomes a Wolf-Rayet star at a central hydrogen abundance of 4 %; the track of this star is discontinued at that point of evolution.

slower-rotating star of same mass and age (Fig. 4.5E1-E3), but they live longer. This is because they initially need less fuel due to their lower luminosity and because they can access a larger supply of fuel by rotationally induced mixing. At later times they evolve to higher luminosities because of the higher average mean molecular weight (Sect. 3.1.1). The helium enrichment in the envelope can also cause the star to evolve to higher surface temperatures at same luminosity, and therefore to a position in the HR diagram where less evolved non-rotating stars of higher initial mass would be located.

These trends are compared in Fig. 4.1 using the example of $12\,M_\odot$ stars with different ZAMS rotational velocities and for the two cases of rotationally induced mixing being insensitive (Fig. 4.1A: Models `D12`, `G12`, `E12`, and `F12`) or sensitive (Fig. 4.1B: Models `D12`, `G12B`, `E12B`, `F12B`, and `H12B`) to μ-gradients. In order to meet the observational constraint on the surface enrichment, the mixing efficiency must be taken lower in the former models (Table 2.3). In these models the mixing occurs continuously without any hindrance by a μ-barrier and the stars gradually evolve towards higher luminosities compared to non-rotating stars. Eventually they reach the end of central hydrogen burning at higher luminosities for higher ZAMS rotational velocity. Since it stays close to uniform rotation, Model `F12` hits the Ω-limit (Sect. 2.4.2) at the end of central hydrogen burning, and therefore cannot contract and move back to higher temperature before the "turn-off" like the other models shown in Fig. 4.1A. The same thing happens to Model `H15B`.

In the case where rotationally induced mixing is sensitive to μ-gradients, it is only weak for the slowly rotating models ($v \lesssim 200\,\mathrm{km\,s^{-1}}$), since the μ-barrier becomes effective early on. These stars evolve very similar to the non-rotating model. The two faster rotating models (`F12B` and `H12B`; see Fig. 4.1B) start their evolution in the HR diagram in a direction parallel to that of the non-rotating models. Since, initially, the rotationally induced mixing operates efficiently enough to penetrate the growing μ-barrier, the stars evolve to higher luminosities and surface temperatures for some time, almost perpendicular to the evolution of the non-rotating Model `D12`. During this time their convective core stays about the same size or even grows (in Model `H12B`). Eventually the μ-barrier becomes strong enough that the stars must continue their evolution in the HR diagram parallel to that of the non-rotating model. The point of this last turn ("μ-turn") occurs later for higher ZAMS rotational velocity (for a given initial mass). It also affects the in the evolution of the surface abundances (Sect. 4.1.3), because it marks the point where the chemical evolution of the envelope becomes disconnected from that of the core. A very similar behavior is also found for the $15\,M_\odot$ (Fig. 4.2) and $20\,M_\odot$ (Fig. 4.3) stars. The effects described above are stronger for the fast-rotating stars of lower mass because those are closer to their critical rotation rate. Additionally, the more massive stars are more dominated by radiation pressure in their interiors, and so helium enrichment affects them less.

Due to the dependence of the stellar evolution on the initial angular momentum, a given point in the HR diagram is not uniquely related to a single initial mass, but stars which differ in initial mass *and* rotation rate can evolve to the same position (Fig. 2 of Fliegner et al. 1996). For example, the fast rotating Models `H12B` and `H15B` share, at the end of their central hydrogen burning, the same position in

the HR diagram as the slowly rotating models of 15 $M_\odot$ and 20 $M_\odot$, respectively (Figs. 4.1B, 4.2, and 4.3). The rotating models can also reach positions in the HR diagram to the right of the main sequence band of non-rotating stars, i.e., the main sequence is broadened by the action of rotation. A distinguishing feature, however, between lower-mass fast rotators and higher-mass slow rotators which share the same position in the HR diagram, is the different evolutionary time they need to get to that position. This can be seen in Fig. 4.5E1-E3: e.g., the fast rotating Model `H12B` reaches the same luminosity and also about the same surface temperature after 25 Myr while the slowly rotating 15 $M_\odot$ stars terminate central hydrogen burning at the same position already after 10 Myr. Another such distinguishing feature is the expected surface abundance pattern, which is discussed in Sect. 4.1.3.

Hot stars may become Wolf-Rayet stars (Langer 1989c) with hydrogen mass fractions at their surface below 40 %. This can be due to mass loss — or due to mixing. As mentioned above, because of their higher luminosity, stars with more internal mixing also have more mass loss. As an example, the extremely rapidly rotating Model `H20B` becomes a Wolf-Rayet star at a central hydrogen abundance of 4 %, i.e., during central hydrogen burning (Fig. 4.3). Thus, rotationally induced mixing can significantly influence the lower limiting initial mass required for Wolf-Rayet star formation during central hydrogen burning in single stars.

4.1.2 Rotational velocities

The evolution of the surface rotational velocity for various models is displayed in Fig. 4.5D1-D3. It is affected by several different contributions: First, the loss of angular momentum due to stellar winds leads to a slow-down of the star. For the models shown in Fig. 4.5D1-D3, this reduces the initial angular momentum of the 20 $M_\odot$ models by $\lesssim$ 40 %, by $\lesssim$ 20 % for the 15 $M_\odot$ models, and $\lesssim$ 10 % for the 12 $M_\odot$ models. The second effect is to change the total moment of inertia of the star. This increases by about a factor of two from core hydrogen ignition until shortly before core hydrogen exhaustion in the stars considered here. Both moment of inertia and angular momentum of the models are dominated by the envelope, which stays close to uniform rotation. Third, the increase of the stellar radius by about a factor two to three during core hydrogen burning leads to a spin-up of the stars by the same factor for a given angular velocity, i.e., the ratio of the moment of inertia to the angular momentum. This effect almost completely cancels out the slowing down due to the two preceding effects, as can be seen from the small change in the surface rotational velocity in Fig. 4.5D1-D3.

The rise in rotational velocity at the end of core hydrogen burning is due to the overall contraction of the star, i.e., the decrease of the moment of inertia before the ignition of hydrogen shell burning. The deep drop of the rotational velocity of Model `H20B` in Fig. 4.5D3 is caused by the angular momentum loss occurring as a consequence of the strong mass loss as it becomes a Wolf-Rayet star. Model `H12B` (Fig. 4.5D3) reaches the Ω-limit (Sect. 2.4.2) at the end of core hydrogen burning, and therefore strongly anisotropic mass loss is expected in this case.

4.1.3 Surface abundances

For different thermonuclear reactions different threshold temperatures exist below which no significant processing occurs during the lifetime of a star. Since the reaction rates scale with high powers of the temperature, the transition between layers in which noticeable processing by a certain reaction occurs and those where none occurs is quite sharp. Main sequence stars in the mass range discussed here have radiative envelopes, and models of non-rotating stars predict no mixing in these layers. The only way for the products of thermonuclear burning to appear at the surface is by removal of the outer, unburned layers either due to stellar winds or binary interaction. For the non-rotating stars discussed in the present work, wind mass loss is by far to small to show any significant abundance changes at the surface during central hydrogen burning. (An exception to this is the depletion of lithium found in Model D20; see Fig. D.1B3 in Appendix D). However, because of rotationally induced mixing, here even nuclei like ^{14}N, which is produced about half way down, in mass, towards the center, appear at the stellar surface.

In Fig. 4.4 the evolution of the surface abundances of ^{12}C, ^{14}N, and ^{16}O relative to their initial values, and that of the ^{4}He mass fraction during central hydrogen burning are shown for 12 $M_\odot$, 15 $M_\odot$ and 20 $M_\odot$ stars with different initial angular momenta. In Fig. 4.5 the corresponding ratios of elemental carbon, nitrogen and oxygen relative to their initial values are displayed. The surface abundances at core hydrogen exhaustion are shown in Table 4.1 for elements up to sodium. Note that the efficiencies of the rotationally induced mixing have been adjusted in Sect. 2.2.5 so that the mean surface abundance trends on the main sequence are consistent with the observations. However, the dependencies of the enrichment or depletion of the various isotopes as a function of rotation rate, time, or initial mass are not adjusted but are new results.

The dominant isotope in the CNO cycle, ^{14}N, is enriched at the surface at the expense of ^{12}C and ^{16}O. This enrichment is very small for the models with a ZAMS equatorial rotational velocity of $\sim 100\,\mathrm{km\,s^{-1}}$ ($\lesssim 0.1$ dex), but for models with typical rotational velocity ($\sim 200\,\mathrm{km\,s^{-1}}$) the nitrogen enrichment at the end of central hydrogen burning is a factor of two to three, and it is increasing with initial mass. At higher initial rotation rates the final enrichment factor is about 6 and 10 for the models with $\sim 300\,\mathrm{km\,s^{-1}}$ and $\sim 400\,\mathrm{km\,s^{-1}}$ ZAMS rotational velocity, respectively. The latter value is already close the CNO equilibrium, i.e., most of the initial ^{12}C and ^{16}O are converted to ^{14}N. A notable depletion of ^{12}C occurs only for ZAMS rotational velocities of $\gtrsim 200\,\mathrm{km\,s^{-1}}$, but becomes as high as a factor of ~ 30 for the fastest rotating models — which is even higher than the depletion factor of ^{12}C in the stellar center, since the ^{12}C CNO equilibrium abundance is lower for lower temperatures (Arnould & Mowlavi 1993). The depletion of ^{16}O and the enrichment of ^{4}He are correlated and become significant only for the stars with ZAMS rotational velocities of $\gtrsim 300\,\mathrm{km\,s^{-1}}$, the stronger the higher the initial mass of the stars. The coupling of these two isotopes is due to the μ-barrier: both, the destruction of ^{16}O and the production of ^{4}He occur within or below the μ-barrier (Sect. 3.1.1).

In the extremely rapidly spinning 20 $M_\odot$ Model H20B at a central hydrogen mass

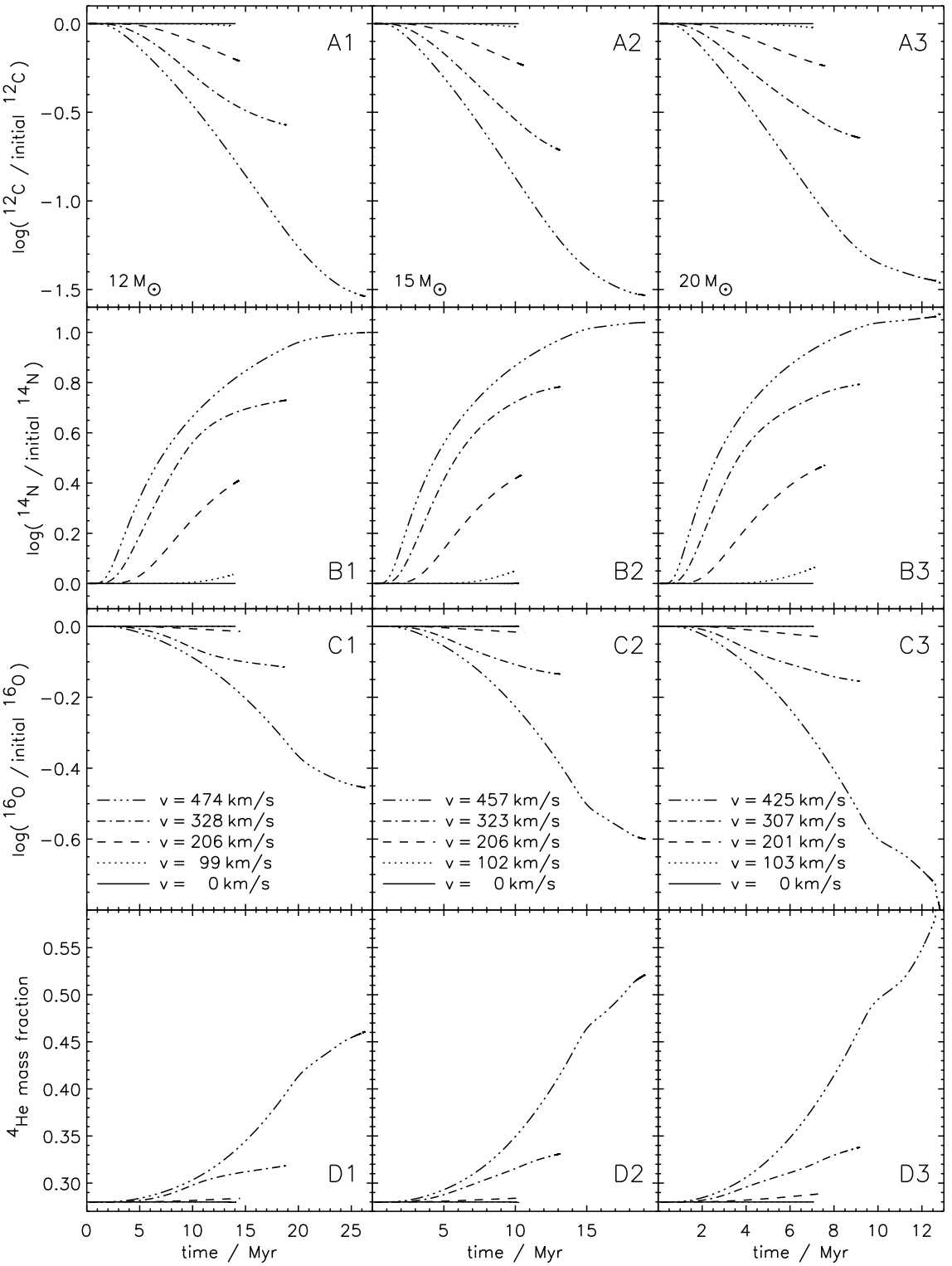

Figure 4.4: Evolution of the surface abundances during central hydrogen burning of $12\,M_\odot$ (left column; models `D12`, `G12B`, `E12B`, `F12B`, and `H12B`), $15\,M_\odot$ (middle column; models `D15`, `G15B`, `E15B`, `F15B`, and `H15B`), and $20\,M_\odot$ (right column; models `D20`, `G20B`, `E20B`, `F20B`, and `H20B`) stars for different ZAMS equatorial rotational velocities (see legend) as a function of time. Displayed are ^{12}C (Panels **A1**–**A3**), ^{14}N (Panels **B1**–**B3**), and ^{16}O (Panels **C1**–**C3**) relative to their initial abundance, and the ^{4}He mass fraction (Panels **D1**–**D3**).

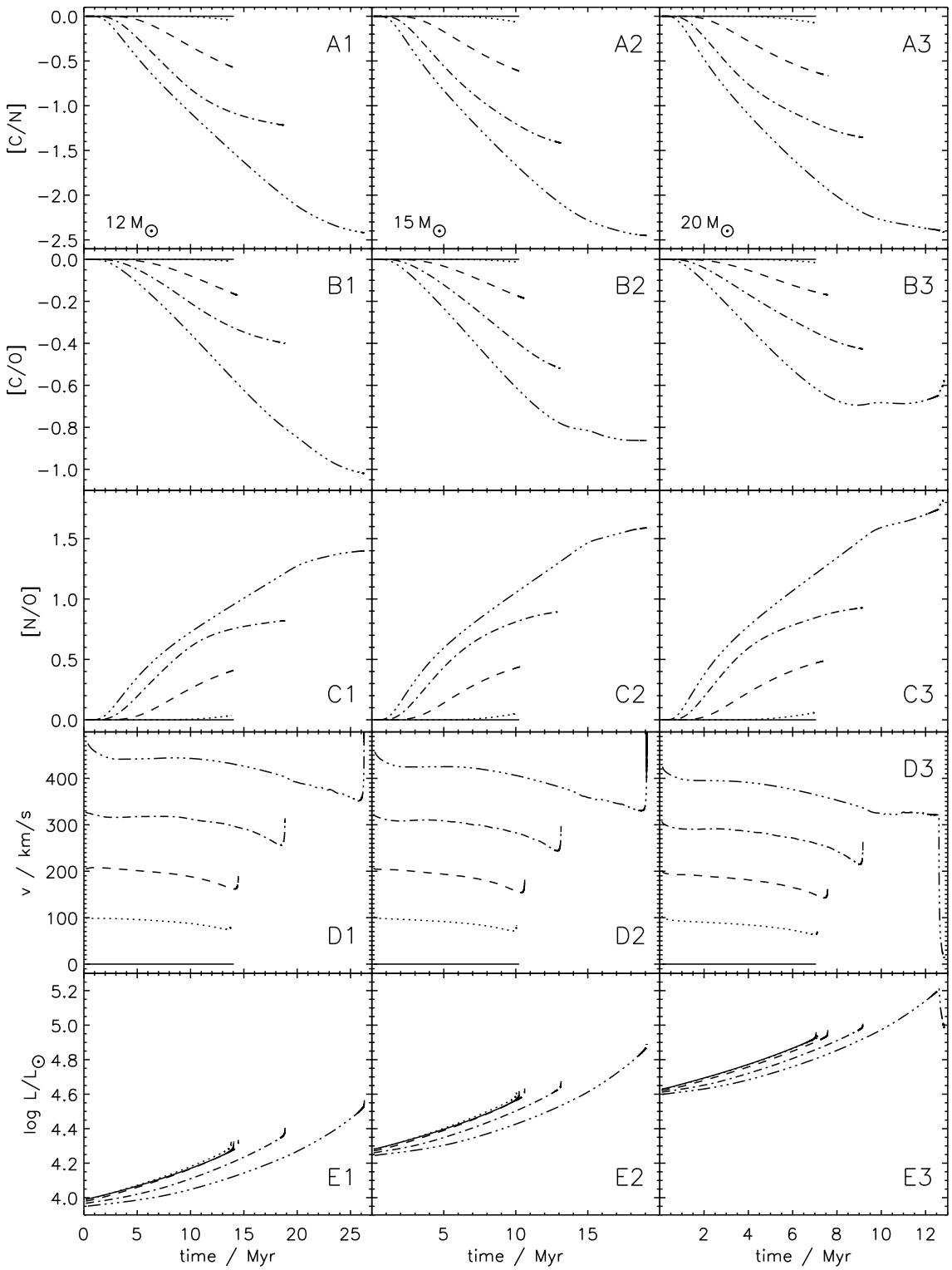

Figure 4.5: Same models and abscissa as in Fig. 4.4, but the ratio of carbon to nitrogen (Panels **A1**–**A3**), the ratio of carbon to oxygen (Panels **B1**–**B3**), and the ratio of nitrogen to oxygen (Panels **C1**–**C3**) are displayed, all relative to the abundance ratios in the initial models. In Panels **D1**–**D3** the evolution of the equatorial rotational velocity is displayed and in Panels **E1**–**E3** that of the luminosity.

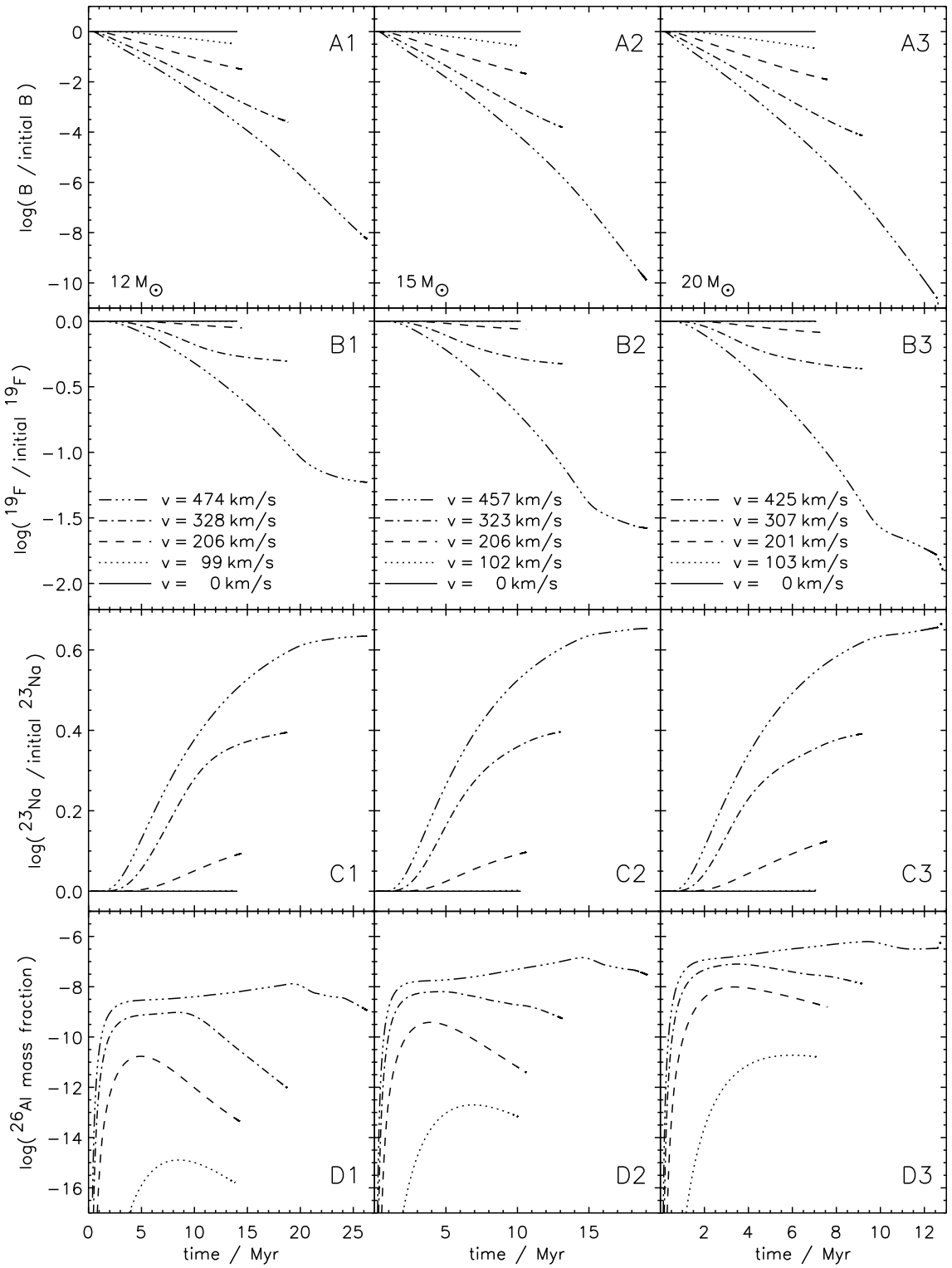

Figure 4.6: Same models and abscissa as in Fig. 4.4, but the evolution of the surface abundances of boron (Panels **A1**–**A3**), ^{19}F (Panels **B1**–**B3**), and ^{23}Na (Panels **C1**–**C3**) are given relative to their initial values; for the radioactive isotope ^{26}Al (Panels **D1**–**D3**) the absolute mass fraction is displayed.

Table 4.1: Surface abundances at core hydrogen exhaustion for the indicated model sequences. Given are the ^{4}He mass fraction, and the logarithm of the ratios of the ^{3}He, lithium, boron, beryllium, ^{12}C, ^{13}C, ^{14}N, ^{15}N, ^{16}O, ^{17}O, ^{18}O, ^{19}F, and ^{23}Na mass fractions relative to their initial values.

model	X(^{4}He)	[^{3}He]	[Li]	[Be]	[B]	[^{12}C]	[^{13}C]	[^{14}N]	[^{15}N]	[^{16}O]	[^{17}O]	[^{18}O]	[^{19}F]	[^{23}Na]
D10	0.280	0.000	0.000	0.000	0.000	0.000	0.000	0.000	0.000	0.000	0.000	0.000	0.000	0.000
D12	0.280	0.000	0.000	0.000	0.000	0.000	0.000	0.000	0.000	0.000	0.000	0.000	0.000	0.000
D15	0.280	0.000	0.000	0.000	0.000	0.000	0.000	0.000	0.000	0.000	0.000	0.000	0.000	0.000
D20	0.280	0.000	−6.006	−0.916	−0.001	0.000	0.000	0.000	0.000	0.000	0.000	0.000	0.000	0.000
D25	0.280	0.000	−0.006	−0.006	−0.001	0.000	0.000	0.000	0.000	0.000	0.000	0.000	0.000	0.000
E08	0.280	0.010	−0.456	−0.456	−0.418	−0.016	0.252	0.053	−0.049	−0.001	0.377	−0.038	−0.002	0.007
E10	0.281	−0.018	−0.633	−0.633	−0.558	−0.033	0.358	0.110	−0.085	−0.003	0.634	−0.071	−0.006	0.020
E12	0.282	−0.042	−0.755	−0.754	−0.637	−0.044	0.413	0.149	−0.108	−0.006	0.735	−0.095	−0.011	0.031
E15	0.286	−0.084	−1.053	−1.052	−0.833	−0.069	0.510	0.238	−0.164	−0.013	0.941	−0.150	−0.023	0.064
E20	0.293	−0.125	−1.457	−1.451	−1.049	−0.090	0.577	0.323	−0.220	−0.027	1.069	−0.207	−0.043	0.102
E25	0.303	−0.149	−5.555	−3.180	−1.237	−0.105	0.566	0.408	−0.246	−0.047	1.196	−0.236	−0.073	0.151
G12	0.280	0.001	−1.569	−0.779	−0.184	0.000	0.005	0.000	−0.001	0.000	0.000	−0.001	0.000	0.000
F12	0.323	−0.232	−8.662	−4.719	−1.600	−0.251	0.612	0.587	−0.409	−0.076	1.571	−0.423	−0.125	0.265
G12B	0.280	−0.013	−3.002	−1.532	−0.491	−0.012	0.231	0.036	−0.043	0.000	0.147	−0.035	−0.001	0.001
G15B	0.280	−0.027	−3.177	−1.685	−0.562	−0.018	0.307	0.052	−0.063	0.000	0.239	−0.053	−0.002	0.002
G20B	0.280	−0.044	−3.496	−1.910	−0.671	−0.024	0.393	0.064	−0.090	0.000	0.307	−0.077	−0.003	0.002
E12B	0.284	−0.201	−8.017	−4.271	−1.503	−0.212	0.651	0.413	−0.404	−0.014	1.426	−0.394	−0.051	0.094
E15B	0.284	−0.264	−8.423	−4.657	−1.680	−0.237	0.722	0.438	−0.486	−0.017	1.464	−0.482	−0.062	0.097
E20B	0.289	−0.311	−8.734	−5.090	−1.908	−0.239	0.785	0.470	−0.558	−0.031	1.519	−0.563	−0.089	0.124
F12B	0.318	−0.466	−9.983	−10.16	−3.596	−0.572	0.714	0.730	−0.970	−0.115	2.048	−1.253	−0.305	0.396
F15B	0.331	−0.624	−9.992	−10.45	−3.810	−0.714	0.562	0.783	−0.986	−0.135	1.971	−1.383	−0.324	0.397
F20B	0.338	−0.671	−9.890	−10.92	−4.140	−0.645	0.651	0.793	−1.002	−0.155	1.926	−1.448	−0.361	0.392
H12B	0.461	−0.984	−9.743	−15.64	−8.257	−1.539	−0.075	1.000	−0.946	−0.455	2.088	−3.397	−1.229	0.635
H15B	0.521	−1.259	−9.778	−14.41	−9.931	−1.532	−0.062	1.040	−0.910	−0.600	1.906	−3.933	−1.579	0.654
H20B	0.654	−1.876	−9.915	−13.02	−16.05	−1.460	0.010	1.074	−0.887	−0.808	1.628	−4.414	−1.904	0.668

fraction of $\sim 4\,\%$ the surface helium enrichment becomes that strong ($\gtrsim 60\,\%$ by mass), that the star can be considered as a Wolf-Rayet star, with correspondingly high mass loss rate. Even though the star experiences high mass loss during that phase, it becomes a red supergiant after core hydrogen exhaustion. The high mass loss rate reduces the rotational velocity and the luminosity of the star, as can be seen in Figs. 4.5D3 and 4.5E3.

The strength of the surface enrichment is correlated with the time when notable enrichment appears first in the evolution. This is a sign of an over-all increasing strength of the mixing with increasing initial angular momentum. It is interesting to note that the μ-turn in the HR diagram (Sect. 4.1.1) for the fast rotating models also coincides to a "kink" in the evolution of the surface abundances, especially for isotopes produced below the μ-barrier, namely ^{16}O and ^{4}He, and to some extent ^{14}N. These μ-turns appear at an age of about 10 Myr, 20 Myr, 15 Myr, and 10 Myr for Models `F12B`, `H12B`, `H15B`, and `H20B`, respectively (Fig. 4.4).

An important feature of rotationally induced mixing is the depletion of light elements, like lithium (Fig. D.1B1-B3) and boron, at the surface. These elements are destroyed at much lower temperatures than those necessary for CNO processing. Therefore, much stronger abundance changes are induced by rotation. The rotating main sequence models computed by Fliegner et al. (1996) predicted that stars which show enrichment in nitrogen should be strongly depleted in boron, which was found in good agreement with the observational data by Venn et al. (1996). This finding is supported by the present work (Figs. 4.4A1-A3 and 4.6A1-A3): the boron depletion is much stronger and appears earlier than the nitrogen enrichment. Even the slow rotators with ZAMS rotational velocities of $\sim 100\,\mathrm{km\,s^{-1}}$, which barely show any nitrogen enrichment, become depleted in boron by $\sim 0.5\,\mathrm{dex}$.

Other interesting changes in the surface abundances due to rotationally induced mixing are the depletion of fluorine (^{19}F) and enrichment in sodium (^{23}Na), both the only stable isotopes of these elements (Figs. 4.6B1-B3,C1-C3). An important product of the magnesium-aluminum cycle (Arnould & Mowlavi 1993), a hydrogen-burning cycle like the CNO cycle, is the production of the radioactive isotope ^{26}Al by ^{25}Mg(p,γ)^{26}Al in the central convective core. Typically, it reaches a mass fraction of a few 10^{-6} in the center for the initial composition used in the present work. This isotope has half-lifetime of 0.716 Myr and emits γ-rays due to its β-decay, which has been observed in the interstellar medium (Oberlack et al. 1996). The isotope ^{26}Al both is produced and decays, and therefore the resulting surface abundance shows the interplay of production, decay, and mixing. This can be seen in the Figs. 4.6D1-D3: at the beginning a steep increase in the abundance appears when ^{26}Al is mixed to the surface within the first few Myr. For the fast rotating models the abundance slowly continues to increase until the mixing between core and envelope is shut off at the μ-turn, and the further evolution of the ^{26}Al surface abundance is mainly governed by its decay. The drop of the ^{26}Al surface abundance, as, e.g., seen in Fig. 4.6D1, corresponds to an exponential decay law. The apparently different slopes in Figs. 4.6D1-D3 are due to the different time axes.

The surface abundance of ^{26}Al strongly increases with the amount of mixing, i.e., with the ZAMS rotational velocity of the star. But it is also a sensitive function of

the initial mass: The fastest rotating $20\,M_\odot$ star (Model H20B) has an about two orders of magnitude higher surface abundance than the fastest rotating $12\,M_\odot$ star (Model H12B). This difference is even larger for the slower rotators.

The larger surface enrichment in ^{26}Al in the more massive stars is due to their shorter lifetime. They show a comparable enrichment in products of central hydrogen burning as a function of the *fraction* of their lifetime, within a factor of two of less massive stars, as can be seen, e.g., from the surface enrichment in helium (Fig. 4.4D1-D3). But during the shorter *absolute* lifetime, less ^{26}Al decays.

Several interesting changes in the surface isotopic ratios occur for different elements. They are shown in Appendix D. In contrast to the changes in the elemental abundances, these isotopic ratios are not easily measurable in the atmospheres of hot stars, and therefore cannot be used as observational tests.

4.2 Post-central hydrogen burning

4.2.1 Evolution in the HR diagram

After core hydrogen exhaustion the stars discussed in the present work become red supergiants. They evolve to the the Hayashi line within a few 10 000 yr. In Figs. 4.7 and 4.8 the evolutionary tracks in the HR diagram of the rotating and non-rotating models with a ZAMS rotational velocity of $\sim 200\,\mathrm{km\,s^{-1}}$ are compared. The tracks go from the ZAMS up to core collapse, except for the lowest mass Models D10, D12, and E08 in Fig. 4.7, which end before neon ignition. The evolution of Model E25 is only shown until it becomes a Wolf-Rayet star during central helium burning, where it loses its hydrogen-rich envelope. In Figs. 4.9, 4.10, and 4.11 the evolution of stars with different initial rotation rates are compared.

Since the rotating stars develop larger helium cores, they become more luminous red supergiants than the non-rotating stars of equal mass. This is shown in Fig. 4.7 for models with inefficient μ-gradients, and in Fig. 4.9, for different initial rotational velocities. In the former case the models also evolve to notably lower effective temperatures than their non-rotating counterparts. These models have considerably larger helium cores and, due to their stronger mass loss, a by far higher envelope to core mass and mass to luminosity ratio. Due to this, these stars, especially the most luminous of them, become highly unstable to radial pulsations (Sect. 4.4).

In the models where the effect of μ-gradients on rotationally induced mixing is taken into account, the effective temperatures reached on the Hayashi line are not significantly different from those of the non-rotating models. The increase in luminosity is much less (Figs. 4.10 and 4.11), except for the fastest rotators, like H12 (Figs. 4.9 and E.22). This model does not become a red supergiant immediately after core hydrogen exhaustion, but burns most of the helium as a blue supergiant before it first moves the Hayashi line.

Stars with initial masses of $\lesssim 12\,M_\odot$ show so-called "blue loops", i.e., they evolve from red into blue supergiants (Figs. 4.7, 4.8, and 4.9). Stars with more rotationally induced mixing evolve to lower effective temperatures and to higher luminosities

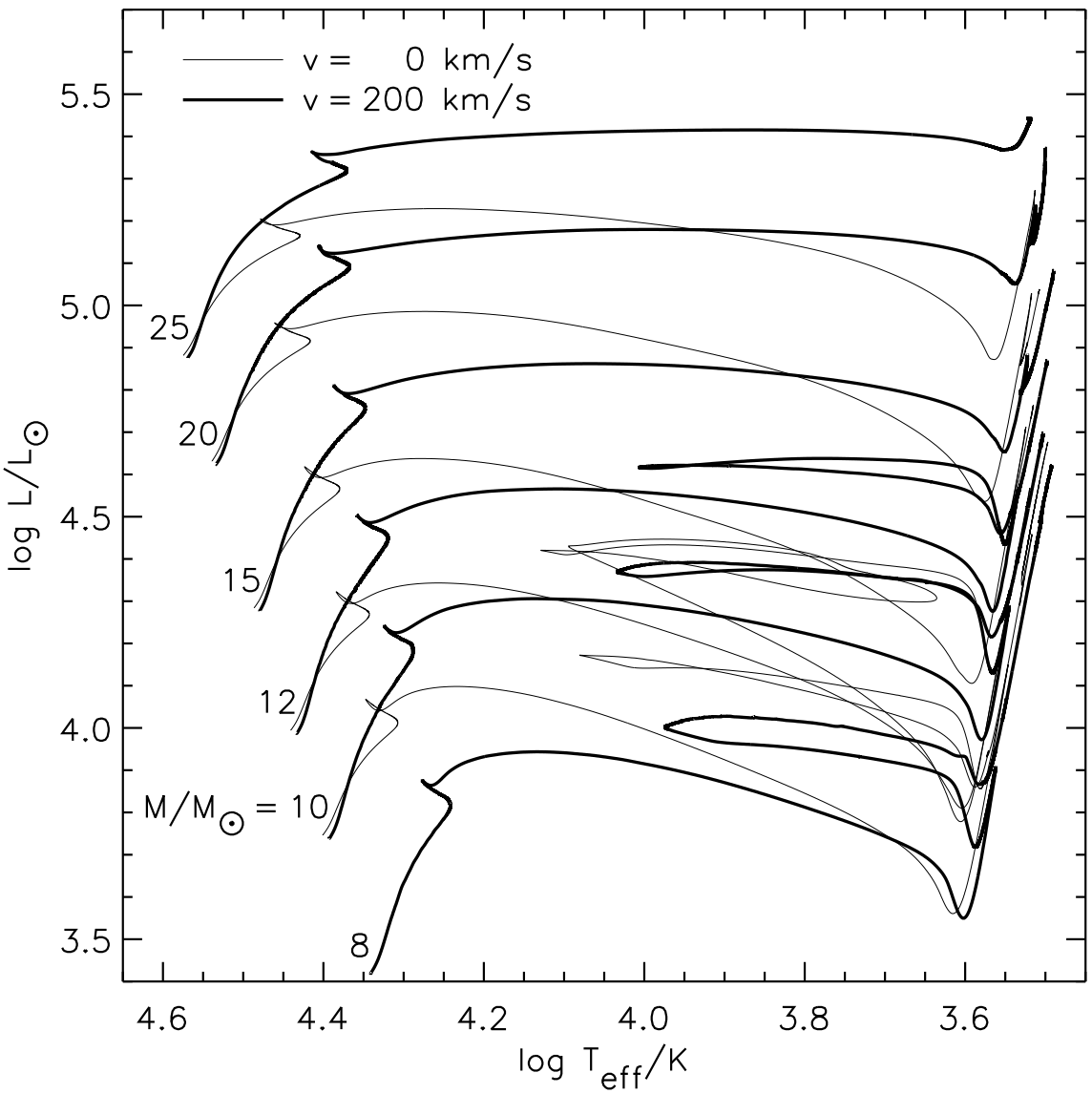

Figure 4.7: Evolutionary tracks in the HR diagram of rotating models in the mass range $8\,M_\odot$ to $25\,M_\odot$ (thick lines) and non-rotating $10\,M_\odot$ to $25\,M_\odot$ models (thin lines) from the ZAMS to the presupernova stage. The tracks are labeled with the initial masses (in $M_\odot$). The tracks are for Models `D10`, `D12`, `D15`, `D20`, and `D25` (no rotation) and for Models `E08`, `E10`, `E12`, `E15`, `E20`, and `E25` (ZAMS equatorial rotational velocities of $\sim 200\,km\,s^{-1}$). The track of the rotating Model `E25` is only shown until it evolves into a Wolf-Rayet star, during core helium burning. See also Heger et al. (1998).

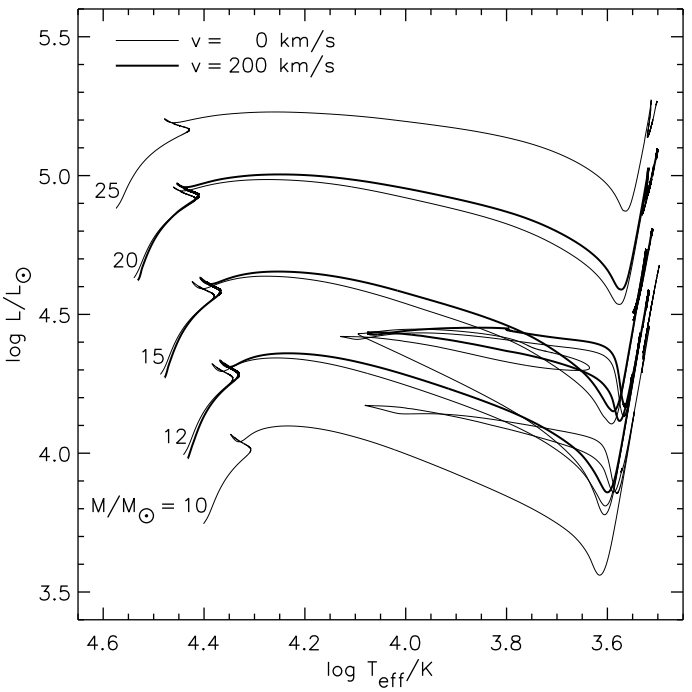

Figure 4.8: Evolutionary tracks in the HR diagram of rotating models in the mass range $12\,M_\odot$ to $20\,M_\odot$ (thick lines) and of non-rotating models in the mass range $10\,M_\odot$ to $25\,M_\odot$ (thin lines) from core hydrogen ignition to the presupernova stage. The tracks are labeled with the initial masses (in $M_\odot$). The tracks are for Models `D10`, `D12`, `D15`, `D20`, and `D25` (non-rotating) and for Models `E12B`, `E15B`, and `E20B` (equatorial rotational velocities of $\sim 200\,km\,s^{-1}$). See also Fig. 4.7.

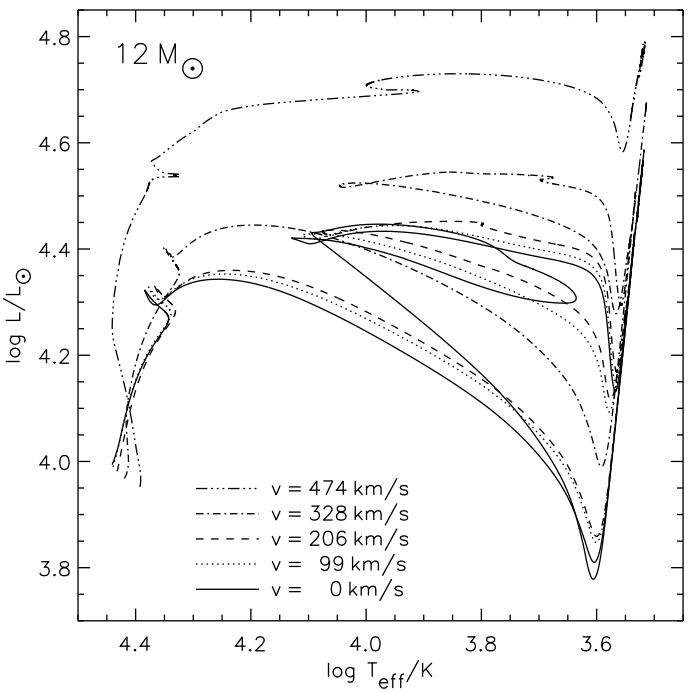

Figure 4.9: Evolutionary tracks in the HR diagram of stars with an initial mass of $12\,M_\odot$ and ZAMS equatorial rotational velocities of $0\,km\,s^{-1}$ (Model `D12`, solid line), $99\,km\,s^{-1}$ (Model `G12B`, dotted line), $206\,km\,s^{-1}$ (Model `E12B`, dashed line), $328\,km\,s^{-1}$ (Model `F12B`, dash-dotted line), and $474\,km\,s^{-1}$ (Model `H12B`, dash-triple-dotted line). The evolution during central hydrogen burning is magnified in Fig. 4.1B. The track start at the ZAMS and are followed until the phase listed in Table 2.3.

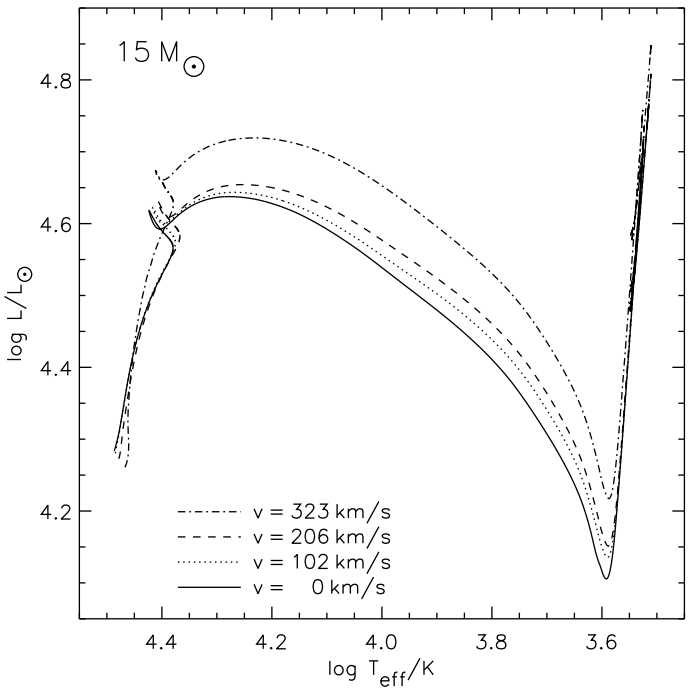

Figure 4.10: Evolutionary tracks in the HR diagram of stars with an initial mass of $15\,M_\odot$ and ZAMS equatorial rotational velocities of $0\,km\,s^{-1}$ (Model `D15`, solid line), $102\,km\,s^{-1}$ (Model `G15B`, dotted line), $206\,km\,s^{-1}$ (Model `E15B`, dashed line), and $323\,km\,s^{-1}$ (Model `F15B`, dash-dotted line) up to core collapse. The evolution during central hydrogen burning is magnified in Fig. 4.2.

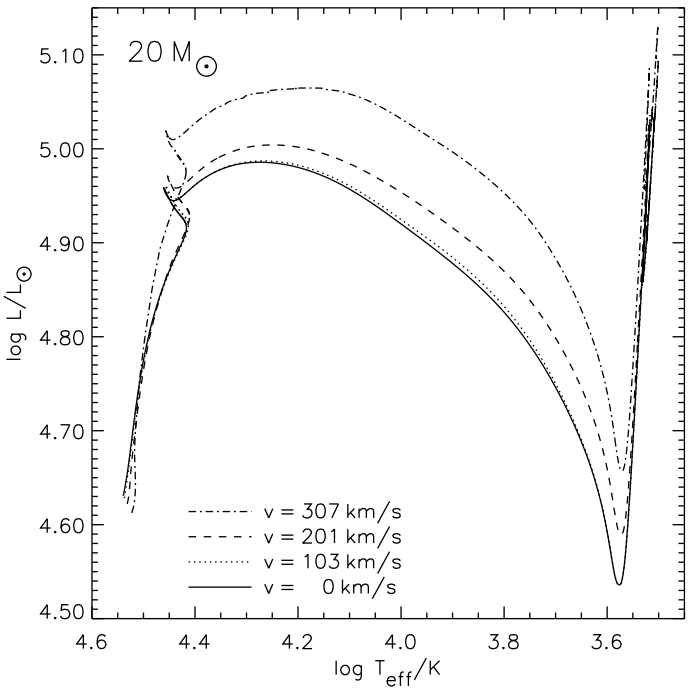

Figure 4.11: Evolutionary tracks in the HR diagram of stars with an initial mass of $15\,M_\odot$ and ZAMS equatorial rotational velocities of $0\,km\,s^{-1}$ (Model `D20`, solid line), $103\,km\,s^{-1}$ (Model `G20B`, dotted line), $201\,km\,s^{-1}$ (Model `E20B`, dashed line), and $307\,km\,s^{-1}$ (Model `F20B`, dash-dotted line) up to core collapse. The evolution during central hydrogen burning is magnified in Fig. 4.3.

during their blue loops (Figs. 4.7, 4.8, and 4.9). The highly peculiar evolution of the surface rotation rate and mass loss during a blue loop is discussed in Sect. 4.3.

4.2.2 First dredge-up abundances

Red supergiant have an extended surface convection zone which comprises the major part of the hydrogen-rich envelope. Since the mixing in the convective regions is much faster than the rotationally induced mixing processes in the envelope during core hydrogen burning, the convective envelope is essentially chemically homogeneous. The thermonuclear processed matter which becomes part of the convective envelope appears instantly at the surface compared to the evolutionary time-scale of the star. This rapid mixing of processed matter to the surface, which occurs also in non-rotating stars, is called a *dredge-up*; its first occurrence after core hydrogen depletion is accordingly called the *first* dredge-up.

In Fig. 4.12 thin lines give the surface abundances of ^{12}C, ^{14}N, and ^{16}O relative to their initial values, and the surface mass fraction of ^{4}He at core hydrogen exhaustion as a function of the ZAMS rotational velocity for three different initial masses and for models where rotationally induced mixing was assumed to be sensitive to μ-gradients. Thick lines give the same quantities after the first dredge-up. The surface abundances of elements up to sodium after the first dredge-up are also given in Table 4.2.

The slowly and non-rotating models show a significant enhancement in ^{14}N due to the dredge-up. In contrast, in the fast rotators the additional changes of the surface abundances due to dredge-up are small in comparison to the surface enrichment which already occurred during central hydrogen burning. The envelope is already well-mixed before the dredge-up.

Since during the dredge-up the convective envelope penetrates into region which was located below the μ-barrier, the surface carbon mass fraction is reduced by diluting the ^{12}C in the envelope with the ^{12}C-depleted matter from deeper inside the star. In a similar way, ^{16}O is depleted and ^{4}He is enriched. The bottom of the convective envelope does not get hot enough for nuclear burning, i.e., the abundance changes at the surface during the dredge-up result only from mixing of already processed matter into the convective envelope as it extends to lower mass coordinates.

In the case of rotationally induced mixing, the conversion of ^{12}C into ^{14}N occurs even above the μ-barrier and therefore matter originally located close to the surface of the stars can also be processed by first mixing it down, then processing it, and mixing it up again. Due to this, the surface enrichment in the faster rotating stars is stronger both before and after the dredge-up than in the slowly or non-rotating stars. The stronger depletion of ^{16}O and enrichment of ^{4}He for the faster rotating stars is mainly because in those the rotationally induced mixing can overcome the μ-barrier for a longer time during core hydrogen burning than in the slow rotators.

Table 4.2: Surface abundances after the first dredge-up for the indicated model sequences. Given are the ^{4}He mass fraction, and the logarithm of the ratios of the ^{3}He, lithium, boron, beryllium, ^{12}C, ^{13}C, ^{14}N, ^{15}N, ^{16}O, ^{17}O, ^{18}O, ^{19}F, and ^{23}Na mass fractions relative to their initial values.

model	X(^{4}He)	[^{3}He]	[Li]	[Be]	[B]	[^{12}C]	[^{13}C]	[^{14}N]	[^{15}N]	[^{16}O]	[^{17}O]	[^{18}O]	[^{19}F]	[^{23}Na]
D10	0.301	−0.113	−1.133	−1.133	−1.087	−0.212	0.490	0.492	−0.318	−0.038	1.346	−0.304	−0.060	0.170
D12	0.305	−0.160	−1.043	−1.043	−1.019	−0.216	0.497	0.511	−0.324	−0.045	1.298	−0.314	−0.067	0.183
D15	0.312	−0.203	−1.147	−1.147	−1.091	−0.219	0.509	0.538	−0.332	−0.056	1.293	−0.326	−0.083	0.204
D20	0.334	−0.250	−7.935	−3.416	−1.309	−0.226	0.527	0.589	−0.346	−0.079	1.229	−0.348	−0.108	0.241
D25	0.354	−0.273	−1.715	−1.714	−1.435	−0.228	0.542	0.631	−0.353	−0.104	1.226	−0.361	−0.138	0.275
E08	0.363	−0.183	−1.326	−1.326	−1.251	−0.336	0.546	0.669	−0.475	−0.100	1.576	−0.498	−0.140	0.305
E10	0.388	−0.300	−1.572	−1.571	−1.409	−0.375	0.544	0.715	−0.515	−0.123	1.502	−0.561	−0.168	0.339
E12	0.403	−0.370	−1.758	−1.757	−1.520	−0.394	0.558	0.741	−0.544	−0.140	1.446	−0.606	−0.187	0.360
E15	0.423	−0.436	−2.030	−2.025	−1.697	−0.409	0.582	0.773	−0.577	−0.167	1.409	−0.659	−0.219	0.388
E20	0.447	−0.492	−2.507	−2.484	−1.948	−0.413	0.613	0.810	−0.611	−0.207	1.365	−0.715	−0.267	0.419
E25	0.627	−0.945	−6.780	−4.776	−2.565	−0.751	0.382	0.981	−0.794	−0.447	1.463	−1.156	−0.732	0.562
G12B	0.310	−0.264	−4.764	−3.017	−1.579	−0.301	0.630	0.574	−0.509	−0.053	1.417	−0.515	−0.087	0.208
G15B	0.317	−0.309	−4.529	−2.873	−1.507	−0.300	0.645	0.592	−0.521	−0.063	1.370	−0.535	−0.100	0.221
G20B	0.337	−0.350	−4.874	−3.132	−1.646	−0.288	0.688	0.628	−0.539	−0.087	1.332	−0.560	−0.127	0.256
E12B	0.314	−0.410	−9.111	−5.631	−2.434	−0.475	0.647	0.656	−0.765	−0.064	1.624	−0.850	−0.127	0.246
E15B	0.322	−0.468	−8.756	−5.734	−2.479	−0.461	0.701	0.672	−0.800	−0.078	1.606	−0.909	−0.147	0.264
E20B	0.345	−0.514	−7.905	−6.090	−2.736	−0.432	0.743	0.702	−0.819	−0.106	1.578	−0.950	−0.185	0.295
F12B	0.358	−0.571	−9.538	−11.42	−4.401	−0.711	0.626	0.818	−1.023	−0.177	2.037	−1.577	−0.395	0.464
F15B	0.369	−0.747	−8.786	−8.246	−4.581	−0.866	0.482	0.841	−1.038	−0.178	1.945	−1.757	−0.379	0.443
F20B	0.394	−0.810	−7.482	−6.096	−4.939	−0.785	0.559	0.863	−1.024	−0.215	1.880	−1.769	−0.434	0.452
H12B	0.481	−1.072	−9.421	−12.97	−9.033	−1.550	−0.085	1.007	−0.945	−0.478	2.065	−3.665	−1.264	0.640
H20B	0.700	−2.080	−6.555	−4.861	−18.00	−1.447	0.023	1.080	−0.883	−0.860	1.570	−4.549	−1.982	0.674

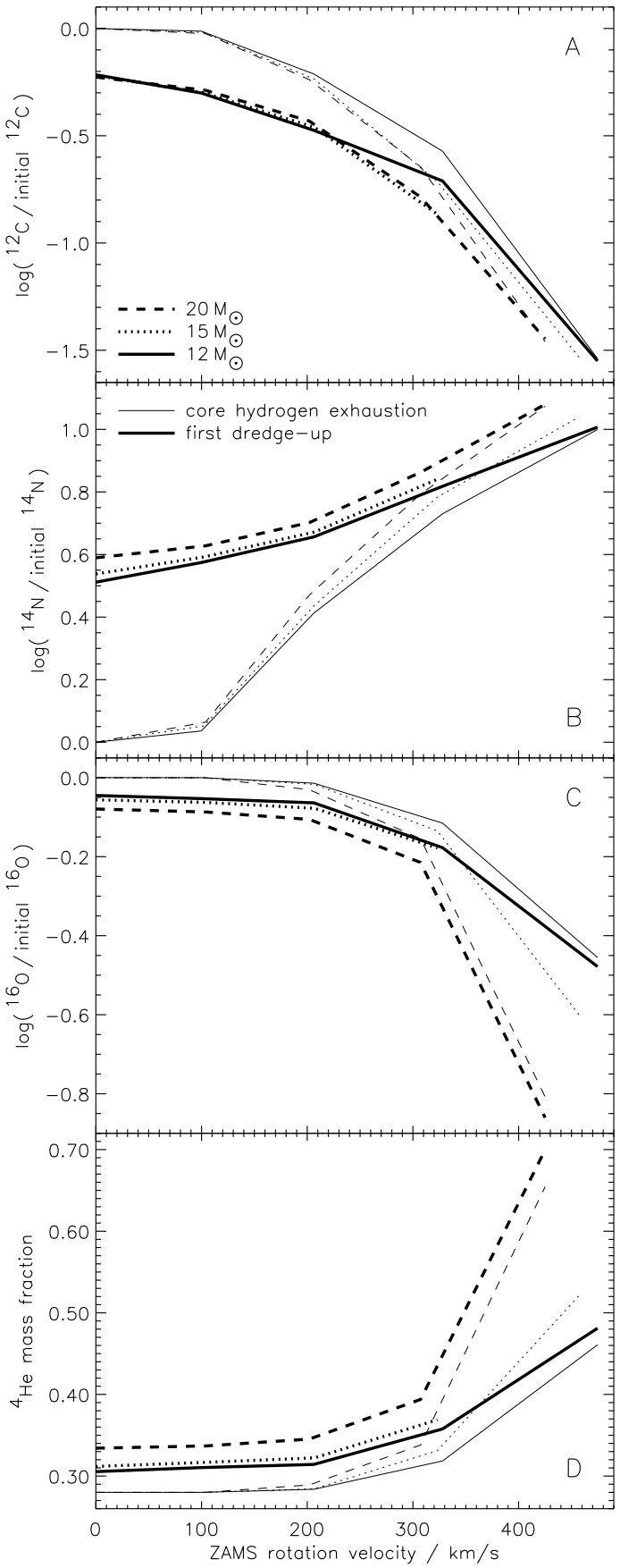

Figure 4.12: Surface mass fractions of ^{12}C (Panel **A**), ^{14}N (Panel **B**), and ^{16}O (Panel **C**), relative to the initial values, as a function the initial equatorial rotation rate. Panel **D** gives the ^{4}He mass fraction. Solid, dotted and dashed lines give the values for the $12\,M_\odot$ (Models `D12`, `G12B`, `E12B`, `F12B`, and `H12B`), $15\,M_\odot$ (Models `D15`, `G15B`, `E15B`, `F15B`, and `H12B`), and $20\,M_\odot$ (Models `D20`, `G20B`, `E20B`, `F20B`, and `H20B`) stars, respectively. The thin lines show the surface composition at the end of central hydrogen burning (Fig. 4.4), the thick lines those after the first dredge-up, i.e., when the star has first become a red supergiant after termination of central hydrogen burning. For the fastest rotating $15\,M_\odot$ star there is no post-dredge-up data.

Table 4.3: Surface abundances after the second dredge-up for the indicated model sequences. Given are the helium mass fraction, and the logarithm of the ratios of the lithium, boron, beryllium, nitrogen, carbon, oxygen, fluorine, and sodium mass fractions relative to their initial values.

model	X(He)	[Li]	[Be]	[B]	[C]	[N]	[O]	[F]	[Na]
D10	0.382	−1.21	−1.21	−1.17	−0.25	0.64	−0.09	−0.12	0.28
D12	0.306	−1.26	−1.26	−1.19	−0.21	0.52	−0.04	−0.07	0.19
D15	0.312	−1.17	−1.17	−1.11	−0.20	0.54	−0.05	−0.08	0.20
D20	0.334	−7.92	−3.43	−1.32	−0.21	0.59	−0.08	−0.11	0.24
D25	0.354	−1.73	−1.73	−1.44	−0.21	0.63	−0.10	−0.14	0.28
E08	0.395	−1.49	−1.49	−1.39	−0.34	0.71	−0.12	−0.17	0.34
E10	0.388	−1.71	−1.71	−1.54	−0.35	0.72	−0.12	−0.17	0.34
E12	0.403	−1.87	−1.87	−1.63	−0.37	0.74	−0.13	−0.19	0.36
E15	0.423	−2.08	−2.07	−1.74	−0.37	0.77	−0.16	−0.22	0.39
E20	0.450	−2.60	−2.55	−2.03	−0.39	0.82	−0.20	−0.27	0.42
G12B	0.312	−4.78	−3.04	−1.60	−0.28	0.58	−0.05	−0.09	0.21
G15B	0.317	−4.56	−2.90	−1.53	−0.27	0.59	−0.06	−0.10	0.22
G20B	0.337	−4.90	−3.16	−1.66	−0.25	0.63	−0.08	−0.13	0.26
E12B	0.315	−9.13	−5.65	−2.45	−0.43	0.66	−0.06	−0.13	0.25
E15B	0.323	−8.77	−5.76	−2.50	−0.41	0.67	−0.07	−0.15	0.27
E20B	0.346	−7.91	−6.11	−2.75	−0.37	0.70	−0.10	−0.19	0.30
F12B	0.358	−9.43	−11.47	−4.45	−0.64	0.82	−0.15	−0.40	0.46
F15B	0.369	−8.80	−8.32	−4.61	−0.78	0.84	−0.16	−0.38	0.44
F20B	0.394	−7.49	−6.16	−4.96	−0.70	0.86	−0.20	−0.43	0.45
H12B	0.490	−9.42	−11.55	−9.08	−1.42	1.01	−0.43	−1.28	0.64

4.2.3 Second dredge-up abundances

After core helium exhaustion, the bottom of the convective envelope of the red supergiants moves to lower mass coordinates. Thus, it can transport matter which has been processed by the hydrogen shell to the surface of the star. However, in most of the models considered here, the convective envelope does not penetrate much deeper during this second dredge-up than it did during the first dredge-up. Additionally, during core helium burning not much mixing occurs in the radiative part of the envelope, and the temperatures are mostly too low for significant thermonuclear processing. Thus, with the exception of the lowest masses (e.g., Models D10 and E08) no strong changes in the surface abundances occur during the second dredge-up. In stars which experience a blue loop, the processing can be slightly stronger, since during this loop the envelope contracts and a larger part of it can become sufficiently hot for thermonuclear reactions. This can be seen by the large extent of the hydrogen-burning shell during the blue loop in Model E12B (Fig. E.16 in Appendix E).

The surface abundances of the most important isotopes after the second dredge-up are given in Table 4.3. Since in the case of the second dredge-up the mixing in the convective envelope is also fast enough to make it chemically homogeneous,

Table 4.4: Radius, R, angular velocity, ω, and equatorial rotational velocity, v, at the end of core helium burning (middle three columns) and for the final models (right three columns). First and second column give model name and ZAMS equatorial rotational velocity.

	ZAMS	core helium burning			presupernova		
model	v	R	ω	v	R	ω	v
	$\mathrm{km\,s^{-1}}$	$\mathrm{R_\odot}$	$\mathrm{rad\,s^{-1}}$	$\mathrm{km\,s^{-1}}$	$\mathrm{R_\odot}$	$\mathrm{rad\,s^{-1}}$	$\mathrm{km\,s^{-1}}$
D10	0	291	0	0	735	0	0
D12	0	357	0	0	486	0	0
D15	0	508	0	0	711	0	0
D20	0	832	0	0	1 043	0	0
D25	0	1 182	0	0	1 393	0	0
E08	205	208	$9.82{\cdot}10^{-9}$	1.43	704	$3.95{\cdot}10^{-10}$	$1.94{\cdot}10^{-1}$
E10	208	353	$2.37{\cdot}10^{-9}$	$5.86{\cdot}10^{-1}$	700	$3.26{\cdot}10^{-10}$	$1.59{\cdot}10^{-1}$
E12	208	506	$5.97{\cdot}10^{-10}$	$2.11{\cdot}10^{-1}$	902	$9.77{\cdot}10^{-11}$	$6.16{\cdot}10^{-2}$
E15	208	767	$2.86{\cdot}10^{-10}$	$1.53{\cdot}10^{-1}$	1 157	$5.68{\cdot}10^{-11}$	$4.59{\cdot}10^{-2}$
E20	202	1 204	$4.03{\cdot}10^{-11}$	$3.39{\cdot}10^{-2}$	1 608	$8.56{\cdot}10^{-12}$	$9.62{\cdot}10^{-3}$
G12B	99	432	$1.22{\cdot}10^{-9}$	$3.69{\cdot}10^{-1}$	489	$8.63{\cdot}10^{-10}$	$2.95{\cdot}10^{-1}$
G15B	102	517	$1.05{\cdot}10^{-9}$	$3.79{\cdot}10^{-1}$	739	$3.81{\cdot}10^{-10}$	$1.97{\cdot}10^{-1}$
G20B	103	807	$3.06{\cdot}10^{-10}$	$1.72{\cdot}10^{-1}$	1 061	$1.15{\cdot}10^{-10}$	$8.53{\cdot}10^{-2}$
E12B	206	439	$1.98{\cdot}10^{-9}$	$6.08{\cdot}10^{-1}$	542	$1.14{\cdot}10^{-9}$	$4.33{\cdot}10^{-1}$
E15B	206	538	$1.79{\cdot}10^{-9}$	$6.72{\cdot}10^{-1}$	773	$6.30{\cdot}10^{-10}$	$3.40{\cdot}10^{-1}$
E20B	201	895	$3.81{\cdot}10^{-10}$	$2.38{\cdot}10^{-1}$	1 110	$1.68{\cdot}10^{-10}$	$1.30{\cdot}10^{-1}$
F12B	328	446	$1.54{\cdot}10^{-9}$	$4.79{\cdot}10^{-1}$	660	$5.32{\cdot}10^{-10}$	$2.45{\cdot}10^{-1}$
F15B	323	576	$1.98{\cdot}10^{-9}$	$7.97{\cdot}10^{-1}$	822	$6.60{\cdot}10^{-10}$	$3.79{\cdot}10^{-1}$
F20B	307	926	$4.27{\cdot}10^{-10}$	$2.76{\cdot}10^{-1}$	1 148	$1.73{\cdot}10^{-10}$	$1.38{\cdot}10^{-1}$
H12B	474	739	$2.18{\cdot}10^{-10}$	$1.13{\cdot}10^{-1}$	751	$1.73{\cdot}10^{-10}$	$9.06{\cdot}10^{-2}$

Table 4.3 gives the presupernova abundances of the entire envelope.

4.2.4 Rotational velocities

The majority of the stellar models investigated here expand to red supergiants after core hydrogen depletion. The expansion of the stellar envelope increases the moment of inertia and the angular velocity of the rigidly rotating convective envelope of the star decreases considerably. This is the most important effect contributing to the slow-down of the star's rotation when evolving from the main sequence to the red supergiant regime. Additionally, strong mass loss sets in during the red supergiant phase, and the corresponding loss of angular momentum due to stellar winds also becomes important for the models of lower initial mass, for which it was almost negligible during central hydrogen burning. Since the rise of the moment of inertia is much larger than the growth in radius, the surface rotational velocity decreases considerably and drops below $1\,\mathrm{km\,s^{-1}}$ in most of the models (Table 4.4). During the second dredge-up after core helium exhaustion the models become more luminous

and extended (Table 4.4).

The stars with an initial mass of $12\,M_\odot$ or below which experience a blue loop can show a remarkable spin-up during this phase, where they can lose the major part of their total angular momentum (see Sect. 4.3). This explains the small difference in the angular velocity of the $12\,M_\odot$ models compared to the corresponding $15\,M_\odot$ models, which do not develop blue loops, in relation to the differences between other models with same input physics but different initial mass (see e.g., Models `E12B`, `E15B`, and `E20B` in Table 4.4).

Model `H12B` evolves as a blue supergiant during the first part of its core helium burning. Since it has a large initial angular momentum and did not experience any significant previous angular momentum loss, it evolves close to critical rotation during this phase. Even the enhancement of the mass loss rate due to rotation does not cause a sufficiently high angular momentum loss to slow it down from critical rotation.

Models `E25` and `H20B` become Wolf-Rayet stars during central helium burning. The evolution of Model `E25` has been followed until core collapse. The strong mass loss during the Wolf-Rayet phase rapidly slows down the rotation of the helium envelope. None of the instabilities considered in the present work is fast enough to keep it in rigid rotation with the core or the rest of the helium-rich layers. Thus strong differential rotation occurs in the envelope and the core is not slowed down significantly. The slower rotation of the core compared to other models (Figs. 3.22, 3.23, and Table 3.2) is mostly due to the loss of angular momentum during core hydrogen burning.

4.3 Spin-up of contracting red supergiants

The circumstellar matter around many stars shows a remarkable axial symmetry. Famous examples are Supernova 1987A (Plait et al. 1995; Burrows et al. 1995), the Homunculus nebula around η Carinae, other nebulae around so called Luminous Blue Variables (Nota et al. 1995), and many planetary nebulae (Schwarz, Corradi & Melnick 1992). Less spectacular examples are B[e] stars — blue supergiants showing properties which might be well explained by a circumstellar disk (Gummersbach, Zickgraf & Wolf 1995; Zickgraf et al. 1996). Many of these axisymmetric structures have been explained in terms of interacting winds of rotating stars (Martin & Arnett 1995; Langer et al. 1998b; García-Segura et al. 1998), which may be axisymmetric when the stars rotate with a considerable fraction of the break-up rate (Ignace, Cassinelli & Bjorkman 1996; Owocki et al. 1996). However, until now little information has been available about the evolution of the surface rotational velocity of stars with time, in particular for their post-main sequence phases.

Single stars which evolve into red giants or supergiants may be subject to a significant spin-down (Endal & Sofia 1979; Pinsonneault, Deliyannis & Demarque 1991). Their radius increases greatly, and if the specific angular momentum were conserved in their surface layers (which may not be the case; see below) they would not only spin down but would also evolve further away from critical rotation. Moreover, they

might lose angular momentum through a stellar wind. Therefore, it appears doubtful at first whether post-red giant or supergiant single stars could retain enough angular momentum to produce aspherical winds due to rotation.

However, by investigating the evolution of rotating massive single stars, Heger & Langer (1998) found that red supergiants, when they evolve off the Hayashi line toward the blue part of the HR diagram, may spin up dramatically, much more than expected from local conservation of angular momentum. In Sect. 4.3.1 the spin-up mechanism and its critical ingredients are described. In Sect. 4.3.2 the results of evolutionary calculations for a rotating $12\,M_\odot$ star are presented which provide a quantitative example for the spin-up. In Sect. 4.3.3 the relevance of these results are discussed for various types of stars. The findings and conclusions of Sect. 4.3 can also be found in Heger & Langer (1998).

4.3.1 The spin-up mechanism

4.3.1.1 Assumptions

As a star evolves into a red supergiant, its envelope structure changes from radiative to convective, starting at the surface. If assumed that the envelope is in solid body rotation initially, it cannot remain in this state without any transport of angular momentum, unless

$$\frac{\partial \ln i}{\partial m} = \frac{1}{2\pi r^3 \rho} \tag{4.1}$$

remains constant with time everywhere, i.e., $r^3\rho$ remains constant. To derive Eq. (4.1), the assumption that the gyration constant, k, does not depend on r is used. Obviously, the above homology condition does not hold for stars which change their mode of energy transport in the envelope, since the polytropic index, n, changes between $n \simeq 3$ in the radiative envelope and $n \simeq 1.5$ in the convective state.

Although, for the considerations in Sect. 4.3.1.2 rigid rotation is assumed to persist in convection zones (Sect. 2.2.4), the necessary condition to make the spin-up mechanism described here work is only that convection transports angular momentum on a time-scale which is short compared to the evolutionary time-scale of the star, and that it leads to a characteristic angular momentum distribution in between the cases of constant angular velocity and constant angular momentum. The efficiency of the spin-up is largest for constant angular velocity and drops to zero for the case of constant angular momentum. The mechanism presented here is not restricted to convection, but any mechanism for transport of angular momentum that acts towards solid body rotation is suitable.

However, the effect of instabilities other than convection on the transport of matter and angular momentum are of no relevance for the conclusions obtained in Sect. 4.3. For example, gradients in the mean molecular weight have no effect on the spin-up process described below since it occurs in a retreating convection zone (see below). Calculations performed with KEPLER confirm the spin-up effect obtained with STERN.

4.3.1.2 The spin-down of convective envelopes

The rotational frequency of a rigidly rotating convective envelope depends on its moment of inertia and its angular momentum. Both are altered by mass loss from this envelope, the former by loss of mass, the latter by the accompanying loss of angular momentum. Additionally, the moment of inertia of the envelope is affected by changes of its density stratification.

Here, two processes are discussed which can change the rotational frequency of a rigidly rotating convective envelope without employing global contraction or expansion of the star, but rather by mass outflow through its upper or lower boundary. It will be shown that the first case leads to a spin-down, while the latter spins the envelope up.

The spin-down of mass losing rigidly rotating envelopes can be understood by breaking up the continuous mass and angular momentum loss into three discrete steps (see the left hand side of Fig. 4.13; see also Langer 1998; Langer & Heger 1997), neglecting secular changes of the stellar structure. Starting from a rigidly rotating envelope extending from R_c to R_0 (A1), the outer part of the convective envelope located between R_1 and R_0 is removed by stellar mass loss within the time interval Δt (A1 $\rightarrow$ A2). In the second step, for which local angular momentum conservation is assumed, the envelope re-expands to roughly its original size (A2 $\rightarrow$ A3). This results in a slow-down of the surface rotation and, as the layers deep inside the envelope expand less, differential rotation below (A3). In the third step, rigid rotation is re-established by an upward transport of angular momentum (A3 $\rightarrow$ A4). As this implies an averaging of the angular velocity, it is clear from Fig. 4.13A4 that now the whole convective envelope rotates slower than at the beginning of the first step. Obviously, the redistribution of angular momentum towards the stellar surface leads to an increase of the angular momentum loss rate.

The efficiency of the angular momentum loss induced by mass loss from the surface of a rigidly rotating envelope, i.e., the amount of angular momentum lost per unit mass lost relative to average specific angular momentum of the envelope, is given by

$$\chi := \frac{\dot{J}}{\dot{M}} \frac{M_{\rm env}}{J_{\rm env}} = \frac{j_{\rm surf}}{\langle j \rangle_{\rm env}} = \frac{i_{\rm surf}}{\langle i \rangle_{\rm env}} \approx \frac{R^2}{\langle r^2 \rangle_{\rm env}} \,, \tag{4.2}$$

where $M_{\rm env}$ and $J_{\rm env}$ are total mass and total angular momentum of the envelope, and $i_{\rm surf}$ is the specific moment of inertia at the surface, respectively. The mean value of a quantity x over the envelope is defined by

$$\langle x \rangle_{\rm env} := \frac{1}{M_{\rm env}} \int_{M-M_{\rm env}}^{M} x(m)\, {\rm d}m \,. \tag{4.3}$$

The larger χ the more efficient is the loss of angular momentum per unit mass lost. A value of $\chi > 1$ corresponds to a decrease of the mean specific angular momentum of the envelope, $\chi < 1$ to an increase. For the case of mass loss from the surface of a rigidly rotating stellar envelope χ is always greater than 1.

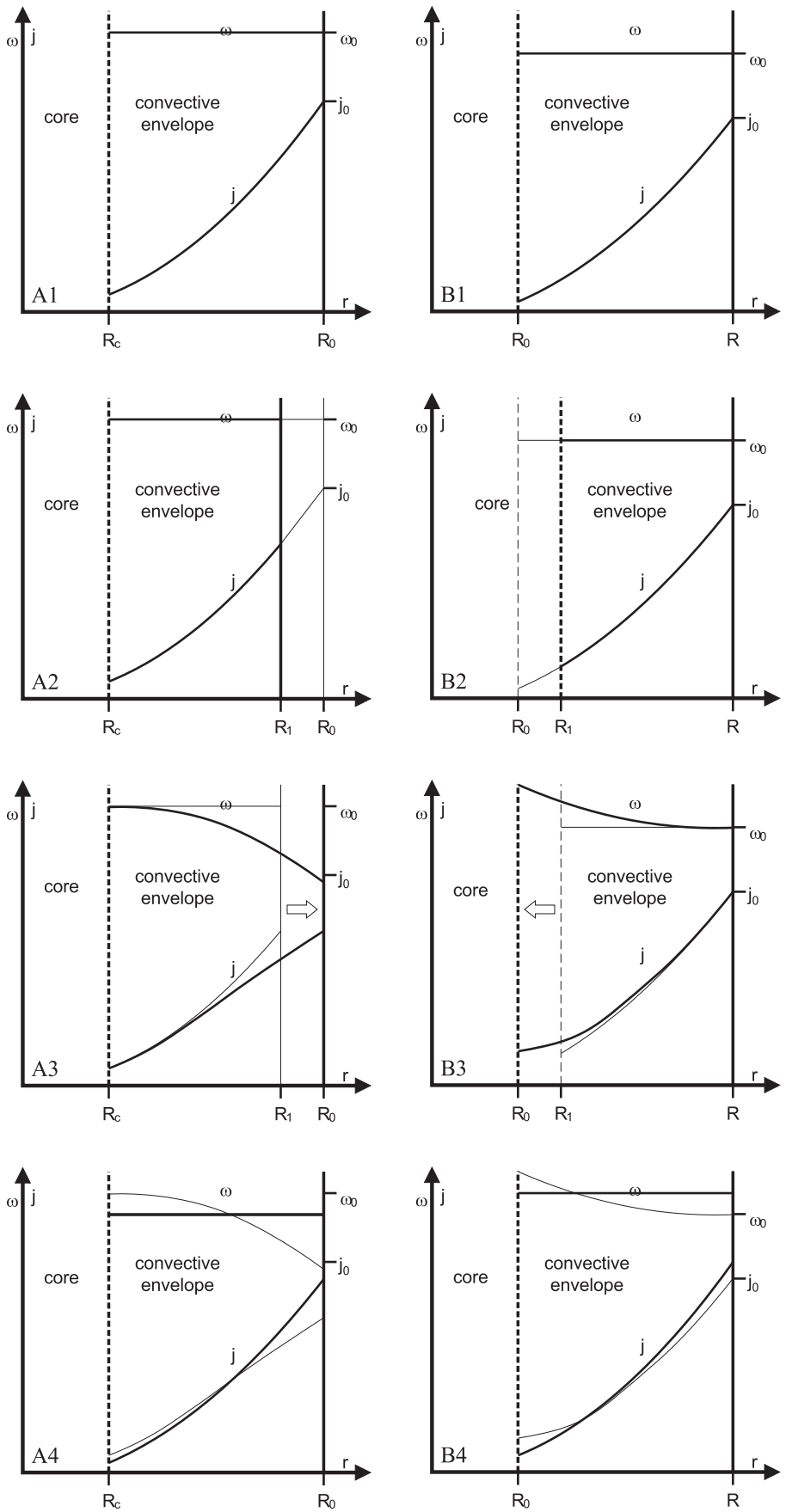

Figure 4.13: Mass loss from a rigidly rotating stellar envelope from the surface (case **A**: left panels) and through its lower boundary (case **B**: right panels). For illustration, the continuous process is split up into three steps. First (Panels **1→2**), mass is removed from the envelope, second, the envelope restores its original radial extent through expansion (Panels **2→3**), and third (Panels **3→4**), the angular momentum is redistributed such that rigid rotation is restored. It leads to spin-down (spin-up) and decrease (increase) of the specific angular momentum for the case of mass loss trough the upper (lower) boundary of the convective envelope. Thin lines show the state of the preceding step.

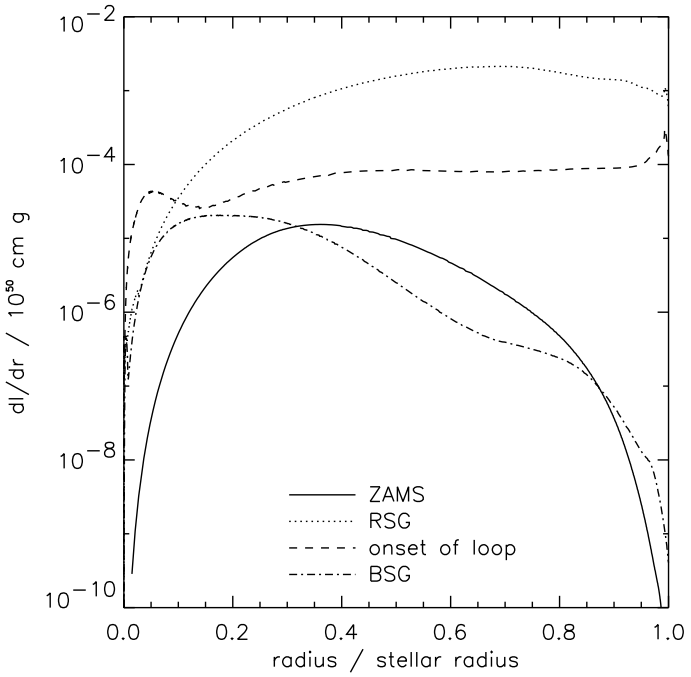

Figure 4.14: Moment of inertia per radius $\mathrm{d}I(r)/\mathrm{d}r$ as a function of radius (in units of the stellar radius) for four different stellar evolutionary stages of the $12\,\mathrm{M}_\odot$ Model E12. The solid line shows a ZAMS star, the dotted line a red supergiant (RSG) with an almost fully convective hydrogen-rich envelope, the dashed line a red supergiant just before the blue loop, and the dash-dotted line a blue supergiant (BSG) during the blue loop.

The density stratification in the envelope determines how much angular momentum is stored in the layers close to the surface relative to the total angular momentum of the envelope. An envelope structure which holds most of the mass close to its bottom favors high angular momentum loss rates, since this decreases $\langle r^2 \rangle_{\mathrm{env}}$. In red supergiants, on the other hand, $\langle r^2 \rangle_{\mathrm{env}}$ is rather high, since those stars store a large fraction of their mass in layers far from the stellar center, thus reducing χ.

This is demonstrated in Fig. 4.14, where the moment of inertia per unit radius, $\mathrm{d}I(r)/\mathrm{d}r = 8\pi r^4 \rho/3$ for spherical symmetry, is plotted as a function of the fractional radius for different types of stars. For a red supergiant with extended convective envelope the major contribution to the total moment of inertia I of the star at radii around $\sim 2/3\,R$ ($\chi \approx 9/4$), whereas at the zero-age main sequence matter at $\sim 1/3\,R$ dominates the moment of inertia of the star ($\chi \approx 9$). As main sequence stars can be approximated by rigid rotators (Zahn 1994), the whole star takes the rôle of the stellar envelope as far as the definition of χ in Eq. (4.2) is concerned. Therefore, the considered main sequence star loses its angular momentum four times more efficient than the red supergiant plotted in Fig. 4.14.

Two other cases are shown in Fig. 4.14, i.e., a red supergiant briefly before its transition into the blue supergiant stage, where I is dominated by the density inversion at the upper edge of the convective region, making the angular momentum loss from the envelope of this star quite inefficient ($\chi \approx 1.5$), and a blue supergiant during central helium burning in which the moment of inertia is concentrated even more towards the center of the star ($\chi \approx 30$) than for the ZAMS model. Thus, if the envelopes of blue supergiants stay close to solid body rotation — which is indicated by the time-dependent calculations in the present work — they experience a more efficient spin-down than main sequence stars.

However, since for blue supergiants the total moment of inertia, I, is smaller than for their progenitor main sequence stars, they may get closer to critical rotation (Sect. 2.4.2) if they keep their angular momentum. In particular may be in particular the case for metal poor massive stars. Those have much smaller mass loss and therefore angular momentum loss rates, and they can evolve from the main sequence directly into a long-lasting blue supergiant stage without an intermediate red supergiant phase (e.g., Schaller et al. 1992). In preliminary evolutionary calculations such stars are found to reach critical rotation as blue supergiants.

4.3.1.3 The spin-up of convective envelopes

The spin-up of convective envelopes which decrease in mass due to an outflow through their *lower* boundary can be understood in a similar way to the mass loss process discussed above. Again this process is split up into three discrete steps (see Panels B1-B4 on the right hand side of Fig. 4.13). Starting from a rigidly rotating envelope extending from R_0 to R (B1), the inner part of the convective envelope, located between R_0 and R_1, becomes radiative within some time Δt (B2). Then the envelope re-expands to its original size. As local angular momentum conservation is assumed in this step, it results in a spin-up of most of the convective envelope, which is weaker for the layers farther out. The outcome is a differentially rotating envelope which spins fastest at its bottom (B3). Since the envelope has to go back to rigid rotation, angular momentum is transported upward in the next step until this is achieved (B4). The star ends up with higher specific angular momentum in the whole convective envelope compared to the initial configuration.

As can be seen in Fig. 4.17, during the evolution of a red supergiant towards the blue part of the HR diagram the radial extent of the convective envelope remains approximately fixed while mass shells drop out of the convective region. If the convective envelope is imagined to consist of moving mass elements or blobs, the spin-up process can thus also be understood as follows. A blob, starting somewhere in the convective region will, as it approaches the lower edge of the convective envelope, decrease its specific moment of inertia and therefore has to lose angular momentum in order to remain in solid body rotation with the whole convective region. Angular momentum has to be transferred to rising blobs such that also they remain in solid body rotation. Mass elements leaving the convective envelope thus only remove small amounts of angular momentum from the convective region. Therefore, the average specific angular momentum of the remaining convective envelope will increase and it will spin up.

Replacing $j_{\rm surf}$, $i_{\rm surf}$, and R in Eq. (4.2) by $j_{\rm low}$, $i_{\rm low}$, and $R_{\rm low}$, the specific angular momentum, the specific moment of inertia and the radius at the lower edge of the convective envelope, respectively, one can define an efficiency of angular momentum loss through the lower boundary, $\tilde{\chi}$. Obviously the quantity has to fulfill the relation $\tilde{\chi} \leq 1$. Especially for those cases where χ is small, as, e.g., for the red supergiant envelopes under consideration here, $\tilde{\chi} \ll 1$ results.

The total change of specific angular momentum of the envelope $\langle j \rangle_{\rm env}$ by mass

loss through the upper and lower boundary is described by the equation

$$\frac{\mathrm{d}\ln\langle j\rangle_{\mathrm{env}}}{\mathrm{d}t} = \frac{\dot{M}\,(1-\chi) + \dot{M}_{\mathrm{low}}\,(1-\tilde{\chi})}{M_{\mathrm{env}}}\ , \tag{4.4}$$

where $\dot{M}_{\mathrm{low}}$ is the rate at which mass leaves the envelope through its lower boundary. For the sample Model `E12` it is $\tilde{\chi} \ll 1$, χ of order unity, and $\dot{M} \ll \dot{M}_{\mathrm{low}}$ during the red supergiant stage preceding the evolution off the Hayashi line, so that $\langle j\rangle_{\mathrm{env}}$ almost increases as M_{env} decreases,

$$\frac{\mathrm{d}\ln\langle j\rangle_{\mathrm{env}}}{\mathrm{d}\ln M_{\mathrm{env}}} \gtrsim -1\ . \tag{4.5}$$

This reflects the fact that angular momentum does not get lost efficiently from the convective envelope through its upper nor its lower boundary. The approximation $\tilde{\chi} \ll 1$ is hardly affected by the small variation of the lower boundary radius seen in Fig. 4.17. Thus, the convective envelope loses most of its mass but keeps a major part of the angular momentum.

When the convective envelope gets depleted in mass and the stellar radius decreases considerably, the global contraction of the stellar envelope results in an additional contribution to its spin-up. Still, mass elements drop out of the convective region (Fig. 4.17), but now the contraction leads to an increase of the rotational velocity, and the star can reach rotational velocities of the order of the break-up velocity (see below). However, the contraction does not contribute to the increase of the specific angular momentum at the surface. This is governed by the transport mechanism described above.

Finally, it should be noted that if the whole star remained rigidly rotating, e.g., due to the action of magnetic fields inside the star or by more efficient shear instabilities, its spin-up would occur very similar to the case described here. In that case, also mass shells from the core would transfer part of their angular momentum to layers above, which would make the spin-up somewhat more efficient. However, since in a red supergiant the mass elements lose the major part of their angular momentum to the convective envelope before they leave it, and the amount of angular momentum contained in the core is small anyway (Sect. 3.2.2), the additional spin-up will be small (Fig. 4.19, before blue loop).

4.3.2 Numerical simulation

In this section the spin-up mechanism is followed using the example of Model `E12`, a $12\,\mathrm{M}_\odot$ star of solar metallicity and an initial angular momentum of $1.1{\cdot}10^{52}\,\mathrm{erg\,s}$, which results in an equatorial rotational velocity of $\sim 200\,\mathrm{km\,s^{-1}}$ at the zero-age main sequence (Sect. 2.1.4).

During the main sequence evolution the star loses 25 % of its initial angular momentum and $0.23\,\mathrm{M}_\odot$ of its envelope due to stellar winds. After the end of central hydrogen burning, the star settles on the red supergiant branch after several $10^4\,\mathrm{yr}$ and develops a convective envelope of $8.3\,\mathrm{M}_\odot$ (Fig. E.9). During this phase it experiences noticeable mass loss ($\dot{M} \approx 8{\cdot}10^{-7}\,\mathrm{M}_\odot\,\mathrm{yr}^{-1}$), but the angular momentum loss

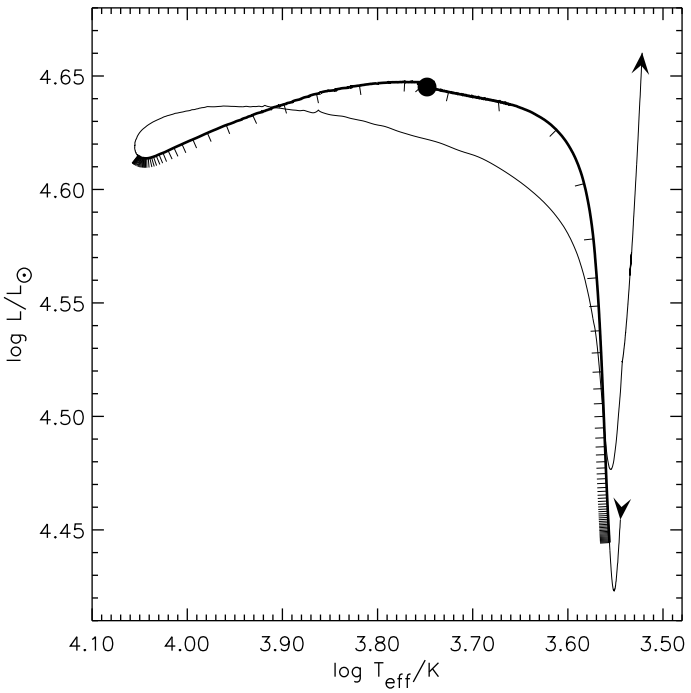

Figure 4.15: Track of the $12\,M_\odot$ star in the HR diagram during its blue loop. The two arrows indicate the direction of the evolution. The thick drawn part of the track corresponds to the time span shown in Figs. 4.18 and 4.19. The star spends 1 000 yr between two neighboring tick marks. The thick dot indicates where the star obtains its maximum mass and angular momentum loss rates; see the dotted line in Fig. 4.18.

per unit mass lost $\dot{J}/\dot{M} \approx 1.7{\cdot}10^{19}\,\mathrm{cm^2\,s^{-1}}$ is lower than during the main sequence phase (Sect. 4.3.1.2).

Shortly after core helium ignition, the bottom of the convective envelope starts to move up slowly in mass. About $4{\cdot}10^5$ yr later (at a central helium mass fraction of 65 %), the convective envelope mass decreases more rapidly. After another $\sim 5{\cdot}10^5$ yr it reaches a value of $\sim 3\,M_\odot$. Up to this time, the star has lost $0.75\,M_\odot$ as a red supergiant, and 43 % of the angular momentum left at the end of the main sequence.

At its largest extent in mass, the convective envelope contains a total angular momentum of $7.7{\cdot}10^{51}$ erg s, of which $1.7{\cdot}10^{51}$ erg s are contained in the lower $4.5\,M_\odot$. After those layers dropped out of the convective envelope, they have kept only $2.8{\cdot}10^{50}$ erg s whereas $4.4{\cdot}10^{51}$ erg s remain in the convective envelope; $3.0{\cdot}10^{51}$ erg s have been lost due to mass loss. Thus, on average the specific angular momentum of the lower part of the convective envelope is decreased by up to a factor of ~ 5, while that of the remaining convective envelope increased on average by a factor of 1.5, despite the angular momentum loss from the surface (Fig. 4.16, Eq. (4.4)). For comparison, the helium core contains never more than $\sim 1.5\,10^{50}$ erg s.

At this point of evolution, the transition to the blue sets in in Model `E12`. Within the next $\sim 25\,000$ yr another $2\,M_\odot$ drop out of the convective envelope which then comprises only about $1\,M_\odot$ but has still the full radial extent of a red supergiant. The ensuing evolution from the Hayashi line to the blue supergiant stage takes about 10 000 yr (Fig. 4.15). During this time, the angular momentum transport to the outermost layers of the star continues, tapping the angular momentum of those layers which drop out of the convective envelope.

The contraction of the star by a factor of $f \approx 10$ (Fig. 4.17) reduces the specific moment of inertia at the surface by $f^2 \approx 100$ and ω would be increased by the same factor if j were conserved locally. This would imply an increase of the equatorial

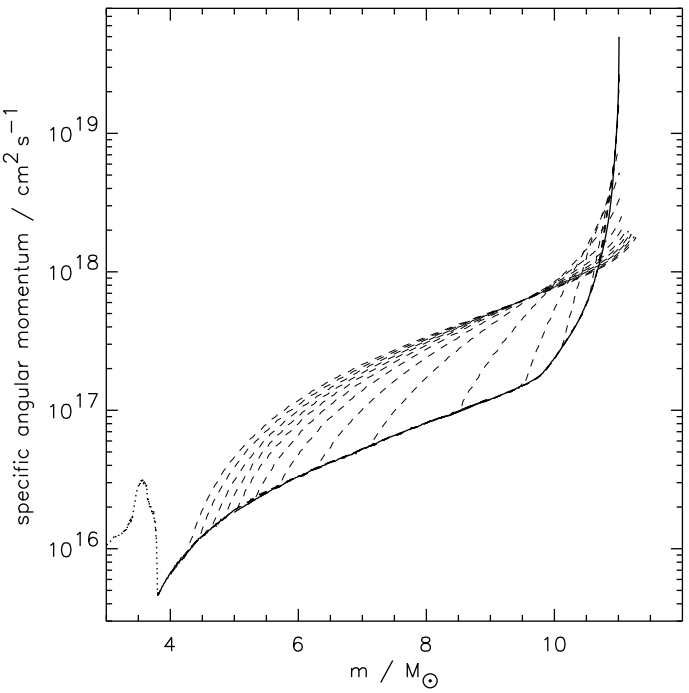

Figure 4.16: Evolution of the internal specific angular momentum profile in the hydrogen-rich envelope of the 12 $M_\odot$ Model E12 during the first part of core helium burning which is spent as a red supergiant. Dashed lines show specific angular momentum versus mass coordinate in the convective part of the envelope for different times, from 420 000 yr to 2 000 yr before the red $\rightarrow$ blue transition, with those reaching down to lower mass coordinates corresponding to earlier times and extending to higher mass coordinates, because the stellar mass decreases with time. The solid line shows the angular momentum profile for those mass zones which have dropped out of the convective envelope, which remains frozen in later on. The dotted line marks the angular momentum profile in the inner stellar region which is never part of the convective envelope.

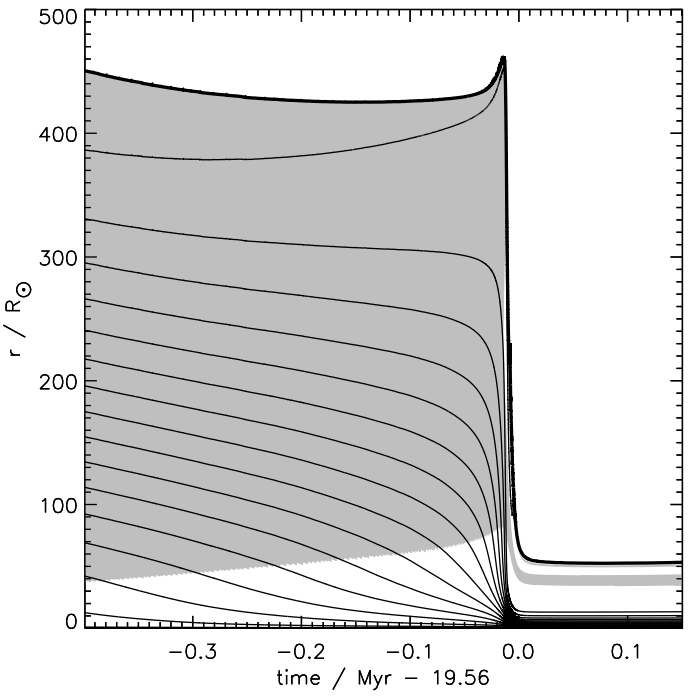

Figure 4.17: Evolution of the radii of different mass shells as a function of time for a period including the transition from the red to the blue supergiant stage of the 12 $M_\odot$ Model E12. The zero-point on the x-axis corresponds to the thick dot in Fig. 4.15 and corresponds roughly to the time of the red $\rightarrow$ blue transition. Except for the uppermost thick solid line, which corresponds to the surface of the star, the lines trace Lagrangian mass coordinates. The mass difference between the lines is 0.5 $M_\odot$. Grey shading indicates convective regions.

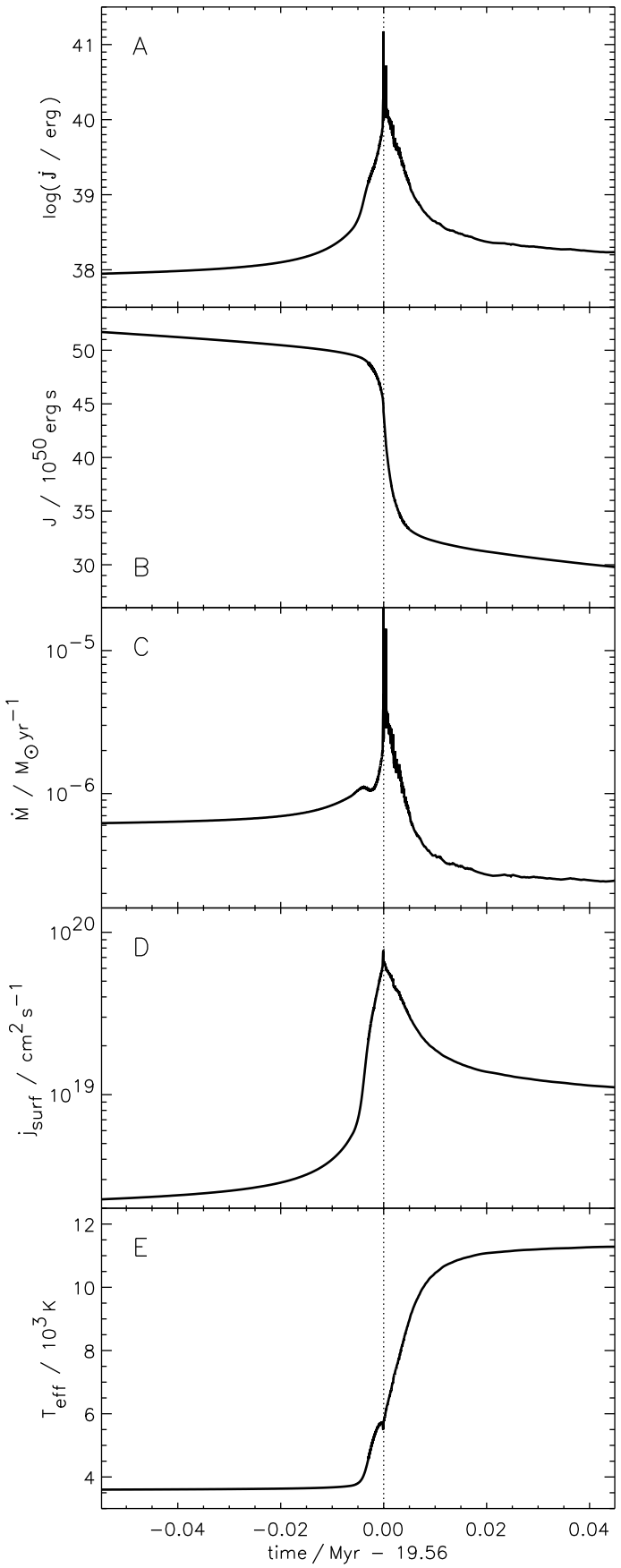

Figure 4.18: Evolution of characteristic stellar properties as function of time, during the first part of the blue loop of the $12\,M_\odot$ Model `E12` (Fig. 4.15). The time zero-point is defined as in Fig. 4.17 and is marked by the dotted line. Displayed are: the angular momentum loss rate $\dot{J}$ (Panel **A**), the total angular momentum J (Panel **B**), the mass loss rate $\dot{M}$ (Panel **C**), the specific angular momentum loss rate $j_{\rm surf} = \dot{J}/\dot{M}$ (Panel **D**), and the effective temperature $T_{\rm eff}$ (Panel **E**). See also Fig. 2.10.

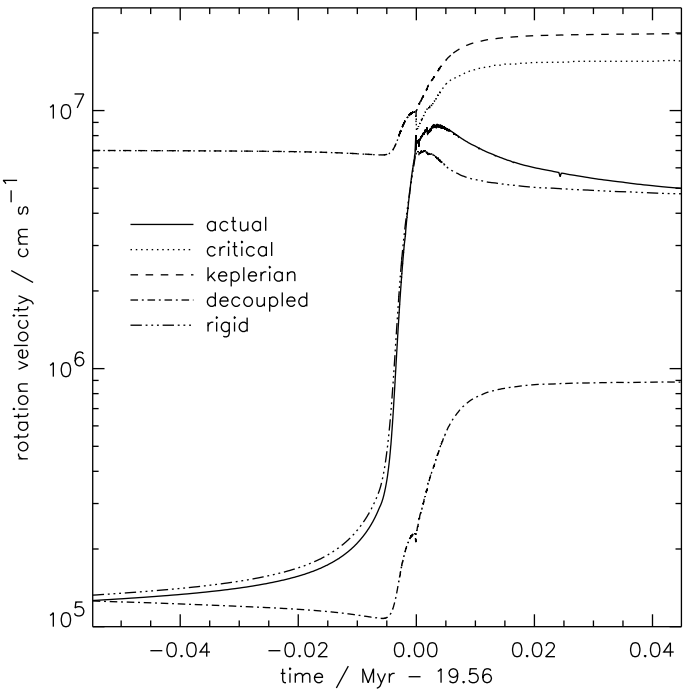

Figure 4.19: Equatorial rotational velocity as function of time (solid line) compared to the Keplerian (dashed line) and the critical (dotted line) rotation rate; the latter two are different by the factor $\sqrt{1-\Gamma}$. During the red supergiant phase it is $\Gamma \ll 1$ and the two lines coincide, while during the blue supergiant phase Γ rises to 0.4. The dash-dotted line shows the evolution of the surface rotation rate if there were no angular momentum transport in the convective envelope, and the dash-triple-dotted line shows how the surface rotation rate would evolve if the whole star would maintain rigid rotation.

rotational velocity by a factor of ~ 10 (Fig. 4.19, "decoupled"). The true increase in the rotational velocity is one order of magnitude larger, due to the spin-up effect described in Sect. 4.3.1, and it would be even larger if the star would not arrive at the Ω-limit (see Fig. 4.19) and lose mass and angular momentum at an enhanced rate.

For local conservation of angular momentum Ω scales as $\Omega \propto 1/\sqrt{(1-\Gamma)R}$ (see Eq. (2.72)). A value of $\Gamma \approx 2{\cdot}10^{-3}$ is found on the red supergiant branch in Model `E12` calculation, and $\Gamma \approx 0.4$ for the blue supergiant stage. This by itself would increase Ω by a factor of ~ 3.9 during the red $\rightarrow$ blue transition. Actually, Ω changes from ~ 0.01 at the red supergiant branch at the beginning of central helium burning to $\Omega \approx 1$ — to critical rotation — at the red $\rightarrow$ blue transition, i.e., by a factor ~ 100, despite significant mass and angular momentum loss.

At an effective temperature of $\sim 6\,000$ K the Eddington Factor Γ at the surface (as defined in Sect. 2.4.1) rises from a few times 10^{-3} to ~ 0.4, mainly due to an increase in the opacity; the luminosity remains about constant. Around 40 % of the angular momentum of the star are then concentrated in the upper $0.01\,M_\odot$. Since Ω becomes close to one, the mass loss rate rises to values as high as several $10^{-5}\,M_\odot\,\mathrm{yr}^{-1}$ (Fig. 4.18) in order to keep the star below critical rotation, with the result that these layer are lost within a few 1 000 yr. This is by far the most dramatic loss of angular momentum, i.e., the highest value of $\dot{J}$, the star ever experiences. The specific angular momentum loss $\dot{J}/\dot{M}$ reaches a peak value of $7.7\,10^{19}\,\mathrm{cm}^2\,\mathrm{s}^{-1}$ (Fig. 4.18).

After arriving at the blue supergiant stage, the star still experiences a high angular momentum loss rate for some time, since the major part of the stellar angular momentum is still concentrated in the vicinity of the surface. Interestingly, the star now even spins faster than when rigid rotation of the whole star were

assumed (Fig. 4.19), because within the radiative envelope of the blue supergiant the angular momentum is not transported downward efficiently. However, due to mass loss, this deviation does not persist long.

Due to the long duration of the blue supergiant phase, several 10^5 yr in comparison to the 10^4 yr the red $\rightarrow$ blue transition takes, the total angular momentum J is reduced by another factor ~ 3 although both, the mass and the angular momentum loss rate, become smaller with time. In total, after the blue loop the star has ~ 5 times less angular momentum than before, and thus red supergiants which underwent a blue loop rotate significantly slower than those which did not. For example, the general trend of decrease of total angular momentum in the pre-collapse models with increasing mass in Table 3.2 is broken between Model `E12` and Model `E15` which does not experience a blue loop.

4.3.3 Discussion and different scenarios

The mechanism to spin-up stellar envelopes presented above enhances the specific angular momentum in the surface layers of the star by some factor (Sect. 4.3.2). A question to be considered separately is the origin of the angular momentum, and also in which cases critical rotation is reached. For single stars, the available angular momentum seems to be limited to that of the ZAMS star, reduced by the angular momentum lost during its evolution. A way to supply a considerable amount of angular momentum to the star would be the capture of a companion star or planet (Soker 1996; Podsiadlowski 1998). This might occur when the star first becomes a red supergiant. The resulting configuration would then have a much higher angular momentum than a normal single star, but still, due to the high moment of inertia of the supergiant, it could initially be far away from critical rotation. Due to the spin-up mechanism described here, such a star might then approach critical rotation even before the transition into a blue supergiant.

The mechanism to spin-up stellar envelopes (Sect. 4.3.1), which is applied to a post-red supergiant $12\,M_\odot$ star, Model `E12`, in Sect. 4.3.2, may operate in all evolutionary phases during which stars evolve from the Hayashi-line towards the hotter part of the HR diagram. These comprise the transition of pre-main sequence stars from their fully convective stage to the main sequence, the transition of low and intermediate mass stars from the asymptotic giant branch (AGB) to central stars of planetary nebulae, the blue loops of stars in the initial mass range $\sim 3\,M_\odot \ldots \sim 25\,M_\odot$, and the transition of massive red supergiants into Wolf-Rayet stars. For all four phases, observational evidence for axisymmetric circumstellar matter exists.

A high value of Ω during the evolution off the Hayashi line can be expected to have notable influence not only on the mass and angular momentum loss rate as in the case studied in Sect. 4.3.2, but also on the geometry of the wind flow. At present, theoretical predictions of the latitudinal dependence of stellar wind properties for rapidly rotating stars are ambiguous. Bjorkman & Cassinelli (1993) have proposed that angular momentum conservation of particles in a pressure free wind which is driven by purely radial forces leads, for sufficiently large values of Ω, to high ratios of equatorial to polar wind density, i.e., to disks or disk-like configurations. Owocki

et al. (1996) found that this might no longer be the case when the non-radial forces occurring in hot star winds are accounted for. For cooler stars, the prospects of disk formation may thus be better (see also Ignace et al. 1996). To discus the geometry of the winds of the models is beyond the scope of this work; however, is has to be pointed out that the maximum values of Ω and $\dot{J}/\dot{M}$ occur at about $T_{\rm eff} \simeq 6\,000\,{\rm K}$ (see Sect. 4.3.2 and Fig. 4.18), so that an equator-to-pole wind density ratio larger than one may still be justified.

4.3.3.1 Blue loops during or after core helium burning

An interesting example where the spin-up mechanism described in this work almost certainly played a rôle is the progenitor star of SN 1987A. In fact, the SN 1987A progenitor is the only star which one is reasonably sure performed a blue loop, in this case after core helium exhaustion (Arnett et al. 1989).

The structures observed around SN 1987A seem to be rotationally symmetric with a common symmetry axis, which may suggest that rotation has played a major rôle in their formation. The inner of the three rings is currently explained by the interaction of the blue supergiant wind with the wind of the red supergiant precursor (Chevalier 1996). However, this interaction would result in a spherical shell in case of spherically symmetric winds. To understand the ring structure of the inner interaction region, and maybe also the two outer rings, significant rotation appears therefore to be required (Martin & Arnett 1995), which may be provided by the spin-up mechanism. It may be noted that for this mechanism to work it is insignificant what actually triggered the blue loop; i.e., it would work as well for single star scenarios with a final blue loop (Langer 1991b; Meyer 1997; Woosley et al. 1998) or for binary merger scenarios which predict a final red $\rightarrow$ blue transition of the merger star (Podsiadlowski 1998).

One does not expect to find ring nebulae frequently around blue supergiants (Brandner et al. 1997), since the time-scale on which Model `E12` (Sect. 4.3.2) shows very high surface rotation rates is rather small compared to the typical lifetime of a blue supergiant (Langer 1991a), and because such rings are quickly eroded by the blue supergiant wind. SN 1987A is an exception, since there the transition to the blue happened only short time ago (i.e., the supernova exploded only shortly after the transition). However, a certain type of B supergiants, the B[e] stars, show emission line features which might be due to a circumstellar disk (Zickgraf et al. 1996). The location of the less luminous subgroup of B[e] stars in the HR diagram (Gummersbach et al. 1995) is, in fact, consistent with a blue loop scenario for their evolution. That is, their disks might be produced by the spin-up mechanism described here (see also Langer & Heger 1998).

4.3.3.2 Red supergiant $\rightarrow$ Wolf-Rayet star transition

The transition of massive, mass losing red supergiants into Wolf-Rayet stars is the massive star analogue of the AGB $\rightarrow$ post-AGB star transition. It occurs when the mass of the hydrogen-rich envelope is reduced below a critical value (e.g., Schaller et al. 1992) and should not be confused with the blue loops discussed in Sect. 4.3.3.1.

As in the post-AGB case (Sect. 4.3.3.4), the spin-up mechanism can be expected to work. Unlike in the case discussed in Sect. 4.3.2, the major part of the envelope is lost due to stellar winds before the red supergiant → Wolf-Rayet star transition, with the consequence of considerable angular momentum loss. Therefore, it may be more difficult for the star to reach critical rotation during the contraction.

However, there are signs of asphericity in the ring nebula NGC 6888 around the Galactic Wolf-Rayet star WR 136 which has been interpreted as swept-up red supergiant wind shell by García-Segura & Mac Low (1995) and García-Segura, Langer & Mac Low (1996). Also, Oudmaijer et al. (1994) report on bi-polar outflows from IRC+10420, a massive star just undergoing the red-supergiant → Wolf-Rayet star transition. IRC+10420 is currently an F type star, i.e., it has an effective temperature at which the maximum effect of the spin-up mechanism discussed here is expected (Sect. 4.3.2). Therefore, in the absence of a binary companion, the spin-up mechanism may yield the most promising explanation for the bipolar flows.

4.3.3.3 Pre-main sequence evolution

As mentioned in Sect. 2.1.4, the initial models in this work are started from a fully convective pre-main sequence configuration. The spin-up mechanism found for the post-red supergiant stage should be expected to be also present in the contraction phase towards the main sequence. An analysis of this evolutionary phase using the example of Model `E12` shows, in fact, that it is present, although the efficiency of the spin-up is found to be somewhat smaller. During that part of the pre-main sequence contraction phase where the convective region retreats from the center of the star to its surface, the star would increase its equatorial rotational velocity by a factor of ~ 3 if angular momentum were conserved locally, but it is spun-up by a factor of ~ 10. That is, the spin-up mechanism described in Sect. 4.3.1 results in an additional increase of the rotational velocity by a factor of ~ 3. This is not enough to bring the any of the stars in the present work to critical rotation in this phase. However, if the initial rotation rate were larger, a phase of critical rotation during the pre-main sequence stage would well be possible.

While a fully convective pre-main sequence stage may not be realistic for massive stars and is just assumed here for mathematical convenience, pre-main sequence stars of low and intermediate mass are supposed to evolve through a fully convective stage (Palla & Stahler 1991). During the transition from this stage to the main sequence, the spin-up mechanism described in the present work might operate. Pre-main sequence stars in the corresponding phase, i.e., past the fully convective stage but prior to core hydrogen ignition, are often found to have disks. They correspond to the T-Tauri stars at low mass (e.g., Koerner & Sargent 1995) and to central stars of Herbig-Haro objects at intermediate mass (e.g., Marti, Rodriguez & Reipurth 1993). However, the disks are usually interpreted as remnants of the accretion process which built up the star. Since pre-main sequence stars are often found to be rapid rotators (Walker 1990), one could speculate about a possible contribution to the disk due to decretion from the star reaching critical rotation due to spin-up (Krishnamurthi et al. 1997).

4.3.3.4 Post-AGB evolution

Low and intermediate mass stars leave the AGB when the mass of their hydrogen-rich envelope decreases below a certain value. When this happens, the envelope deflates, the stellar radius decreases, and the energy transport in the envelope changes from convective to radiative. The spin-up mechanism described in Sect. 4.3.1 can be expected to operate in this situation, as in the red supergiant → Wolf-Rayet star transition (Sect. 4.3.3.2).

Whether or not post-AGB stars can reach critical rotation due to this spin-up is not clear. Certainly, the rapid mass loss during the evolution on the AGB spins the envelope down according to the mechanism sketched in Fig. 4.13. The ratio of the rotation rate to the critical rotation rate Ω may be further affected by random kicks due to asymmetric mass loss, which may keep the envelope at some level of rotation (Spruit 1998), or by transport of angular momentum from the core to the envelope, which may be efficient during the thermal pulses, and by the evolution of the critical rotation rate, which depends on the Eddington factor, Γ, and thereby on the opacity coefficient (García-Segura et al. 1998).

Clearly, the spin-up mechanism described in Sect. 4.3.1 may help to bring post-AGB stars — or more specific: stars which just left the AGB, i.e., central stars of protoplanetary nebulae — closer to critical rotation. It may play a rôle in explaining axisymmetric flows which are often observed in central stars of protoplanetary nebulae (Kwok 1993) and the shapes of bi-polar planetary nebulae (Schwarz et al. 1992; Stanghellini, Corradi & Schwarz 1993; García-Segura et al. 1998).

4.4 Pulsations

According to the standard picture, based on stellar evolution calculations (see also, e.g., Schaller et al. 1992) and on the interpretation of Type II supernova light curves (Eastman et al. 1994), not only the stellar models investigated in the present work, but most presupernova stars are red supergiants with massive hydrogen-rich envelopes. In this section a property of the structure of this majority of the presupernova stars, which is usually neglected, is discussed: they are pulsationally unstable. In particular, the possibility for this instability to become violent several 10 000 yr before the supernova explosion is suggested, with prominent consequences for the envelope structure of the exploding star as well as the distribution of the circumstellar matter at the time of the supernova event.

Observations of long-period variables (LPV) in the Galaxy and particularly in the Magellanic Clouds (Wood, Bessell & Fox 1983; Wood et al. 1992; Whitelock et al. 1994) reveal two distinct groups of pulsating cool stars: intermediate mass stars on the asymptotic giant branch with zero-age main sequence masses of $M_{\rm ZAMS} \lesssim 8\,{\rm M}_\odot$, and red supergiants, massive stars with $M_{\rm ZAMS} \gtrsim 8\,{\rm M}_\odot$. While the periods of the visible LPVs are generally shorter than 1 000 days, longer periods are found in OH/IR sources (Engels et al. 1983; Le Bertre 1993; Jones et al. 1994). Most of the OH/IR sources seem to lie on the period-luminosity relation observed for AGB stars (Whitelock, Feast & Catchpole 1991; Feast et al. 1989; Groenewegen & Whitelock

1996). Interestingly enough, some of them show bolometric luminosities much higher than expected for Miras. It might be attempted to associate these sources with red supergiants. However, known pulsating red supergiants show generally small amplitudes whereas the long-period OH/IR sources are usually associated to high amplitudes, as expected for AGB stars (Wood et al. 1992). Therefore, it is puzzling that the most luminous OH/IR-sources found by Le Bertre (1993) show in fact very large amplitudes.

Recently, a theoretical analysis of red supergiant evolution and pulsations in the Large Magellanic Cloud has been performed by Li & Gong (1994). By coupling linear stability analysis and evolutionary models, they could follow the evolution of stars from $15\,M_\odot$ to $30\,M_\odot$ in the period-luminosity diagram. They concluded that red supergiant models can reproduce the observed period-luminosity (P-L) relationship of LPVs in the Large Magellanic Cloud, which is, however, on the red supergiant branch restricted to periods below ~ 900 days.

In this section the pulsational properties of the red supergiant models of solar composition, as they result for the rotating massive stars of the present work, are analyzed for their linear pulsation properties (Heger et al. 1997). Using the hydrodynamic stellar evolution code STERN also allows to follow the pulsations of the models in the non-linear regime. The physical effects of stellar rotation on the evolution, the increase of the core sizes, of the luminosity, and of the mass loss, results in a remarkable increase of the ratio of luminosity to mass L/M of the models on the main sequence and later on (Sect. 4.2.1). More dramatically, the L/M ratio increases at and beyond central helium exhaustion, as it also does for non-rotating stars. It is shown that this property leads to a strong increase of the growth rate of the fundamental mode, which may have considerable consequences for the presupernova structure of the stars and of the circumstellar matter. Finally, the results are compared with recent observations of luminous OH/IR sources and with supernova observations. The results presented in this section can also be found in Heger et al. (1997).

4.4.1 Model properties

The main effect of rotation in relation to the pulsational properties of the red supergiants is the increased core masses causing a larger luminosity during the advanced evolution, an effect which is produced similarly by efficient convective core overshooting (e.g., Stothers & Chin 1992). The dynamical effect of rotation on the structure is found to be negligible and does not affect the pulsational properties of the models in the red supergiant stage. The ratio of rotational velocity to the critical value at the surface is below $\sim 0.3\,\%$ for all red supergiant models considered for the pulsational analysis.

The four Models `E10`, `E12`, `E15`, and `E20` with initial masses of $10\,M_\odot$, $12\,M_\odot$, $15\,M_\odot$, and $20\,M_\odot$, and an initial equatorial rotational velocity of about $200\,\mathrm{km\,s^{-1}}$ (see Sect. 2.1.4 and Tables 2.3 and 4.5) are investigated. Due to the assumed insensitivity of the rotationally induced mixing to μ-gradients and the resulting large helium cores, these models show a higher L/M ratio than the corresponding models

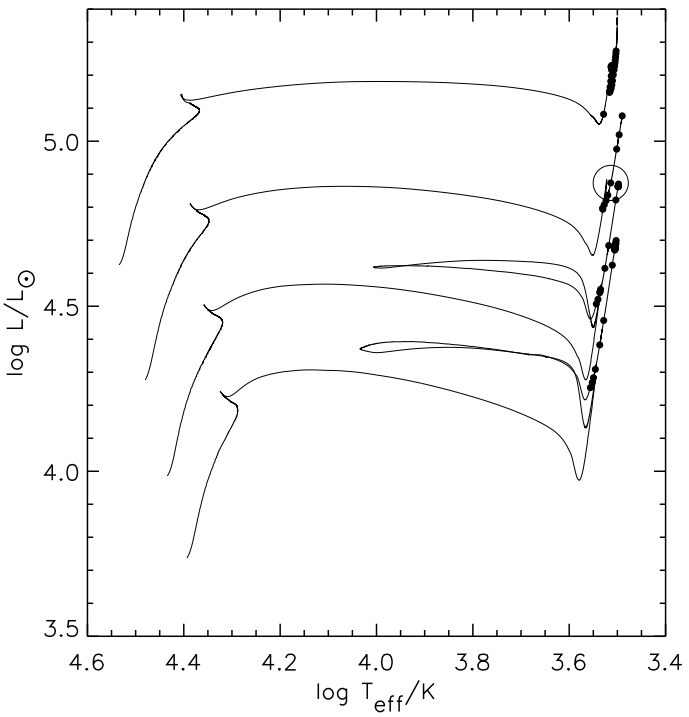

Figure 4.20: Evolutionary tracks of the $10\,M_\odot$, $12\,M_\odot$, $15\,M_\odot$ and $20\,M_\odot$ stars Models `E10`, `E12`, `E15`, and `E20` from the ZAMS to central neon exhaustion. Evolutionary time-points for which a linear pulsation analysis has been performed (Sect. 4.4.2) are marked by dots. The circle marks the initial model investigated in Sect. 4.4.3; see Figs. 4.7, 4.22, and 4.24.

model	`E10`	`E12`	`E15`	`E20`
$M_{\rm initial}/\,M_\odot$	10	12	15	20
$\tau_{\rm H}/\,$Myr	25.5	18.9	13.8	9.6
$\tau_{\rm He}/\,$Myr	2.86	1.99	1.22	0.64
$\tau_{\rm red}/\,$Myr	0.39	0.46	1.23	0.66
$Y_{\rm surf}$	0.39	0.40	0.42	0.45
$\log(L/\,L_\odot)$	4.66	4.86	5.05	5.36
$T_{\rm eff}/\,$K	3203	3152	3107	3164
$R/R_\odot$	702	903	1161	1614
$M_{\rm final}/M_\odot$	9.2	10.4	10.9	11.0
$M_{\rm env}/M_\odot$	6.4	6.7	5.8	3.3
$M_{\rm He}/M_\odot$	2.8	3.6	5.1	7.7
$\tau_{\rm KH,env}/$yr	28.7	17.1	7.7	1.5

Table 4.5: Model name, initial mass $M_{\rm initial}$, time-scales of hydrogen burning $\tau_{\rm H}$, helium burning $\tau_{\rm He}$, and lifetime at $T_{\rm eff} < 5\,000\,$K before the supernova explosion $\tau_{\rm red}$. Furthermore, properties of the last computed model of each sequence are given (Fig. 4.20): mass fraction of helium at the surface $Y_{\rm surf}$, luminosity L, effective temperature $T_{\rm eff}$, radius R, final stellar mass $M_{\rm final}$, helium core mass $M_{\rm He}$, and Kelvin-Helmholtz time-scale of the hydrogen-rich envelope $\tau_{\rm KH,env}$. All these models have a ZAMS rotational velocity of $\sim 200\,{\rm km\,s^{-1}}$.

of the "`B`" series (see Tables 2.3 and 3.2). The evolutionary tracks of the models investigated for pulsations in the HR diagram are shown in Fig. 4.20, starting at hydrogen-ignition (see also Fig. 4.7).

The evolution of the models in the red supergiant stage (Fig. 4.20) is qualitatively similar to that obtained by previous calculations including overshooting (Schaller et al. 1992; Stothers & Chin 1992). The total mass lost by the stars is dominated by red supergiant winds. Due to the larger luminosity during central helium burning compared to the tracks of Schaller et al. (1992), somewhat smaller final masses are obtained (Table 4.5); they are comparable to those obtained by Meynet et al. (1994). The effect of rotation on the final L/M ratio can be summarized as follows: it results in an increase of the luminosity due to a larger helium core, and the

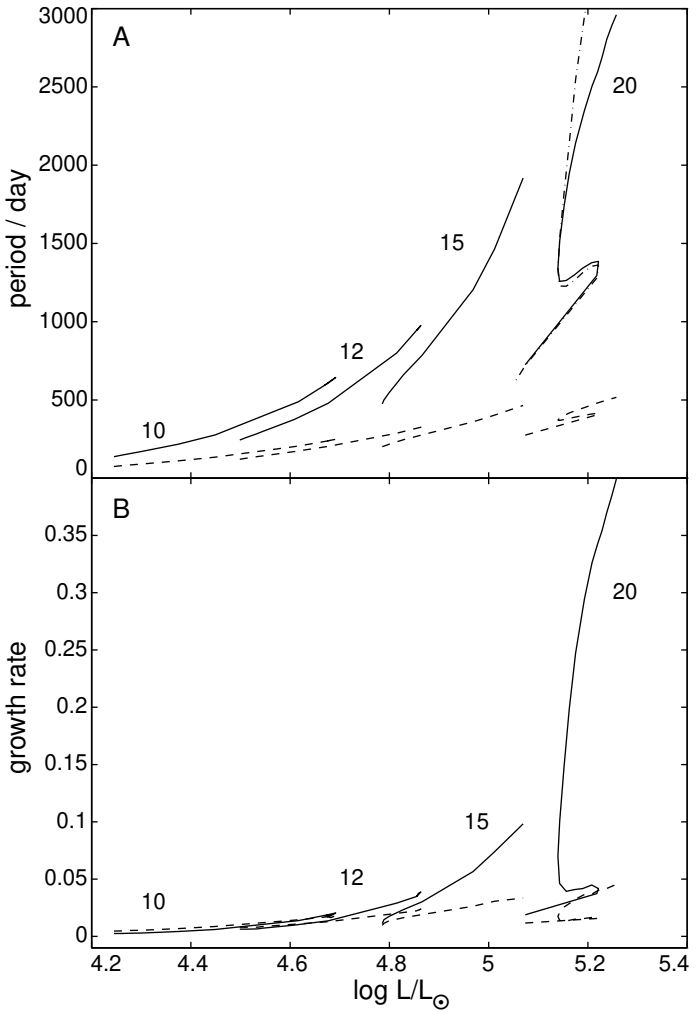

Figure 4.21: Period $\mathcal{P}$ (Panel **A**) and growth rate η (Panel **B**) of the pulsations found in the stellar models of the $10\,M_\odot$, $12\,M_\odot$, $15\,M_\odot$ and $20\,M_\odot$ stars (Models `E10`, `E12`, `E15`, and `E20`, respectively) marked in Fig. 4.20. The full drawn lines correspond to the fundamental mode, the dashed lines to the first overtone. The dash-dotted line in Panel **A** corresponds to the adiabatic period of the $20\,M_\odot$ star.

correspondingly higher mass loss rate yields a smaller final mass; both properties translate into a higher L/M value (Sect. 4.2.1), which is a key parameter for the pulsations (Sect. 4.4.2).

4.4.2 Linear stability analysis

Heger et al. (1997) performed a linear non-adiabatic stability analysis of the red supergiant models marked by dots in Fig. 4.20. For the two lower-mass stars of $10\,M_\odot$ (Model `E10`) and $12\,M_\odot$ (Model `E12`), the stability analysis is started after they returned from their blue loop (Fig. 4.20) near the end of central helium burning. For the $15\,M_\odot$ (Model `E15`) and $20\,M_\odot$ (Model `E20`) stars, the analysis begins at a central helium mass fraction of 0.43 and 0.97, respectively.

The radial pulsation code used for this study is described in Jeannin et al. (1996). The analysis is based on complete stellar models, i.e., the whole stellar structure from the center to the surface is taken into account. The convective flux is assumed to be frozen in for the stability analysis (Sect. 4.4.3).

The linear pulsation code assumes that the stellar models are in complete ther-

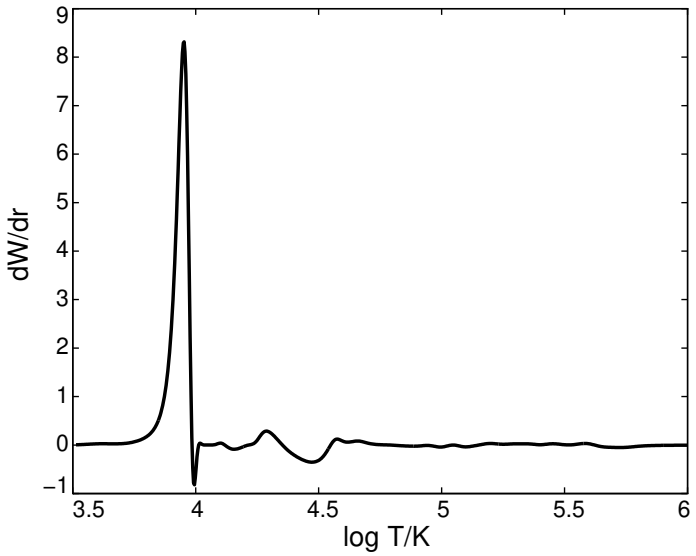

Figure 4.22: Differential work (in arbitrary units) as a function of temperature for the $15\,\mathrm{M}_\odot$ Model `E15` marked by a circle in Fig. 4.20 and used as initial model in Fig. 4.24. It is characterized by $\log L/\mathrm{L}_\odot = 4.89$, $T_{\rm eff} = 3260\,\mathrm{K}$ and $M \simeq 11\,\mathrm{M}_\odot$, and indicated by a circle in Fig. 4.20. Excitation zones correspond to $\mathrm{d}W/\,\mathrm{d}r > 0$.

mal and hydrostatic equilibrium. Although the evolutionary models include rotation and slightly depart from thermal equilibrium, the consistency of this approximation is verified. Rotation has no dynamical effect on the red supergiant pulsations, because of the dramatic spin-down of the star when it becomes a red supergiant (but see Sect. 4.3). Since the oscillations take place only in the envelope, they are not affected by the rotation of the helium core. For each model at a given mass, luminosity, and effective temperature, static envelope models with the same input physics (opacity, mixing length, composition) are constructed. The pulsation properties of the envelopes are then compared to those of the corresponding evolutionary model. In all cases, the differences are less than 5 % for the period. The analysis is stopped for the brightest models, when the decreasing evolutionary time-scale starts to invalidate the above approximation.

The periods $\mathcal{P}$ and relative growth rates η (defined as minus the ratio of the imaginary part of the eigenfrequency σ to its real part, adopting a time dependence of the form $\exp(\mathbf{i}\sigma t)$, where here $\mathbf{i}$ is the imaginary unit $\sqrt{-1}$) of the two lowest-order modes of the four stellar sequences are displayed in Fig. 4.21. Typical values of the period for the fundamental mode range between 200 days and 3 000 days. The periods found for the first overtone do not exceed 500 days in any case. Both modes are unstable ($\eta > 0$) for all models investigated, and the growth rates increase with luminosity for a given ZAMS mass. The higher the ZAMS mass, the higher the maximum value of the growth rate reached. The growth rate derived for the fundamental mode is always larger than that of the first overtone. The latter remains systematically smaller than 0.05, whereas a maximum value of 0.4 for the fundamental mode is obtained in the $20\,\mathrm{M}_\odot$ case. For the $15\,\mathrm{M}_\odot$ model, the fundamental mode growth rate increases from ~ 0.01 to ~ 0.1. It remains smaller than 0.04 for the $10\,\mathrm{M}_\odot$ and $12\,\mathrm{M}_\odot$ stars (Fig. 4.21).

The excitation mechanism appears to be related to the traditional κ-mechanism as indicated by the work integral W of the models. The driving of the pulsation is essentially provided in the hydrogen ionization zone. This is illustrated in Fig. 4.22

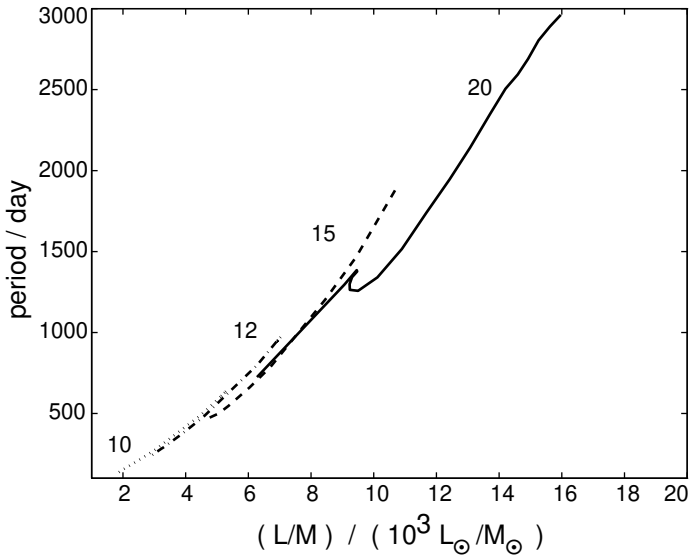

Figure 4.23: Period of the fundamental mode (in days) as a function of the ratio of luminosity to mass L/M. The different curves correspond to different ZAMS masses as indicated.

where $\mathrm{d}W/\mathrm{d}r$ is displayed as a function of temperature for the $15\,\mathrm{M}_\odot$ Model `E15` at the end of central helium burning.

The large values of the periods and growth rates mentioned above can be related to the large L/M values obtained from the evolutionary calculations. This behavior is illustrated in Fig. 4.23, which shows the variation of the period $\mathcal{P}$ with L/M for the four investigated sequences. The variation $\mathcal{P} \propto L/M$ is connected to the properties of convective pulsating *envelopes* which obey a period-radius relation $\mathcal{P} \propto R^2/M$ rather than the canonical $\mathcal{P} \propto \sqrt{R^3/M}$. This has been shown analytically by Gough, Ostriker & Stobie (1965) for polytropic envelopes of index $n = 3/2$, corresponding to a fully convective structure. Since the effective temperature varies hardly on the red supergiant branch, the variation $\mathcal{P} \propto R^2/M$ is equivalent to $\mathcal{P} \propto L/M$.

The relevant quantity for the growth or decay of pulsations, connected to the growth rate, is the Kelvin-Helmholtz or thermal time-scale of the hydrogen-rich envelope $\tau_{\mathrm{KH,env}} \propto MM_{\mathrm{env}}/LR$. It governs the degree of non-adiabaticity in the envelope and thus the heat exchange with the pulsations. In the models investigated here, $\tau_{\mathrm{KH,env}}$ decreases as the models get brighter (and lose mass), and for the brightest models $\tau_{\mathrm{KH,env}}$ becomes very close to the fundamental period (see Fig. 4.26 below). Non-adiabatic effects are thus important and are responsible for the high values of the growth rates found as the luminosity increases and $\tau_{\mathrm{KH,env}}$ decreases (see also Ostlie & Cox 1986).

The large fundamental to first overtone period ratio $\mathcal{P}_0/\mathcal{P}_1$ displayed by the models (Fig. 4.21) can be directly related to the internal structure of the stars. With increasing luminosity, the star tends toward a dynamically unstable configuration with the mean value of the adiabatic exponent[1] $\Gamma_1 \approx 4/3$. In this case, the solution of the linear adiabatic wave equation (Cox 1980) shows that the square of the adiabatic pulsation frequency becomes negative and the adiabatic period becomes mathematically infinite. The divergence of the adiabatic period for the fundamental mode is

[1] Γ_1 id defined by $\left(\frac{\mathrm{d}\ln P}{\mathrm{d}\ln \rho}\right)_{\mathrm{ad}}$. See also Sect. 2.2.1.1.

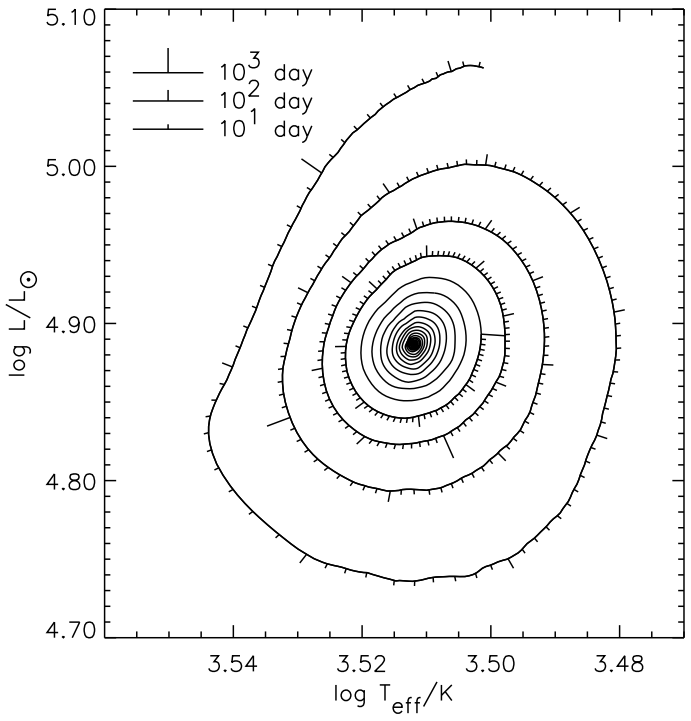

Figure 4.24: Growing pulsational instability of a $\sim 11\,\mathrm{M}_\odot$ red supergiant model (evolved from the $15\,\mathrm{M}_\odot$ Model `E15`) at the end of central helium burning, traced by STERN. The period of the oscillation is about 800 days, the Kelvin-Helmholtz time-scale of the stellar envelope is roughly 30 yr. About 75 pulsation cycles are followed.

illustrated in Fig. 4.21A for the $20\,\mathrm{M}_\odot$ sequence. As long as the non-adiabatic effects remain small, the non-adiabatic period is rather close to the adiabatic value and follows the same behavior. When the non-adiabatic effects become strong, however, the non-adiabatic period starts to depart from the adiabatic solution (Fig. 4.21A).

4.4.3 Non-linear computation of the pulsations

Since STERN is a hydrodynamic stellar evolution code, it is therefore able to follow instabilities on a dynamical time-scale. Usually, those instabilities are not found because the evolutionary time steps used are large compared to the dynamical time-scale of the stars. However, during the late nuclear burning phases (carbon shell burning and beyond), nucleosynthesis imposes extremely small time steps, comparable to or even smaller than the dynamical time-scale. That is, only the combination of hydrodynamic stellar evolution calculations of mass losing red supergiants in late nuclear burning stages is responsible for the discovery of the strong instability described here.

Fig. 4.24 displays, in the HR diagram, the growth of the pulsational instability of the $15\,\mathrm{M}_\odot$ Model `E15` at the end of central helium burning (0.2 % helium left in the center). The initial evolutionary model for the non-linear pulsation analysis, indicated by a circle in Fig. 4.20, is characterized by $\log L/\mathrm{L}_\odot = 4.89$, $T_{\mathrm{eff}} = 3\,260\,\mathrm{K}$ and $M \simeq 11\,\mathrm{M}_\odot$. The first 50 pulsation cycles give a period $\mathcal{P} \simeq 800$ days and an estimated growth rate $\eta = 0.033$, corresponding to the fractional increase of the radius amplitude per pulsation cycle. These values are in excellent agreement with those found for the fundamental mode by the linear stability analysis performed on the equilibrium model ($\mathcal{P}_0 = 802$ days and $\eta_0 = 0.033$). Fig. 4.24 shows that after

75 cycles, the luminosity amplitude has already grown to a factor of two, i.e., to 0.75 mag in M_{bol}.

The non-linear calculations are limited for two reasons. The first is that the STERN code is fully implicit and therefore subject to strong numerical damping (Appenzeller 1970). Thus the pulsations predicted by the linear theory (Sect. 4.4.2) cannot be detected for the case of small growth rates (e.g., for the $10\,M_\odot$ Model `E10`). Secondly, we are limited on the other extreme to not too large amplitudes, since the STERN code is not set up to deal with shock waves. For this reason the calculation shown in Fig. 4.24 is stopped when the surface velocity reached about $10\,km\,s^{-1}$, and it is not attempted to compute non-linear pulsations for increasing amplitudes.

The main uncertainty in the description of the pulsational behavior of the present models is certainly due to the unknown feedback of convection. As in Miras, the convective and the pulsation time-scale are comparable, and at present no solution to the coupled problem exists (Gautschy & Saio 1995). In contrast to the linear stability analysis presented in Sect. 4.4.2, where the convective flux is frozen in, it is assumed to adjust instantaneously in the hydrodynamic stellar evolution code. Both treatments thus represent simple, but different, possibilities to deal with the convective flux feedback and give essentially the same periods and growth rates. Even within a "phase-lag" approach (Arnett 1969) to describe time-dependent convection, Langer (1971) has shown that the general pulsation properties (period, growth rate) derived from linear stability analysis do not depend strongly on the phase-lag parameters. However, the growth rates derived in the present work, as they depend on the energy transport, should only be taken as indicative. A physically correct treatment of thermal and dynamical coupling of convection and pulsation — which is not yet available — may be necessary to predict them reliably. The values of the period, which essentially depend on the structure and the sound speed in the envelope, are more reliable.

The results of the present analysis and the fate of the star thus remain uncertain, since the effects of convection on the pulsational driving is ignored. Nevertheless, the example shown in Fig. 4.24 and the similarity of the pulsational properties (linear and non-linear) discussed above with those obtained for AGB stars, in particular the huge increase in period and growth rate during the final evolutionary stages, may suggest the possibility of pulsations of large amplitude in red supergiants in connection with a strong increase in the mass loss rate, i.e., a "superwind" phase as that observed for Miras and expected for the terminal AGB evolution. This is discussed in the next section.

4.4.4 Discussion

Fig. 4.25 shows the P-L relation derived from the present models in comparison to observations of long-period OH/IR sources from Engels et al. (1983); Le Bertre (1991, 1993); and Jones et al. (1994). The mean P-L relation observed for oxygen-rich Miras (Feast et al. 1989) is also shown. Though most of the OH/IR sources follow the latter P-L relationship and may thus be identified as AGB stars, some

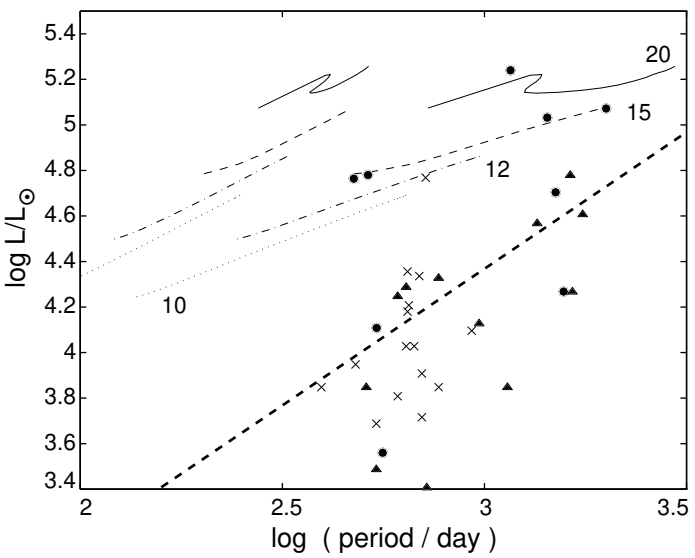

Figure 4.25: Evolution of the luminosity as a function of the period of the red supergiant models for the fundamental mode (right curves) and for the first overtone (left curves). The ZAMS masses are indicated for the fundamental periods of the $10\,M_\odot$ (dotted), $12\,M_\odot$ (dash-dotted), $15\,M_\odot$ (dashed) and $20\,M_\odot$ (solid line) stars (Models `E10`, `E12`, `E15`, and `E20`, respectively). The thick dashed line corresponds to the relationship observed for oxygen-rich Miras (Feast et al. 1989). Observations of OH/IR sources are indicated by triangles (Engels et al. 1983), full circles (Le Bertre 1991, 1993), and crosses (Jones et al. 1994).

objects, mostly from Le Bertre (1993), are overluminous and fall on the curves of the present red supergiant models. It shall be noted that the narrow relation between the period and the L/M-ratio found in Fig. 4.23 might provide an interesting tool to deduce actual masses of these sources.

Although the overluminous sources show large amplitudes (1 to 3 mag), a feature which is generally attributed to AGB stars, the red supergiant nature of at least some of them appears to be consistent with the above results, which suggests that red supergiants may also be able to develop large amplitude pulsations. Most of the overluminous OH/IR sources show extremely strong mass loss from the central object, with mass loss rates as high as $10^{-4} M_\odot\,\mathrm{yr}^{-1}$ (Le Bertre 1991). This is in support of the idea of high mass loss in connection with large periods, growth rates and amplitudes. The order of magnitude of the observed mass loss rates is similar to what is discussed for the final AGB "superwind" (Vassiliadis & Wood 1993); however, the sources of Le Bertre (1991, 1993) are oxygen-rich while the classical AGB superwind is expected in carbon-rich sources.

Fig. 4.26 shows that very large pulsation periods and consequently large amplitudes and mass loss rates may be expected to occur at and beyond central helium exhaustion for the models of the present work, over a time-scale of some 10 000 yr, implying the loss of most of the hydrogen-rich envelope which remained on the star so far (Table 4.5). In this context the self-enhancing character of the pulsational mass loss increase has to be emphasized: as the envelope mass decreases, L/M is increased and the Kelvin-Helmholtz time-scale of the envelope is decreased. This effect is not yet taken into account in the present calculations, where only the mass loss according to Nieuwenhuijzen & de Jager (1990) is adopted. Consequently, the superwind instability may even develop stronger than Fig. 4.26 might suggest.

The probability of observing red supergiants in a stage of large amplitude pulsation or in a "superwind" phase is not very large (Fig. 4.26); however, such events

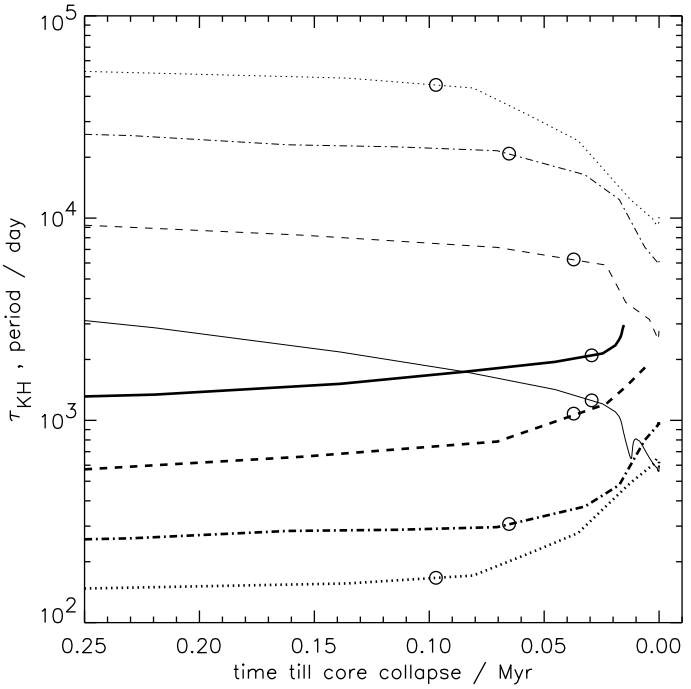

Figure 4.26: Kelvin-Helmholtz time-scale of the hydrogen-rich stellar envelope (thin lines) as function of the time left until core collapse for the $10\,M_\odot$ (dotted), $12\,M_\odot$ (dash-dotted), $15\,M_\odot$ (dashed), and $20\,M_\odot$ (solid line) stars (Models `E10`, `E12`, `E15`, and `E20`, respectively; see Fig. 4.20). The thick lines show the period of the fundamental mode as derived from the linear stability analysis (Sect. 4.4.2). Small circles designate the time when the central helium mass fraction has reached 1 %, i.e., roughly central helium exhaustion. It is evident that, at least for the $15\,M_\odot$ and $20\,M_\odot$ stars, pulsation periods of the order of the Kelvin-Helmholtz time-scale occur. For the last stages of these two models pulsation periods could not be derived due to strong departures from thermal and hydrostatic equilibrium.

might have marked consequences on the appearance of the supernova explosion. Weiler et al. (1992) have found a periodic modulation of the presupernova mass loss from the radio light curve of SN 1979C. Although in this case the inferred period in the presupernova mass loss ($\sim 4\,000$ yr) does not fit to dynamical pulsations discussed here, this work shows the potential of radio observations of supernovae to find evidence for those. A period of the radio signal of the order of few days would be expected in the early phase of the supernova evolution.

A "superwind" occurring some 10 000 yr before the explosion could reduce the mass of the hydrogen-rich envelope of the star to less than $1\,M_\odot$; this would make the star helium-rich and hotter than a typical red supergiant (Höflich, Langer & Duschinger 1993). These features are reminiscent of SN 1993J, which apparently was a helium-enriched K supergiant with an envelope mass of less than $\sim 0.5\,M_\odot$ (Nomoto et al. 1993; Woosley et al. 1994). The progenitor structure of this supernova is currently interpreted as a result of close binary interaction (e.g., Nomoto et al. 1993); however, no companion star could be found yet. This situation is similar to that of SN 1987A: there also, the circumstellar matter clearly indicates that the progenitor star experienced a major structural change several 10^4 yr before the supernova explosion.

Another example of a presupernova star which experienced the loss of most of the hydrogen-rich envelope before the explosion appears to be the progenitor of SN 1054, i.e., the progenitor of the Crab nebula. Hydrogen-rich gas associated with this supernova remnant has only been found recently by Murdin (1994) in the form of an hydrogen-rich halo of several solar masses (see, however, Fesen, Shull

& Hurford 1997). Tsiopa (1995) has summarized evidence from supernova spectra for the ejection of material some 10^4 yr before the explosion; she found evidence in about half a dozen cases, including the well known SN 1983K and SN 1988Z.

The scenario outlined above has also consequences for the formation of Wolf-Rayet stars. If the critical L/M value for the occurrence of strong pulsations and associated strong mass loss would occur in a red supergiant already during central helium burning, it would evolve into a Wolf-Rayet star. This happens only for larger initial masses than those considered above (see Model `E25` in Fig. E.12), or for larger initial rotation rates (see Model `H20B` in Fig. 4.3). The transition objects may be the so called yellow hypergiants, highly variable and very luminous stars evolving off the red supergiant branch (Smoliński, Climenhaga & Fletcher 1989). Correspondingly, the minimum ZAMS mass for Wolf-Rayet star formation might be reduced below values currently found in stellar evolution calculations (i.e., $25 \ldots 35\,\mathrm{M}_\odot$; Schaller et al. 1992; Meynet et al. 1994), thereby increasing the number of single stars contributing to supernovae of Type Ib/c (Woosley, Langer & Weaver 1993; Langer & Woosley 1996).

In this context it is noteworthy that García-Segura et al. (1996), on the basis of hydrodynamic computations for the presupernova evolution of the circumstellar material around massive stars, concluded from the location of the quasi-stationary flocculi of the Cas A supernova remnant that the progenitor star evolved from the red supergiant branch into a Wolf-Rayet star roughly 10 000 yr before the supernova explosion. An increased mass loss due to pulsations during the last few 10^4 yr in the evolution of red supergiants makes such a scenario even more likely.

Chapter 5

Effects of rotation on the nucleosynthesis

Similar to overshooting or semiconvection, rotationally induced mixing is important for the nucleosynthesis in stars, in general, and for massive stars in particular. In addition to the direct effect of mixing on the thermonuclear reaction chains, the stellar structure may also change. Therefore, stars which experience additional mixing may take quite different evolutionary paths. This also changes the final yields of the chemical species the stars return to the interstellar medium. The stars may even display a different kind of final supernova explosion.

5.1 Presupernova yields resulting from large network calculations

As described in Sect. 2.1.6.2, KEPLER uses a 19 isotope network to determine the nuclear energy release during stellar evolution. Additionally, a large network can be used to follow the nucleosynthesis in more detail. The isotopes in this network are evolved in co-processing mode, taking into account the local conditions in the star and all mixing processes during each time-step. The network used in the present work is essentially the same as that of Woosley & Weaver (1995), except for revisions of a few reaction rates (Hoffman, Woosley & Weaver 1998). The network contains 200 isotopes from hydrogen to germanium of which 80 are stable (Table 5.2) and 120 are radioactive.

The evolution of a $12\,M_\odot$ star (Model `KE12`) and a $15\,M_\odot$ star (Model `KE15B`), both with a rotational velocity of $\sim 200\,km\,s^{-1}$ on the ZAMS, is followed with KEPLER from the pre-main sequence to core collapse. These two models correspond to the Models `E12` and `E15B`, respectively, discussed in the previous chapters. The models have the same initial angular momentum and use identical input physics for mixing processes as their counterparts (Table 2.3 and Sect. 2.2.1), only in this case the entire evolution (i.e., not just post carbon burning) is followed with KEPLER using the 200 isotope network. The two models correspond to the two different assumption about the efficiency of inhibiting effect of μ-gradients on rotationally

model	M_{ZAMS} $\mathrm{M}_\odot$	M_{final} $\mathrm{M}_\odot$	M_{He} $\mathrm{M}_\odot$	$M_{\mathsf{C/O}}$ $\mathrm{M}_\odot$	M_{Fe} $\mathrm{M}_\odot$
KE12	12.00	10.12	3.67	2.33	1.39
KE15B	15.00	13.26	3.78	2.11	1.52
s135s7b	13.57	13.57	3.75	2.06	1.43
s145s7b	14.58	14.58	4.12	2.31	1.51

Table 5.1: Model properties of the models of the present work (Models KE12 and KE15B) and those from Weaver & Woosley (1995). Given are the initial mass, final mass, and terminal masses of the helium, the C/O, and the iron core.

induced mixing made in the present work. In Model KE15B μ-gradients are taken into account while in KE12 the rotationally induced mixing is assumed insensitive to them. In order to distinguish these models from those for which the first part of the evolution is computed with STERN, a lowercase initial letter is chosen for the model name.

Because of differences in the prescription of convection and semiconvection in STERN and KEPLER (Sect. 2.2.1.2), Model KE12 does not show the blue-loop found in Model E12 (Sect. 4.3). However, this difference appears not to be important for the nucleosynthesis. For example, about the same helium and C/O core masses result in both calculations (Tables 3.2 and 5.1).

For comparison with representative calculations of non-rotating stars, models from Weaver & Woosley (1995) are listed along with the models of the present work (see Tables 5.2 and 5.3). These models were used by Woosley & Weaver (1995) for their study of nucleosynthesis in core collapse supernovae. The initial composition of these models is close to that of the present work, 70.57 % hydrogen, 27.52 % helium, and the rest, 1.91 %, are metals (Woosley & Weaver 1995; Anders & Grevesse 1989). For consistency with the models investigated in the previous chapters, values of 70 %, 28 %, and 2 %, respectively, are used here, but with the same relative abundance ratios within each of the three isotope groups. Further different assumptions for the models of Weaver & Woosley (1995) were:

- No rotation, i.e. no rotationally induced mixing Sect. 2.2.2. The effect of centrifugal forces included in STERN is still neglected in KEPLER.
- The semiconvection parameter of $\alpha_{\mathrm{sem}} = 0.1$ (Sect. 2.2.1.2), and an overshooting (Sect. 2.2.1.1) of 0.01 pressure scale-heights at the boundaries of convection zones.
- No mass loss (Sect. 2.4).
- Older opacity tables (Sect. 2.1.6.2).
- Less spatial resolution in the atmosphere layers.
- Hydrogen burning released $\sim 13.32\,\%$ too much energy (Appendix B).

Table 5.2: Nucleosynthetic yields for stable isotopes, after all decays of unstable species, for presupernova models (in units of solar masses). For comparison with representative calculations of non-rotating stars, Models `s135s7b` and `s145s7b` from Weaver & Woosley (1995) are given (see also Table 5.1). Listed are the masses of individual isotopes outside the iron core including the matter lost by stellar winds; all radioactive isotopes are assumed to have decayed to stable isotopes (except for ^{40}K which has a half-life of 1.28 Gyr). After the list of the individual isotopes, their sum, the mass of the iron core, the total mass (equal to the initial mass), and the mass lost in the stellar wind are also displayed. The last three lines give the yield of ^{26}Al: the total mass of ^{26}Al (first line), composed of the mass of ^{26}Al inside the star at onset of core collapse (second line) and the mass of ^{26}Al ejected by stellar winds during the life of the star until core collapse (third line). The value $f_{N\sigma}n_{\rm cap}$ given in the last line is a rough measure of the strength of the s-process in the helium core (Sect. 5.3.4).

isotope	KE12	KE15B	s135s7b	s145s7b
^{1}H	5.063	7.003	6.483	6.822
^{2}H	$3.303\cdot10^{-5}$	$8.041\cdot10^{-6}$	$8.441\cdot10^{-5}$	$8.874\cdot10^{-5}$
^{3}He	$2.066\cdot10^{-5}$	$5.032\cdot10^{-6}$	$4.028\cdot10^{-4}$	$4.195\cdot10^{-4}$
^{4}He	4.085	5.418	4.674	5.036
^{6}Li	$4.745\cdot10^{-10}$	$1.158\cdot10^{-10}$	$1.142\cdot10^{-9}$	$1.201\cdot10^{-9}$
^{7}Li	$7.769\cdot10^{-9}$	$4.118\cdot10^{-9}$	$1.644\cdot10^{-8}$	$1.728\cdot10^{-8}$
^{9}Be	$1.261\cdot10^{-9}$	$1.401\cdot10^{-8}$	$2.922\cdot10^{-10}$	$3.072\cdot10^{-10}$
^{10}B	$8.205\cdot10^{-10}$	$2.517\cdot10^{-10}$	$1.153\cdot10^{-8}$	$1.223\cdot10^{-8}$
^{11}B	$3.472\cdot10^{-9}$	$8.742\cdot10^{-10}$	$8.316\cdot10^{-9}$	$8.743\cdot10^{-9}$
^{12}C	$1.245\cdot10^{-1}$	$1.614\cdot10^{-1}$	$1.320\cdot10^{-1}$	$1.529\cdot10^{-1}$
^{13}C	$1.172\cdot10^{-3}$	$1.829\cdot10^{-3}$	$1.179\cdot10^{-3}$	$1.258\cdot10^{-3}$
^{14}N	$4.878\cdot10^{-2}$	$6.666\cdot10^{-2}$	$4.876\cdot10^{-2}$	$5.277\cdot10^{-2}$
^{15}N	$1.307\cdot10^{-4}$	$2.612\cdot10^{-4}$	$2.026\cdot10^{-5}$	$2.148\cdot10^{-5}$
^{16}O	$7.486\cdot10^{-1}$	$5.337\cdot10^{-1}$	$4.901\cdot10^{-1}$	$6.195\cdot10^{-1}$
^{17}O[1]	$7.349\cdot10^{-5}$	$1.250\cdot10^{-4}$	$5.359\cdot10^{-4}$	$5.686\cdot10^{-4}$
^{18}O	$4.701\cdot10^{-3}$	$7.382\cdot10^{-3}$	$3.468\cdot10^{-3}$	$3.826\cdot10^{-3}$
^{19}F	$3.795\cdot10^{-5}$	$7.353\cdot10^{-5}$	$4.348\cdot10^{-6}$	$4.562\cdot10^{-6}$
^{20}Ne	$1.537\cdot10^{-1}$	$9.448\cdot10^{-2}$	$8.941\cdot10^{-2}$	$1.019\cdot10^{-1}$
^{21}Ne	$1.327\cdot10^{-4}$	$1.170\cdot10^{-4}$	$1.390\cdot10^{-4}$	$1.274\cdot10^{-4}$
^{22}Ne	$2.086\cdot10^{-3}$	$3.359\cdot10^{-3}$	$5.521\cdot10^{-3}$	$6.890\cdot10^{-3}$
^{23}Na	$3.635\cdot10^{-3}$	$2.795\cdot10^{-3}$	$2.442\cdot10^{-3}$	$2.212\cdot10^{-3}$
^{24}Mg	$3.522\cdot10^{-2}$	$3.252\cdot10^{-2}$	$2.964\cdot10^{-2}$	$3.102\cdot10^{-2}$
^{25}Mg	$9.328\cdot10^{-3}$	$9.077\cdot10^{-3}$	$5.420\cdot10^{-3}$	$6.637\cdot10^{-3}$
^{26}Mg	$1.673\cdot10^{-2}$	$1.433\cdot10^{-2}$	$5.131\cdot10^{-3}$	$6.797\cdot10^{-3}$
^{27}Al	$4.869\cdot10^{-3}$	$4.251\cdot10^{-3}$	$3.982\cdot10^{-3}$	$4.683\cdot10^{-3}$
^{28}Si	$1.454\cdot10^{-1}$	$6.126\cdot10^{-2}$	$8.202\cdot10^{-2}$	$9.340\cdot10^{-2}$
^{29}Si	$1.824\cdot10^{-3}$	$2.263\cdot10^{-3}$	$2.296\cdot10^{-3}$	$2.437\cdot10^{-3}$
^{30}Si	$9.915\cdot10^{-4}$	$2.724\cdot10^{-3}$	$2.458\cdot10^{-3}$	$1.631\cdot10^{-3}$

CONTINUED ON NEXT PAGE

[1]Due to an updated reaction rate for ^{17}O(p,α)^{14}N, enhanced production of ^{17}O occurred in the calculations by Weaver & Woosley (1995) compared to the present work (Hoffman et al. 1998). See also Sect. 5.2.4.

NUCLEOSYNTHESIS YIELDS (CONTINUED)

isotope	KE12	KE15B	s135s7b	s145s7b
^{31}P	$1.309{\cdot}10^{-3}$	$8.634{\cdot}10^{-4}$	$6.154{\cdot}10^{-4}$	$5.557{\cdot}10^{-4}$
^{32}S	$9.398{\cdot}10^{-2}$	$2.940{\cdot}10^{-2}$	$4.381{\cdot}10^{-2}$	$6.968{\cdot}10^{-2}$
^{33}S	$4.599{\cdot}10^{-4}$	$1.988{\cdot}10^{-4}$	$2.213{\cdot}10^{-4}$	$2.386{\cdot}10^{-4}$
^{34}S	$5.233{\cdot}10^{-3}$	$2.246{\cdot}10^{-3}$	$2.363{\cdot}10^{-3}$	$2.889{\cdot}10^{-3}$
^{36}S	$1.453{\cdot}10^{-5}$	$1.477{\cdot}10^{-5}$	$5.746{\cdot}10^{-6}$	$7.668{\cdot}10^{-6}$
^{35}Cl	$1.154{\cdot}10^{-3}$	$2.292{\cdot}10^{-4}$	$2.793{\cdot}10^{-4}$	$2.660{\cdot}10^{-4}$
^{37}Cl	$1.660{\cdot}10^{-4}$	$1.015{\cdot}10^{-4}$	$8.175{\cdot}10^{-5}$	$8.984{\cdot}10^{-5}$
^{36}Ar	$1.731{\cdot}10^{-2}$	$4.910{\cdot}10^{-3}$	$7.954{\cdot}10^{-3}$	$1.421{\cdot}10^{-2}$
^{38}Ar	$8.612{\cdot}10^{-3}$	$2.381{\cdot}10^{-3}$	$3.142{\cdot}10^{-3}$	$5.044{\cdot}10^{-3}$
^{40}Ar	$5.746{\cdot}10^{-6}$	$5.673{\cdot}10^{-6}$	$2.096{\cdot}10^{-6}$	$3.033{\cdot}10^{-6}$
^{39}K	$1.384{\cdot}10^{-3}$	$2.827{\cdot}10^{-4}$	$4.066{\cdot}10^{-4}$	$4.882{\cdot}10^{-4}$
^{40}K	$2.954{\cdot}10^{-6}$	$1.248{\cdot}10^{-6}$	$4.850{\cdot}10^{-7}$	$5.575{\cdot}10^{-7}$
^{41}K	$5.577{\cdot}10^{-5}$	$1.555{\cdot}10^{-5}$	$1.887{\cdot}10^{-5}$	$2.315{\cdot}10^{-5}$
^{40}Ca	$1.262{\cdot}10^{-2}$	$2.964{\cdot}10^{-3}$	$5.987{\cdot}10^{-3}$	$1.135{\cdot}10^{-2}$
^{42}Ca	$3.373{\cdot}10^{-4}$	$8.747{\cdot}10^{-5}$	$1.231{\cdot}10^{-4}$	$1.869{\cdot}10^{-4}$
^{43}Ca	$3.398{\cdot}10^{-6}$	$2.124{\cdot}10^{-6}$	$1.670{\cdot}10^{-6}$	$1.777{\cdot}10^{-6}$
^{44}Ca	$2.342{\cdot}10^{-5}$	$2.343{\cdot}10^{-5}$	$2.131{\cdot}10^{-5}$	$2.342{\cdot}10^{-5}$
^{46}Ca	$5.727{\cdot}10^{-8}$	$9.953{\cdot}10^{-8}$	$1.947{\cdot}10^{-7}$	$3.003{\cdot}10^{-7}$
^{48}Ca	$1.450{\cdot}10^{-6}$	$1.900{\cdot}10^{-6}$	$1.635{\cdot}10^{-6}$	$1.756{\cdot}10^{-6}$
^{45}Sc	$1.543{\cdot}10^{-6}$	$1.351{\cdot}10^{-6}$	$1.454{\cdot}10^{-6}$	$1.615{\cdot}10^{-6}$
^{46}Ti	$1.070{\cdot}10^{-4}$	$3.196{\cdot}10^{-5}$	$6.242{\cdot}10^{-5}$	$6.334{\cdot}10^{-5}$
^{47}Ti	$4.918{\cdot}10^{-6}$	$3.751{\cdot}10^{-6}$	$3.462{\cdot}10^{-6}$	$3.317{\cdot}10^{-6}$
^{48}Ti	$2.212{\cdot}10^{-5}$	$2.852{\cdot}10^{-5}$	$2.541{\cdot}10^{-5}$	$2.680{\cdot}10^{-5}$
^{49}Ti	$4.196{\cdot}10^{-6}$	$4.316{\cdot}10^{-6}$	$3.167{\cdot}10^{-6}$	$3.334{\cdot}10^{-6}$
^{50}Ti	$6.309{\cdot}10^{-6}$	$6.616{\cdot}10^{-6}$	$3.457{\cdot}10^{-6}$	$4.073{\cdot}10^{-6}$
^{50}V	$3.001{\cdot}10^{-8}$	$5.867{\cdot}10^{-8}$	$3.798{\cdot}10^{-8}$	$3.461{\cdot}10^{-8}$
^{51}V	$9.719{\cdot}10^{-6}$	$7.030{\cdot}10^{-6}$	$7.901{\cdot}10^{-6}$	$6.637{\cdot}10^{-6}$
^{50}Cr	$8.181{\cdot}10^{-5}$	$3.302{\cdot}10^{-5}$	$7.302{\cdot}10^{-5}$	$6.385{\cdot}10^{-5}$
^{52}Cr	$1.562{\cdot}10^{-4}$	$2.027{\cdot}10^{-4}$	$1.931{\cdot}10^{-4}$	$1.857{\cdot}10^{-4}$
^{53}Cr	$2.125{\cdot}10^{-5}$	$2.806{\cdot}10^{-5}$	$3.969{\cdot}10^{-5}$	$2.357{\cdot}10^{-5}$
^{54}Cr	$1.224{\cdot}10^{-5}$	$1.431{\cdot}10^{-5}$	$9.674{\cdot}10^{-6}$	$1.100{\cdot}10^{-5}$
^{55}Mn	$1.618{\cdot}10^{-4}$	$1.980{\cdot}10^{-4}$	$2.045{\cdot}10^{-4}$	$1.748{\cdot}10^{-4}$
^{54}Fe	$9.185{\cdot}10^{-4}$	$1.020{\cdot}10^{-3}$	$1.467{\cdot}10^{-3}$	$1.030{\cdot}10^{-3}$
^{56}Fe	$1.154{\cdot}10^{-2}$	$1.520{\cdot}10^{-2}$	$1.357{\cdot}10^{-2}$	$1.431{\cdot}10^{-2}$
^{57}Fe	$4.725{\cdot}10^{-4}$	$5.902{\cdot}10^{-4}$	$4.285{\cdot}10^{-4}$	$4.485{\cdot}10^{-4}$
^{58}Fe	$3.203{\cdot}10^{-4}$	$3.657{\cdot}10^{-4}$	$2.402{\cdot}10^{-4}$	$2.712{\cdot}10^{-4}$
^{59}Co	$1.167{\cdot}10^{-4}$	$1.316{\cdot}10^{-4}$	$1.208{\cdot}10^{-4}$	$1.335{\cdot}10^{-4}$
^{58}Ni	$4.995{\cdot}10^{-4}$	$6.300{\cdot}10^{-4}$	$6.171{\cdot}10^{-4}$	$6.141{\cdot}10^{-4}$
^{60}Ni	$4.717{\cdot}10^{-4}$	$3.943{\cdot}10^{-4}$	$3.490{\cdot}10^{-4}$	$4.963{\cdot}10^{-4}$
^{61}Ni	$4.346{\cdot}10^{-5}$	$4.510{\cdot}10^{-5}$	$4.721{\cdot}10^{-5}$	$6.156{\cdot}10^{-5}$
^{62}Ni	$9.865{\cdot}10^{-5}$	$1.331{\cdot}10^{-4}$	$1.347{\cdot}10^{-4}$	$1.430{\cdot}10^{-4}$

CONTINUED ON NEXT PAGE

NUCLEOSYNTHESIS YIELDS (CONTINUED)

isotope	KE12	KE15B	s135s7b	s145s7b
^{64}Ni	$1.363{\cdot}10^{-4}$	$1.639{\cdot}10^{-4}$	$1.003{\cdot}10^{-4}$	$1.503{\cdot}10^{-4}$
^{63}Cu	$4.211{\cdot}10^{-5}$	$4.417{\cdot}10^{-5}$	$6.372{\cdot}10^{-5}$	$9.337{\cdot}10^{-5}$
^{65}Cu	$3.873{\cdot}10^{-5}$	$4.488{\cdot}10^{-5}$	$1.918{\cdot}10^{-5}$	$2.413{\cdot}10^{-5}$
^{64}Zn	$1.952{\cdot}10^{-5}$	$2.470{\cdot}10^{-5}$	$1.329{\cdot}10^{-5}$	$1.475{\cdot}10^{-5}$
^{66}Zn	$6.490{\cdot}10^{-5}$	$7.570{\cdot}10^{-5}$	$2.826{\cdot}10^{-5}$	$3.389{\cdot}10^{-5}$
^{67}Zn	$1.562{\cdot}10^{-5}$	$1.485{\cdot}10^{-5}$	$5.823{\cdot}10^{-6}$	$9.193{\cdot}10^{-6}$
^{68}Zn	$2.310{\cdot}10^{-4}$	$2.351{\cdot}10^{-4}$	$3.792{\cdot}10^{-5}$	$6.122{\cdot}10^{-5}$
^{70}Zn	$1.740{\cdot}10^{-8}$	$1.381{\cdot}10^{-6}$	$4.691{\cdot}10^{-7}$	$2.016{\cdot}10^{-6}$
^{69}Ga	$3.316{\cdot}10^{-5}$	$3.025{\cdot}10^{-5}$	$4.310{\cdot}10^{-6}$	$6.930{\cdot}10^{-6}$
^{71}Ga	$4.322{\cdot}10^{-4}$	$3.359{\cdot}10^{-4}$	$1.856{\cdot}10^{-5}$	$3.911{\cdot}10^{-5}$
^{70}Ge	$5.630{\cdot}10^{-5}$	$9.904{\cdot}10^{-5}$	$9.685{\cdot}10^{-6}$	$8.397{\cdot}10^{-6}$
sum	$1.074{\cdot}10^{+1}$	$1.348{\cdot}10^{+1}$	$1.215{\cdot}10^{+1}$	$1.307{\cdot}10^{+1}$
"Fe" core	1.392	1.517	1.428	1.508
total	$1.200{\cdot}10^{+1}$	$1.500{\cdot}10^{+1}$	$1.357{\cdot}10^{+1}$	$1.458{\cdot}10^{+1}$
wind	1.880	1.744	0.000	0.000
^{26}Al	$1.220{\cdot}10^{-5}$	$2.001{\cdot}10^{-5}$	$3.010{\cdot}10^{-5}$	$5.137{\cdot}10^{-5}$
... star	$1.202{\cdot}10^{-5}$	$1.984{\cdot}10^{-5}$	$3.010{\cdot}10^{-5}$	$5.137{\cdot}10^{-5}$
... wind	$1.777{\cdot}10^{-7}$	$1.649{\cdot}10^{-7}$	0.000	0.000
$f_{N\sigma}n_{\rm cap}$	4.518	4.326	1.435	1.831

The models from Weaver & Woosley (1995) are selected such that Models `s135s7b` and `s145s7b` have (about), at core collapse, the same helium core mass and C/O core mass as Model `KE12`, respectively. Model `s135s7b` has about the same helium and C/O core, and Model `s145s7b` about the same iron core as Model `KE15B` (Table 5.1).

The masses of all stable isotopes lighter than germanium and the corresponding production factors are given for the presupernova models in Tables 5.2 and 5.3. Yields and production factors include the mass lost due to stellar winds. The pre-collapse masses and production factors should be close to the post-explosion values for most of the light elements up to silicon, and not too bad up to calcium. Most of the isotopes heavier than calcium depend on the nucleosynthesis in the supernova explosion, but are given for completeness (e.g., Woosley & Weaver 1995; Hoffman et al. 1998; Nomoto & Hashimoto 1988; Thielemann et al. 1996). Artificially large amounts of germanium and gallium occur because these two isotopes are at the end of the reaction network and no destruction reactions for them or their radioactive progenitors are taken into account. The distribution of selected isotopes in the innermost part of the stars are shown in Figs. 5.2 and 5.3 as a function of the mass coordinate.

Table 5.3: Production factors of pre-collapse models. The production factor of a species is here defined by the total mass fraction of a species in the stars, excluding the iron core, but including the mass lost in stellar winds, divided by the mass fraction of that species in the solar composition.

isotope	KE12	KE15B	s135s7b	s145s7b
^{1}H	0.68	0.74	0.76	0.74
^{2}H	0.06	0.01	0.14	0.14
^{3}He	0.07	0.01	1.13	1.10
^{4}He	1.40	1.46	1.40	1.40
^{6}Li	0.07	0.01	0.14	0.14
^{7}Li	0.08	0.03	0.14	0.14
^{9}Be	0.72	6.25	0.14	0.14
^{10}B	0.07	0.02	0.89	0.88
^{11}B	0.07	0.01	0.14	0.14
^{12}C	3.87	3.95	3.58	3.86
^{13}C	3.03	3.72	2.66	2.64
^{14}N	4.16	4.47	3.63	3.65
^{15}N	2.82	4.44	0.38	0.38
^{16}O	7.36	4.13	4.21	4.94
^{17}O[1]	1.78	2.38	11.35	11.19
^{18}O	20.45	25.26	13.18	13.51
^{19}F	8.83	13.46	0.88	0.86
^{20}Ne	8.95	4.33	4.55	4.81
^{21}Ne	3.03	2.10	2.77	2.36
^{22}Ne	1.51	1.91	3.49	4.05
^{23}Na	10.26	6.21	6.02	5.07
^{24}Mg	6.45	4.68	4.74	4.61
^{25}Mg	13.00	9.95	6.60	7.50
^{26}Mg	20.32	13.69	5.44	6.70
^{27}Al	7.91	5.43	5.65	6.17
^{28}Si	20.99	6.96	10.34	10.94
^{29}Si	5.02	4.90	5.52	5.44
^{30}Si	3.97	8.59	8.60	5.31
^{31}P	15.13	7.85	6.21	5.21
^{32}S	22.38	5.51	9.11	13.47
^{33}S	13.46	4.58	5.66	5.67
^{34}S	26.44	8.93	10.43	11.84
^{36}S	14.60	11.68	5.04	6.25
^{35}Cl	42.96	6.71	9.08	8.04
^{37}Cl	18.31	8.81	7.88	8.04
^{36}Ar	21.09	4.70	8.46	14.05
^{38}Ar	52.79	11.48	16.82	25.09
^{40}Ar	21.42	16.64	6.83	9.18
^{39}K	37.57	6.04	9.64	10.76

CONTINUED ON NEXT PAGE

PRODUCTION FACTORS (CONTINUED)

isotope	KE12	KE15B	s135s7b	s145s7b
^{40}K	50.22	16.69	7.20	7.69
^{41}K	19.96	4.38	5.90	6.72
^{40}Ca	19.86	3.67	8.23	14.50
^{42}Ca	75.79	15.46	24.16	34.08
^{43}Ca	3.57	1.76	1.53	1.52
^{44}Ca	1.55	1.22	1.23	1.26
^{46}Ca	1.93	2.64	5.74	8.23
^{48}Ca	0.99	1.02	0.97	0.97
^{45}Sc	3.74	2.57	3.08	3.17
^{46}Ti	45.17	10.61	23.01	21.69
^{47}Ti	2.23	1.34	1.37	1.22
^{48}Ti	0.97	0.98	0.97	0.95
^{49}Ti	2.42	1.96	1.59	1.56
^{50}Ti	3.62	2.98	1.73	1.90
^{50}V	3.06	4.70	3.38	2.86
^{51}V	2.43	1.38	1.73	1.35
^{50}Cr	10.39	3.30	8.10	6.58
^{52}Cr	0.99	1.01	1.07	0.96
^{53}Cr	1.17	1.21	1.90	1.05
^{54}Cr	2.65	2.44	1.83	1.93
^{55}Mn	1.15	1.11	1.27	1.01
^{54}Fe	1.21	1.06	1.69	1.11
^{56}Fe	0.93	0.96	0.96	0.94
^{57}Fe	1.56	1.53	1.24	1.20
^{58}Fe	8.17	7.34	5.35	5.61
^{59}Co	3.28	2.91	2.96	3.04
^{58}Ni	0.95	0.95	1.03	0.95
^{60}Ni	2.27	1.49	1.47	1.94
^{61}Ni	4.77	3.89	4.52	5.48
^{62}Ni	3.35	3.56	3.99	3.94
^{64}Ni	17.68	16.73	11.37	15.82
^{63}Cu	6.90	5.69	9.12	12.42
^{65}Cu	13.79	12.57	5.97	6.97
^{64}Zn	1.85	1.85	1.10	1.14
^{66}Zn	10.41	9.55	3.96	4.41
^{67}Zn	16.81	12.57	5.47	8.03
^{68}Zn	53.65	42.96	7.69	11.54
^{70}Zn	0.12	7.65	2.88	11.52
^{69}Ga	78.89	56.63	8.96	13.38
^{71}Ga	1 549.15	947.21	58.11	113.77
^{70}Ge	122.84	170.03	18.46	14.87

isotope	KE12	KE15B
^{1}H	23.11	17.04
^{2}H	37.18	57.74
^{3}He	37.17	57.73
^{4}He	16.47	9.52
^{6}Li	37.18	57.61
^{7}Li	35.99	39.36
^{9}Be	3.70	0.14
^{10}B	36.66	48.39
^{11}B	37.13	57.07
mass	17.50	12.94

Table 5.4: Percentage of mass in the wind relative to the sum of mass in the wind and star, excluding the iron core, for the light isotopes. For comparison the fraction of the total mass in the wind, including all isotopes, is given at the end of the table (Table 5.2).

5.2 Nucleosynthesis during hydrogen burning

5.2.1 Depletion of light elements

The light isotopes, ^{2}H, ^{3}He, ^{6}Li, ^{7}Li, ^{9}Be, ^{10}B, and ^{11}B are already destroyed at rather low temperatures in the stellar envelope. They are depleted much more efficiently in the rotating stars of the present work than in the non-rotating models of Weaver & Woosley (1995) (Sections 3.1). During central hydrogen burning, matter from the surface layers is transported downward by rotationally induced mixing into regions sufficiently hot for the light elements to be destroyed, and this depleted matter appears at the surface. This is discussed in Sect. 4.1.3 (Fig. 4.6) for boron and shown in Fig. D.1 for ^{3}He, lithium, and beryllium. The decrease in the final yields would even be greater were it not for mass loss, which protects some of the initial stellar matter from this depletion. This is shown in Table 5.4, where the fraction of the light isotopes lost from the star by winds is given relative to the total amount in the star at onset of core collapse. The fraction of light isotopes destroyed is not large, because they are lost unprocessed in the wind.

The depletion of boron at the surface of single rotating massive stars was previously investigated by Fliegner et al. (1996). They predicted that boron depletion should occur much before an enrichment of nitrogen sets in, i.e., there exit stars which are boron depleted but not nitrogen enriched at the surface, but no stars should be found which are nitrogen enriched and not depleted in boron. They found good agreement with observational data. This result is also reproduced in the present work (Sect. 4.1.3).

An exception is ^{9}Be which, as can be seen in Table 5.3, appears to be much less destroyed in Model KE12 than in the models of Weaver & Woosley (1995), and even produced in Model KE15B. This is not in contradiction to the previous discussion. Outside the C/O core it is indeed destroyed, but a major production of ^{9}Be occurs in the carbon-burning shell (Figs. 5.2B and 5.3B).

The depletion of light elements is more severe in Model KE15B than in Model KE12, since the mixing in the stellar envelope during central hydrogen burning is more efficient in this model and the temperatures above the μ-barrier are already

high enough for their destruction (Sect. 4.1.3). When the star is a red supergiant, the envelope becomes convective and efficient mixing occurs from the surface down to the deep interior of the star, close to the core. However, the temperatures there do not get high enough to cause any important thermonuclear reactions like the destruction of the fragile isotopes, or the production of ^{14}N.

For the sake of computational cost, in currently used parameter settings for KEPLER, the large network considers nuclear reactions only for temperatures above 10^7 K. This hardly affects the CNO isotopes or heavier nuclei. However, the destruction of light isotopes might be underestimated, since some of them, like ^{7}Li, are already destroyed at a view times 10^6 K. Additionally, some of the relevant reaction involving these isotopes are not considered, since the structure of these reaction does not fit into the standard scheme followed by the vast majority of reactions involving heavier isotopes follow, where only n, p, α, and γ is one of the reactants (Sect. C). Note also that a large amount of several of the light elements may be produced during the supernova explosion by the neutrino process (Woosley & Weaver 1995).

5.2.2 Production of ^{14}N

A major difference for rotating stars compared to their non-rotating counterparts is also observed in nitrogen: ^{14}N is about 25 % (15 %) more abundant in Model KE15B (Model KE12; Table 5.2) than in the models of Weaver & Woosley (1995). The main enhancement relative to non-rotating stars occurs in the envelope during central hydrogen burning (Fig. 5.4). During the first dredge-up, ^{14}N enhanced matter is only redistributed in the envelope, but not produced. This helps, however, to protect some of it from destruction during later evolutionary phases. The second dredge-up after core helium exhaustion mixes some of the ^{14}N which was produced in the hydrogen-burning shell into the convective envelope (Sect. 4.2.3). But this gives only a minor contribution to the total yield of ^{14}N (Sect. 4.2.3).

5.2.3 Production of the radioactive isotope ^{26}Al

The radioactive decay of ^{26}Al in the interstellar medium has been directly observed through the emission of a 1.8 MeV γ-ray line from the excited ^{26}Mg* state, to which the ^{26}Al ground state decays. The first excited ^{26}Al* state does decay directly to the ground state of ^{26}Mg and therefore does not emit the 1.8 MeV line (Prantzos & Diehl 1996). For its radioactive decay to become observable, the ^{26}Al has to liberated from the star. One way for it to leave the stellar interior is by mass loss from the surface (Sect. 2.4). In the range of initial stellar masses considered in the present work, rotationally induced mixing can bring ^{26}Al to the surface during central hydrogen burning (Sect. 4.1.3). In red supergiants, which additionally show higher mass loss rates, the dredge-up process is responsible for an increased abundance of ^{26}Al in the wind. This first dredge-up may even reach below the former μ-barrier, i.e., into regions with even higher ^{26}Al abundances than accessible to the rotationally induced mixing in Model KE15B. Also, the layers above the μ-barrier are more enriched in ^{26}Al due rotationally induced mixing. After central hydrogen burning, the remaining

stellar lifetime becomes comparable to lifetime of ^{26}Al against β^+-decay. Therefore a large fraction of the ^{26}Al produced during hydrogen shell burning can survive until the supernova explosion.

During central and shell hydrogen burning, the radioactive isotope ^{26}Al is produced by ^{25}Mg(p,γ)^{26}Al. Since no "new" ^{25}Mg is produced during these burning phases, essentially only the initial amount of ^{25}Mg is converted into ^{26}Al, which thereafter decays with a half life of 0.72 Myr. The destruction by ^{26}Al(p,γ)^{27}Al becomes only important in stars more massive than those considered in the present work (Walter & Maeder 1989).

Loss of ^{26}Al by stellar winds contributes only about 1 % ($1.78{\cdot}10^{-7}$ M$_\odot$) to the total yield of ^{26}Al of the Models `KE12` and `KE15B` (Table 5.2). Almost all of this is due to red supergiant winds after the first dredge-up, thus massive main sequence stars are should not give a large contribution to the Galactic ^{26}Al production, even if rotation is taken into account. For comparison, the rapidly rotating Model `H20B` loses $4.29{\cdot}10^{-6}$ M$_\odot$ as a Wolf-Rayet star during core hydrogen burning (Sect. 4.1.3), i.e., not on the main sequence.

In massive close binary stars, however, ^{26}Al can be exposed to the surface by mass transfer between the stars in different evolutionary stages and by the mass loss from the system during these mass transfer phases (e.g., Braun & Langer 1995; Braun 1997; Langer, Braun & Wellstein 1998a and references therein).

5.2.4 Revised reaction rates and ^{17}O production

The isotope ^{17}O is mainly produced from ^{16}O by ^{16}O(p,γ)^{17}F($\beta^+\nu_e$)^{17}O during hydrogen burning. Due to the rotationally induced mixing it can be enriched in the envelope, where it is not destroyed in subsequent burning phases. Its destruction during hydrogen burning is chiefly by ^{17}O(p,α)^{14}N and by ^{17}O(p,γ)^{18}F($\beta^+\nu_e$)^{18}O. During helium burning it is destroyed by ^{17}O(α,n)^{20}Ne, ^{17}O(α,γ)^{21}Ne, and ^{17}O(n,α)^{14}C, with decreasing importance. At core-collapse, essentially all ^{17}O contained in Models `KE12` and `KE15B` is located in the stellar envelope.

The much lower yield of ^{17}O in the models of the present work compared to those of Weaver & Woosley (1995) can be understood by the recent revision of the ^{17}O(p,γ)^{18}F and the ^{17}O(p,α)^{14}N destruction rates in KEPLER (Aubert, Prantzos & Baraffe 1996; Hoffman et al. 1998). This revision also decreases the production of ^{18}O in the non-rotating models of Hoffman et al. (1998). However, in Model `KE15B` ^{17}O is lower by a factor of ~ 4 and ^{18}O higher by a factor of ~ 14 (!) compared to the 15 M$_\odot$ star of Hoffman et al. (1998). As already mentioned above, ^{18}O is mainly produced in the convective helium-burning shell from ^{14}N.

5.3 Nucleosynthesis during helium burning and beyond

5.3.1 Sodium

The only stable isotope of sodium, ^{23}Na, is partially produced during hydrogen burning by the reaction ^{22}Ne(p,γ)^{23}Na (leading to enrichment in the envelope and in the helium shell), and during helium burning by ^{22}Ne(n,γ)^{23}Ne($\beta^-\bar{\nu}_e$)^{23}Na. But the major part of sodium is synthesized during carbon burning by ^{12}C(^{12}C,p)^{23}Na. Especially at oxygen burning, it is again destroyed by ^{23}Na(p,α)^{20}Ne, and, to lesser extent, by ^{23}Na(p,γ)^{24}Mg. In the presupernova model it is therefore mainly found in the carbon-burning convective shell. In Model KE12, ^{23}Na is produced about twice as much as in the comparable models of Weaver & Woosley (1995).

5.3.2 ^{26}Al content in the presupernova models

During helium burning, ^{26}Al is effectively destroyed by neutron capture through the reaction ^{26}Al(n,p)^{26}Mg (Prantzos & Diehl 1996). This affects both the ^{26}Al remaining in the core after hydrogen exhaustion and most of the ^{26}Al produced during hydrogen shell burning. The latter destruction is mainly by convective helium shell burning, which arises only shortly before core collapse (Sect. 5.4). In the non-rotating models of Woosley & Weaver (1995) this effect is less expressed, since they find smaller convective helium shells than here. However, the efficiency of this destruction is only low, since in the deeper layers of the helium shell, into which the convective helium shell penetrates first, part of the ^{26}Al produced during hydrogen-burning shell has already decayed.

The most important source of ^{26}Al in the presupernova models computed here is its production during carbon and neon burning. The same reaction as during hydrogen burning, ^{25}Mg(p,γ)^{26}Al, is the main production channel. This is possible, since, in contrast to hydrogen burning, ^{25}Mg is produced during carbon burning. Additionally, ^{23}Na(α,n)^{26}Al and ^{23}Mg(α,p)^{26}Al contribute to the production of ^{26}Al. At the same time, the production competes with the ^{26}Al sinks, which are dominated by the neutron and proton capture reactions ^{26}Al(n,p)^{26}Mg and ^{26}Al(p,α)^{23}Na, but is fast enough to keep an appreciable ^{26}Al abundance in the carbon-burning shell. At temperatures above several times 10^8 K, ^{26}Al may also be destroyed through decay from the first excited state ^{26}Al(γ)^{26}Al*($\beta^+\nu_e$)^{26}Mg. After carbon burning, ^{26}Al is destroyed again in the subsequent neon or oxygen burning regions, but not in the radiative C/O shell.

In Model KE15B, about half of the ^{26}Al is located in the convective carbon-burning shell, the other half is found in the helium layer *above* the convective helium-burning shell (Fig. 5.3C). In Model KE12, the convective carbon shell contains about 2/3 of the total ^{26}Al, the other third is in the radiative helium layer (Fig. 5.2C). In comparison to this, the models of Weaver & Woosley (1995) have rather high yield of ^{26}Al. Only a small part of this discrepancy can be explained by the much smaller expansion of the convection zone in the helium shell, but, similar to the present

work, more than 80 % of the ^{26}Al is located in the convective carbon-burning shell.

Thus, the most important mechanism for expelling ^{26}Al in single stars which are not massive enough to become Wolf-Rayet stars is the supernova explosion. In this case, all of the ^{26}Al present in the stellar interior is immediately ejected into the interstellar medium. Since the lifetime of the stars considered here is much longer than that of ^{26}Al, most of the ^{26}Al produced during central hydrogen burning decays before the supernova explosion, and therefore the ^{26}Al yield by this source stays much below the initial ^{25}Mg content of the star (Sect. 5.2.3).

Some ^{26}Al is also made by the neutrino process during the supernova explosion.

5.3.3 Neutron-rich isotopes of magnesium, silicon, and sulfur

The magnesium isotope ^{25}Mg is about two times more abundant in Model KE12 than in Weaver & Woosley (1995). In hydrogen-burning regions the initial ^{25}Mg is mostly destroyed by proton capture and produces ^{26}Al (Sect. 5.2.3). But it is produced during helium burning by ^{24}Mg(n,γ)^{25}Mg, and also during carbon burning (and to a smaller extent during oxygen burning). A slow destruction appears during helium burning by ^{25}Mg(n,γ)^{26}Mg, and a faster one during carbon burning by ^{25}Mg(p,γ)^{26}Al and ^{25}Mg(p,γ)^{26}Al*($\beta^{+}\nu_{e}$)^{26}Mg (less than 50 % of the ^{25}Mg produced during helium burning is destroyed in those regions in the Models KE12 and KE15B). It is almost completely destroyed during oxygen burning by ^{25}Mg(α,n)^{28}Si and by the photodisintegration reaction ^{25}Mg(γ,n)^{24}Mg. At core collapse, most ^{25}Mg can be found in the radiative carbon shell, somewhat less in the convective carbon shell and a minor fraction in the convective helium-burning shell.

Similar to ^{25}Mg, the more neutron-rich magnesium isotope ^{26}Mg shows a larger production factor (by $\sim$ 3 to 9) than found by Weaver & Woosley (1995). Compared to that work, this isotope is also more abundant in Model KE15B by a factor of $\sim$ 2 than in Model s145s7b. It is produced during central helium burning by neutron capture on ^{25}Mg. During carbon shell burning also the reaction ^{23}Na(α,p)^{26}Mg contributes and dominates over the destruction by ^{26}Mg(p,γ)^{27}Al. Most of the ^{26}Mg is located in the carbon shell, and a small contribution is found in the convective helium shell (Figs. 5.2C and 5.3C). The contribution from the decay of ^{26}Al (see Sect. 5.2.3) is negligible.

The most neutron-rich sulfur isotope ^{36}S is produced during central helium burning, chiefly from ^{34}S by ^{34}S(n,γ)^{35}S($\beta^{+}\nu_{e}$)^{35}Cl(n,γ)^{36}Cl(p,n)^{36}S. This reaction chain involves the capture of three neutrons. The ^{36}S is destroyed during oxygen burning by ^{36}S(p,γ)^{37}Cl, and also some reduction appears by proton capture during carbon burning. In the presupernova models most of the ^{36}S is located in the carbon shell and in the convective helium shell (at about half the abundance). In comparison to Weaver & Woosley (1995) the production factor of ^{36}S is about 2 to 3 times larger.

5.3.4 The s-process

The abundances of heavier neutron-rich isotopes are chiefly a product of the neutron capture during helium burning. This is the stage were most of the s-process occurs in massive stars. Woosley & Weaver (1995) derive a method of estimating the s-process exposure using the depletion of ^{54}Fe (i.e. its initial mass fraction $\sim 7.5{\cdot}10^{-5}$ and its depletion). As usual the neutron exposure is defined

$$\tau_{\mathsf{n}} = \int_0^\infty \rho X_{\mathsf{n}} \, \mathrm{d}t \ , \tag{5.1}$$

where X_{n} is the neutron mass fraction. Before oxygen burning, ^{54}Fe(n,γ)^{55}Fe is the by far dominant destruction rate for ^{54}Fe and essentially no new ^{54}Fe is produced. Thus the neutron exposure during helium, carbon, and neon burning is (Woosley & Weaver 1995)

$$\tau_{\mathsf{n}} = 2.4{\cdot}10^{-7}\,\mathrm{g\,s\,cm^{-3}} \times \ln\left(\frac{\text{initial } ^{54}\text{Fe mass fraction}}{\text{final } ^{54}\text{Fe mass fraction}}\right) . \tag{5.2}$$

Values of $\tau_{\mathsf{n}} \approx (5\ldots6){\cdot}10^{-7}\,\mathrm{g\,s\,cm^{-3}}$ are implied by the ^{54}Fe abundance after central helium depletion in the centers of the Models KE12 and KE15B. This is to be compared to $\tau_{\mathsf{n}} = 1.3{\cdot}10^{-6}\,\mathrm{g\,s\,cm^{-3}}$ in a $25\,\mathrm{M}_\odot$ stellar model of initially solar composition studied by Woosley & Weaver (1995). During early helium burning (70 % helium left in the core) values of $\tau_{\mathsf{n}} \approx 9{\cdot}10^{-7}\,\mathrm{g\,s\,cm^{-3}}$ are reached temporarily, but later during central helium burning this is diluted by mixing ^{54}Fe from above the core. Therefore the "true" local neutron exposure may be much higher than estimated by Eq. (5.2) if mixing does appear. After termination of central helium burning, the ^{54}Fe mass fraction drops to $\sim 10^{-8}$ in a small region at the upper edge of the former convective helium core, corresponding to $\tau_{\mathsf{n}} \approx 2{\cdot}10^{-6}\,\mathrm{g\,s\,cm^{-3}}$. This region becomes later part of the outer C/O core which contains most of the neutron-rich sulfur and magnesium isotopes. However, as a major difference to Woosley & Weaver (1995), the models of the present work show a stronger s-process in the convective helium shell, $\tau_{\mathsf{n}} \approx 2{\cdot}10^{-7}\mathrm{g\,s\,cm^{-3}}$, and consequently a higher abundance of the neutron-enriched species like ^{36}S.

Another measure of the strength of the s-process is the total amount of neutrons captured by the elements with mass number 56 and higher. Before oxygen burning, the neutron capture is the only way to change the total mass fraction of these elements. In Table 5.2 the mean value of neutrons captured by heavy elements per ^{56}Fe seed nucleon inside the helium core, excluding the iron core, are given. This takes only those nuclei into account which are included in the presently used reaction network. That is, only a fraction $f_{N\sigma}$ of all neutrons that actually would be captured if all heavy isotopes were taken into account. The quantity $f_{N\sigma}$ is the ratio of the neutron capture cross section per gram, $N_\mathrm{A} \sum_k Y_k \sigma_k$, for the heavy isotopes included to the "true" neutron capture cross section per gram for all isotopes. Here, σ_k is the neutron capture cross section of species k, and N_A is the Avogadro constant. Unfortunately, $f_{N\sigma}$ is not constant but changes with the strength of the s-process. From the solar distribution of s-process nuclei a value of ~ 0.5 might be a good

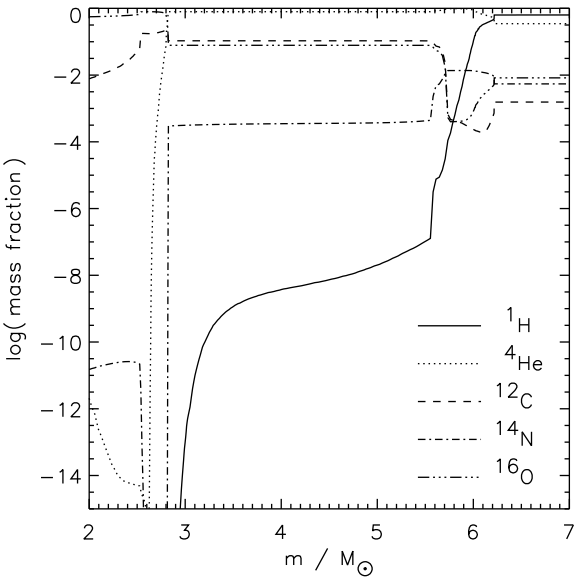

Figure 5.1: Mass fractions of ^{1}H, ^{4}He, ^{12}C, ^{14}N, and ^{16}O at onset of the core-collapse in a $20\,M_\odot$ model with an initial equatorial rotation rate of $200\,\mathrm{km\,s^{-1}}$, as a function of the mass coordinate m (Model E20B). Note that the proton mass fraction exceeds $1{\cdot}10^{-7}$ at the outer edge of the convective helium burning shell ($m = 5.6\,M_\odot$) and stays around $1{\cdot}10^{-8}$ in the major part of it.

estimate (Clayton 1968, Fig. 7-20), i.e., the n_{cap} should be about two times higher than $f_{N\sigma}n_{\mathrm{cap}}$.

In the two models of the present work, $f_{N\sigma}n_{\mathrm{cap}}$ is about three times higher than in those of Weaver & Woosley (1995), indicating a much stronger s-process. Inside the carbon shell values as high as $f_{N\sigma}n_{\mathrm{cap}} \approx 9$ are reached. The neutrons are released by the destruction of ^{22}Ne, ^{23}Na, and other nuclei with an excess of neutrons relative to the α-chain isotopes.

5.4 Nucleosynthesis in the growing helium shell

In Sect. 3.2.1 it was already noted the that rotationally induced mixing allows for the dredge-down of protons into the helium burning shell. This injection of protons into hot burning layers can cause interesting new nucleosynthesis paths (Jorison & Arnould 1989). In Fig. 5.1 an extreme case is shown as it appeared in Model E20B. Shortly before core collapse, hydrogen becomes as abundant as 10^{-7} by mass at the upper edge of the convective helium shell. Where the hydrogen abundance in the helium convective shell drops to 10^{-10} the temperature already exceeds $1.4{\cdot}10^{8}\,\mathrm{K}$. The two cases displayed in Figs. 5.2 and 5.3 are less extreme in this respect, but still some major differences in the final yields relative to the calculations of Weaver & Woosley (1995) arise.

The other important mixing due to the expansion of the convective helium shell is that of ^{14}N into these hot burning layers. Since this mixing occurs only shortly before the core collapse, products of the reaction chains starting from ^{14}N, which would otherwise be destroyed during helium burning, can survive and be expelled by the supernova explosion.

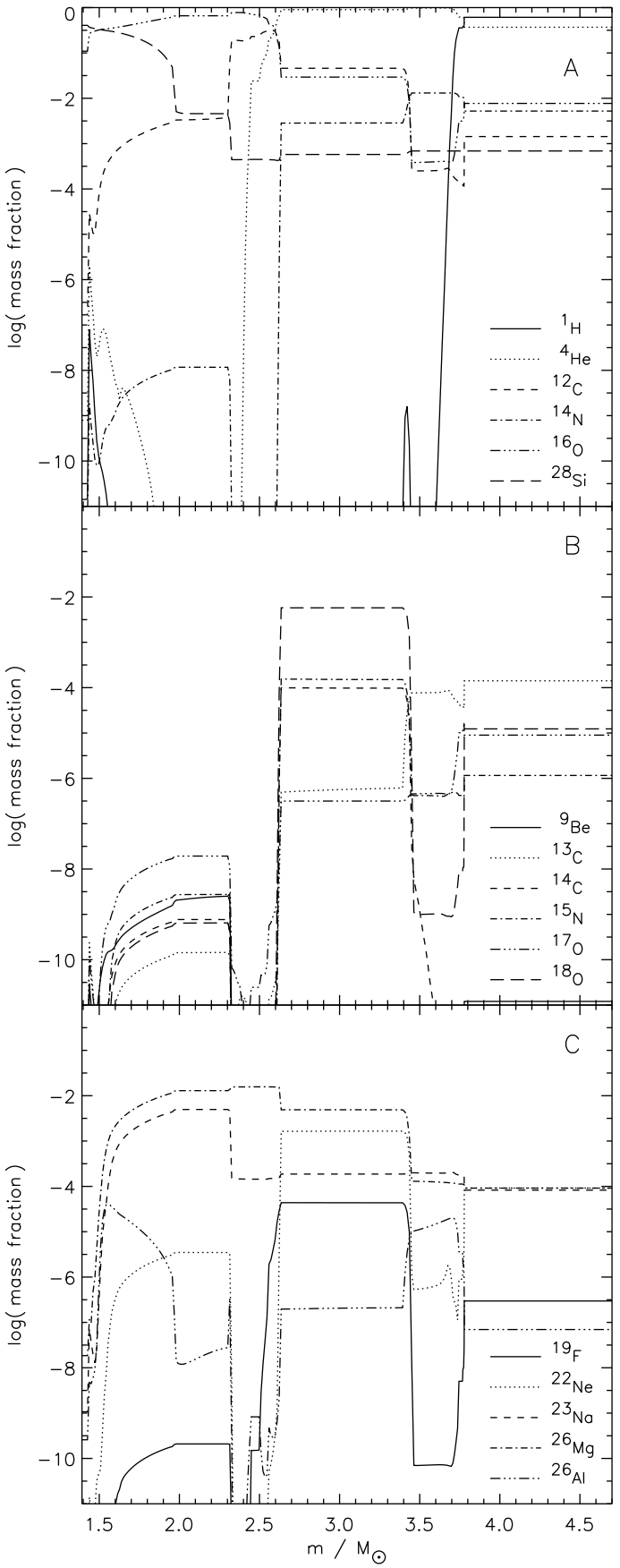

Figure 5.2: Mass fractions of selected isotopes at onset of the core collapse in a $12\,M_\odot$ star with a ZAMS equatorial rotational velocity of $\sim 200\,km\,s^{-1}$ (Model KE12), as function of the mass coordinate m from the outer edge of the iron core out to some point in the convective envelope (the chemical composition does not change from this point on). Panel **A** gives the major species responsible for the nuclear energy generation, ^{1}H, ^{4}He, ^{12}C, ^{14}N, ^{16}O, and ^{28}Si. In Panel **B** the distribution of ^{9}Be, ^{13}C, ^{14}C, ^{15}N, ^{17}O, and ^{18}O are displayed and in Panel **C** ^{19}F, ^{22}Ne, ^{23}Na, ^{26}Mg, and ^{26}Al are shown. Model KE12 is calculated with the same set of mixing-parameters as Model E12 (Table 2.3), but the whole evolution is followed with KEPLER and using the 200 isotope network of Weaver & Woosley (1995).

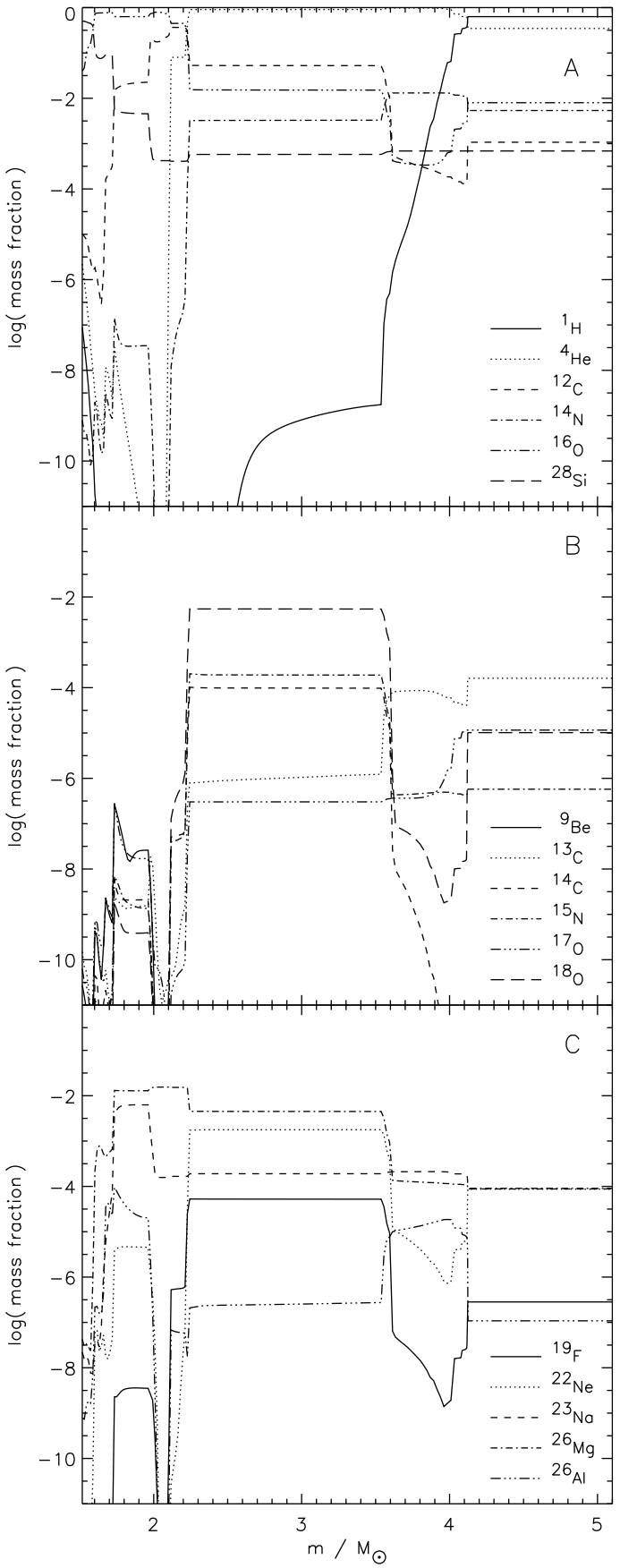

Figure 5.3: Mass fractions of selected isotopes at onset of the core collapse in a $15\,M_\odot$ star with a ZAMS equatorial rotational velocity of $200\,km\,s^{-1}$ (Model `KE15B`), as function of the mass coordinate m from the outer edge of the iron core out to some point in the convective envelope (the chemical composition is constant from this point on). Panel **A** gives the major species responsible for the energy generation, ^{1}H, ^{4}He, ^{12}C, ^{14}N, ^{16}O, and ^{28}Si. In Panel **B** the distribution of ^{9}Be, ^{13}C, ^{14}C, ^{15}N, ^{17}O, and ^{18}O are displayed and in Panel **C** ^{19}F, ^{22}Ne, ^{23}Na, ^{26}Mg, and ^{26}Al are shown. Model `KE15B` is calculated with the same set of mixing-parameters as Model `E15B` (Table 2.3), but the whole evolution is followed with KEPLER, using the 200 isotope network of Weaver & Woosley (1995).

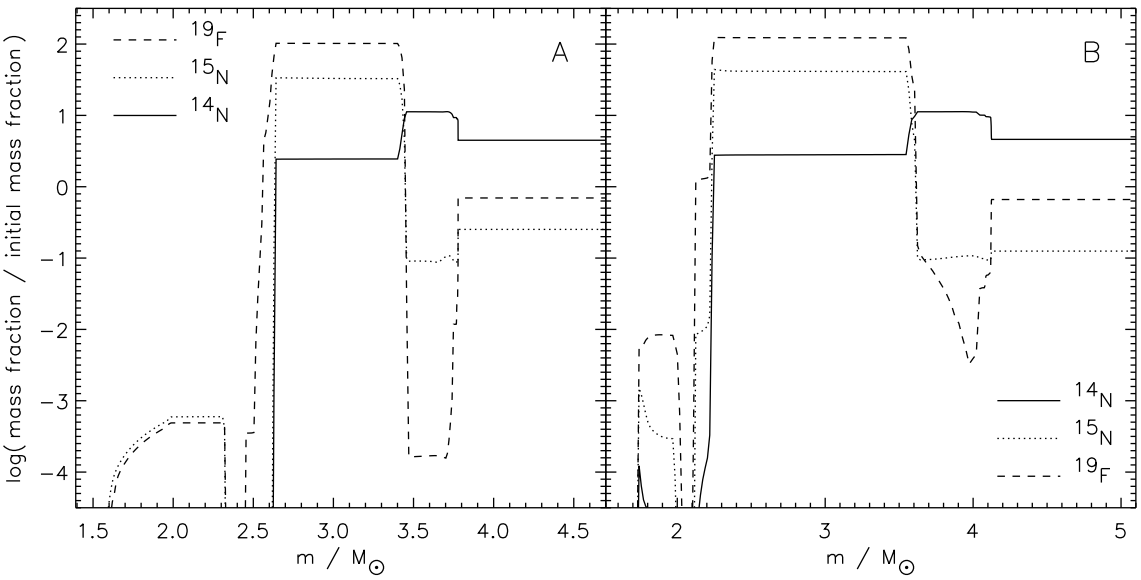

Figure 5.4: Abundance of ^{14}N (solid line), ^{15}N (dotted line), and ^{19}F (dashed line) relative to the initial abundance, as a function of the mass coordinate m. Shown are the distribution at onset of core collapse for Model KE12 (Panel **A**) and Model KE15B (Panel **B**) from the upper edge of the iron core to some point in the convective envelope.

5.4.1 Conversion of ^{14}N into ^{14}C and ^{18}O

The final production factors of ^{14}N in the rotating models of the present work would be even larger than actually found at the presupernova stage were if not for mechanism that is absent in the models of Weaver & Woosley (1995) but which operates here to destroy it again. After core and shell hydrogen burning, ^{14}N has its CNO equilibrium abundance (Sect. 3.1) in the helium layers above the C/O core, and is the most abundant isotope of the CNO group. However, during helium burning the reaction ^{14}N(α,γ)^{18}F($\beta^+\nu_e$)^{18}O destroys ^{14}N. Now the rotating models of the present work show an extended convection zone in the helium shell, and this is responsible for the destruction of the major part of the ^{14}N contained in the helium core (see the lower value of ^{14}N in the convective helium shell compared to the layers above in Figs. 5.2 and 5.3). During this phase, the destruction of ^{14}N is much stronger than its primary production by ^{13}C(p,γ)^{14}N, as can be seen from the decrease of the ^{14}N mass fraction in Fig. 5.4 and its lower value inside the convective helium shell compared to the radiative helium layers.

The ^{18}O produced by α-capture on ^{14}N is again destroyed by ^{18}O(p,α)^{15}N and ^{18}O(α,γ)^{22}Ne during helium burning. The latter reaction becomes important only at the high temperatures of the helium-burning shell shortly before core collapse. Since ^{14}N is also mixed down into the growing convective helium-burning region shortly before core collapse, much of the ^{18}O remains in the helium shell (Figs. 5.2 and 5.3), and that increases the amount of ^{18}O in Model KE15B relative to Models s135s7b and s145s7b.

A high concentration of the radioactive isotope ^{14}C (half life 5776 yr) is built up in the convective helium shell at the onset of core collapse. This is mainly

produced by ^{14}N(n,p)^{14}C and by ^{17}O(p,α)^{14}C. Its destruction is by β^--decay at low temperatures, but dominated by ^{14}C(p,γ)^{18}O at the bottom of the convective helium shell. Neither its contribution to the production of ^{18}O, nor that of ^{15}N by ^{14}C(p,γ)^{15}N, is important, but it might become observable in the remnant of a supernova.

5.4.2 Fluorine

In the reaction chains of the CNO isotopes in the hot burning regime of the extended convective helium shell an appreciable amount of fluorine is produced by ^{18}O(p,γ)^{19}F and ^{15}N(α,γ)^{19}F Fig. 5.4. Both production channels are possible due to the dredge-down of protons into the convective helium shell. The first is affected directly and the second is due to the production of ^{15}N from ^{14}N. At the high temperatures of the contracting helium shell shortly before core collapse the reaction ^{18}O(n,γ)^{19}O($\beta^-\bar{\nu}_e$)^{19}F might also contribute, but it is not taken into account in KEPLER, because ^{19}O is not part of the 200 isotope nuclear reaction network. The dominant destruction processes of ^{19}F are ^{19}F(p,α)^{16}O and ^{19}F(n,γ)^{20}F at the bottom of the convective helium shell, but both do not become very important in the present calculations. Note that neutrino-induced reactions may also produce significant amounts of ^{19}F during the supernova explosion.

5.4.3 Production of ^{15}N

The isotope ^{15}N is destroyed during hydrogen burning by the reaction ^{15}N(p,α)^{12}C, which is reflected in the small production factors in the two models of Weaver & Woosley (1995). This is commonly found in simulation of the nucleosynthesis in non-rotating massive stars.

However, in the rotating models of the present work the convective helium-burning shell grows considerably in mass shortly before core collapse, and ^{15}N is *produced* by ^{18}O(p,α)^{15}N (see above). Other channels of production during this phase are ^{18}F(n,α)^{15}N and ^{14}N(n,γ)^{15}N. The main channels of destruction are ^{15}N(α,γ)^{19}F and ^{15}N(p,α)^{12}C in about equal amounts. Similar to ^{18}O, enough ^{15}N remains in the convective helium shell at core collapse to obtain a notable production, about one order of magnitude more than in the Models `s135s7b` and `s145s7b`.

This agrees much better with the observations than Weaver & Woosley (1995). In a recent study of molecular clouds in the Large Magellanic Cloud Chin et al. (1998) derived a ratio of ^{15}N/^{14}N of $\sim$ 100. This ratio is only 2...3 times higher than the yields of the present work, while the ratio in the models of Weaver & Woosley (1995) is $\gtrsim$ 25 times smaller than these observations. An additional contribution to the total yield of ^{15}N can be expected from the neutrino-induced nuclear reactions during the supernova (Woosley & Weaver 1995; Hoffman et al. 1998). Interesting to note is that in the regions above the C/O core where high values of ^{15}N is found, low values of ^{14}N are present and vice versa (Figs. 5.4, 5.2, and 5.3). This may cause extreme ratios of ^{14}N/^{15}N in grains that form after the supernova explosion on the matter originating from different regions of the star.

isotope	Model KE12	Model KE15B
^{12}C	$4.597{\cdot}10^{-2}$	$5.262{\cdot}10^{-2}$
^{13}C	$5.620{\cdot}10^{-7}$	$1.048{\cdot}10^{-6}$
^{14}N	$2.848{\cdot}10^{-3}$	$3.267{\cdot}10^{-3}$
^{15}N	$1.516{\cdot}10^{-4}$	$1.902{\cdot}10^{-4}$
^{16}O	$2.934{\cdot}10^{-2}$	$1.519{\cdot}10^{-2}$
^{17}O	$3.154{\cdot}10^{-7}$	$3.027{\cdot}10^{-7}$
^{18}O	$5.767{\cdot}10^{-3}$	$5.433{\cdot}10^{-3}$
^{19}F	$4.358{\cdot}10^{-5}$	$5.231{\cdot}10^{-5}$
^{20}Ne	$1.675{\cdot}10^{-3}$	$1.677{\cdot}10^{-3}$
^{21}Ne	$1.004{\cdot}10^{-5}$	$9.116{\cdot}10^{-6}$
^{22}Ne	$1.650{\cdot}10^{-3}$	$1.774{\cdot}10^{-3}$
^{23}Na	$1.868{\cdot}10^{-4}$	$1.901{\cdot}10^{-4}$
^{24}Mg	$4.373{\cdot}10^{-4}$	$4.426{\cdot}10^{-4}$
^{25}Mg	$3.377{\cdot}10^{-3}$	$3.266{\cdot}10^{-3}$
^{26}Mg	$4.895{\cdot}10^{-3}$	$4.496{\cdot}10^{-3}$
^{27}Al	$9.231{\cdot}10^{-5}$	$8.880{\cdot}10^{-5}$
^{28}Si	$5.767{\cdot}10^{-4}$	$5.782{\cdot}10^{-4}$
^{29}Si	$9.188{\cdot}10^{-5}$	$8.998{\cdot}10^{-5}$
^{30}Si	$1.238{\cdot}10^{-4}$	$1.199{\cdot}10^{-4}$

Table 5.5: Mass fractions of the stable isotopes from carbon to silicon in the convective helium shell at onset of core collapse for the two Models KE12 and KE15B.

ratio	Model KE12	Model KE15B
^{12}C/^{13}C	$8.860{\cdot}10^{4}$	$5.442{\cdot}10^{4}$
^{14}N/^{15}N	$2.013{\cdot}10^{1}$	$1.840{\cdot}10^{1}$
^{16}O/^{17}O	$9.884{\cdot}10^{4}$	$5.331{\cdot}10^{4}$
^{16}O/^{18}O	5.723	3.145
^{20}Ne/^{21}Ne	$1.752{\cdot}10^{2}$	$1.932{\cdot}10^{2}$
^{20}Ne/^{22}Ne	1.116	1.040
^{24}Mg/^{25}Mg	$1.349{\cdot}10^{-1}$	$1.411{\cdot}10^{-1}$
^{24}Mg/^{26}Mg	$9.679{\cdot}10^{-2}$	$1.066{\cdot}10^{-1}$
^{28}Si/^{29}Si	6.501	6.655
^{28}Si/^{30}Si	4.990	5.167

Table 5.6: Isotopic abundance ratios of the stable isotopes from carbon to silicon in the convective helium shell at onset of core collapse for the two Models KE12 and KE15B.

5.4.4 X-grains

In recent investigations of grains in meteorites, the so-called "X-grains" indeed show isotopic anomalies which are compatible with what is found in the helium burning shells of the rotating presupernova models (see Tables 5.5 and 5.6; Hoppe et al. 1994). The low ^{14}N/^{15}N abundance ratio of ~ 20 lies within the range of 13 . . . 180 found in the X-grains. The rather high abundances ratio ^{12}C/^{13}C above $5{\cdot}10^4$ compared to the detected range of 170 . . . 2 500, i.e., low ^{13}C abundance, might easily increase before grain formation by admixing of matter from the radiative helium layers. The silicon abundance ratios in the convective helium shell of the rotating models, however, are more neutron rich than the solar composition and therefore are not in agreement with the X-grain abundances.

5.5 The influence of μ-barriers

A prominent feature of both rotating models investigated here are the mixing inside the envelope and between the envelope and the core during core hydrogen burning. This leads to enrichment of CNO-processed matter (and other species which react at similar temperatures) in the envelope and the depletion of light elements at

the surface. Especially the mixing of helium causes larger helium cores after core hydrogen exhaustion and also at core collapse. This results in a larger destruction of hydrogen and thus in a higher production of helium and other α-nuclei in the core. During central helium burning, the hydrogen-burning shell constitutes an efficient barrier and the mixing in its vicinity is not fast enough to result in nucleosynthesis absent in non-rotating stars. After core helium depletion the rotationally induced mixing becomes slow enough compared to the evolution to significantly alter the nucleosynthesis inside the C/O core. Only the growing helium shell, which mixes ^{14}N and protons, which have been enriched in the outer layers of the helium core due to rotationally induced mixing, into hot helium-burning layers, has significant influence on the nucleosynthesis.

5.5.1 Nucleosynthesis in the envelope

Almost all of the nucleosynthesis and enrichment of processed matter in the envelope occurs during core hydrogen burning. Since the efficiencies of rotationally induced mixing were adjusted to satisfy the observational constraints on surface enrichment during central hydrogen burning (Sect. 2.3), this does not fix the amount of internal mixing during that phase — at least within some limits. Indeed, both models, Models `KE12` and `KE15B`, show important differences in their interiors, which later are reflected in the nucleosynthesis yield.

If the rotationally induced mixing is assumed to be insensitive to μ-gradients (Model `KE12`), a gradient of processed matter builds up which reaches from the convective core to the surface of the star, including enrichment of helium (Sect. 3.1.1). In contrast, if μ-gradients are important for the rotationally induced mixing, a μ-barrier forms which prevents further mixing between core and envelope early during core hydrogen burning. As replacement for this inhibitation, the rotationally induced mixing is (assumed to be) more efficient above that the μ-barrier, in order to meet the requirements for the surface abundance changes. In this latter case, above the μ-barrier the gradient of processed matter in the envelope is much flatter than in Model `KE12`. This means the the total amount of matter processed in the core or close to it is less in the envelope of `KE15B`. An example for this is the stronger enrichment of helium in the envelope of Model `12` at core collapse. However, during core hydrogen burning the nuclear processing that occurs above the μ-barrier is stronger in Model `KE15B`. At core collapse, this is reflected, for example, in the stronger depletion of ^{12}C in the envelope of Model `KE15B`.

5.5.2 Core sizes and late nucleosynthesis

Even though Model `KE15B` has a smaller helium core than Model `s145s7b`, the total production of ^{4}He is larger. Two effects are chiefly responsible for this. First, the C/O core is smaller in Model `KE15B` due to the less efficient semiconvective mixing and the inhibiting effect of μ-gradients on the rotationally induced mixing. The second and more important contribution is the larger enrichment of helium in the envelope caused by the rotationally induced mixing during central hydrogen burning.

Some of the first effect may also be attributed to the improved treatment of hydrogen burning (Appendix B) compared to Woosley & Weaver (1995), which should cause a faster growth of the helium core during central helium burning.

In contrast, Model `KE12` develops a larger C/O core than Model `s135s7b` of Weaver & Woosley (1995) which has a comparably massive helium core. This effect is large enough to balance the higher helium enrichment in the envelope and therefore the total production factor of ^{4}He is comparable to Model `s135s7b`. However, the larger C/O core, about the size of that of Model `s145s7b`, contains a comparable amount of ^{16}O and ^{12}C, but because of the smaller initial mass, higher production factors result. Most of ^{16}O is found in the carbon-burning shell and the region between the carbon-burning shell and the helium-burning shell. In the latter region, also the major part of ^{12}C is found which remained from central helium burning. In the pre-collapse model, ^{20}Ne and ^{24}Mg are mainly found in the carbon-burning shell. The high mass of ^{28}Si can be understood from the small iron core (1.39 $M_\odot$) inside the rather large C/O core (2.33 $M_\odot$; see Table 5.1). It is found in the oxygen-burning convective shell.

Chapter 6

Summary

This work presents the first numerical simulation of the evolution of rotating stars from the ignition of nuclear burning until the supernova stage. Emphasis has been placed on the modification of the evolution induced by rotation. This includes an examination of the transport process for redistributing angular momentum and composition and the resultant changes that occur in the stellar structure and nucleosynthesis. The distribution of angular momentum in the presupernova stage has also been of particular interest.

For this investigation, two different one-dimensional hydrodynamic stellar evolution codes were extended to include angular momentum as a new local variable. The effects of centrifugal forces on the stellar structure were treated in latitudinally averaged way. Rotationally induced instabilities were included (Sect. 2.2). They comprise secular and dynamic shear instabilities, the Solberg-Høiland instability, the Eddington-Sweet circulation, and the Goldreich-Schubert-Fricke instability. Uncertain parameters of rotationally induced mixing were calibrated using observational constraints, namely the surface abundances of massive main sequence stars (Sect. 2.3). Observed surface enrichments with CNO-processed matter were reproduced for stars in the mass range from $5\,M_\odot$ to $60\,M_\odot$, for typical initial stellar rotation rates. Stellar mass loss and its dependence on the surface rotation rate were taken into account (Sect. 2.4).

The evolution of stars of approximately solar composition in the mass range from $10\,M_\odot$ to $25\,M_\odot$ was modeled up to iron core collapse, the immediate presupernova stage. The initial total angular momentum of the models was chosen to give an equatorial rotational velocity of $\sim 200\,\mathrm{km\,s^{-1}}$ at central hydrogen ignition, a typical value for these stars (Sect. 2.1.4). Models with lower and higher initial rotation rate were also investigated, and non-rotating stars were calculated for comparison. Models that used different assumptions about the stabilizing effect of gradients in the mean molecular weight on rotationally induced instabilities were computed and compared. Observations seem to require that gradients in the mean molecular weight inhibit rotationally induced mixing much less than in the pioneering models of Endal & Sofia (1978). This conclusion is also supported by recent investigations of the physics of meridional circulations, shear instabilities, and semiconvective mixing (Maeder & Zahn 1998).

Internal stellar structure. During central hydrogen burning, the products of the burning are mixed into the stellar envelope and new fuel is supplied to the convectively burning stellar core by rotationally induced mixing. Since this mixing proceeds on a time-scale comparable to the thermonuclear time-scale of hydrogen burning, a gradient of processed matter builds up inside the radiative envelope. The processed matter has a higher mean molecular weight, μ, than the pristine matter of the star, and therefore a gradient of the mean molecular weight results.

If rotationally induced mixing occurs by processes that depend sensitively upon these gradients, they act as a barrier (μ-barrier), and mixing between the core and the envelope is inhibited. Exactly when this inhibitation becomes important depends on the initial angular momentum of the star. The amount of mixing that occurs between the core and the envelope is affected accordingly. Mixing inside the envelope also increases for larger initial angular momentum, since the dominant mixing process, Eddington-Sweet circulation, has an efficiency that increases as the square of the stellar rotation rate.

As the evolution of the star proceeds to later stages, the time-scale for rotationally induced mixing becomes too long in comparison to the evolutionary time-scales to constitute an important source of large-scale mixing. Also, the mixing is not able to dissolve the molecular weight barrier which forms in the core during central helium burning. In general, rotationally induced mixing does not strongly affect the stellar structure after central helium ignition. The evolution of the star from this point until core collapse is similar to that of a non-rotating star of same structure at this time, except for the differences in the nucleosynthesis discussed below.

For models where rotationally induced mixing is assumed to be insensitive to gradients in the mean molecular weight, no μ-barrier inhibits the mixing. This affects the mixing between the core and the envelope during central hydrogen burning. The μ-barrier in the superadiabatic part of the core during central helium burning is eroded by shear instabilities. Consequently, the convective core can grow unhindered. As a result, the helium cores are more massive, corresponding to non-rotating stars with about 25 % higher initial mass. Inside this helium core, the C/O core is also larger than that of a non-rotating star with same helium core mass. Towards the end of central helium burning, fresh helium is mixed into the convective core both by the continuing growth of this core and by rotationally induced mixing. The fresh helium preferentially converts carbon into oxygen instead of producing new carbon by the triple-alpha process. This reduces the carbon abundance in the core. Except for this, the effect of rotationally induced mixing is small after helium ignition for the reason outlined above. In particular, also in this case, the hydrogen burning shell constitutes an efficient barrier for mixing processes — indeed even more efficient, because the core rotates slower as in the case where μ-gradients were considered (see below). A consequence of the enlarged cores is that the limit on the initial stellar mass for core collapse supernovae is smaller for higher initial rotation rates.

At central hydrogen ignition, the stars establish almost uniform rotation. If a molecular weight barrier forms during central hydrogen burning, angular momentum is trapped inside the core and differential rotation results, with up to a factor of ~ 3

in the rotation rate between the core and the envelope. If μ-barriers are unimportant for the rotationally induced mixing, the stars stay close to rigid rotation until the end of central hydrogen burning. Since this barrier forms later in the faster rotators, stars having different initial rotation rates may end up with similar specific angular momenta in the core at the end of central hydrogen burning (Figs. 3.6B and 3.9). Due to angular momentum transport during core helium burning, they may become even more similar in the pre-collapse stage (Fig. 3.20). Some angular momentum gets lost from the core during the restructuring that occurs after core hydrogen exhaustion, but during central helium burning the hydrogen-burning shell constitutes an efficient barrier that inhibits the transport of angular momentum out of the core. Even so, the average angular momentum of the core may decrease somewhat, since it grows into regions with lower specific angular momentum on top of it. The helium core itself stays close to uniform rotation (Fig. 3.5). During central helium burning rotationally induced mixing processes already become slow compared to the evolution, and after core helium exhaustion they do not cause any relevant transport of angular momentum.

Only convective processes are rapid enough to notably redistribute angular momentum during the late stages of stellar evolution. Within the assumptions made, rigid rotation results in convective regions, transporting angular momentum from their bottom to their top. Subsequent phases of convective central and shell burning stages give some outward transport of angular momentum inside the carbon-oxygen core. Since none of the convective shells penetrates through the outer boundary of the C/O core, the angular momentum remains trapped inside (Figs. 3.7B and 3.10). The outer boundary of the helium core constitutes a similar barrier.

This has interesting consequence for the final angular momentum in the core. First, the different convective burning shells leave their fingerprint not only in the chemical composition, but also in the angular momentum distribution: a spiky profile results at the onset of core collapse (Fig. 3.20). The high peaks correspond to the upper edges of the most recently active convection zones and the deep valleys to their bottoms. Shells of similar composition tend to rotate almost rigidly. Second, even the slowest rotating core of the Type II supernova progenitor stars considered here would result in a neutron star rotating close to break-up if angular momentum were conserved during the collapse. This is not necessarily in contradiction with observations of young neutron stars in supernova remnants, even though the fastest of these rotates much slower. These pulsars are already hundreds of years old, and recent theoretical investigations of hot, newly born neutron stars indicate they may spin down to the observed rotation rates within about a year by emitting gravitational waves (Lindblom et al. 1998). The electro-magnetic radiation emanating from pulsars is trapped inside the supernova ejecta during that time, but the gravitational radiation of these very young neutron stars might become detectable in the future (Owen et al. 1998).

Surface properties. In the HR diagram the rotating stars ignite central hydrogen burning at lower effective temperatures and luminosities than their non-rotating counterparts of same initial mass. In the course of central hydrogen burning they

evolve to the higher luminosities the more internal mixing occurs, i.e., the higher the initial angular momentum of the star. A widening of the main sequence results. But the strength of the inhibiting effect of gradients in the mean molecular weight on the rotationally induced mixing processes also plays an important rôle here (Fig. 4.1). Depending on their initial rotation rate, stars of same initial composition but different initial angular momentum can evolve to the same position in the HR diagram. Therefore a given position on the main sequence band in the HR diagram does not unambiguously correspond to one initial mass (Sect. 4.1.1), i.e., there is no unique mass-luminosity relation for main sequence stars.

During central hydrogen burning, the products of nuclear burning in the stellar interior appear at the surface of the star. This effect for the CNO isotopes and helium was used here to calibrate the mixing efficiencies. Additionally, the isotopes of lithium, beryllium and boron are rapidly depleted at the surface, in agreement with the observations (Sect. 4.1.3). These abundance changes become more marked with increasing stellar mass and with larger initial angular momentum of the star. Also the radionuclide ^{26}Al appears at the surface.

The dredge-up by the convective envelope in the red supergiant stage enhances the surface abundance of ^{14}N at the expense of ^{12}C and ^{16}O. It can penetrate the μ-barrier built up during central hydrogen burning and deplete ^{16}O at the surface. In the faster rotators, however, strong mixing occurs already during central hydrogen burning, so that the abundance changes due to dredge-up are much smaller (Fig. 4.12).

In Sect. 4.3 the effect of mass outflow through the inner or outer boundary of a rigidly rotating stellar envelope on its rotational frequency is discussed (Heger & Langer 1998). It causes a change of the specific angular momentum in the envelope and alters its rotation rate besides what results from contraction or expansion (Fig. 4.19). For constant upper and lower boundaries of the envelope, which is found a good approximation for convective envelopes (Fig. 4.17), a spin-down occurs for mass outflow through the upper boundary — which corresponds, e.g., to the case of stellar wind mass loss from a convective envelope (Langer 1998) — while a spin-up results from mass outflow through the lower boundary (Fig. 4.13).

The latter situation is found in evolutionary models of a rotating $12\,M_\odot$ star at the transition from the Hayashi-line to the blue supergiant stage. The star increases its surface rotational velocity by one order of magnitude above the value which would result in case of local angular momentum conservation. The star would increase its rotational velocity even further would it not arrive at critical rotation (Sect. 4.3.2, Fig. 4.19), with the consequence of strong mass and angular momentum loss. At this point, the specific angular momentum loss $\dot{J}/\dot{M}$ reaches about $8\,10^{19}\,\mathrm{cm^2\,s^{-1}}$ (Fig. 4.18).

The geometry of circumstellar matter around stars which undergo a red $\rightarrow$ blue transition may be strongly affected by the spin-up. It is proposed that this was the case for the progenitor of SN 1987A, the only massive star of which we know that it actually performed a red $\rightarrow$ blue transition. The blue supergiant studied by Brandner et al. (1997), around which they found a ring nebula as well, is another candidate. Also, B[e] stars may be related to the post-red supergiant spin-up

(Sect. 4.3.3.1). Finally, the spin-up mechanism studied here may be relevant for bipolar outflows from central stars of protoplanetary nebulae (Sect. 4.3.3.4), from stars in the transition phase from the red supergiant stage to the Wolf-Rayet stage (Sect. 4.3.3.2), and from pre-main sequence stars (Sect. 4.3.3.3).

In Sect. 4.4, the pulsational properties of red supergiant models are analyzed (Heger et al. 1997). Due to the inclusion of rotation in the stellar evolution calculations, the red supergiant models evolve to high values of L/M. Consequently, their pulsations are characterized by long periods (up to 3 000 days) and large growth rates, much greater than previously found in the work of Li & Gong (1994). It thus may be argued that red supergiants might display large amplitude pulsations like AGB stars, preferentially as OH/IR sources, and perhaps even evolve a "superwind". Due to the marked increase in the luminosity of red supergiants during the last couple of 10^4 yr, such a behavior is most likely to happen during the final evolutionary phases preceding the supernova explosion. Observed properties of Type II supernovae and their remnants, and of overluminous OH/IR sources, give some support to this scenario.

However, more detailed and extended analysis, taking into account non-linear effects occurring at high amplitudes and the possible effects of shock waves should be performed in the future, in order to determine more precisely the amplitudes of the pulsations and to accurately estimate the region in which red supergiant pulsations are important for the evolution of the stars and the presupernova circumstellar matter.

Nucleosynthesis. The nucleosynthesis occurring in the rotating massive stars has been studied in detail using an extended 200 isotope nuclear reaction network. The evolution of two typical models has been followed from core hydrogen ignition until core collapse.

The mixing inside the envelope and between core and envelope during core hydrogen burning leads to an enrichment of processed matter in the envelope up to the surface of the star. For example, nitrogen, sodium and the radioisotope ^{26}Al are enriched, while carbon is depleted. Due to this, the envelope, and thus the whole stars, gets enriched in these isotopes. The strength of the enrichment varies for different isotopes, depending on the sensitivity of the rotationally induced mixing to gradients in the mean molecular weight. The mixing in the envelope also causes a rapid destruction of the light isotopes early during core hydrogen burning.

An interesting effect caused by rotationally induced mixing is the dredge-down of protons into the hot burning region of the convective helium-burning shell during the late evolution of the star (Sect. 3.2.1). After the extinction of the hydrogen shell source, protons can be transported downward into the upper layers of the helium core by rotationally induced mixing without being burned immediately. While the C/O core continues its contraction, the convective region in the helium shell grows and eventually reaches layers, still inside the helium core, where hydrogen is enriched. At the same time, ^{14}N, is mixed down. This produces, e.g., large amounts of ^{18}O and from this ^{19}F by proton capture and ^{22}Ne by α capture (Figs. 5.2 and 5.3). An important feature is the production of ^{15}N from ^{18}O by ^{18}O(p,α)^{15}N. The production

of ^{15}N is about ten times higher than in the models by Weaver & Woosley (1995), and therefore a ^{15}N/^{14}N ratio is obtained which is much closer to that observationally determined by Chin et al. (1998) in a young stellar cluster of the Large Magellanic Cloud. This means that ^{15}N becomes a product of massive stars and not only of novae (Timmes et al. 1995). The peculiarities in the abundance ratios found in the convective helium shell at core collapse may be related to those found in the X-grains in some meteorites.

A big effect of the rotationally induced mixing is a stronger production of alpha-nuclei, ^{4}He, ^{12}C, ^{16}O, ^{20}Ne, ^{24}Mg, and ^{28}Si. This is caused by the helium mixing during central hydrogen burning and the resulting larger core sizes. The ratio of their production also changes (Table 5.3), but depends on the sensitivity of rotationally induced mixing on gradients in the mean molecular weight, especially whether rotationally induced mixing is able to dissolve the barrier which stops the growth of the central convection zone during core helium burning.

Another important difference is the higher production of the neutron-rich isotopes ^{25}Mg, ^{26}Mg, ^{36}S, and the s-process in comparison to Weaver & Woosley (1995). Their main production during helium burning is caused by the higher neutron exposure strength in comparison to Woosley & Weaver (1995).

Despite ^{26}Al appears at the surface already during core hydrogen burning due to rotationally induced mixing, its abundance and the mass loss rate are too low in the Type II supernova progenitor stars to have a significant contribution to the Galactic ^{26}Al mass. Most of the ^{26}Al lost in winds is expelled after the first dredge-up while the star is a red supergiant (Sect. 5.2.3). However, the total yield is dominated by the amount of ^{26}Al released during the supernova explosion (Sect. 5.3.2).

Appendix A

An improved treatment of nuclear burning in the STERN code

In the stellar evolution code STERN (Sect. 2.1.6.1) the hydrodynamic evolution and the energy transport (stellar structure equations; Sect. 2.1.1), chemical mixing processes (by convection and rotationally induced mixing; Sect. 2.2), and the nuclear reaction network (Sect. 2.1.5) are solved in "operator split", a method used in many stellar evolution codes (see also Hofmeister et al. 1964; Langer et al. 1988). Different methods are used in KEPLER (Weaver et al. 1978; Sect. 2.1.6.2) and, e.g., by Eggleton (1971). The advantage of solving the nuclear reaction network separately from the stellar structure equations is the increased computational performance. In STERN, the energy generation rates are computed from the composition at the beginning of a time-step, the nuclear reaction network and mixing processes are then treated subsequently, using high resolution in time for the burning where necessary. However, a problem occurs if the local energy generation is dominated by some trace elements injected into regions where they burn on time-scales short compared to the problem time-step. This causes temporarily a false high energy generation rate, although it would actually not contribute much to the total energy release during the time-step. In this case the energy generation rate estimated from the composition at the beginning of the time-step may strongly deviate from the energy release that would result from the total change of the abundances.

Here an approximated correction factor is described. It allows to correct the energy released by each nuclear reaction for the changes of the abundances of the species during a large time-step without having to resolve the nuclear burning time-scale, which could be smaller by orders of magnitude than the time-step necessary for the hydrodynamic evolution. The goal is to achieve a better approximation to the global conservation of energy.

A.1 Simple reactions

Instead of the general case Eq. (2.17), first simple binary reactions of type

$$i + j \rightarrow k + l \tag{A.1}$$

are considered, in which two reactants ($i \neq j$) react to two products (k and l). The temporal change of one species i is then given by (Clayton 1968)

$$\frac{\mathrm{d}Y_i}{\mathrm{d}t} = \sum_{j,k,l} \lambda_{k,l\to i,j}(\rho,T)\, Y_k Y_l - \sum_{j,k,l} \lambda_{i,j\to k,l}(\rho,T)\, Y_i Y_j \ . \tag{A.2}$$

Here $\lambda_{i,j\to k,l}$ is the *reaction rate* of the reaction (A.1), which depends on the density ρ and the temperature T only.

To calculate the temporal evolution of the concentration of the species i in first order, the concentration of the species $j,k,l \neq i$ and the reaction rates $\lambda_{i,j\to k,l}$ are assumed constant. Then, only the simple, ordinary differential equation (ODE)

$$\frac{\mathrm{d}Y_i}{\mathrm{d}t} = C_{1,i} - C_{2,i} Y_i \tag{A.3}$$

has to be integrated, where

$$C_{1,i} = \sum_{j,k,l} \lambda_{k,l\to i,j}(\rho,T)\, Y_k Y_l \tag{A.4}$$

and

$$C_{2,i} = \sum_{j,k,l} \lambda_{i,j\to k,l}(\rho,T)\, Y_j \ . \tag{A.5}$$

For $t \to \infty$ the left hand side of Eq. (A.3) becomes zero and the *equilibrium concentration* $Y_{\mathrm{eq},i}$ adjusts

$$Y_{\mathrm{eq},i} := \lim_{t\to\infty} Y_i = \frac{C_{1,i}}{C_{2,i}} \ .$$

The general solution of the differential equation (A.3) is given by

$$Y_i(t) = \zeta_i\, e^{-tC_{2,i}} + Y_{\mathrm{eq},i} \ ,$$

where the integration constant ζ_i is chosen such that for $t = 0$ the initial concentration $Y_{0,i} := Y_i(t=0)$ results, i.e. $\zeta_i := Y_{0,i} - Y_{\mathrm{eq},i}$, and thus

$$Y_i(t) = (Y_{0,i} - Y_{\mathrm{eq},i})\, e^{-tC_{2,i}} + Y_{\mathrm{eq},i} \ . \tag{A.6}$$

The energy generation rate

$$\varepsilon_{i,j\to k,l} := E_{i,j\to k,l}\, \lambda_{i,j\to k,l}(\rho,T)\, Y_i Y_j$$

of the reaction (A.1) in turn is a function of time t, even if, as above, $\lambda_{i,j\to k,l}$ is assumed to be constant with time, because, in the approximation considered here, Y_i and Y_j themselves are functions of the time. The quantity $E_{i,j\to k,l}$ designates the energy released per reaction (A.1).

Considering a finite interval of time $[0,\tau]$, a mean energy generation rate

$$\overline{\varepsilon}_{i,j\to k,l} := \frac{1}{\tau}\int_0^\tau \varepsilon_{i,j\to k,l}(t)\ \mathrm{d}t = \frac{\varepsilon_{i,j\to k,l}(0)}{\tau}\int_0^\tau \frac{Y_i(t)}{Y_{0,i}}\frac{Y_j(t)}{Y_{0,j}}\ \mathrm{d}t \tag{A.7}$$

can be estimated. To first approximation, as above, the temporal evolution of the concentrations Y_i of the individual species is assumed to be independent of each other. In many cases the temporal averaging over the product of the concentrations can be approximated by the product of the time-averaged concentrations $\overline{Y_i}$

$$\overline{\varepsilon}_{i,j\to k,l} \approx \varepsilon_{i,j\to k,l}(0) f_i f_j \ , \tag{A.8}$$

where

$$f_i := \frac{\overline{Y_i}}{Y_{0,i}} \qquad \text{and} \qquad \overline{Y_i} := \frac{1}{\tau}\int_0^\tau Y_i(t)\,\mathrm{d}t \ . \tag{A.9}$$

Otherwise, the integral on the right hand side of Eq. (A.7) has to be computed as a whole (see below), but this has to be done separately for each reaction considered and thus is computationally more expensive.

By inserting Eq. (A.6) in Eq. (A.9) the equation

$$f_i = \frac{1}{\tau}\int_0^\tau \left(\left(1-\frac{Y_{\mathrm{eq},i}}{Y_{0,i}}\right)e^{-\tau C_{2,i}} + \frac{Y_{\mathrm{eq},i}}{Y_{0,i}}\right)\,\mathrm{d}t$$

results and after quadrature

$$f_i = \frac{Y_{\mathrm{eq},i}}{Y_{0,i}} + \frac{1}{\tau C_{2,i}}\left(1-\frac{Y_{\mathrm{eq},i}}{Y_{0,i}}\right)\left(1-e^{-\tau C_{2,i}}\right) \ . \tag{A.10}$$

The numerical evaluation of f_i according to Eq. (A.10) requires a careful examination of the last factor of the last summand on the right hand side, since the difference occurring here leads to numerical extinction for $\tau \ll C_{i,2}^{-1}$ when evaluated naïvely.

For simplification be

$$f_{0,i} := \frac{Y_{\mathrm{eq},i}}{Y_{0,i}} \qquad \text{and} \qquad \alpha_i := \tau C_{i,2}$$

defined such that Eq. (A.10) can be written as

$$f_i = f_{0,i} + (1-f_{0,i})\frac{1-e^{-\alpha_i}}{\alpha_i} \ . \tag{A.11}$$

For $\alpha_i \ll 1$ (i.e. $\tau \ll C_{i,2}$) the numerator of the quotient on the right hand side can be transformed into a rapidly converging series

$$\frac{1-e^{-\alpha_i}}{\alpha_i} = \frac{\alpha_i - \frac{\alpha_i^2}{2} + \ldots}{\alpha_i} = 1 - \frac{\alpha_i}{2} + \ldots$$

and one gets instead of Eq. (A.11) the expression

$$f_i \approx f_{0,i} + (1-f_{0,i})\left(1-\frac{\alpha_i}{2}\right) \ . \tag{A.12}$$

which is numerically stable for small values of α_i.

To decide where to use which of the formulae given above, the following simple rule can be used: If ϵ is the (relative) precision of the data type used, then Eq. (A.11) should be taken if $\alpha_i > \sqrt{\epsilon}$ and Eq. (A.12) otherwise. Substituting f_i (or f_j, respectively) into Eq. (A.8) then gives an approximative value for $\overline{\varepsilon}_{i,j\to k,l}$ in the time interval $[0,\tau]$.

If the integral on the right hand side of Eq. (A.7) is evaluated as a whole

$$\overline{\varepsilon}_{i,j\to k,l} = \varepsilon_{ij\to k,l}(0)\, f_{ij} \tag{A.13}$$

results, where

$$\begin{aligned} f_{ij} \;:=\; & f_{0,i}\, f_{0,j} + f_{0,j}\,(f_i - f_{0,i}) + f_{0,i}\,(f_j - f_{0,j}) \\ & + \frac{(1-f_{i,0})\,(1-f_{j,0})}{\tau\,(C_{2,i}+C_{2,j})}\left(1 - e^{-t(C_{2,i}+C_{2,j})}\right) . \end{aligned}$$

The last term, should again be evaluated numerically as outlined for f_i. Comparing Eqs. (A.8) and (A.13) the relation

$$\ln\frac{f_i\, f_j}{f_{ij}} = \frac{C_{2,i}C_{2,j}\,(1-f_{0,i})\,(f_{0,j}-1)}{12}\tau^2 + \mathcal{O}\left(\tau^3\right) \quad \propto \alpha_i\,\alpha_j + \mathcal{O}\left(\tau^3\right) \tag{A.14}$$

can be found and therefore Eq. (A.8) is a good approximation if $\alpha_i\,\alpha_j \ll 1$. E.g., this is fulfilled if the time-scales on which Y_i and Y_j change are large in comparison to τ.

Another case where approximation (A.8) can be applied is when the time-scale on which one of the species involved (say i) changes is much shorter than τ ($\alpha_i \ll 1$) and the other (say j) is large in comparison to τ ($\alpha_j \gg 1$). In this case the quality of the approximation is

$$\ln\frac{f_i\, f_j}{f_{ij}} \propto \left(\alpha_i + \mathcal{O}\left(\alpha_i^2\right)\right)\left(\frac{1}{2}\alpha_j^{-1} + \mathcal{O}\left(\alpha_j^{-2}\right)\right) .$$

A.2 Self reactions

If also reactions of the type

$$2i \to k + l \tag{A.15}$$

are considered additionally to reactions of type (A.1), then Eq. (A.2) becomes

$$\frac{\mathrm{d}Y_i}{\mathrm{d}t} = \sum_{j,k,l}\lambda_{k,l\to i,j}(\rho,T)\,Y_kY_l - \sum_{j,k,l}\lambda_{i,j\to k,l}(\rho,T)\,Y_iY_j - \sum_{k,l}\lambda_{2i\to k,l}(\rho,T)\,\frac{1}{2}Y_i^2$$

and, following the discussion above,

$$\frac{\mathrm{d}Y_i}{\mathrm{d}t} = C_{1,i} - C_{2,i}Y_i - \frac{1}{2}C_{3,i}\,Y_i^2 \tag{A.16}$$

results instead of Eq. (A.3), where $C_{1,i}$ and $C_{2,i}$ are defined by Eqs. (A.4) and (A.5), and

$$C_{3,i} = \sum_{k,l} \lambda_{2i\to k,l}(\rho, T) \ .$$

The ODE (A.16) is solved by

$$Y_i(t) = Y_{\mathrm{eq},i} + \frac{D_i}{C_{3,i}} \left(\tanh\left(\frac{D_i}{2} t + \xi_i \right) - 1 \right) \ , \tag{A.17}$$

where

$$D_i := \sqrt{C_{2,i}^2 + 2 C_{1,i}\, C_{3,i}}$$

and the integration constant

$$\xi_i = \operatorname{artanh} \frac{C_{3,i} Y_{0,i} + C_{2,i}}{D_i}$$

is determined such that the initial concentration $Y_{0,i}$ is obtained at $t = 0$. The equilibrium concentration is now given by

$$Y_{\mathrm{eq},i} := \lim_{t\to\infty} Y_i = \frac{D_i - C_{2,i}}{C_{3,i}} \ .$$

The determination of the mean energy generation rate for this reaction renders more complicated than in the simple case (A.1), since

$$\overline{\varepsilon}_{2i\to k,l} := \frac{1}{\tau} \int_0^\tau \varepsilon_{2i\to k,l}(t)\ \mathrm{d}t = \frac{\varepsilon_{2i\to k,l}(0)}{\tau} \int_0^\tau \left(\frac{Y_i(t)}{Y_{0,i}} \right)^2 \mathrm{d}t$$

has to be solved, where, accordingly,

$$\varepsilon_{2i\to k,l} := E_{2i\to k,l}\, \lambda_{2i\to k,l}(\rho, T)\, \frac{1}{2} Y_i^2 \ .$$

Substituting Eq. (A.17) into $\overline{\varepsilon}_{2i\to k,l}$ and carrying out the quadrature one obtains

$$\overline{\varepsilon}_{2i\to k,l} = \varepsilon_{2i\to k,l}(0) f_{2i} \ ,$$

where

$$\begin{aligned} f_{2i} \ = \ & \frac{1}{\left(C_{3,i} Y_{0,i}\right)^2 \tau} \Bigg\{ 4 C_{2,i} \ln \frac{\cosh\left(\xi_i\right)}{\cosh\left(\frac{D_i}{2}\tau + \xi_i\right)} \\ & + \left(C_{2,i}^2 + D_i^2\right) \tau - 2\, D_i \frac{\sinh\left(\frac{D_i}{2}\tau\right)}{\cosh\left(\xi_i\right) \cosh\left(\frac{D_i}{2}\tau + \xi_i\right)} \Bigg\} \ . \end{aligned}$$

The last summand can also be rewritten as

$$+2 \left(C_{3,i}\, Y_{0,i} + C_{2,i} - D_i \tanh\left(\frac{D_i}{2}\tau + \xi_i \right) \right) \ ,$$

but this form involves additional numerical extinction. Here the simple approximation (A.8) of the previous section is acceptable for time-steps below $\tau \approx \left(Y_{0,i}\, C_{3,i}\right)^{-1}$:

$$\ln \frac{f_i^2}{f_{2i}} = \frac{C_{3,i}\, Y_{0,i}}{2} \tau + \mathcal{O}\left(\tau^2\right) .$$

A.3 Application

The types of reactions (A.1) and (A.15) used in the two preceding sections involve both exactly two reactants and two products. However, the method can be generalized easily to more or less reactants and products. The constants $C_{1,i}$, $C_{2,i}$ and $C_{3,i}$ have to be redefined such that $C_{1,i}$ contains all source terms for species i, $C_{2,i}$ all sink terms which involve one particle of type i and $C_{3,i}$ all those sink terms which take two particles of species i. The derivation in Sections A.1 and A.2 then applies accordingly.

The method presented here was originally developed in order to treat the burning of trace elements injected into a region were they burn on time-scales which are small in comparison to the stellar evolution time-scale. In case of operator split between computation of energy generation, nuclear reaction network and mixing processes these corrections improve the global energy conservation, i.e. the corrected energy release corresponds better to the amount of matter burned during the time-step τ by the nuclear reaction network.

Unfortunately, if both, the time-scale for mixing and for burning are short in comparison to the model time-step τ, the spatial location of the burning in the mixed region is not be resolved, and therefore also the total effective burning rate is not reproduced. If only the mixing time-scale is short in comparison to τ, but the burning time-scale is comparable or larger, the plain operator split treatment still introduces inconsistencies between the amount of matter processed by nuclear burning and the energy generation rate. A typical example for that is burning of abundant elements in convective regions. The method presented here corrects for the global energy conservation, but at the cost of reducing the effective energy generation rate. The stellar models react to this by adjusting their structure appropriately. Due to the strong temperature-dependence of the nuclear reaction rates, only small deviations in the temperature result. If τ is small in comparison to both, the burning time-scale and the mixing time-scale, the method presented here corrects for the energy conservation and no negative side-effects are to be expected. A typical example for this case is the burning in radiative layers of the star.

Finally it shall be noted that in stellar evolution calculations mostly the burning time-scales for the different species involved in a reaction are longer than the problem time-step. In this case Eq. (A.8) already gives a good approximation.

Appendix B

Improvement of hydrogen burning in the KEPLER code

The treatment of nuclear burning in KEPLER was improved by taking into account neutrino losses and corrections to the energy released during hydrogen burning.

B.1 Binding energy versus released energy

In General, until oxygen burning, KEPLER calculates the nuclear energy generation rate by simply subtraction the total nuclear binding energy of the composition before and after a time-step. However, during hydrogen burning weak interactions are present, with implications for the energy generation which do not occur in other pre-oxygen burning stages. In particular, the mass difference of n and $\mathsf{p} + \mathsf{e}^-$ of $782.3\,\mathrm{MeV\,c^{-2}}$ has to be taken into account. This reduces the energy release per $^4\mathsf{He}$ formed by twice that value, i.e., from 28.296 MeV for the binding energy of two protons and two neutrons, to 26.731 MeV for the total difference in rest mass. That is a relative reduction of the energy generation rate of hydrogen burning by 5.85 %.

B.2 Neutrino losses

Additionally, within the CNO main cycle the weak reaction $^{13}\mathsf{N}(\beta^+\nu_\mathsf{e})^{13}\mathsf{C}$ releases in average 0.71 MeV in the form of neutrinos, $^{15}\mathsf{O}(\beta^+\nu_\mathsf{e})^{15}\mathsf{N}$ releases 1.0 MeV, and the reaction $^{17}\mathsf{F}(\beta^+\nu_\mathsf{e})^{17}\mathsf{O}$ of the secondary CNO cycle, which has a probability of only $\sim 10^{-4}$ relative to the main cycle, 0.94 MeV (Clayton 1968). On average, 1.71 MeV are lost due to neutrinos for each four $^1\mathsf{H}$ burned, reducing the effective energy release by another 6.4 % from 26.731 MeV to about 24.97 MeV per $^4\mathsf{He}$ formed. KEPLER was also corrected for the appropriate neutrino losses of the three pp-chains, but they do not contribute in the high-mass stars of the present work.

B.3 Implications

These two effects sum up to a total reduction of the energy release of hydrogen burning by 13.32 %. However, the stellar structure on the zero-age main sequence is altered only slightly by this, since the energy generation rate for CNO hydrogen burning depends on a high power of the temperature (16 to 18) and thus a slight increase of the central temperature compensates the lower energy generation rate. The nucleosynthesis, as far as the ratios of the CNO isotopes are concerned, are not altered notably by the higher temperature.

The lower total energy release of hydrogen burning reduces the lifetime of the star during central hydrogen burning by about the same factor. The convective mixing in the core is not affected by the smaller duration of central hydrogen burning, since the convective mixing time-scale is still much shorter. For mixing processes which act on a secular time-scale comparable to that of central hydrogen burning, e.g., semiconvection, the reduction of the main sequence lifetime can become noticeable. It is particularly important for rotationally induced mixing and mass loss from the stellar surface. Mass loss rates mostly depend only on stellar surface properties (Sect. 2.4) and thus, to first approximation, the total mass loss scales with the evolutionary time-scale. The stellar angular momentum loss from the surface is also altered by this and the amount of products of hydrogen burning exposed to the surface of the star depends on both the time available for the rotationally induced mixing processes to transport them to the surface and the amount of matter removed from the surface. Furthermore, a higher angular momentum loss from the surface can introduce more shear and correspondingly more mixing.

After termination of central hydrogen burning, hydrogen continues burning in a shell above the helium core. Since the stellar structure determines the rate at which energy has to be released by hydrogen burning, more hydrogen is burned in order to release the same amount of energy using the corrected energy generation rate. This increases the rate at which the helium core grows and thus its final size.

In all models computed with KEPLER in the present work, the corrected treatment of hydrogen burning was employed.

Appendix C

Nuclear reactions in STERN

Table C.1 lists all reactions included in the two nuclear networks of STERN (see next page). The reactions marked with an asterisk are solved in a separate network and are not taken into account for the determination of the nuclear energy generation rate (see Sect. 2.1.6.1).

Table C.1: List of reaction taken into account in STERN. Reactions marked with an asterisk are solved in a separate network (Sect. 2.1.6.1).

No.	reaction	realisation
1	^{1}H (p,$\beta^+\nu_e$) ^{2}H (p,γ) ^{3}He	3 ^{1}H + $\rightarrow$ ^{3}He
2	^{3}He (^{3}He,2p) ^{4}He	
3	^{3}He (α,γ) ^{7}Be ($\beta^+\nu_e$) ^{7}Li	^{3}He + ^{4}He $\rightarrow$ ^{7}Li
4	^{4}He (α,γ) ^{8}Be (α,γ) ^{12}C	3 ^{4}He $\rightarrow$ ^{12}C
5	^{6}Li (p,α) ^{3}He	
6	^{7}Li (p,α) ^{4}He	
7	^{7}Li (α,γ) ^{11}B	
8	^{7}Be ($\beta^-\bar{\nu}_e$) ^{7}Li	
9	^{7}Be (^{3}He,2p) ^{4}He + ^{4}He	
10	^{7}Be (p,γ) ^{8}B	
11	^{7}Be (α,γ) ^{11}C	
12	^{9}Be (p,^{2}H) ^{4}He + ^{4}He	
13	^{9}Be (p,α) ^{6}Li	
14	^{8}B ($\beta^+\nu_e$) ^{4}He + ^{4}He	
15	^{8}B (α,p) ^{11}C	
16	^{8}B (γ,p) ^{7}Be	
17	^{10}B (p,α) ^{7}Be	
18	^{11}B (p,γ) ^{12}C	
19	^{11}B (p,α) ^{4}He + ^{4}He	
20	^{11}C ($\beta^+\nu_e$) ^{11}C	
21	^{11}C (p,γ) ^{12}N	
22	^{12}C (p,γ) ^{13}N ($\beta^+\nu_e$)^{13}C	^{12}C + ^{1}H $\rightarrow$ ^{13}C
23	^{12}C (α,γ) ^{16}O	
24	^{12}C (^{12}C,p) ^{23}Na	
25	^{12}C (^{12}C,α) ^{20}Ne	
26	^{12}C (n,γ) ^{13}C	
27	^{13}C (p,γ) ^{14}N	
28	^{13}C (α,n) ^{16}O	
29	^{12}N ($\beta^+\nu_e$) ^{12}C	
30	^{14}N (p,γ) ^{15}O ($\beta^+\nu_e$)^{15}N	^{14}N + ^{1}H $\rightarrow$ ^{15}N
31	^{14}N (α,γ) ^{18}O	
32	^{15}N (p,α) ^{12}C	
33	^{15}N (p,γ) ^{16}O	
34	^{15}N (α,γ) ^{19}F (α,γ) ^{23}Na	^{15}N + 2 ^{4}He $\rightarrow$ ^{23}Na
35	^{16}O (p,γ) ^{17}F ($\beta^+\nu_e$)^{17}O	^{16}O + ^{1}H $\rightarrow$ ^{17}O
36	^{16}O (α,γ) ^{20}Ne	
37	^{16}O (^{12}C,α) ^{24}Mg	
38	^{16}O (^{16}O,α) ^{28}Si	
39	^{17}O (p,γ) ^{18}F ($\beta^+\nu_e$)^{18}O	^{17}O + ^{1}H $\rightarrow$ ^{18}O
40	^{17}O (p,α) ^{14}N	

CONTINUED ON NEXT PAGE

NUCLEAR REACTIONS IN STERN (CONTINUED)

No.	reaction	realisation
41	^{17}O (α,n) ^{20}Ne	
42*	^{18}O (p,γ) ^{19}F	
43	^{18}O (p,α) ^{15}N	
44	^{18}O (α,γ) ^{22}Ne	
45*	^{19}F (p,γ) ^{20}Ne	
46*	^{19}F (p,α) ^{16}O	
47	^{20}Ne (γ,α) ^{16}O	
48	^{20}Ne (n,γ) ^{21}Ne	
49*	^{20}Ne (p,γ) ^{21}Na $(\beta^+\nu_\mathrm{e})^{21}$Ne	^{20}Ne + ^{1}H $\rightarrow$ ^{21}Ne
50	^{20}Ne (α,γ) ^{24}Mg	
51*	^{21}Ne (p,γ) ^{22}Na $(\beta^+\nu_\mathrm{e})^{22}$Ne	^{21}Ne + ^{1}H $\rightarrow$ ^{22}Ne
52	^{21}Ne (n,γ) ^{22}Ne	
53	^{21}Ne (α,γ) ^{25}Mg	
54	^{21}Ne (α,n) ^{24}Mg	
55*	^{22}Ne (p,γ) ^{23}Na	
56	^{22}Ne (p,α) ^{20}Ne	
57	^{22}Ne (α,γ) ^{26}Mg	
58	^{22}Ne (α,n) ^{25}Mg	
59*	^{23}Na (p,γ) ^{24}Mg	
60*	^{23}Na (p,α) ^{20}Ne	
61*	^{24}Mg (p,γ) ^{25}Al $(\beta^+\nu_\mathrm{e})^{25}$Mg	^{24}Mg+ ^{1}H $\rightarrow$ ^{25}Mg
62	^{24}Mg (n,γ) ^{25}Mg	
63	^{24}Mg (α,γ) ^{28}Si	
64*	^{25}Mg (p,γ) ^{26}Al	
65*	^{25}Mg (p,γ) ^{26}Al* $(\beta^+\nu_\mathrm{e})^{26}$Mg	^{25}Mg+ ^{1}H $\rightarrow$ ^{26}Mg
66	^{25}Mg (n,γ) ^{26}Mg	
67	^{25}Mg (α,γ) ^{29}Si	
68	^{25}Mg (α,n) ^{28}Si	
69*	^{26}Mg (p,γ) ^{27}Al	
70	^{26}Mg (α,γ) ^{30}Si	
71	^{26}Mg (α,n) ^{29}Si	
72*	^{26}Al $(\beta^+\nu_\mathrm{e})$ ^{26}Mg	
73*	^{26}Al (p,γ) ^{27}Si $(\beta^+\nu_\mathrm{e})^{27}$Al	^{26}Al + ^{1}H $\rightarrow$ ^{27}Al
74*	^{27}Al (p,γ) ^{28}Si	
75*	^{27}Al (p,α) ^{24}Mg	
76	^{28}Si (n,γ) ^{29}Si	
77	^{29}Si (n,γ) ^{30}Si	

Appendix D

Surface abundance changes during the main sequence evolution

In addition to the figures in Sect. 4.1.3 the evolution of various abundances and abundance ratios during core hydrogen burning are shown in the following diagrams in the same way as before.

Fig. D.1 shows the depletion of the light isotope ^{3}He, the two light elements lithium (^{6}Li + ^{7}Li; the latter is the by far dominant) and beryllium (^{9}Be + the unstable ^{7}Be), and the decrease of ^{15}N relative to ^{14}N, which is a superposition of two effects, the destruction of ^{15}N and the production of ^{14}N by the CNO cycle.

Fig. D.2 shows the surface enrichment of ^{13}C relative to ^{12}C and the evolution of the stable oxygen isotopes relative to each other. For strong CNO enrichment, as it occurs preferentially towards the end of the main-sequence evolution in the fast rotating stars, ^{13}C starts to decrease, but ^{12}C still is decreased stronger, leading to a continuous increase of the ^{13}C/^{12}C ratio with time.

Fig. D.3 shows the evolution of the mass fractions of the respective two stable neutron-rich isotopes of neon (^{21}Ne, ^{22}Ne) and magnesium (^{25}Mg, ^{26}Mg). While the depletion of ^{21}Ne shows a remarkable dependence on stellar mass, ^{22}Ne shows only the expected dependence on the initial rotation. The changes in the magnesium isotopes remain rather small.

The abundant α-isotopes ^{20}Ne and ^{24}Mg, as well as the silicon isotopes ^{28}Si, ^{29}Si, and ^{30}Si show no significant abundance changes at the surface; the change in ^{27}Al remains below 0.03 dex.

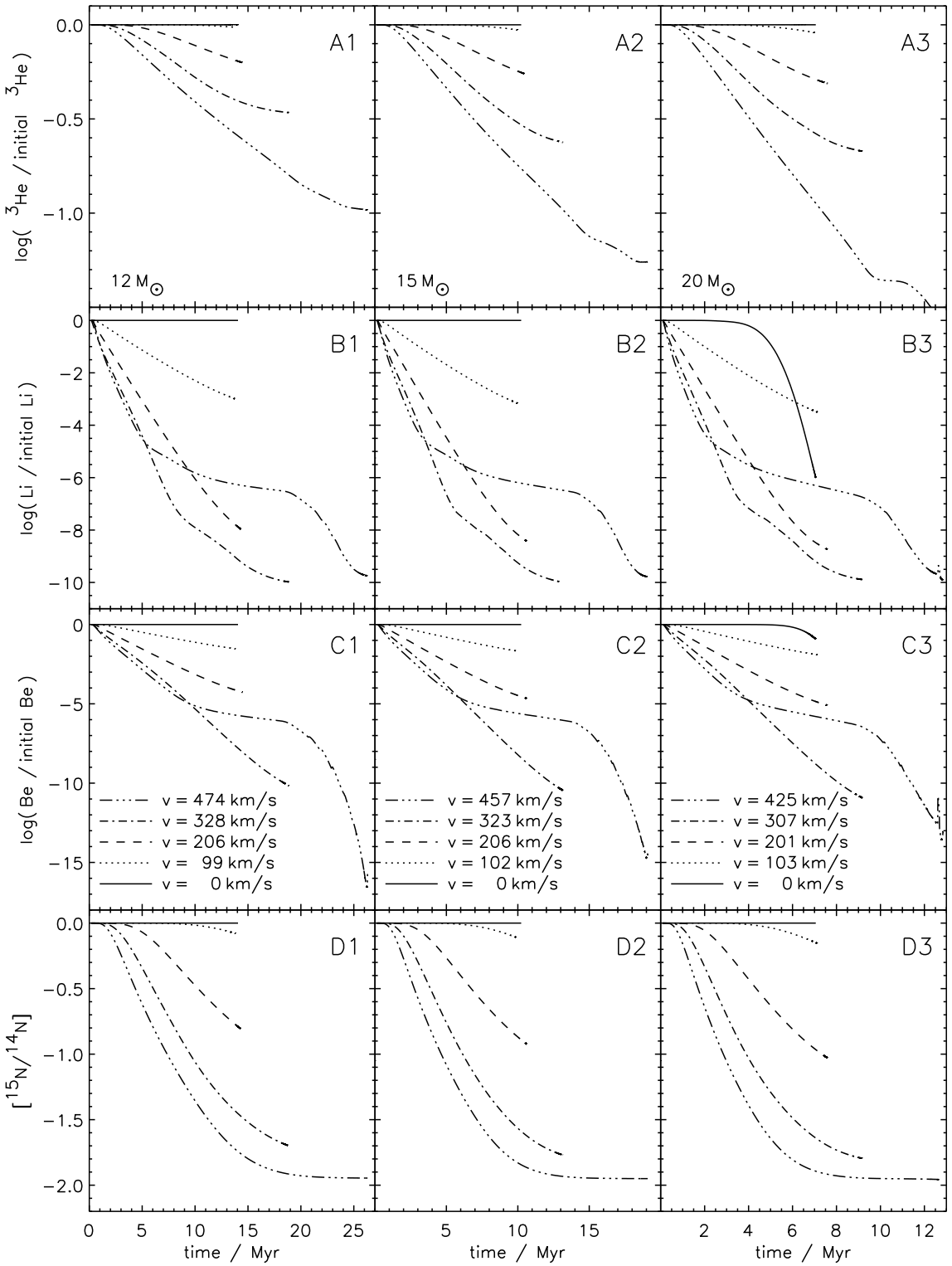

Figure D.1: Evolution of ^{3}He (Panels **A1**–**A3**), Li (Panels **B1**–**B3**), Be (Panels **C1**–**C3**), and ^{15}N/^{14}N (Panels **D1**–**D3**) at the surface, as a function of time during central hydrogen burning for 12 $M_\odot$ (Panels **A1**–**D1**), 15 $M_\odot$ (Panels **A2**–**D2**), and 20 $M_\odot$ (Panels **C3**–**D3**) stars for different initial equatorial rotational velocities, v (see legend). All values are given relative to their initial values (Table 2.1).

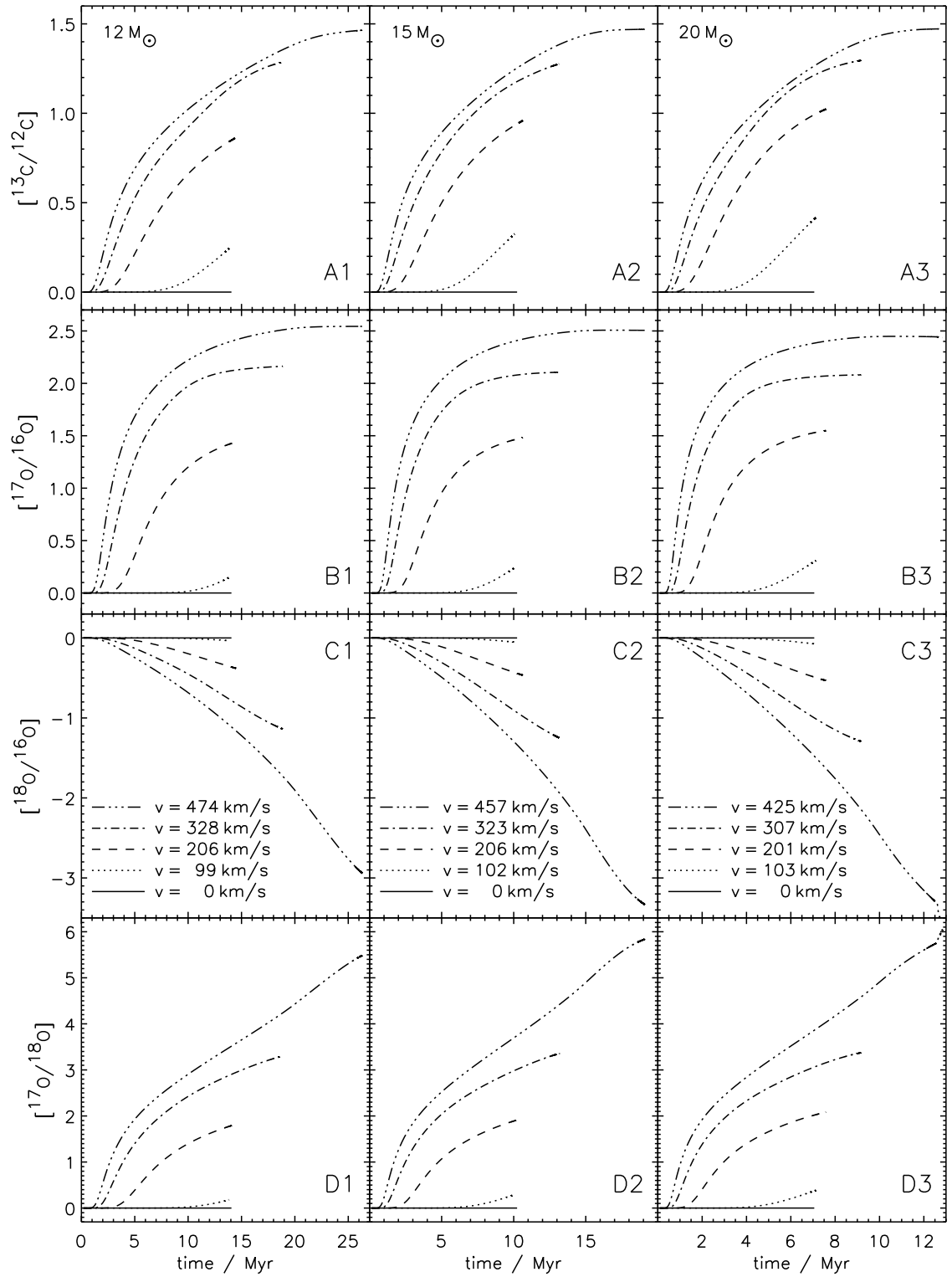

Figure D.2: Evolution of the isotope ratios $^{13}C/^{12}C$ (Panels **A1**–**C1**), $^{17}O/^{16}O$ (Panels **A2**–**C2**), $^{18}O/^{16}O$ (Panels **A3**–**C3**), and $^{17}O/^{18}O$ (Panels **A4**–**C4**) at the surface, as a function of time during central hydrogen burning of $12\,M_\odot$ (Panels **A1**–**D1**), $15\,M_\odot$ (Panels **A2**–**D2**), and $20\,M_\odot$ (Panels **A3**–**D3**) stars for different initial equatorial rotational velocities, v (see legend). All ratios are given in a logarithmic scale relative to their initial values (Table 2.1).

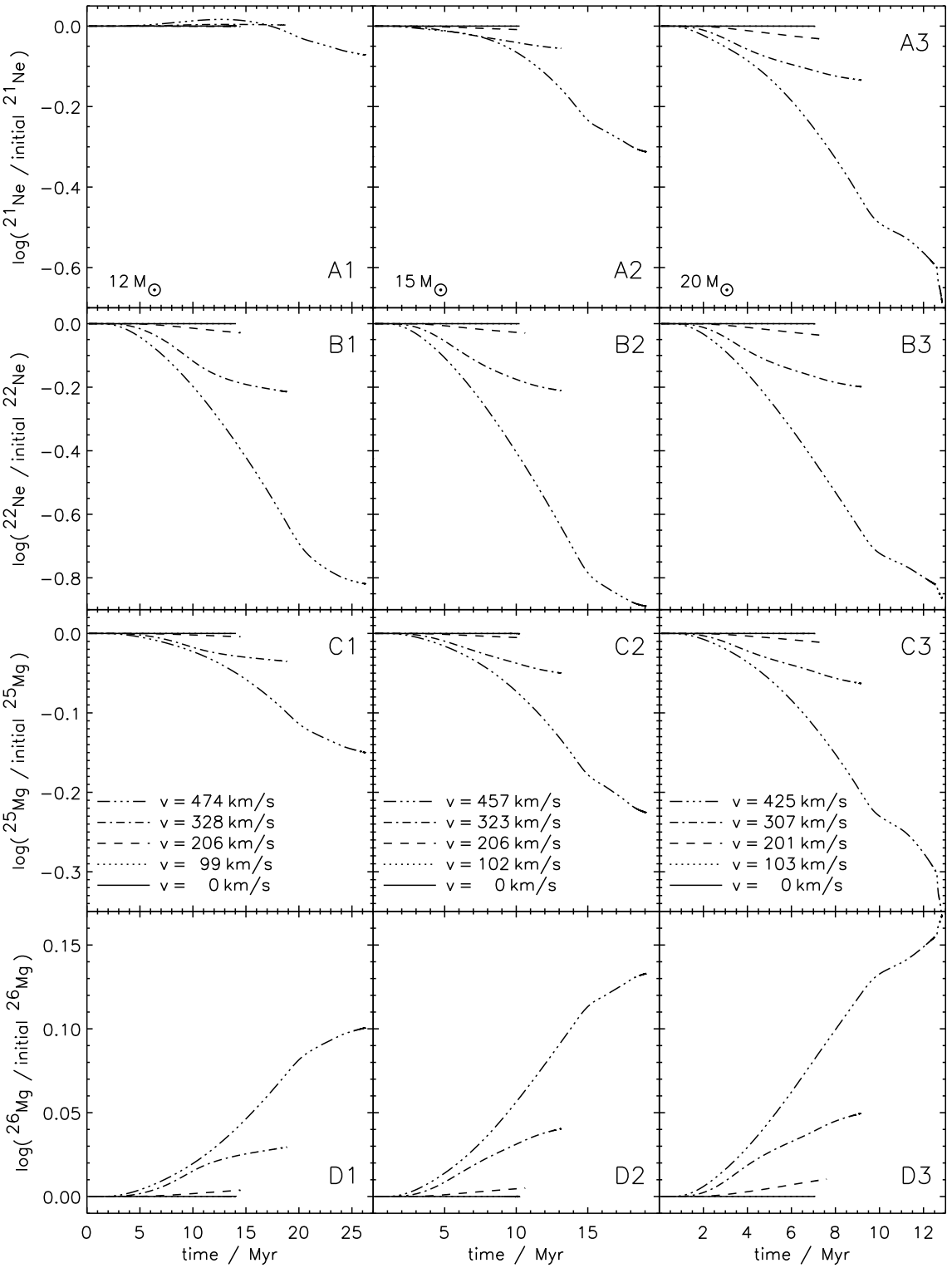

Figure D.3: Evolution of the isotope mass fractions of ^{21}Ne (Panels **A1**–**C1**), ^{22}Ne (Panels **A2**–**C2**), ^{25}Ne (Panels **A3**–**C3**), and ^{26}Ne (Panels **A4**–**C4**) at the surface, as a function of time during central hydrogen burning of 12 $M_\odot$ (left column), 15 $M_\odot$ (middle column), and 20 $M_\odot$ (right column) stars for different initial equatorial rotational velocities, v (see legend). All abundances are given in a logarithmic scale relative to their initial values (Table 2.1).

Appendix E

Diagrams for the evolution of the internal stellar structure

In this section, "Kippenhahn diagrams" of the convective structure and the nuclear energy generation rate as a function of time are given for various model sequences. In Sect. E.1 the setup of the figures is explained. Sect. E.3 briefly discusses the contributions of nuclear energy release and neutrino losses in the plots, and Table E.1 lists sequences for which Kippenhahn diagrams are given.

E.1 Explanation of the diagrams

Since the duration of subsequent burning phases in massive stars decreases considerably, from hydrogen burning lasting millions of years until silicon shell burning which takes only hours, a time-axis was chosen that gives the logarithm of the time left until core collapse (in yr). This remaining time is a rough estimate for illustrative purposes only and should not be taken too literally. The value of $10^{-7.5}$ yr (~ 1 s) used in the Figures for the models computed until core collapse is estimated from the infall velocities occurring in the last computed models and from the radius at which the maximum infall velocity occurs ($\sim 10^3$ km s^{-1} and 10^3 km, respectively). This is actually an estimate of the time until "core bounce". Several models are stopped before neon ignition or during off-center neon burning. In these cases the estimates must remain very uncertain.

The y-axis gives the (interior) mass coordinate in units of solar masses. The total mass of the star is indicated by a thick solid line and shows the mass loss from the stellar surface. Note that because of the way the time-axis is chosen, the slope of this curve does directly correspond to the mass loss rate (compare, e.g., Figs. 2.10 and E.9).

Diagonal hatching indicates convective regions. In order to better visualize the mass coordinates where individual convection zones start or end, thin horizontal lines are drawn at their upper and lower edges. Semiconvection is indicated by narrow cross-hatching.

The net nuclear contribution to the energy generation rate including neutrino

losses are shown as grey shading. Increasingly darker grey scale levels correspond to increasing orders of magnitude of the energy generation rate. The lightest grey shows regions with an energy generation rate of $10^{-1}\,\mathrm{erg\,g^{-1}\,s^{-1}}$ or less, the next darker shade of grey underlies regions with an energy generation rate of $10^{-1}\,\mathrm{erg\,g^{-1}\,s^{-1}}$ or above, and so forth.

E.2 Brief description of the evolutionary phases

The first evolutionary phase displayed in the figures is central hydrogen burning. In the massive stars considered in this work, it is accompanied by a central convective region, which usually shrinks (in mass) in the course of evolution. This takes about one to a few times $10^7\,\mathrm{yr}$. The envelope remains essentially radiative except for tiny convective layer very close to the surface, which are not resolved in the diagrams. Depending on the stellar mass and the effects of rotationally induced mixing, semi-convection alternating with small convective layers can form above the convective core. The energy generation (grey shading) occurs predominantly in the innermost $\sim 10 \ldots 20\,\%$ of the mass, with some – negligible – burning extending beyond the convective core.

The next burning stage is central helium burning. By the time this occurs, the stars have become extended red supergiants with deep convective envelopes (except for Model `H12B` in Fig. E.22). The central helium burning is also convective, but more concentrated to the center and with higher central energy generation rate than core hydrogen burning. Between the convective envelope and the convective core, hydrogen continues to burn in a shell at the upper edge of the hydrogen-depleted core ("helium core"), to which it adds its ashes, causing it to grow. Some of the stars (initial masses $\lesssim 12\,\mathrm{M_\odot}$, e.g., Model `E12` in Fig. E.9) experience "blue loops" during central hydrogen burning, during which the envelope becomes fully radiative and the stars reach surface temperatures of $\sim 10\,000\,\mathrm{K}$. Due to the smaller supply of fuel and especially the much lower energy release per unit mass, this phase takes only of the order of $\sim 10^6\,\mathrm{yr}$.

After central helium burning, helium continues burning in a shell, while the hydrogen-burning shell extincts (notably lower energy generation rates). The helium-burning shell usually develops a growing convection zone, except for the stars with the smallest helium cores. In the helium-depleted carbon/oxygen core (C/O core) below the helium shell, neutrino losses start to become important (Sect. E.3). For the remainder of the star's life they reduce the evolutionary time-scales significantly. The stars become more luminous in neutrinos than in photons. The next important burning stage is carbon burning, which starts with a central convective burning phase[1] and a subsequent cascade of shell burning phases which approach the helium burning shell. Next follows central neon burning, closely followed by oxygen

[1] If the mass of the helium core is large enough, otherwise it might ignite off-center. If the carbon mass fraction produced by the preceding helium burning phase is too low, it does not form a convection zone.

burning, which takes of the order of 1 yr to 10 yr[2]. This is followed by subsequent episodes of shell neon burning (short-lasting) and oxygen burning. The last major burning phase is central silicon burning. It takes a couple of days and is followed by silicon shell burning. At last, when the iron core has grown large enough, core-collapse sets in (past the end of all plots). The later burning stages show higher and higher energy generation rates. In some cases, the fuel remaining after the extinction of a convective burning phase burns non-convectively in the vicinity of the former bottom of the convection zone. This is the reason for most of the burning events inside the C/O core which are not connected to convection zones. In some models extended burning occurs in the helium-burning convection zone. This is due to the mixing of protons into these hot regions.

E.3 Nuclear energy generation and neutrino losses

In the middle Panel of Fig. E.1 the net nuclear energy generation rate including neutrino losses, as described above, is displayed. In contrast to that, in the bottom panel grey shading indicates net nuclear energy loss including neutrino losses, dominating the major part of the C/O core. For comparison, the grey shading in the top Panel shows the nuclear energy release without neutrino losses. The "white" patch in right bottom corner is due to endothermic nuclear reactions in the iron core.

[2]For small C/O core masses these burning stages ignite not in the center of the star, but somewhat off-center (Models `D12` and `E12B`). Models `E08`, `D10`, `G12B`, `F12B`, and `H12B` are stopped before neon ignition.

Table E.1: Models and corresponding figures.

model	figure	page
`D10`	E.2	173
`D12`	E.3	174
`D15`	E.4	175
`D20`	E.5	176
`D25`	E.6	177
`E08`	E.7	178
`E10`	E.8	179
`E12`	E.9	180
`E15`	E.10	181
`E20`	E.11	182
`E25`	E.12	183

model	figure	page
`G12B`	E.13	184
`G15B`	E.14	185
`G20B`	E.15	186
`E12B`	E.16	187
`E15B`	E.17	188
`E20B`	E.18	189
`F12B`	E.19	190
`F15B`	E.20	191
`F20B`	E.21	192
`H12B`	E.22	193

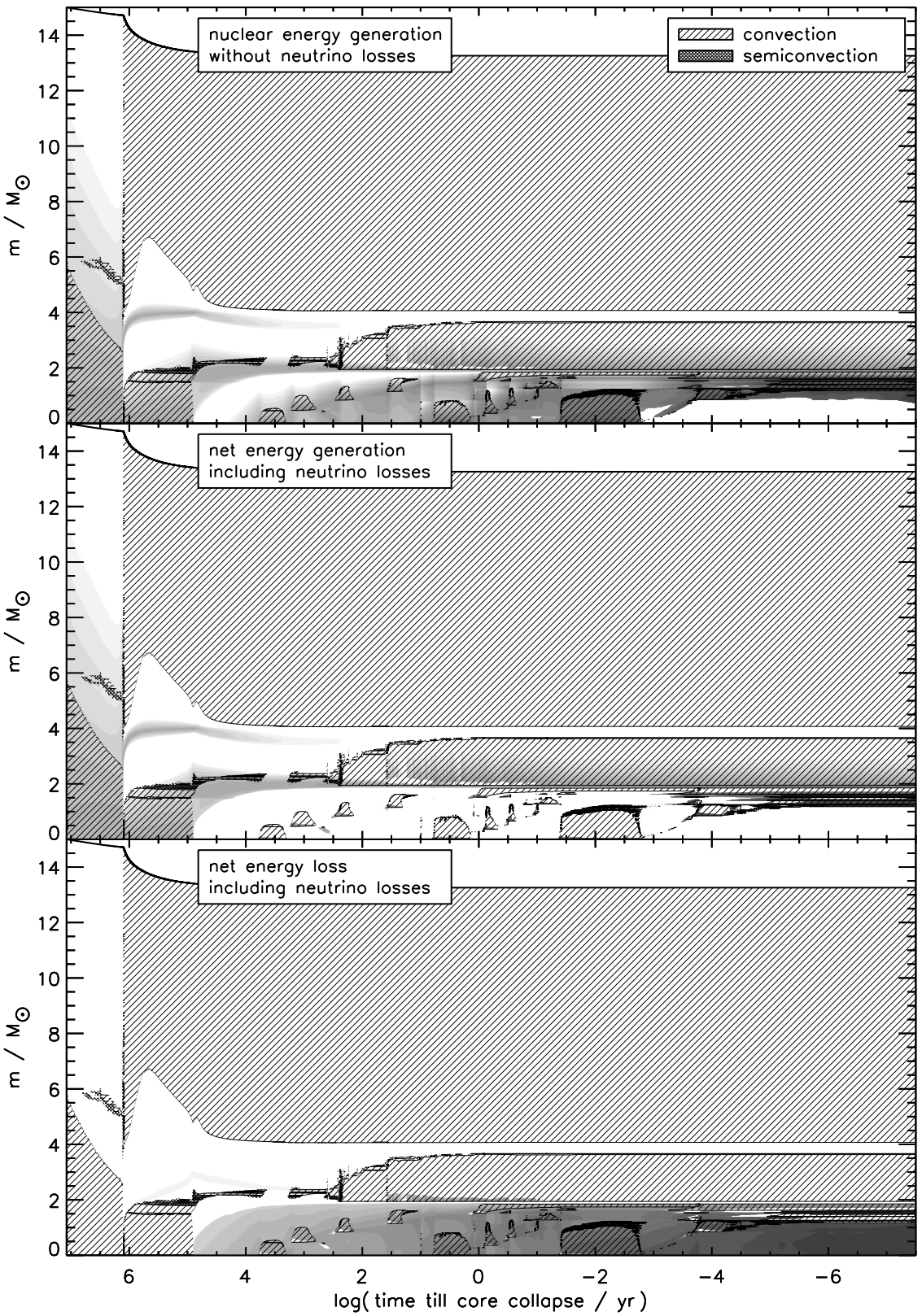

Figure E.1: Evolution of Model E15B until core collapse. Nuclear energy generation and neutrino losses. See Sections E.1 and E.3 for details.

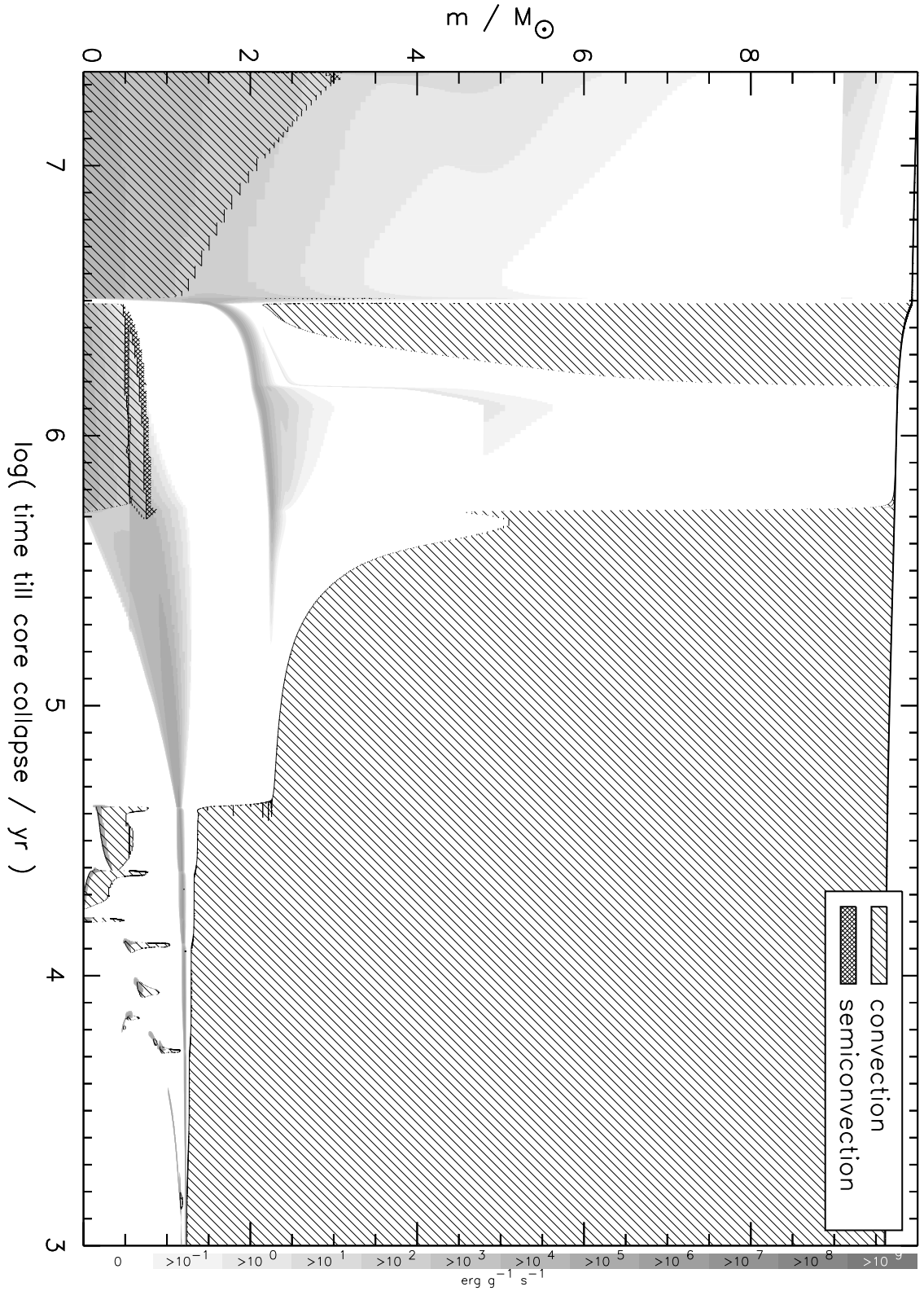

Figure E.2: Evolution of Model `D10` until post-central carbon burning. Convection and net nuclear energy generation. See Sect. E.1 for details.

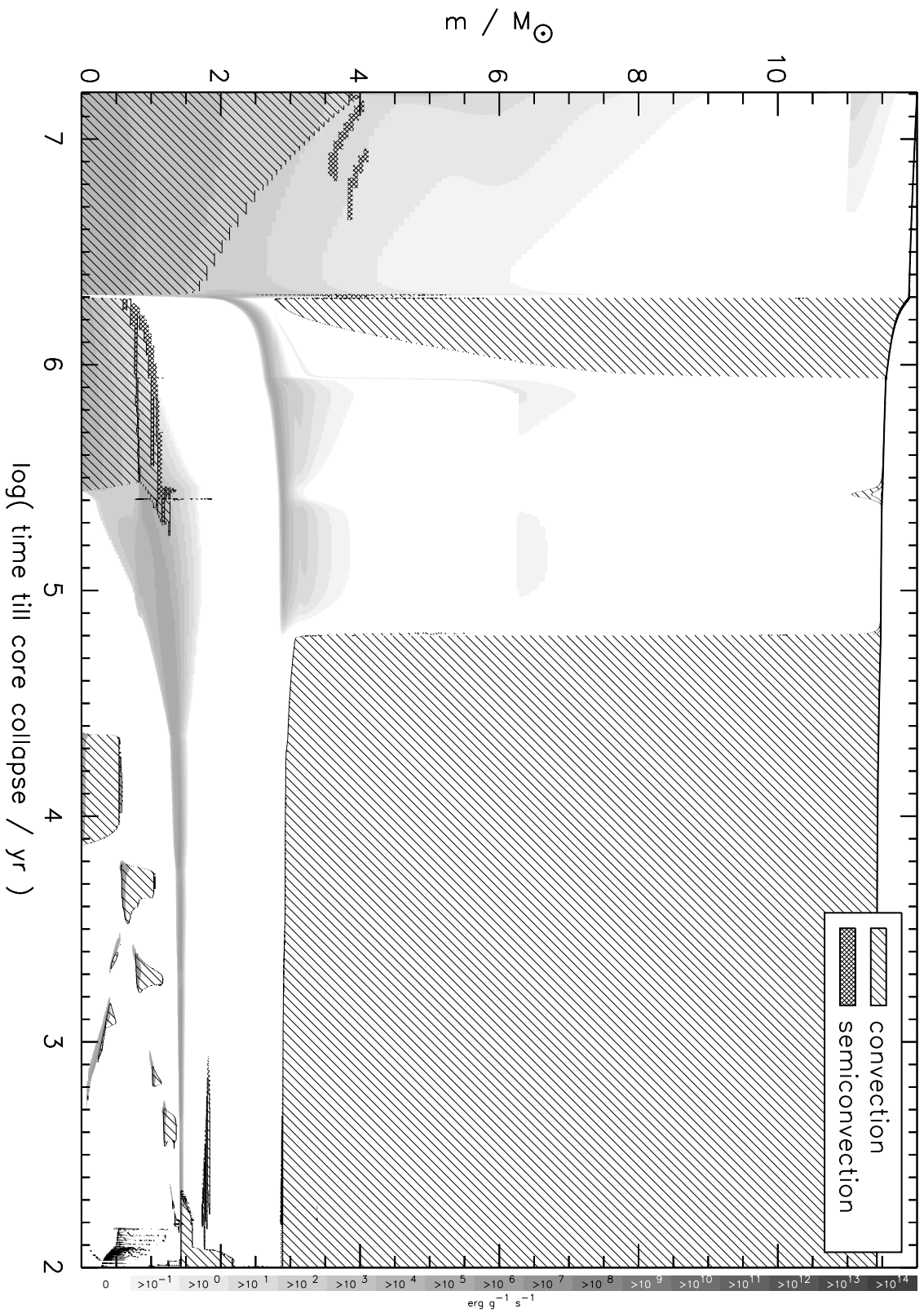

Figure E.3: Evolution of Model D12 until off-center neon burning. Convection and net nuclear energy generation. See Sect. E.1 for details.

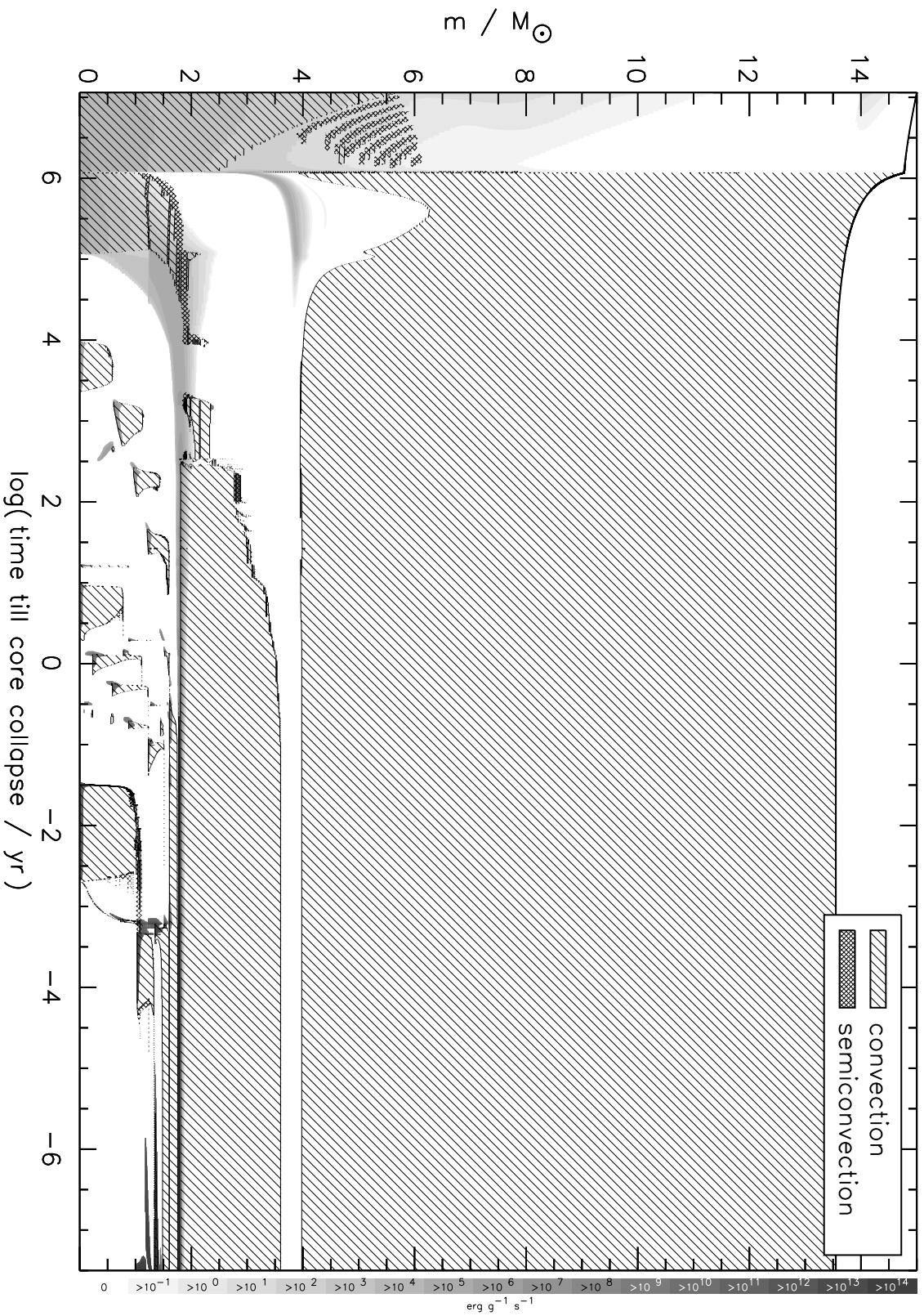

Figure E.4: Evolution of Model `D15` until core collapse. Convection and net nuclear energy generation. See Sect. E.1 for details.

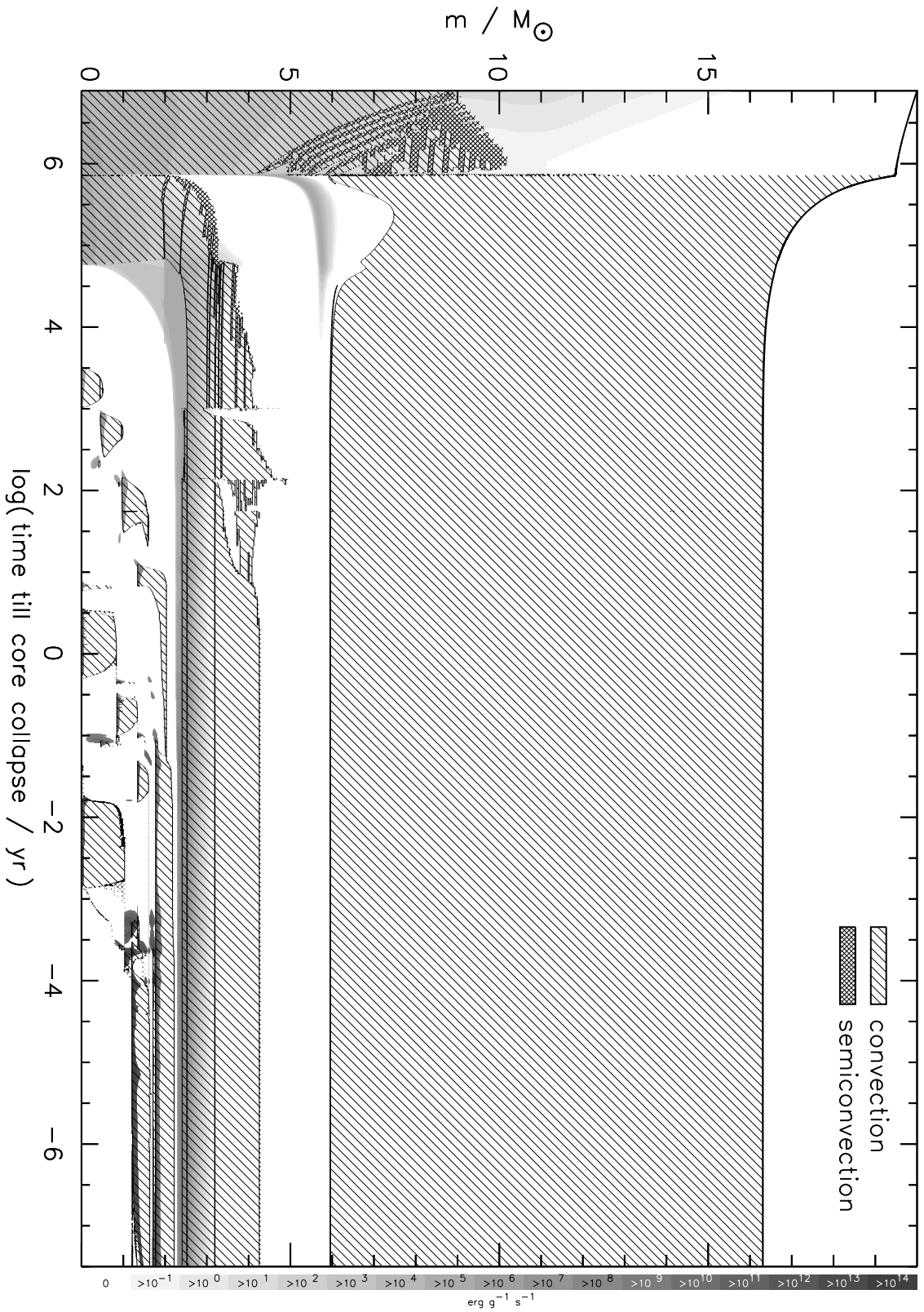

Figure E.5: Evolution of Model D20 until core collapse. Convection and net nuclear energy generation. See Sect. E.1 for details.

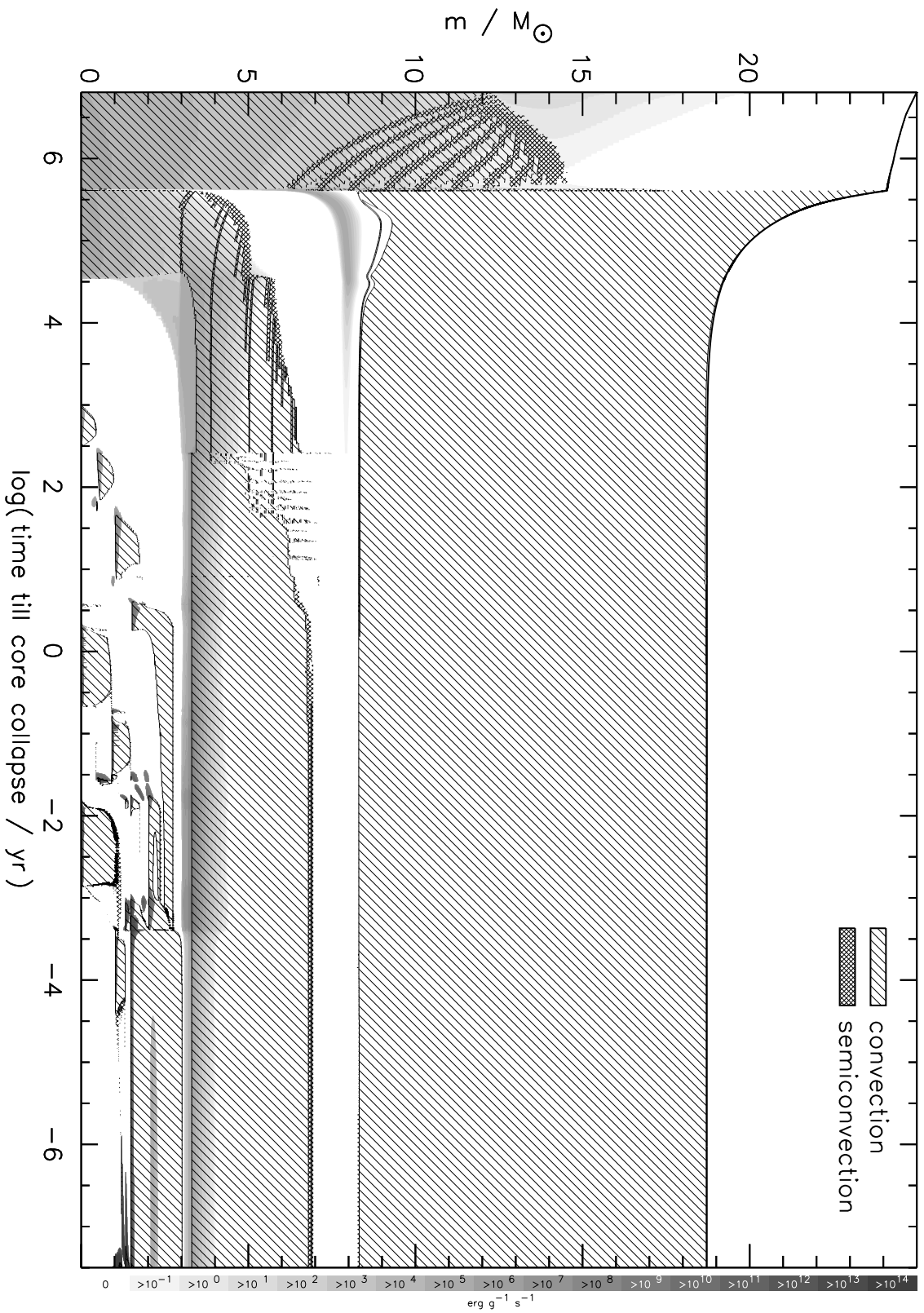

Figure E.6: Evolution of Model D25 until core collapse. Convection and net nuclear energy generation. See Sect. E.1 for details.

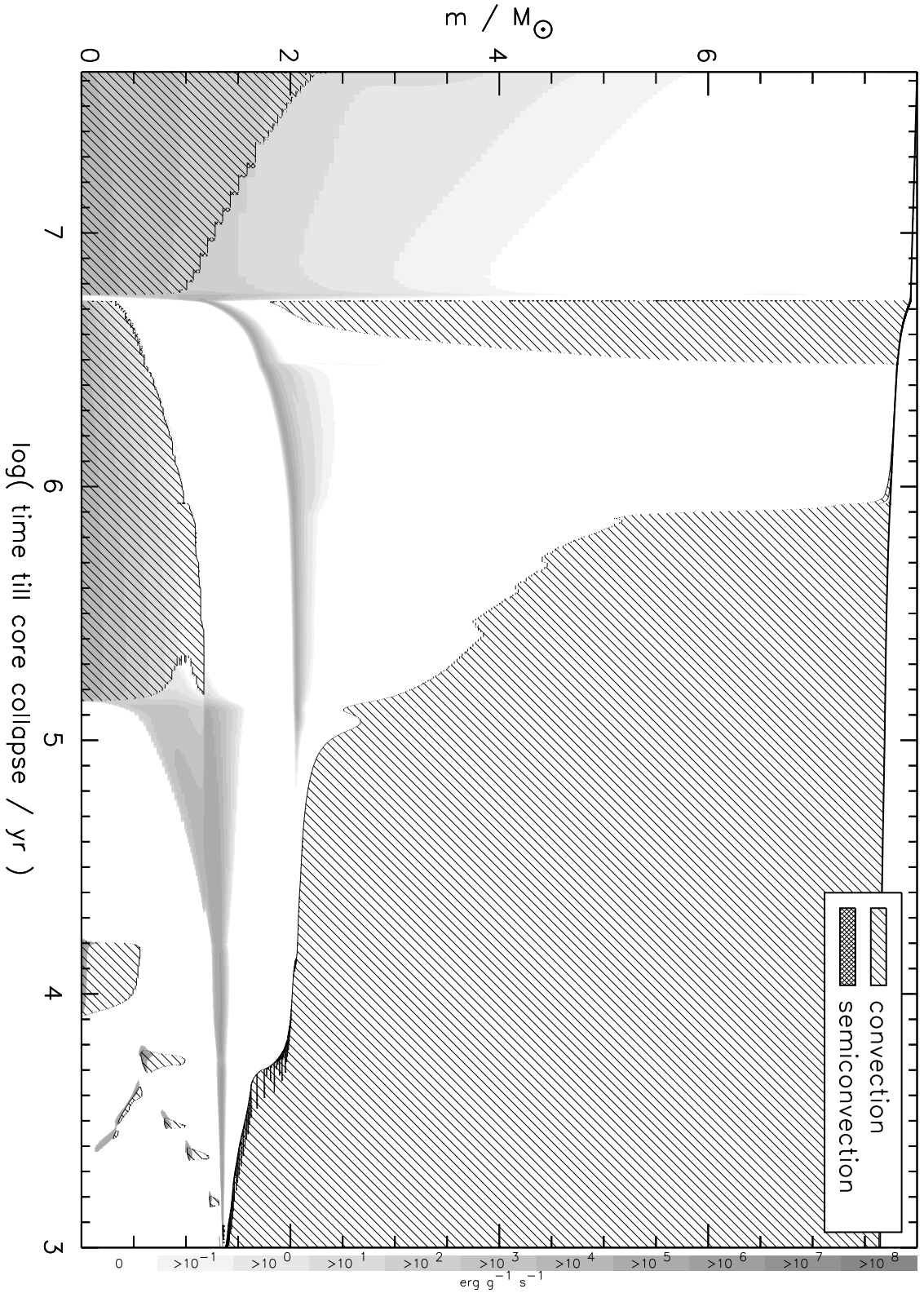

Figure E.7: Evolution of Model E08 until post-central carbon burning. Convection and net nuclear energy generation. See Sect. E.1 for details.

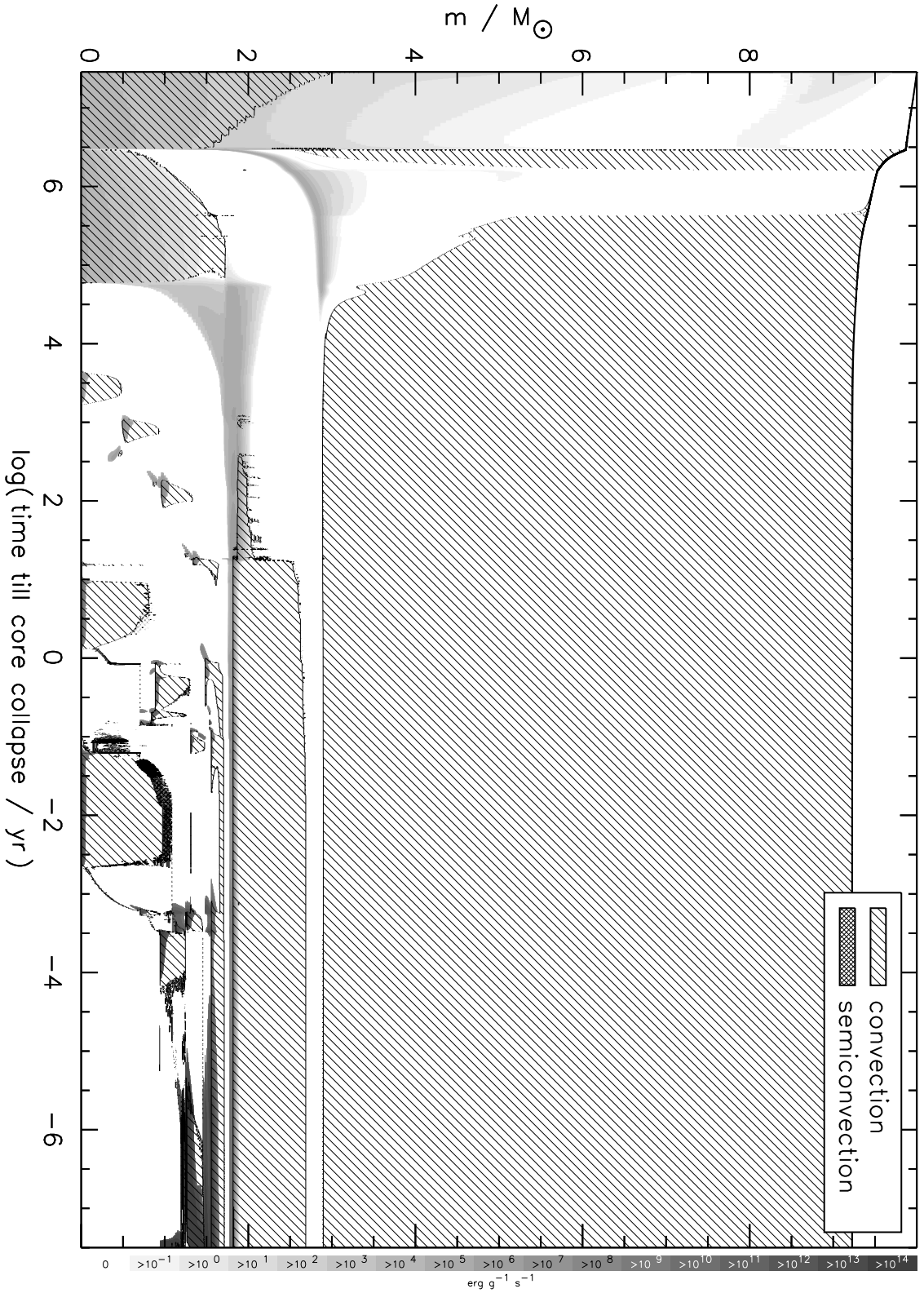

Figure E.8: Evolution of Model E10 until core collapse. Convection and net nuclear energy generation. See Sect. E.1 for details.

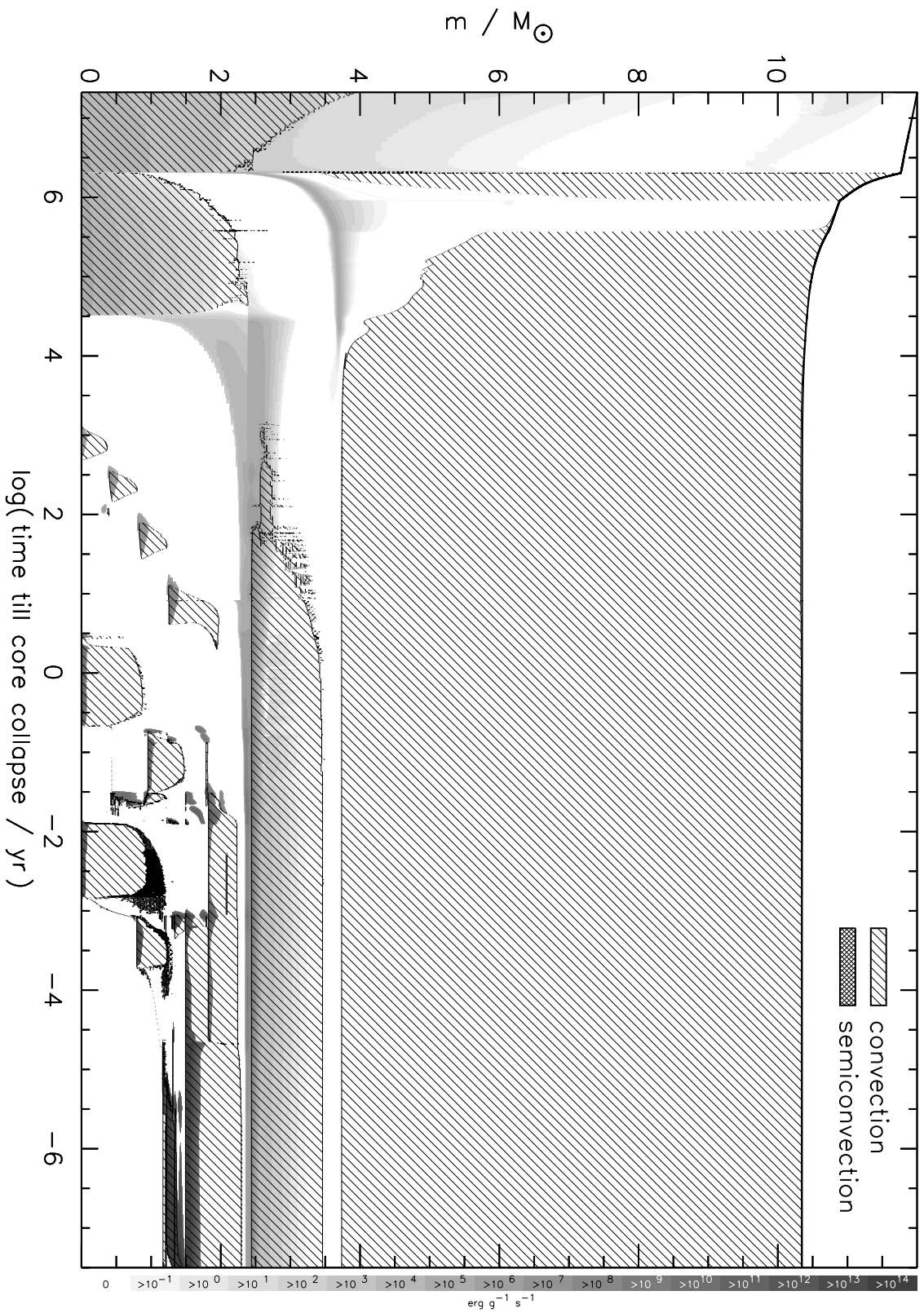

Figure E.9: Evolution of Model E12 until core collapse. Convection and net nuclear energy generation. See Sect. E.1 for details.

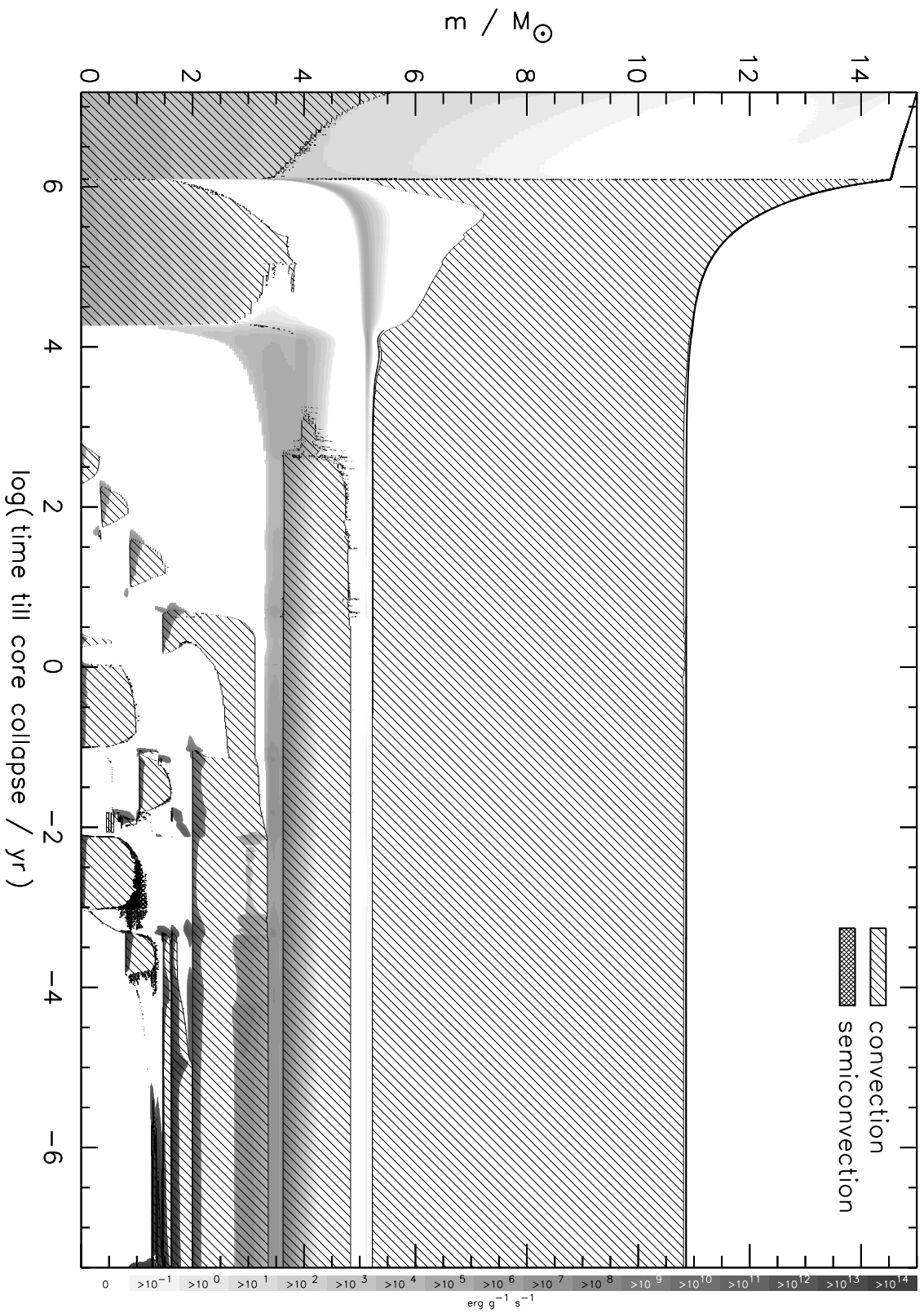

Figure E.10: Evolution of Model E15 until core collapse. Convection and net nuclear energy generation. See Sect. E.1 for details.

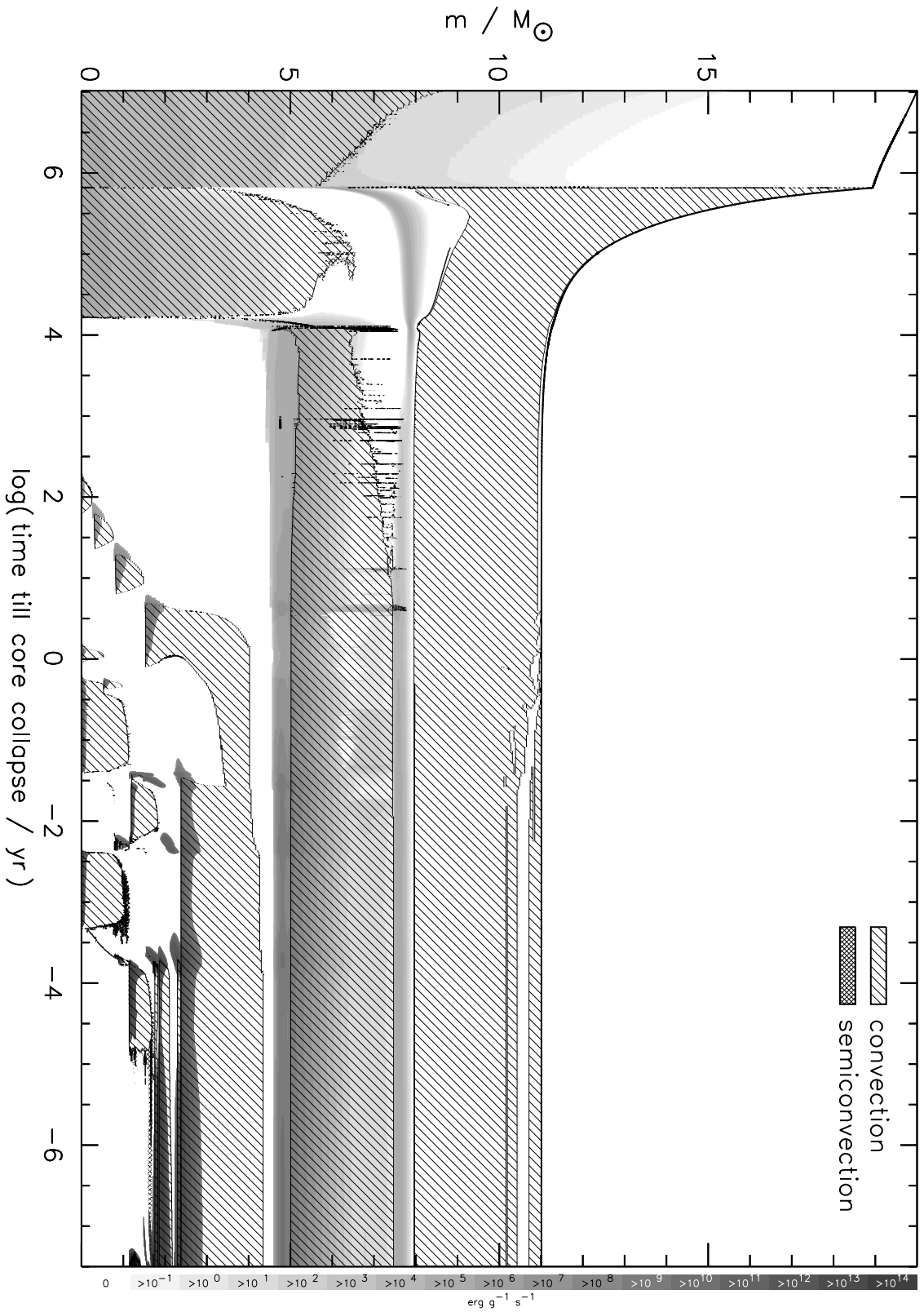

Figure E.11: Evolution of Model E20 until core collapse. Convection and net nuclear energy generation. See Sect. E.1 for details.

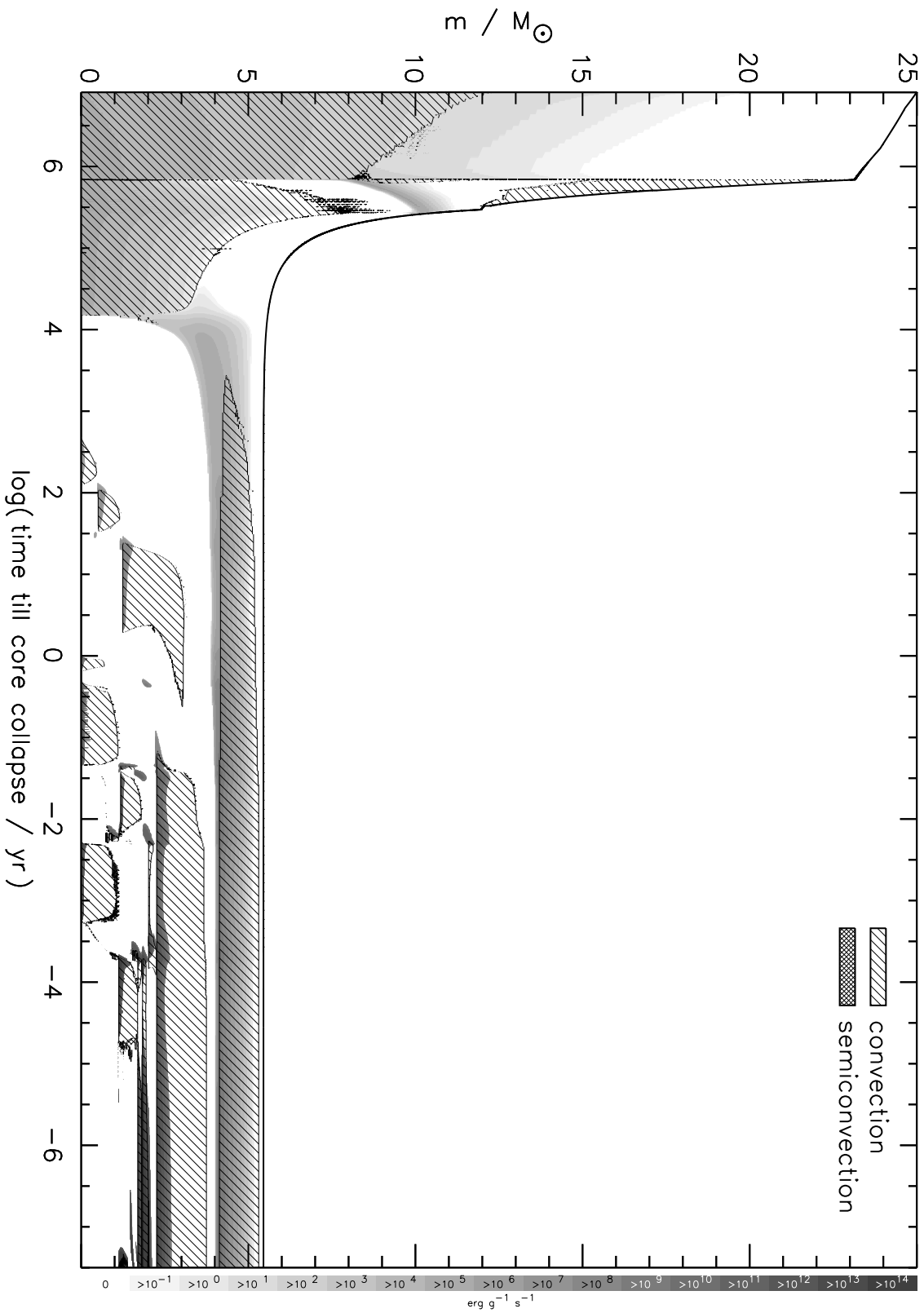

Figure E.12: Evolution of Model E25 until core collapse. Convection and net nuclear energy generation. See Sect. E.1 for details.

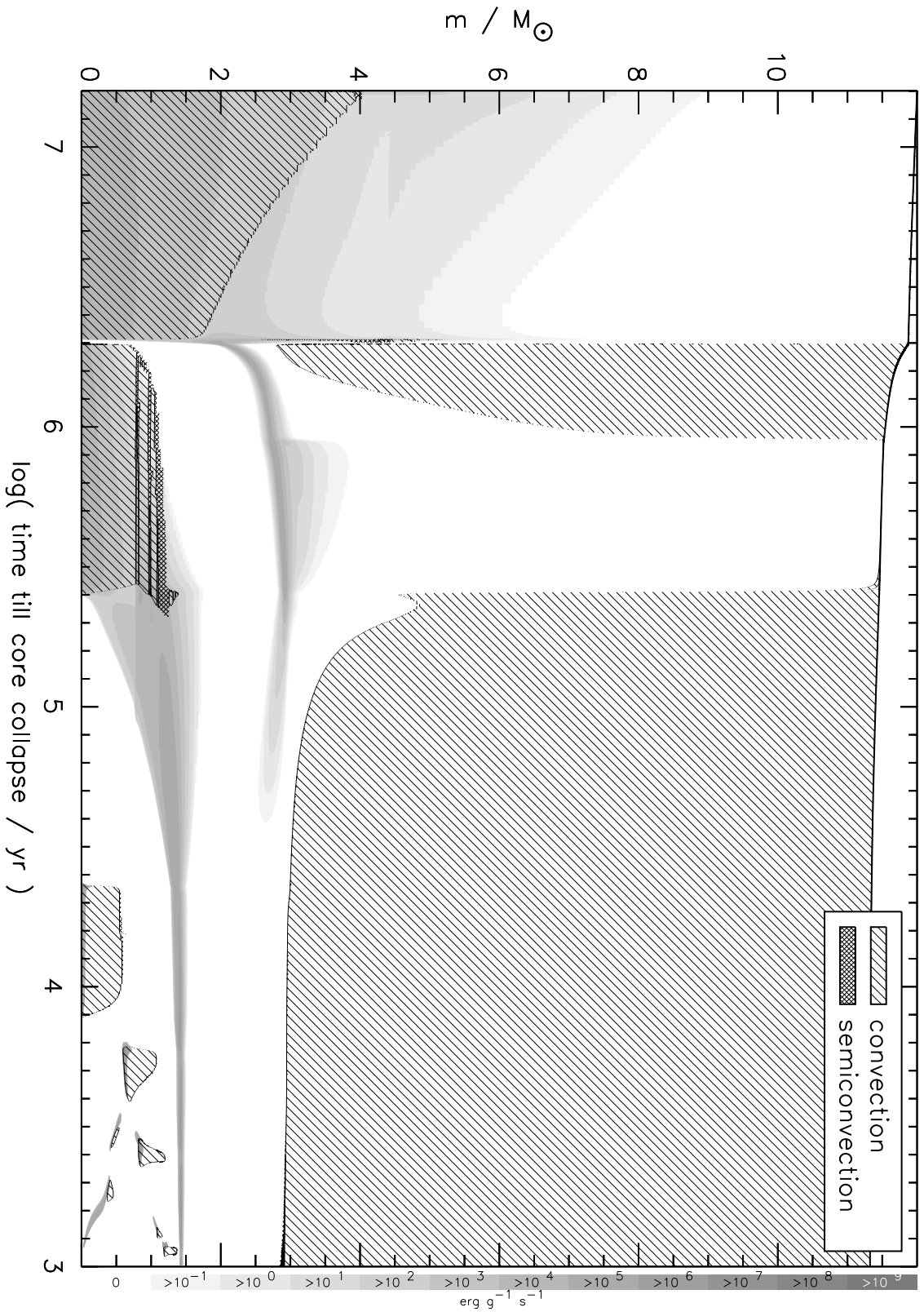

Figure E.13: Evolution of Model G12B until post-central carbon burning. Convection and net nuclear energy generation. See Sect. E.1 for details.

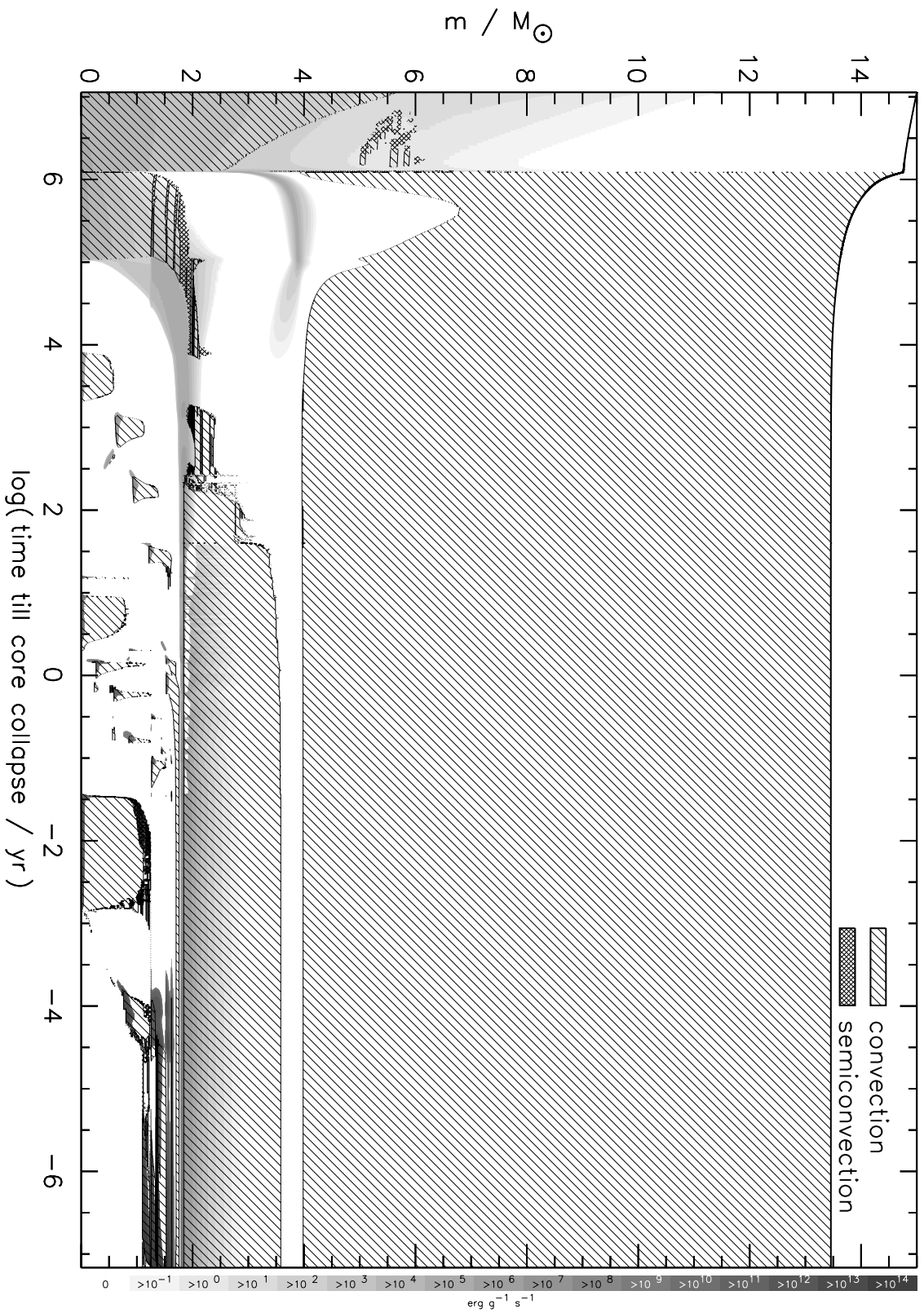

Figure E.14: Evolution of Model `G15B` until core collapse. Convection and net nuclear energy generation. See Sect. E.1 for details.

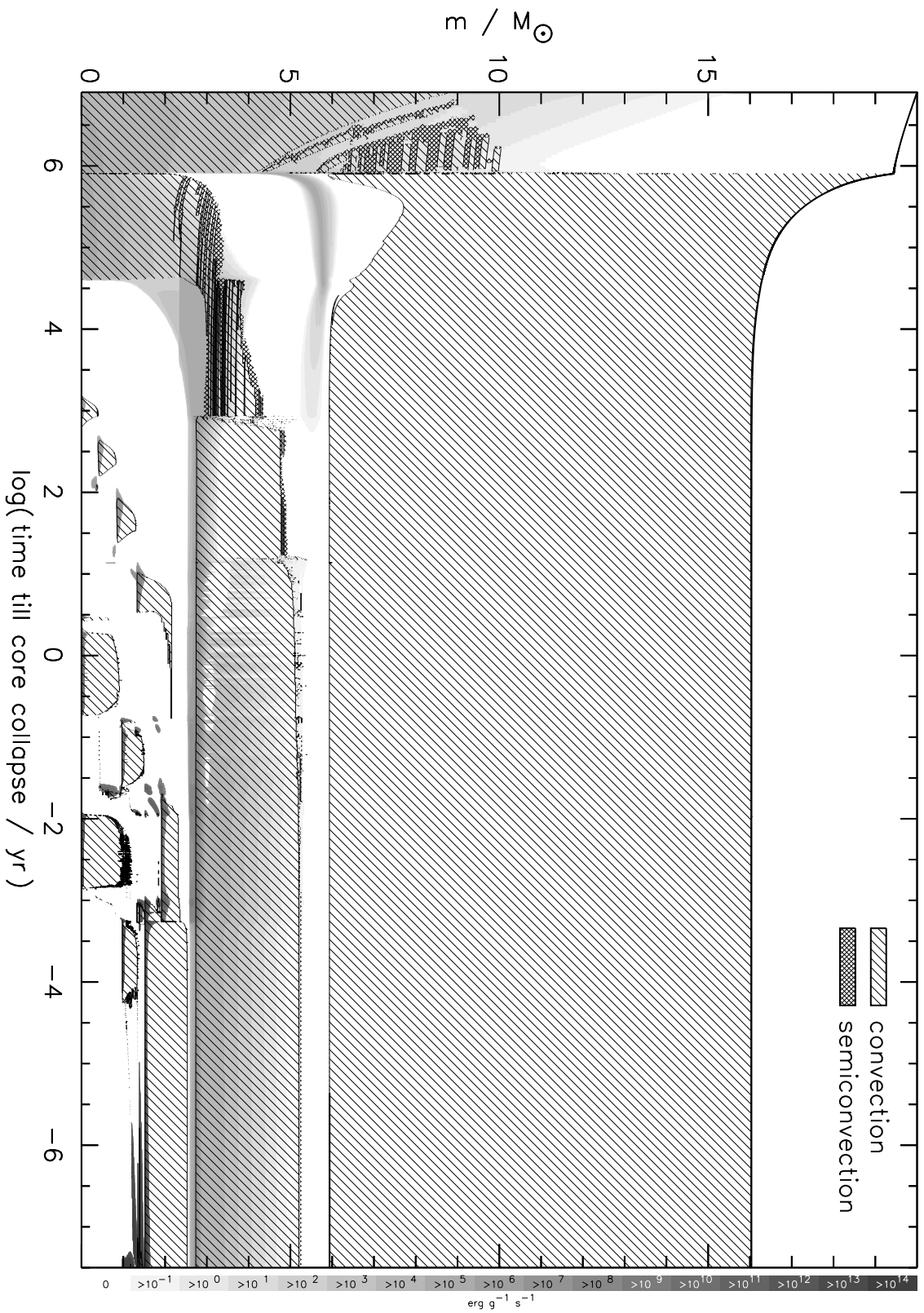

Figure E.15: Evolution of Model G20B until core collapse. Convection and net nuclear energy generation. See Sect. E.1 for details.

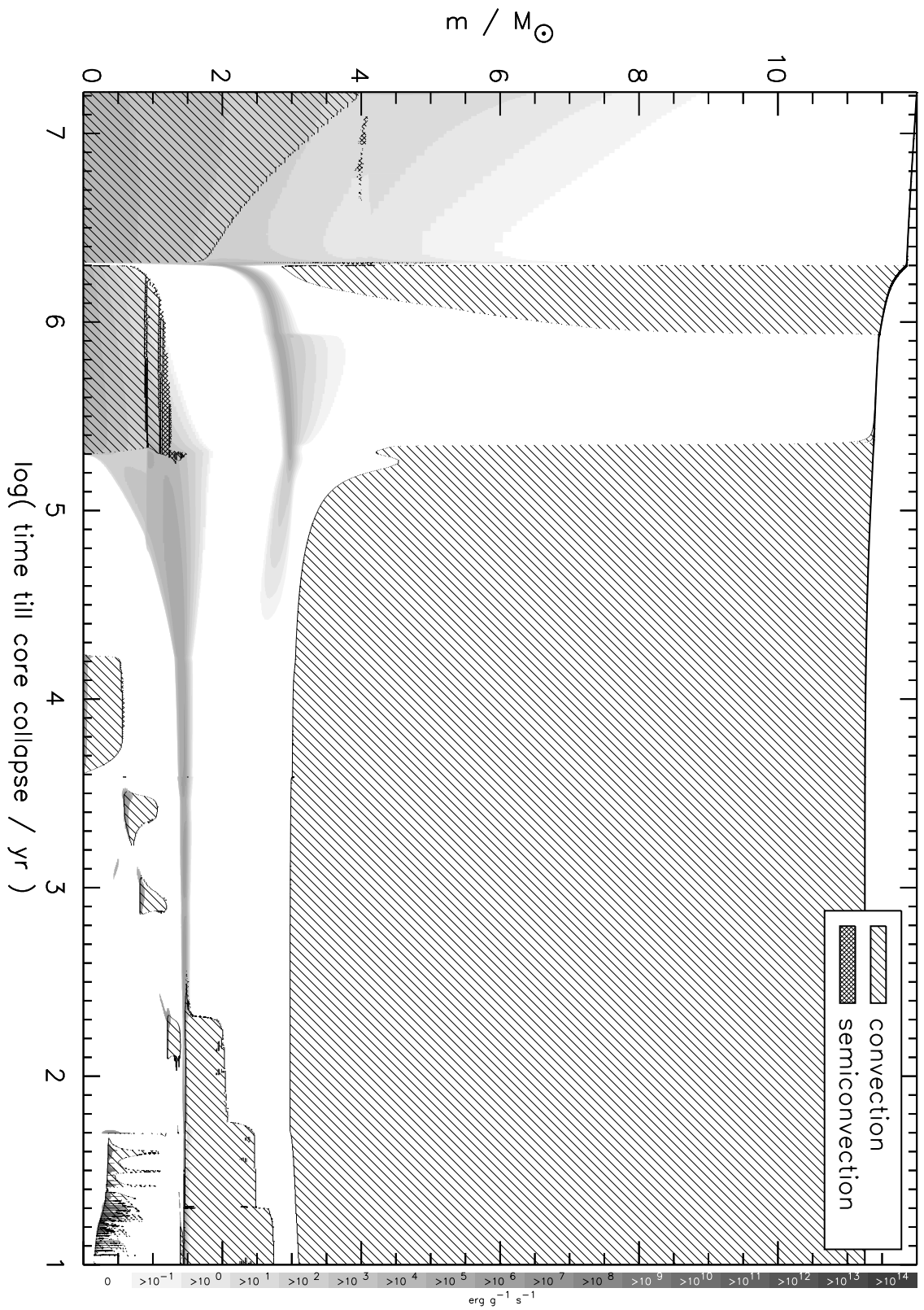

Figure E.16: Evolution of Model E12B until off-center neon burning. Convection and net nuclear energy generation. See Sect. E.1 for details.

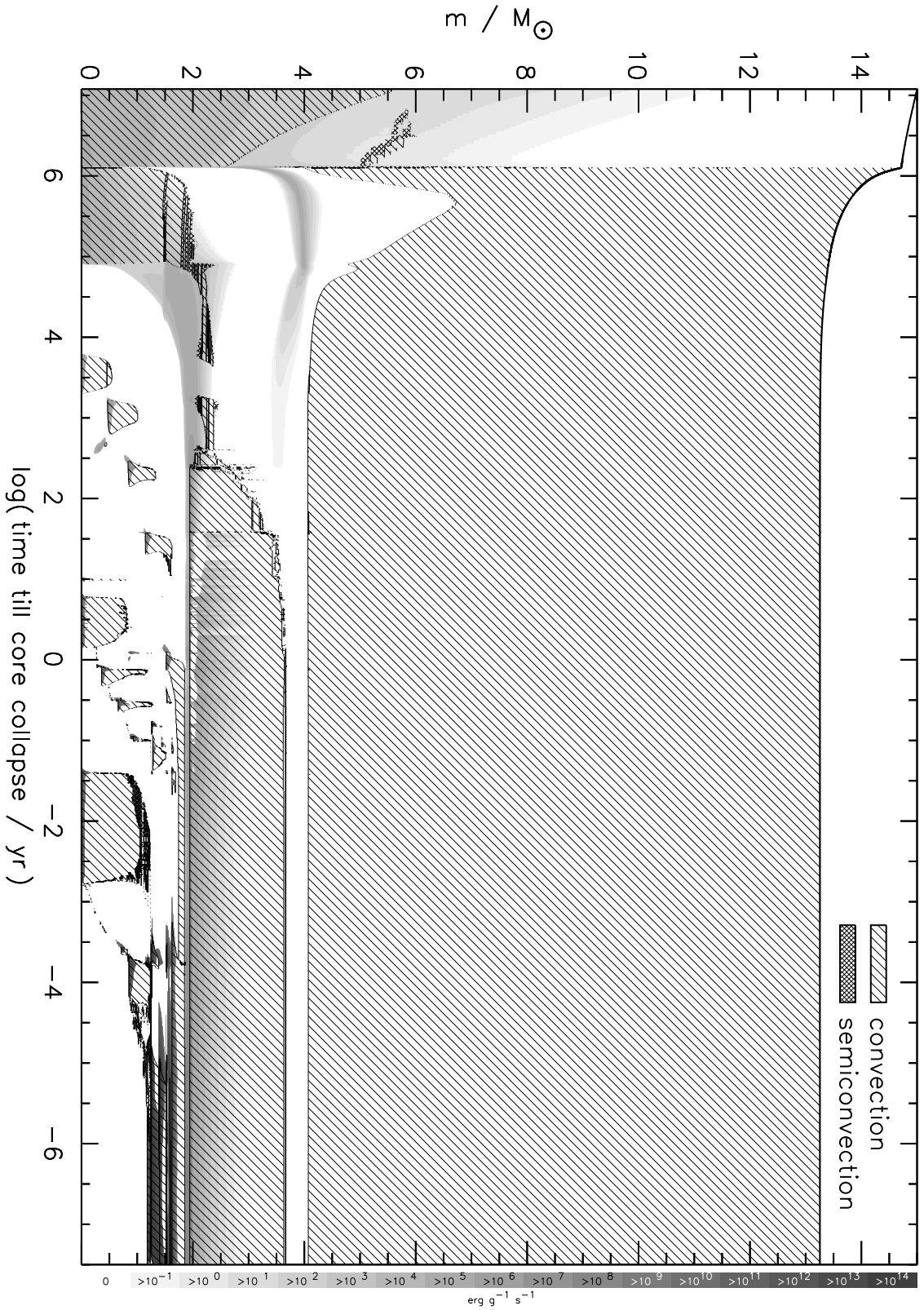

Figure E.17: Evolution of Model E15B until core collapse. Convection and net nuclear energy generation. See Sect. E.1 for details.

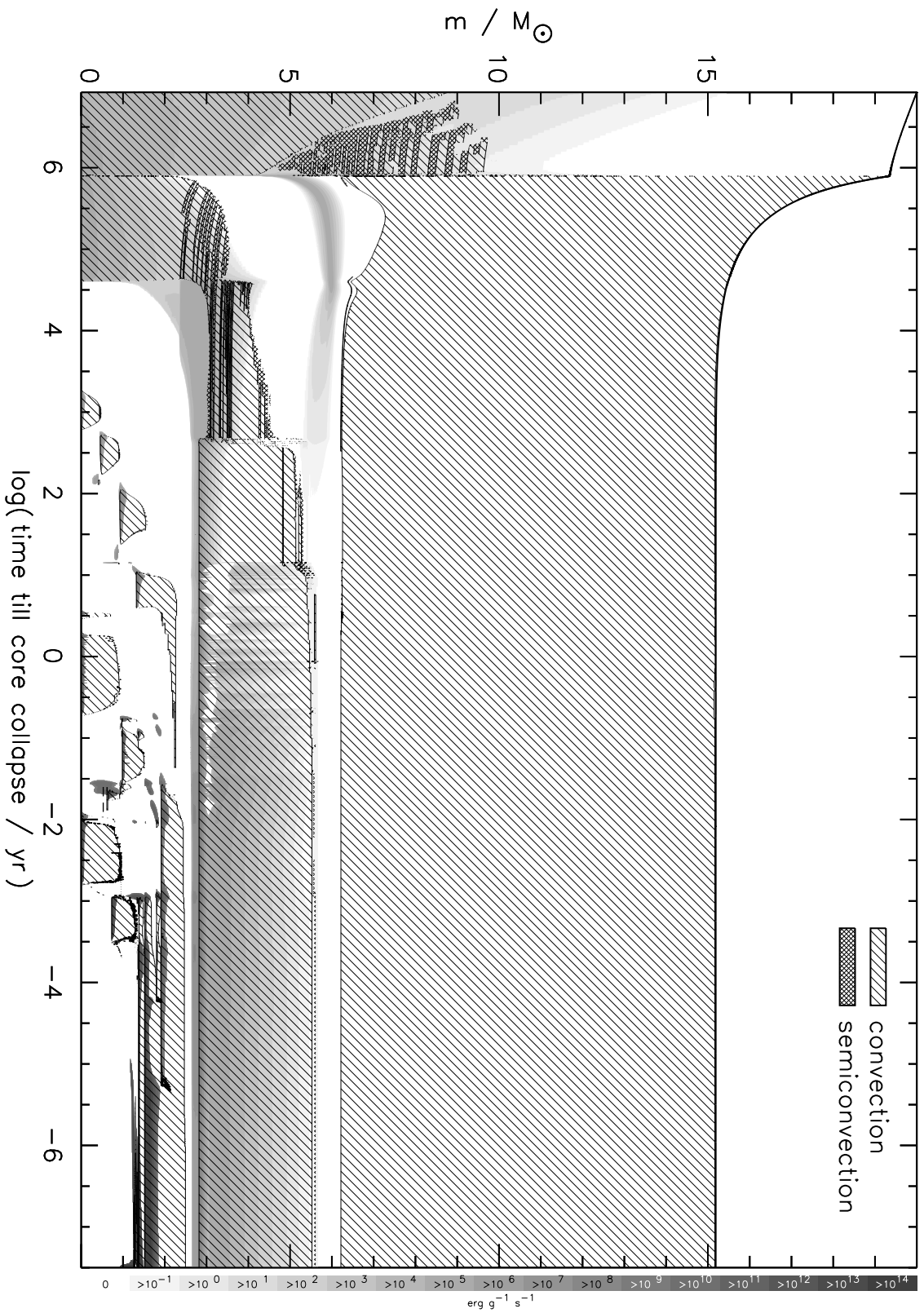

Figure E.18: Evolution of Model E20B until core collapse. Convection and net nuclear energy generation. See Sect. E.1 for details.

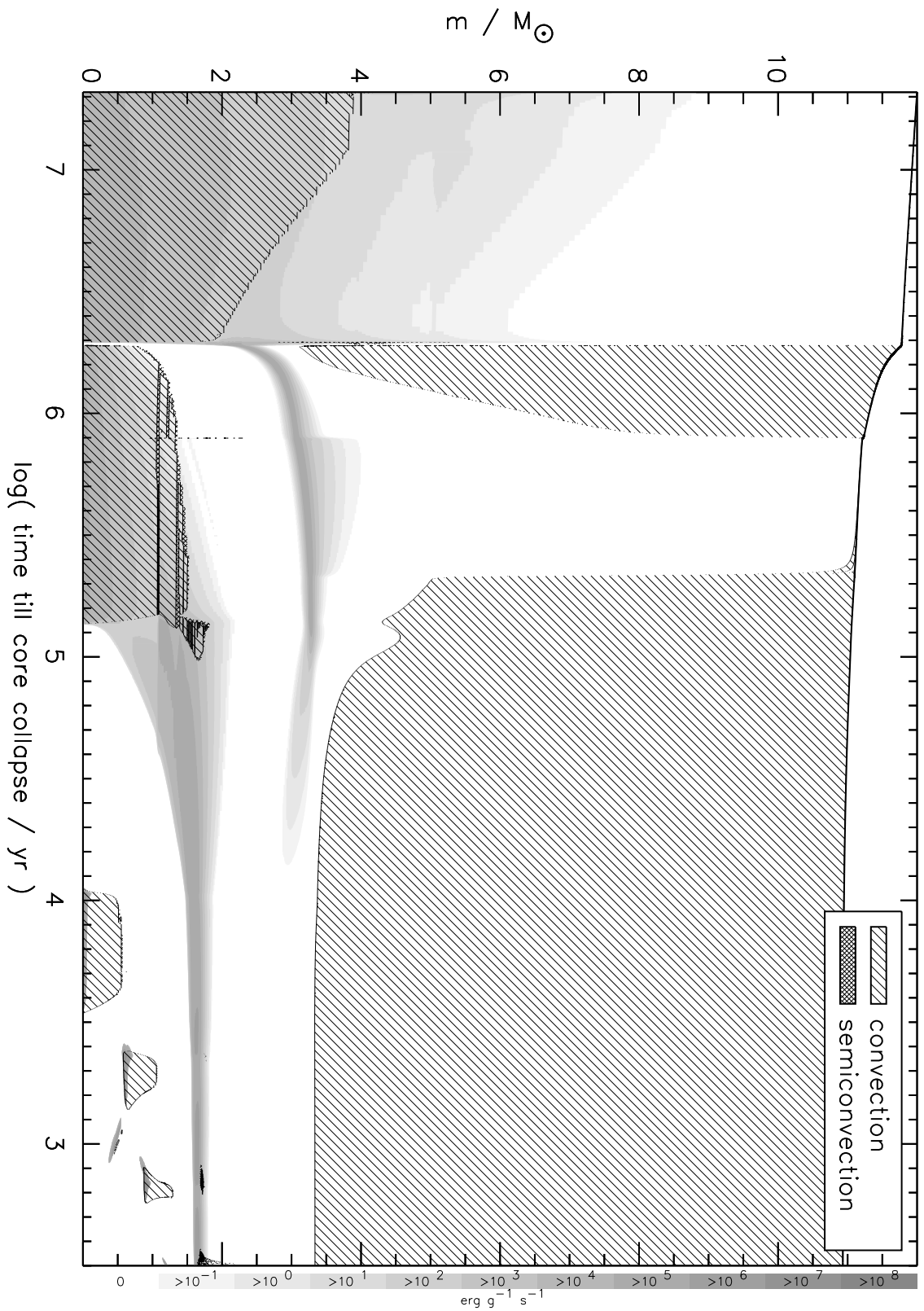

Figure E.19: Evolution of Model F12B until post-central carbon burning. Convection and net nuclear energy generation. See Sect. E.1 for details.

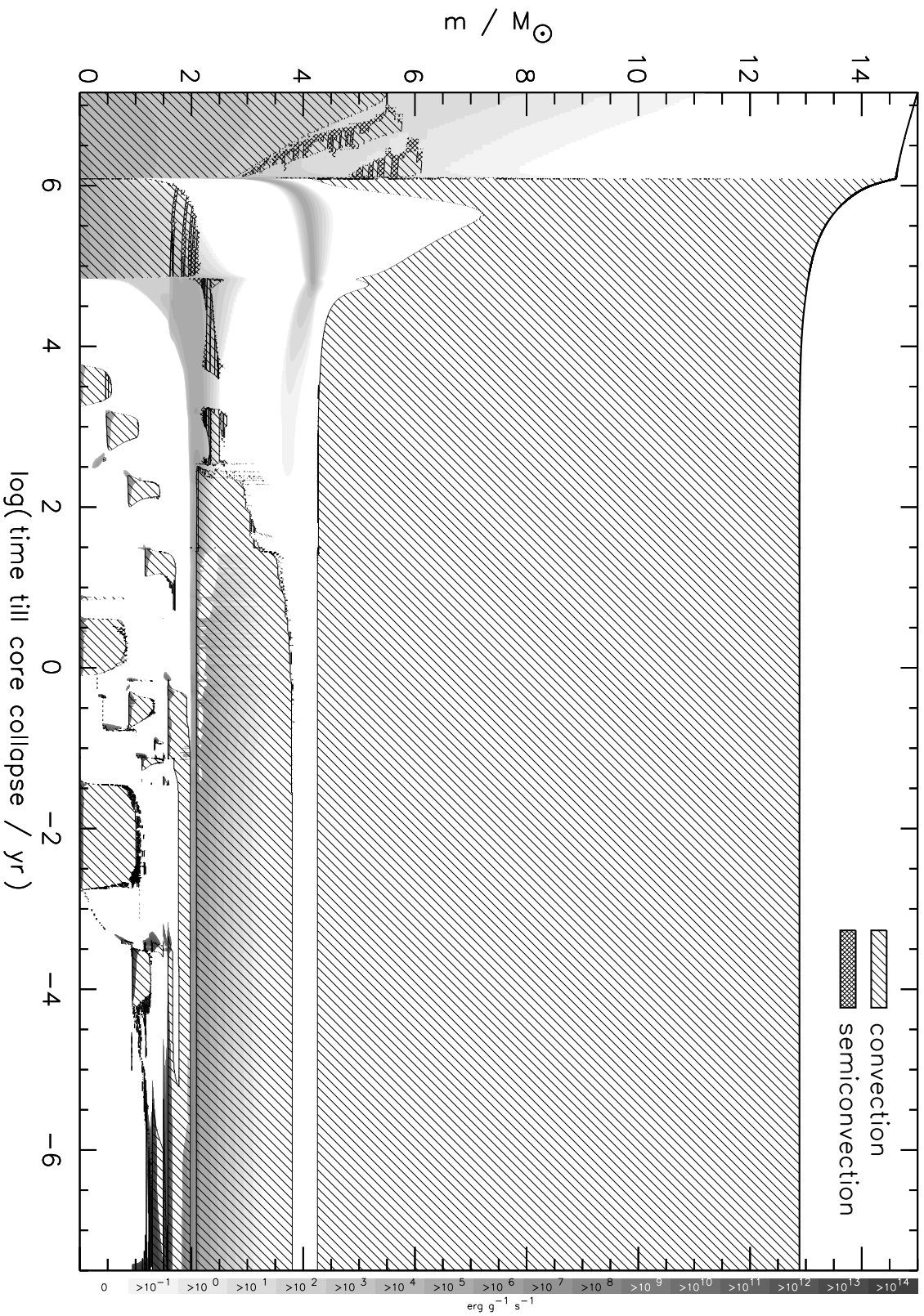

Figure E.20: Evolution of Model F15B until core collapse. Convection and net nuclear energy generation. See Sect. E.1 for details.

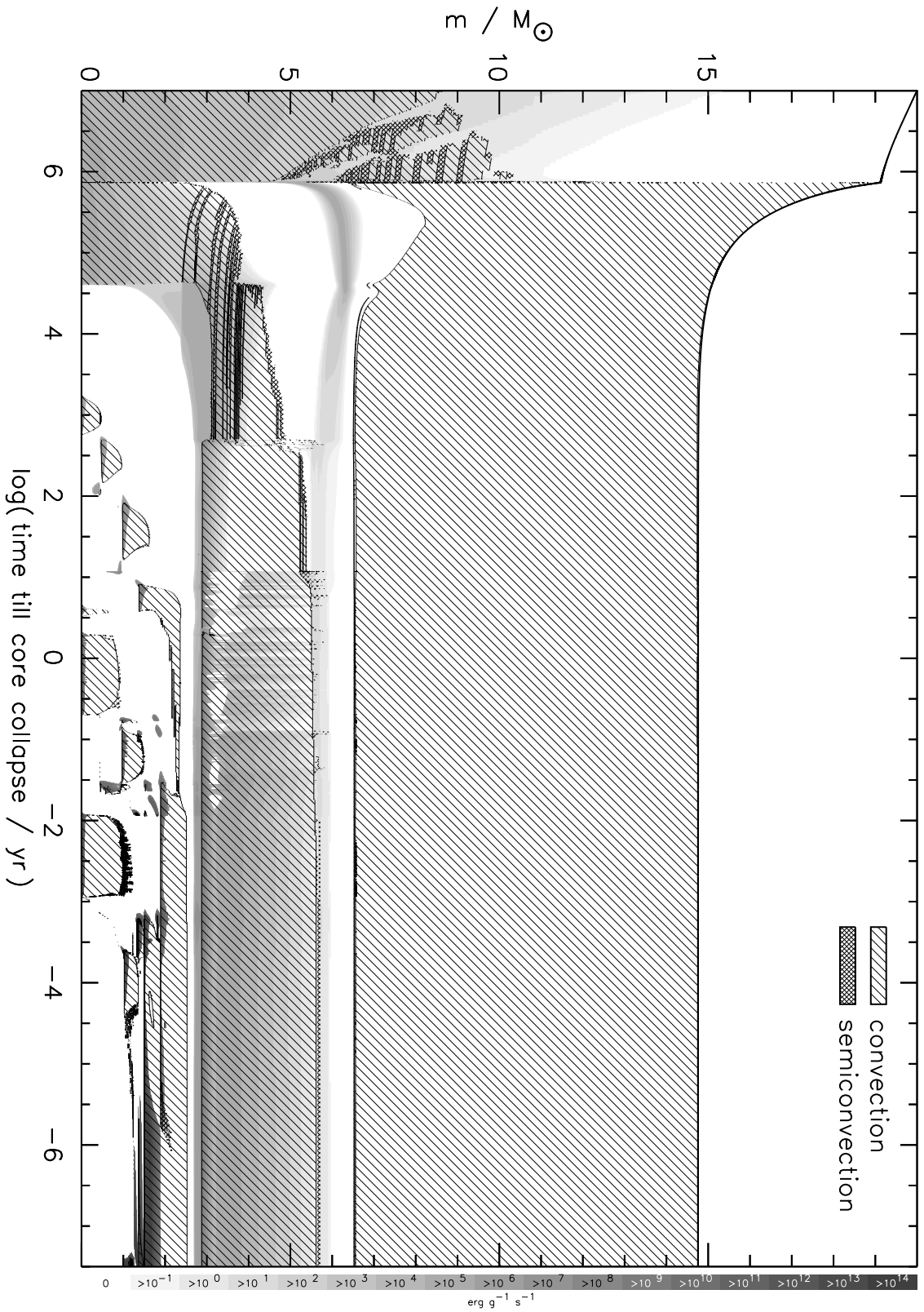

Figure E.21: Evolution of Model F20B until core collapse. Convection and net nuclear energy generation. See Sect. E.1 for details.

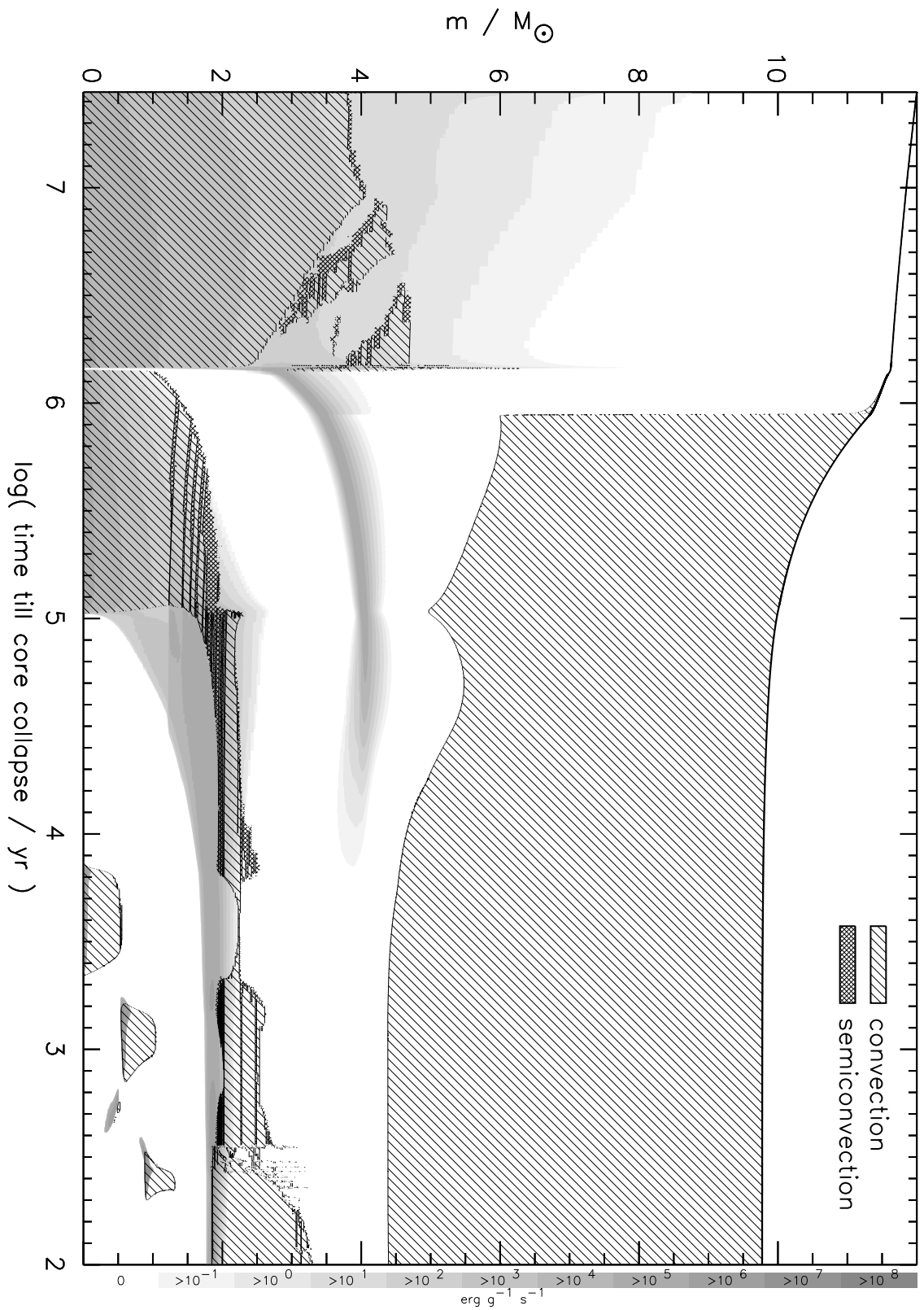

Figure E.22: Evolution of Model H12B until post-central carbon burning. Convection and net nuclear energy generation. See Sect. E.1 for details.

Appendix F

Presupernova structure of the stars

In this section the presupernova structures of all models followed until core collapse are shown. Panel **A** gives the distribution of the dominant chemical species, ^{1}H, ^{4}He, ^{12}C, ^{14}N, ^{16}O, and ^{28}Si, above the "iron" core. The plot ends at some point in the envelope. At higher mass coordinates the composition is constant. Panel **B** gives the run of temperature T (left scale, solid line) and density ρ (right scale, dotted line). In Panel **C** the entropy per baryon and the individual contributions from ions, electrons, pairs, radiation, and ionization are displayed (left scale). The number of electrons per baryon is shown as grey line (right scale). Panel **D** gives the specific angular momentum (averaged over equipotential surfaces; solid line; left scale) and the angular velocity (dotted line, right scale).

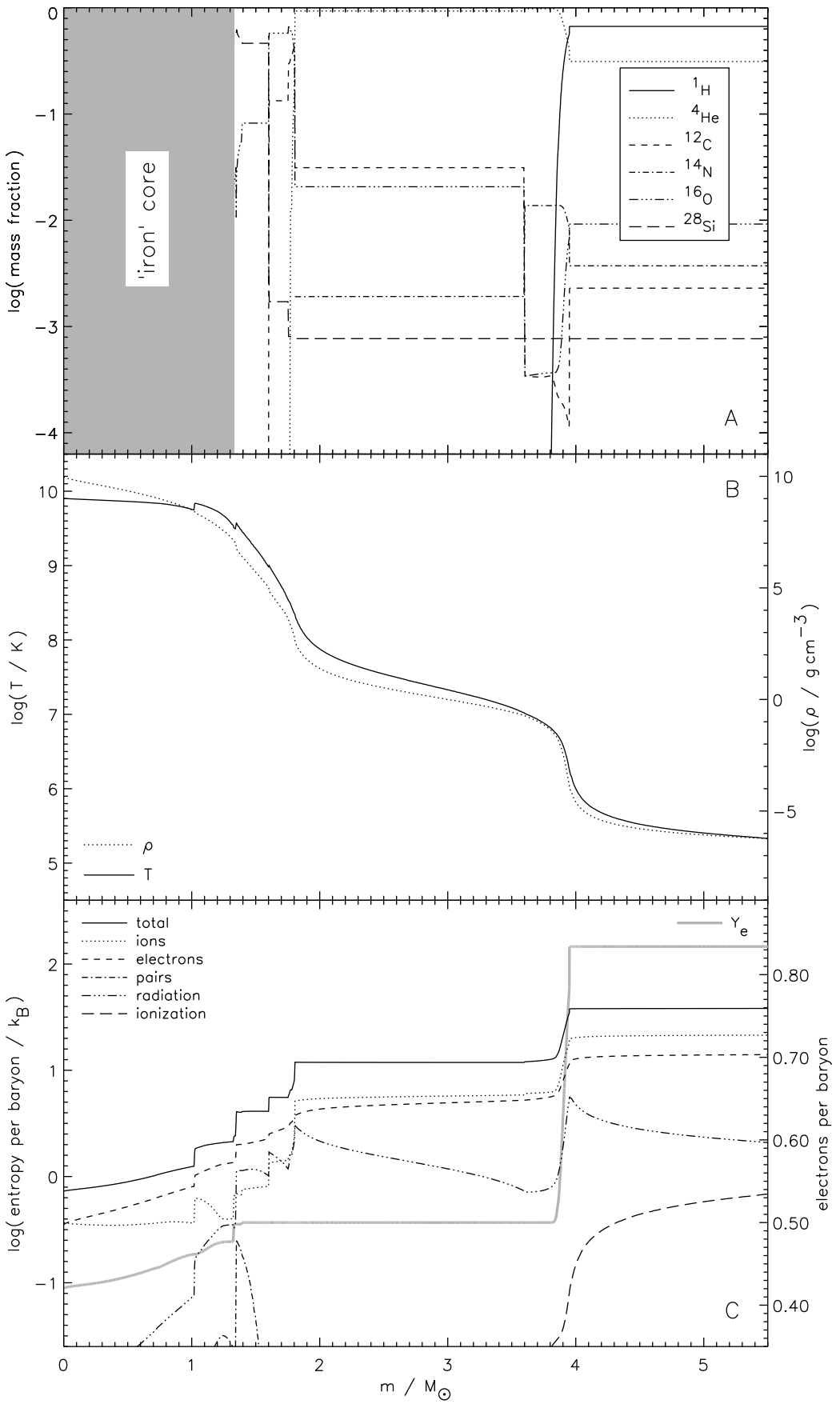

Figure F.1: Presupernova structure of Model D15.

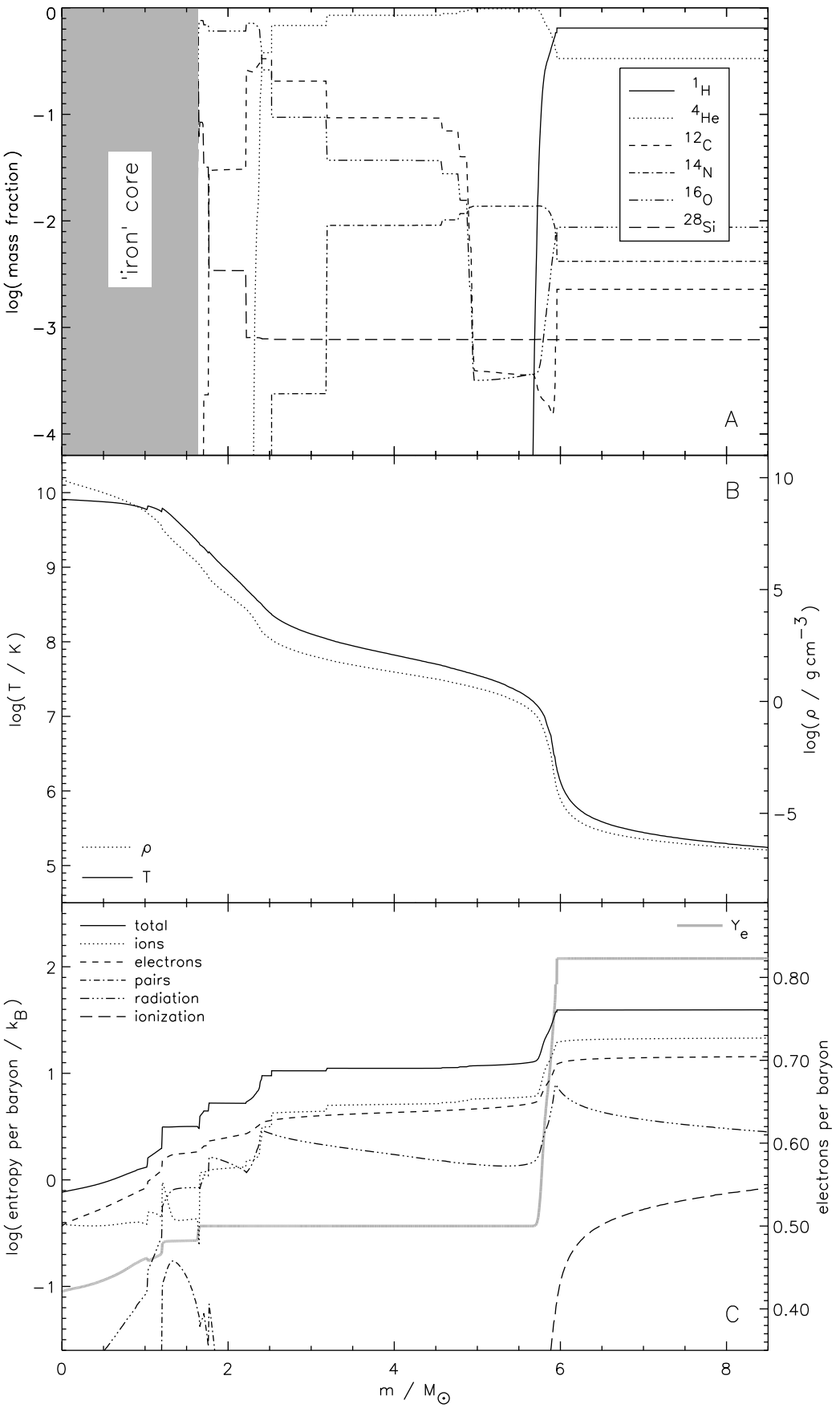

Figure F.2: Presupernova structure of Model D20.

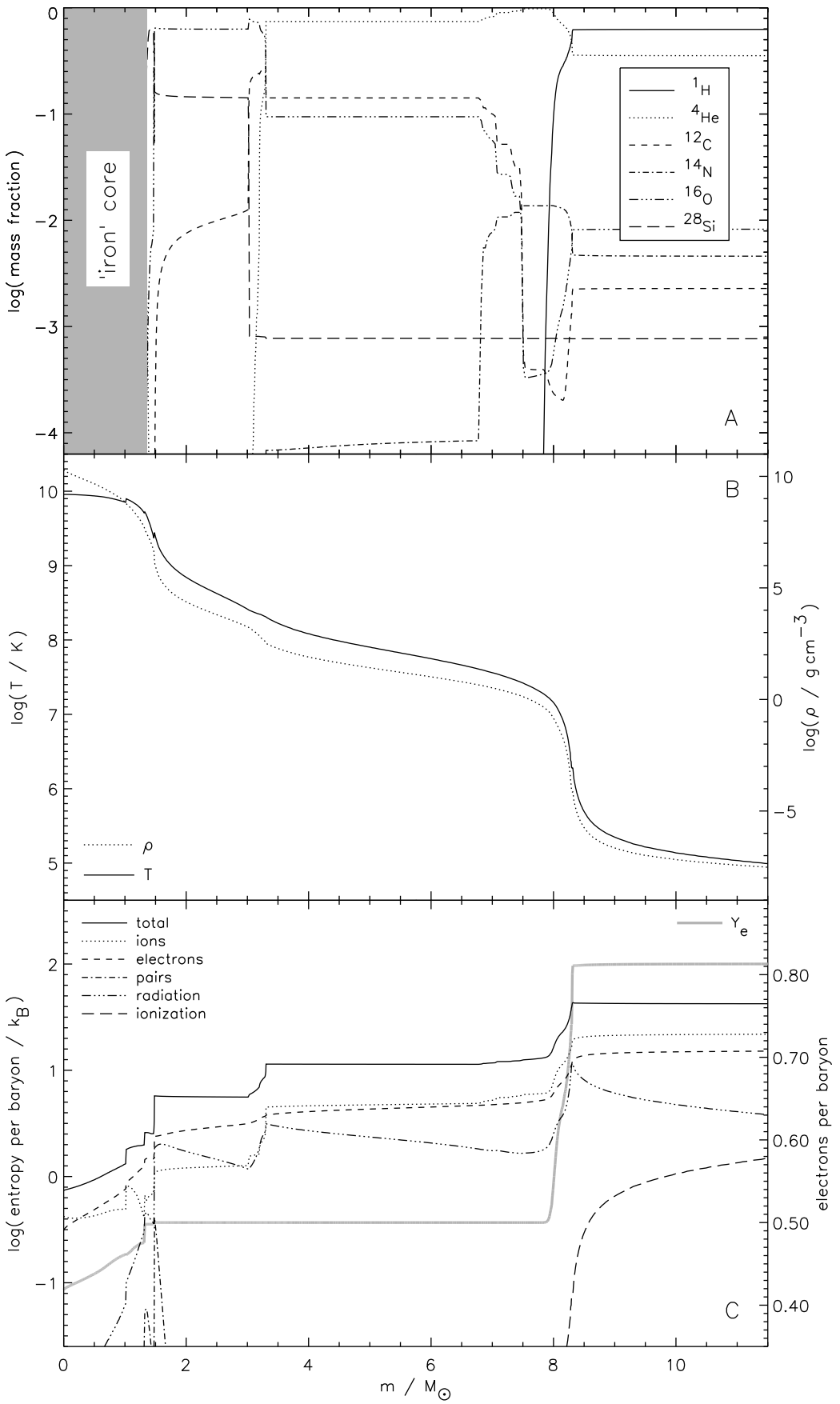

Figure F.3: Presupernova structure of Model D25.

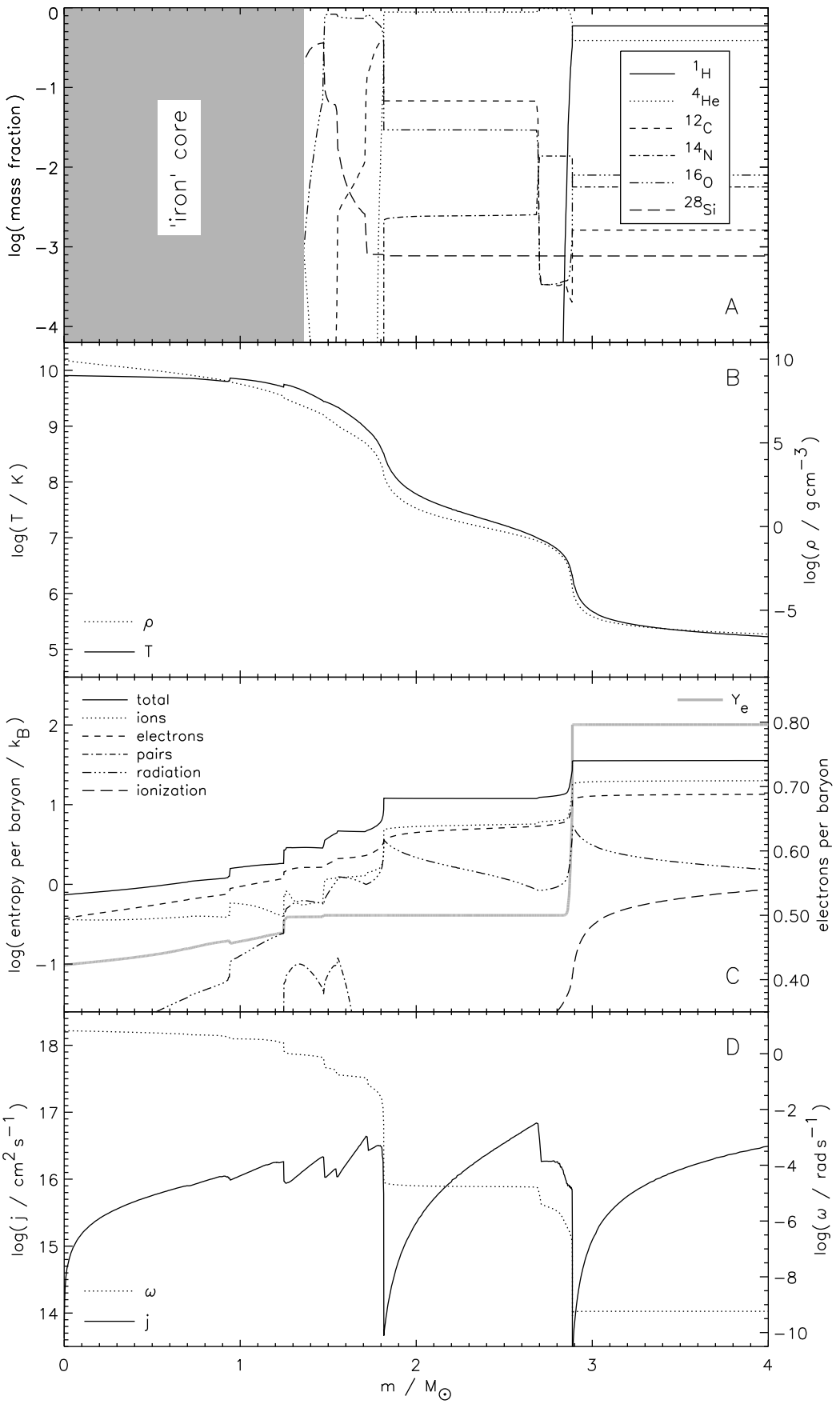

Figure F.4: Presupernova structure of Model E10.

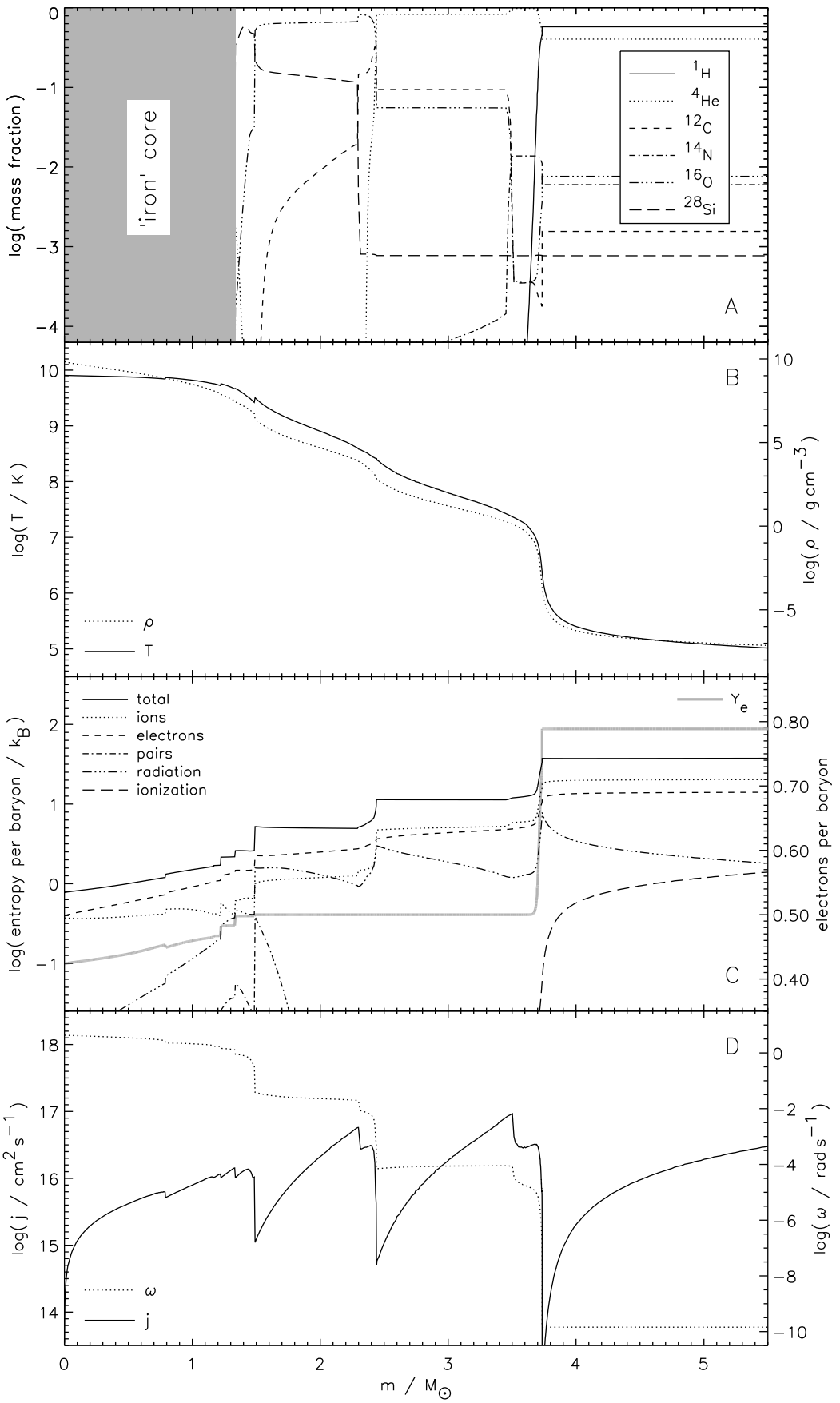

Figure F.5: Presupernova structure of Model E12.

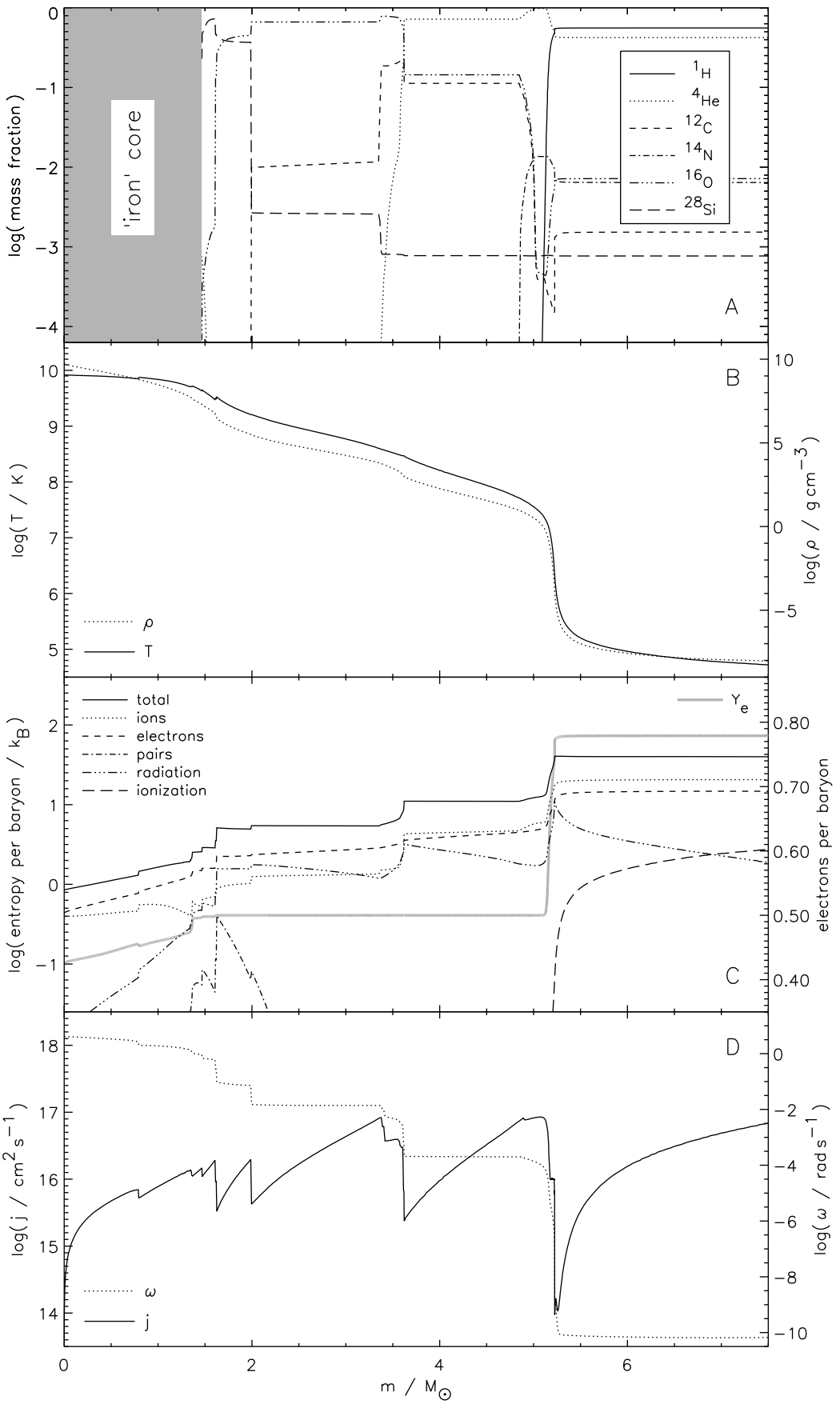

Figure F.6: Presupernova structure of Model E15.

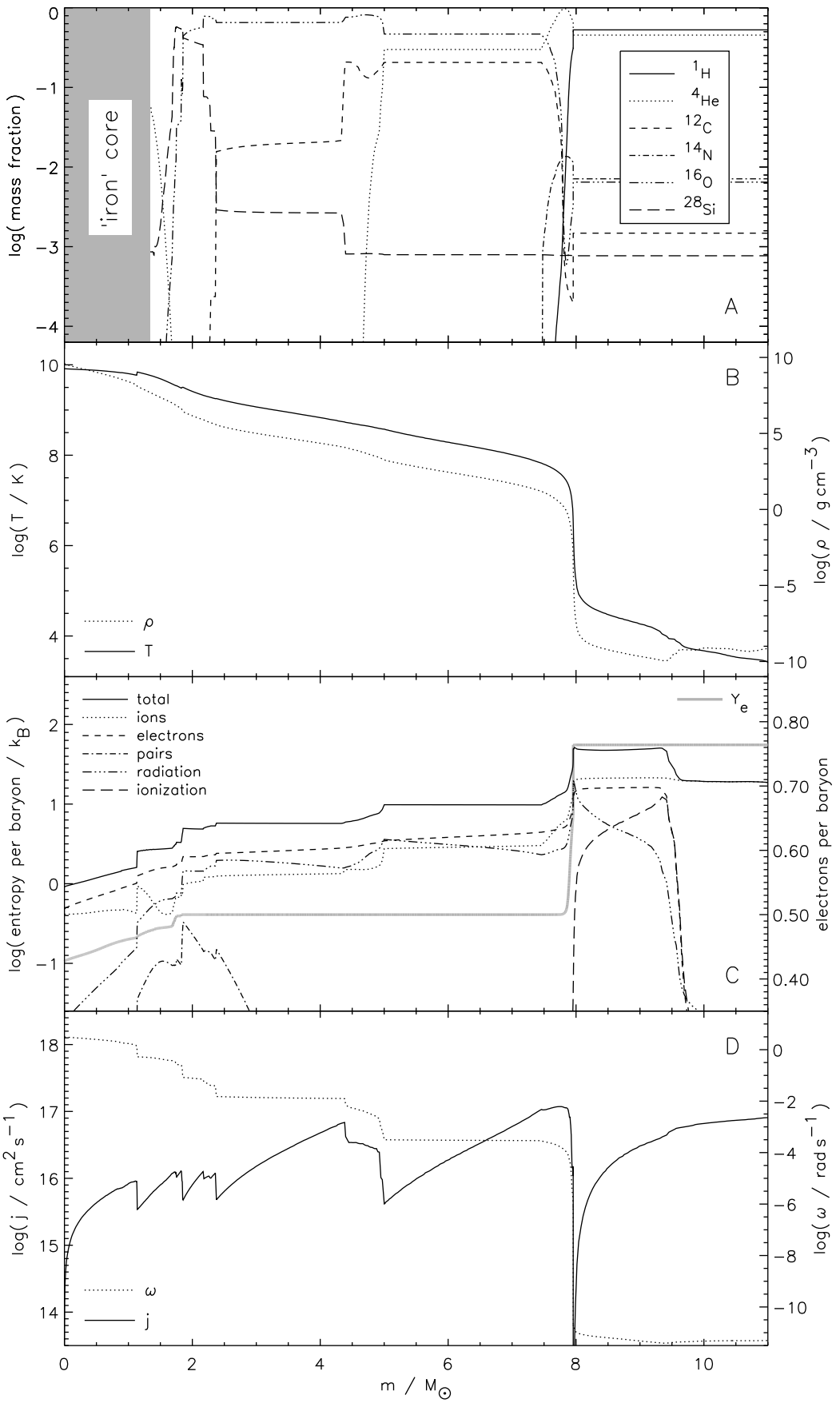

Figure F.7: Presupernova structure of Model E20.

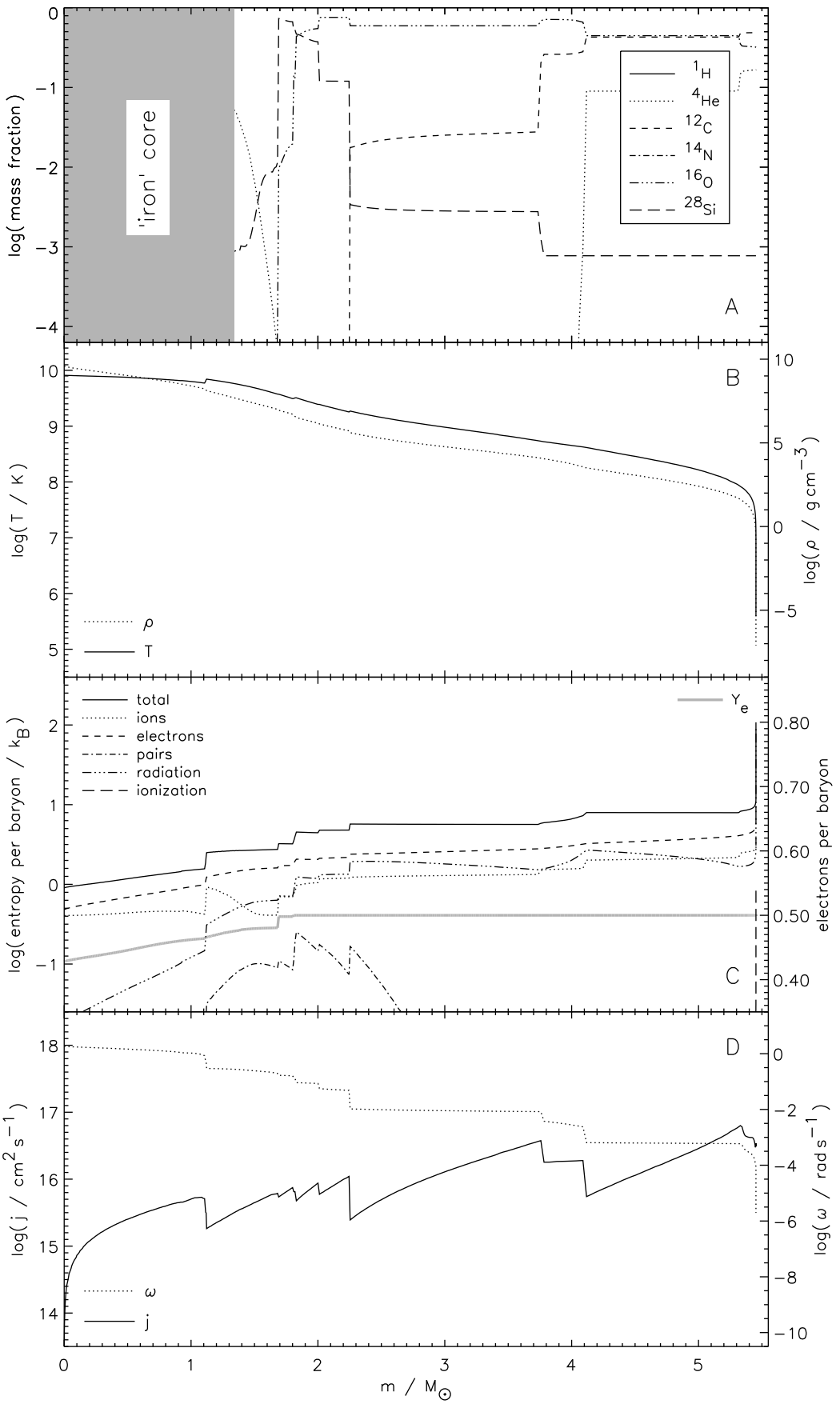

Figure F.8: Presupernova structure of Model E25.

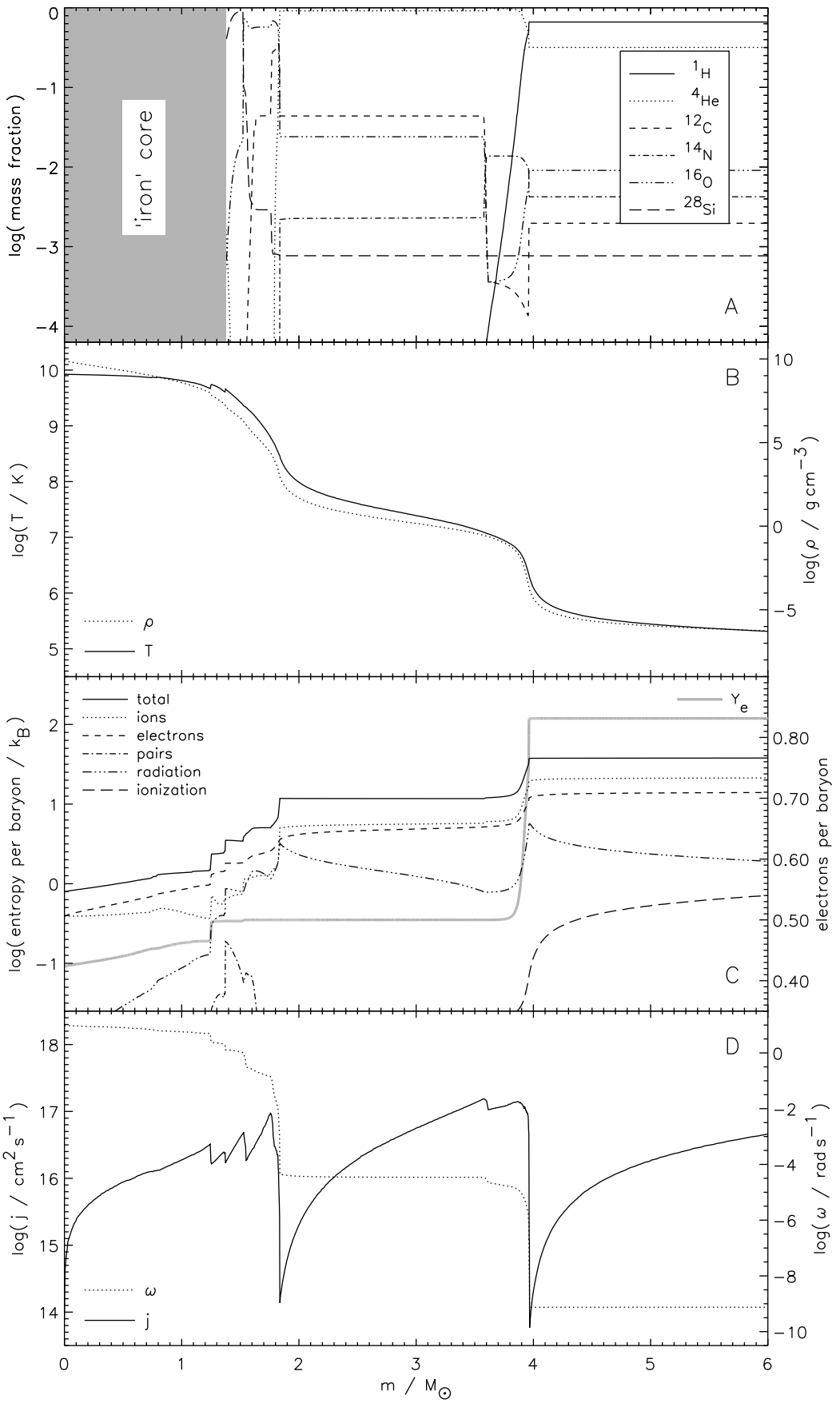

Figure F.9: Presupernova structure of Model G15B.

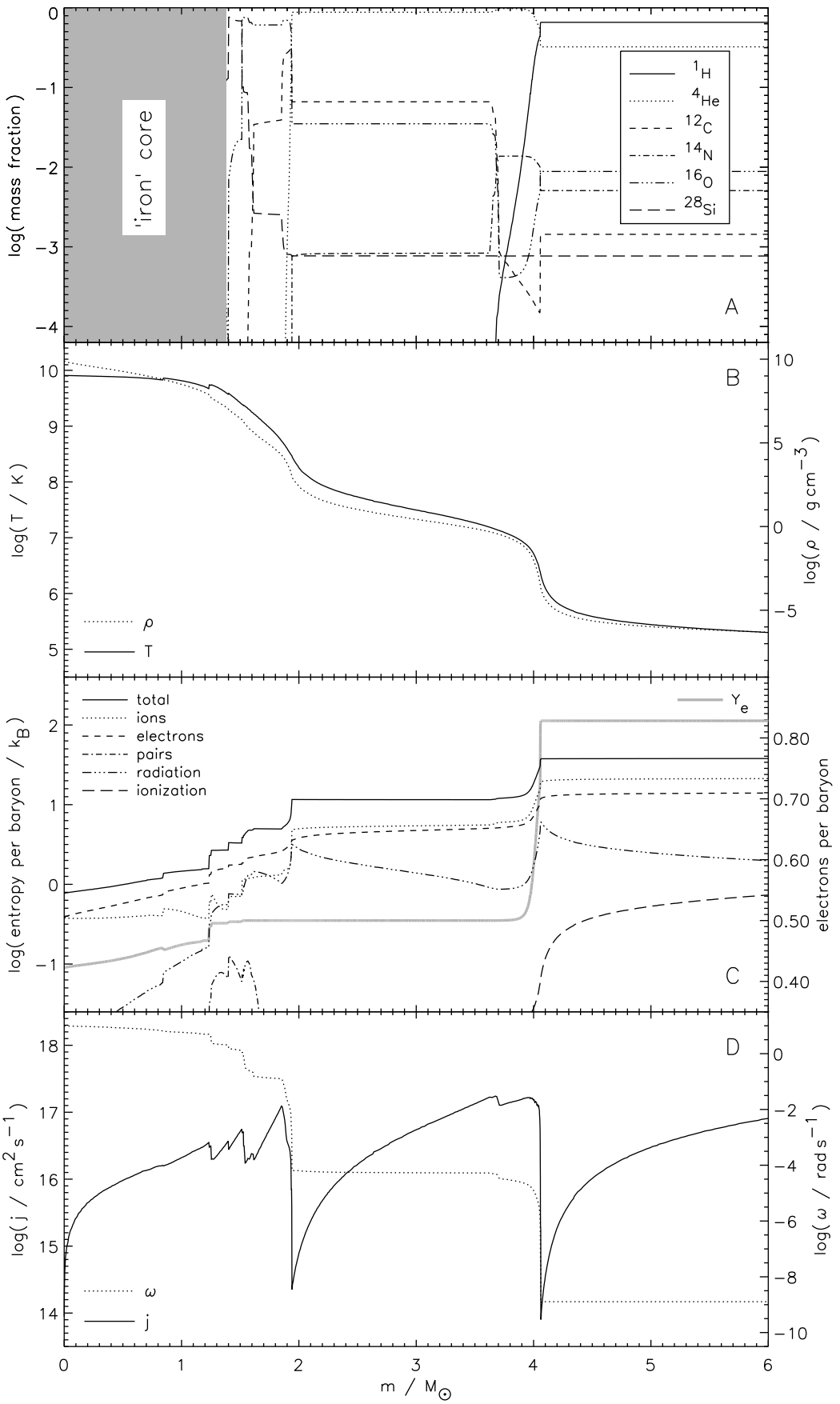

Figure F.10: Presupernova structure of Model E15B.

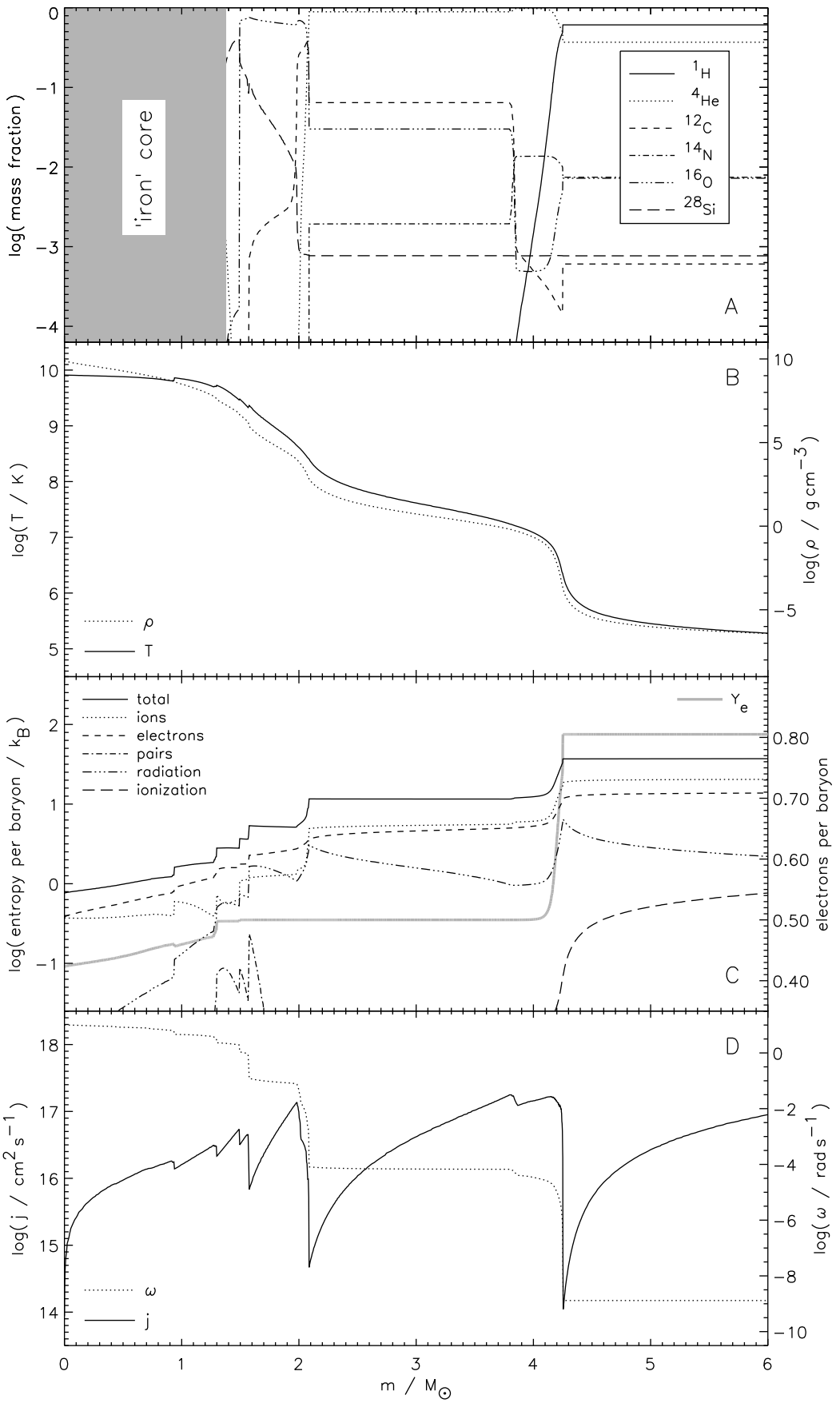

Figure F.11: Presupernova structure of Model F15B.

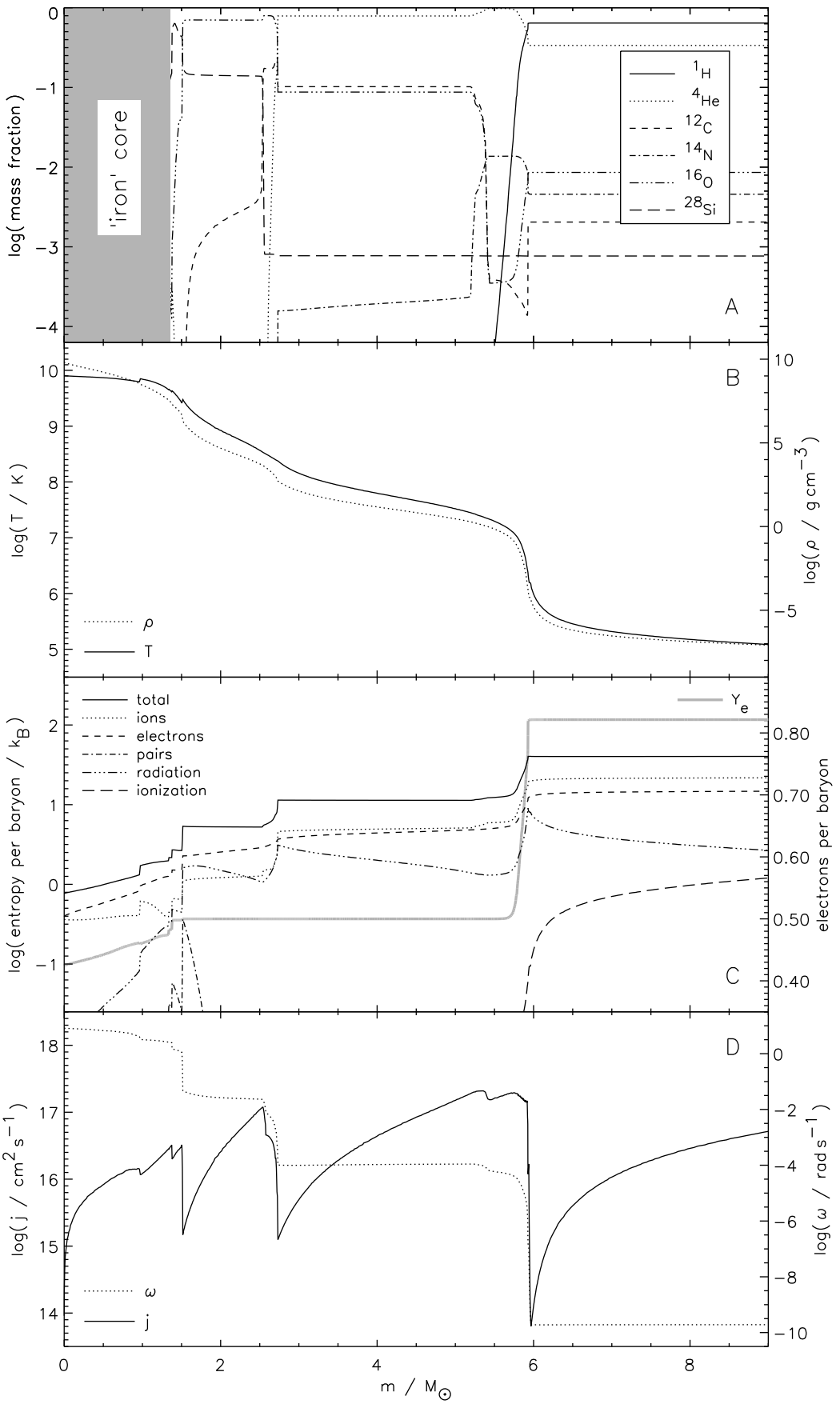

Figure F.12: Presupernova structure of Model G20B.

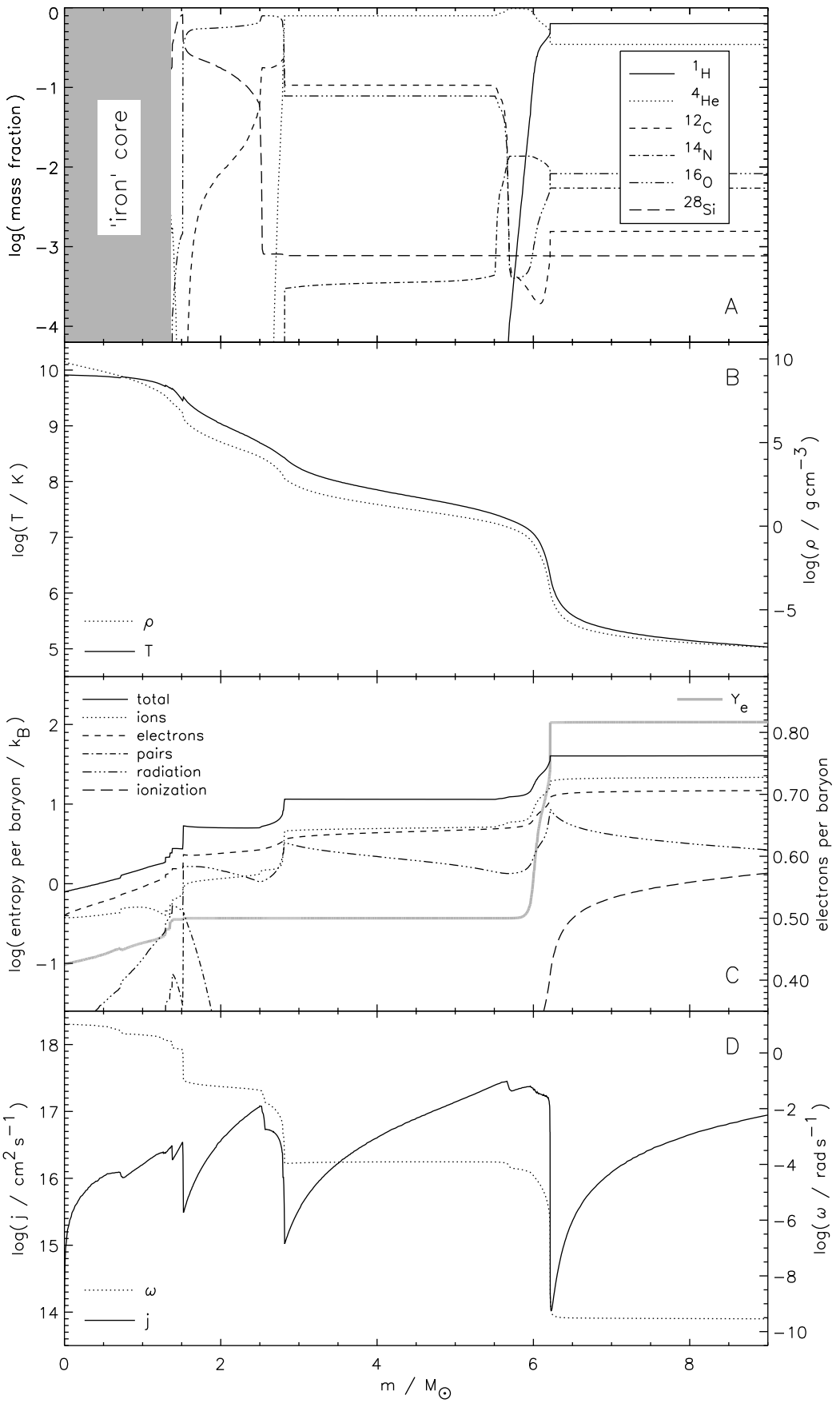

Figure F.13: Presupernova structure of Model E20B.

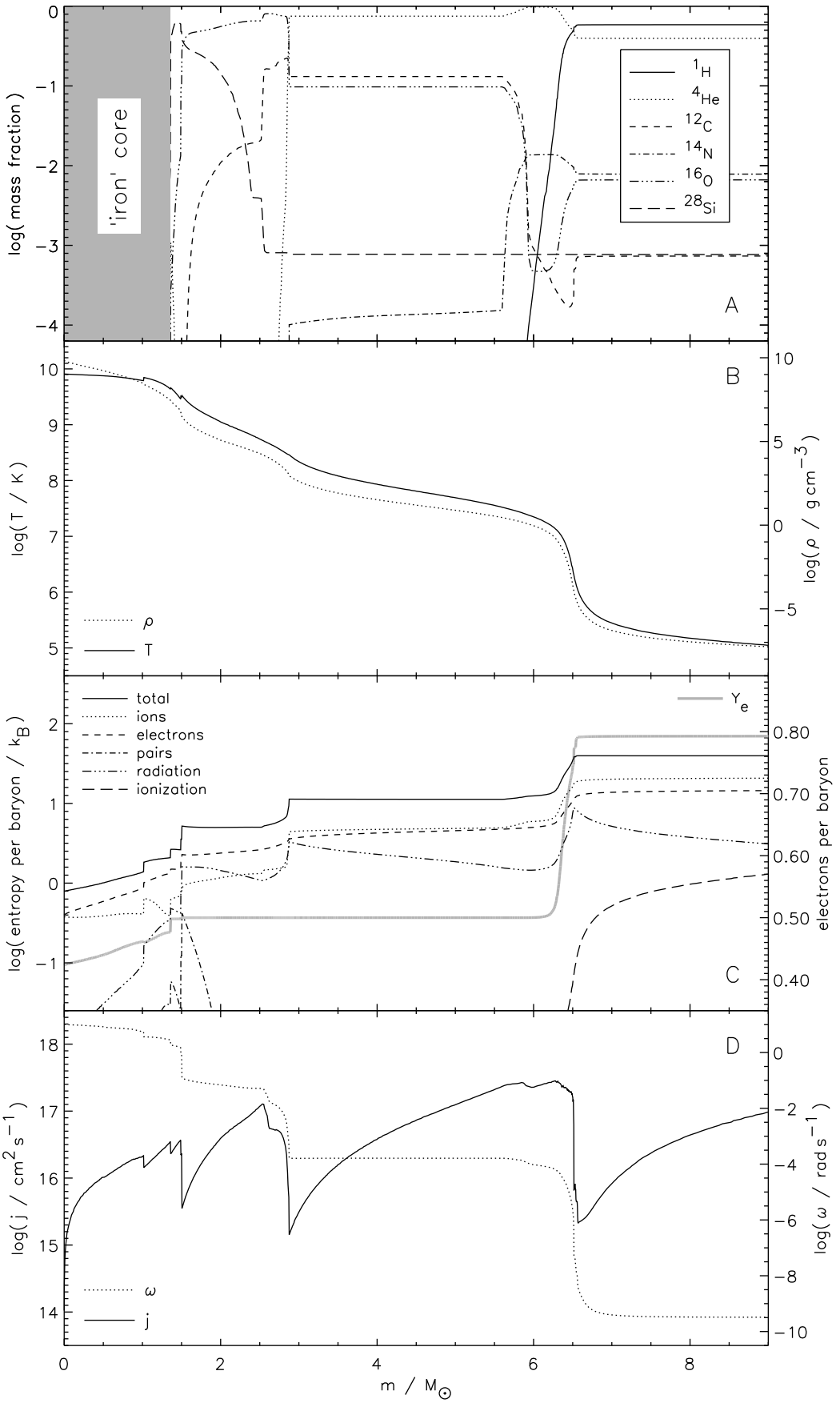

Figure F.14: Presupernova structure of Model F20B.

Bibliography

List of some abbreviations:

A&A :	Astronomy and Astrophysics
A&AS :	Astronomy and Astrophysics Supplement
AJ :	Astronomical Journal
ApJ :	Astrophysical Journal
ApJS :	Astrophysical Journal Supplement
Ap&SS :	Astrophysics and Space Science
ARA&A :	Annual Review of Astronomy and Astrophysics
ASPC :	Astronomical Society of the Pacific Conference Series
BAAS :	Bulletin of the American Astronomical Society
IAU Symp. :	IAU Symposium
J. Fluid Mech. :	Journal of Fluid Mechanics
MNRAS :	Monthly Notices of the Royal Astronomical Society
Nuc. Phys. A :	Nuclear Physics A
PASJ :	Publications of the Astronomical Society Japan
PASP :	Publications of the Astronomical Society of the Pacific
PASPC :	PASP Conference Series Proceedings
Phys. Rev. Lett. :	Physical Review Letters
Phys. Rev. D :	Physical Reviews
Phys. Rev. :	Physical Reviews D
Sci. :	Science
Space Sci. Rev. :	Space Science Review
ZfAp :	Zeitschrift für Astrophysik

Acheson, D.J. 1978, *Phil. Trans. Roy. Soc. London A*, **289**, 40.
Aksenov, A.G., Zabrodina, E.A., Imshennik, V.S., Nadezhin, D.K. 1997, *Astronomy letters*, **23**, 779.
Alexander, D.R. 1994, *BAAS*, **184**, #55.10.
Alexander, D.R., Fergusson, J.W. 1994, *ApJ*, **437**, 879.
Anders, E., Grevesse, N. 1989, *Geochim. Cosmochim. Acta*, **53**, 197.
Antia, H.M., Basu, S., Chitre, S.M. 1997, *MNRAS*, **298**, 543.
Appenzeller, I. 1970, *A&A*, **5**, 355.
Arcoragi, J.-P., Langer, N., Arnould, M. 1991, *A&A*, **249**, 134.
Arnett, W.D. 1969, *Ap&SS*, **5**, 180.

Arnett, W.D. 1996, *Supernovae and Nucleosynthesis*, Princeton University Press, Princeton.
Arnett, W.D., Bahcall, J.N., Kirshner, R.P., Woosley, S.E. 1989, *ARA&A*, **27**, 629.
Arnould, A., Mowlavi, N. 1993, in *Inside the Stars*, ed. W.W. Weiss, A. Baglin, ASPC, **40**, p. 310.
Aubert, O., Prantzos, N., Baraffe, I. 1996, *A&A*, **312**, 845.
Baker, N., Kippenhahn, R. 1959, *ZfAp*, **48**, 140.
Beech, M., Mitalas, R. 1994, *ApJS*, **95**, 517.
Bernasconi, P.A., Maeder, A. 1996, *A&A*, **307**, 829.
Bethe, H. 1939, *Phys. Rev.*, **55**, 434.
Bildsten, L. 1998, private communication.
Bjorkman, J.E. 1997, in *Stellar atmospheres: theory and observations*, ed. J.P. De-Greve, R. Blomme, H. Hensberge, Springer, Berlin, p. 239.
Bjorkman, J.E., Cassinelli, J.P. 1993, *ApJ*, **409**, 429.
Bodenheimer, P. 1971, *ApJ*, **176**, 153.
Böhm-Vitense, E. 1958, *ZfAp*, **46**, 108.
Brandner, W., Grebel, E.K., Chu, Y.-H., Weis, K. 1997, *ApJ*, **457**, L45.
Braun, H. 1997, PhD thesis, Ludwig-Maximilians-Universität München.
Braun, H., Langer, N. 1995, *A&A*, **297**, 483.
Burbidge, E.M., Burbidge, G.R., Fowler, W.A., Hoyle, F. 1957, *Rev. Modern Physics*, **29**, 574.
Burrows, C.J. 1994, press release no. STScI-PR94-22.
Burrows, C.J. et al. 1995, *ApJ*, **452**, 680.
Chaboyer, B., Zahn, J.-P. 1992, *A&A*, **253**, 173.
Chevalier, R.A. 1996, *Ap&SS*, **245**, 255.
Chin, C.-W., Stothers, R.B. 1991, *ApJS*, **77**, 299.
Chin, Y.-N., Henkel, C., Langer, N., Mauersberger, R. 1998, *A&A*, submitted.
Chiosi, C., Maeder, A. 1986, *ARA&A*, submitted.
Clayton, D.D. 1968, *Principles of Stellar Evolution and Nucleosynthesis*, McGraw-Hill, New York.
Collins II, G.W. 1974, *ApJ*, **191**, 157.
Cox, J.P. 1980, *Theory of Stellar Pulsations*, Princeton University Press, Princeton.
Cox, J.P., Giuli, R.T. 1968, *Principles of Stellar Structure*, Gordon and Breach, Science Publishers, Inc., New York.
de Jager, C., Nieuwenhuijzen, H., van der Hucht, K.A. 1986, *IAU Symp.*, **116**, 109.
de Jager, C., Nieuwenhuijzen, H., van der Hucht, K.A. 1988, *A&AS*, **72**, 259.
Denissenkov, P.A. 1994, *A&A*, **287**, 113.
Eastman, R.G., Woosley, S.E., Weaver, T.A., Pinto, P.A. 1994, *ApJ*, **430**, 300.
Eberl, T. 1997, private communication.
Eddington, A.S. 1925, *Observatory*, **48**, 73.
Eddington, A.S. 1929, *MNRAS*, **90**, 54.
Eggleton, P.P. 1971, *MNRAS*, **151**, 351.
El Eid, M.F., Langer, N. 1986, *A&A*, **176**, 274.
Emden, R. 1907, *Gaskugeln: Anwendungen der mechanischen Wärmetheorie auf kosmologische und meteorologische Probleme*, Teubner, Leipzig.

Endal, A.S., Sofia, S. 1976, *ApJ*, **210**, 184.
Endal, A.S., Sofia, S. 1978, *ApJ*, **220**, 279.
Endal, A.S., Sofia, S. 1979, *ApJ*, **232**, 531.
Engels, D., Kreysa, E., Schultz, G.V., Sherwood, W.A. 1983, *A&A*, **124**, 123.
Eriguchi, Y., Müller, E. 1985, *A&A*, **147**, 161.
Eryurt, D., Kırbıyık, H., Kızıloğlu, N., Civelek, R., Weiss, A. 1994, *A&A*, **282**, 485.
Feast, M.W. 1992, in *Instabilities in evolved super- and hypergiants*, ed. C. de Jager, H. Nieuwenhuijzen, North-Holland, Amsterdam, p. 18.
Feast, M.W., Glass, I.S., Whitelock, P.A., Catchpole, R.M. 1989, *MNRAS*, **241**, 375.
Fesen, R.A., Shull, J.M., Hurford, A.P. 1997, *AJ*, **113**, 354.
Filippenko, A.V. 1997, in *Thermonuclear supernovae*, ed. P. Ruiz-Lapuente, R. Canal, J. Isern, Kluwer, Dordrecht, p. 1.
Fliegner, J. 1993, diploma thesis, Universitäts-Sternwarte Göttingen.
Fliegner, J., Langer, N., Venn, K. 1996, *A&A*, **308**, L13.
Fricke, K. 1968, *ZfAp*, **68**, 317.
Friend, D.B., Abbott, D.C. 1986, *ApJ*, **311**, 701.
Fukuda, I. 1982, *PASP*, **94**, 271.
Fullerton, A.W. 1997, in *Stellar atmospheres: theory and observations*, ed. J.P. DeGreve, R. Blomme, H. Hensberge, Springer, Berlin, p. 187.
García-Segura, G., Langer, N., Mac Low, M.-M. 1996, *A&A*, **316**, 133.
García-Segura, G., Langer, N., Mac Low, M.-M. 1997, in *Luminous Blue Variables: Massive Stars in Transition*, ed. A. Nota, H.J.G.L.M. Lamers, ASPC, **120**, p. 332.
García-Segura, G., Langer, N., Różyczka, M., Franco, J. 1998, in preparation.
García-Segura, G., Mac Low, M.-M. 1995, *ApJ*, **455**, 160.
Gautschy, A., Saio, H. 1993, *MNRAS*, **262**, 213.
Gautschy, A., Saio, H. 1995, *ARA&A*, **33**, 75.
Gies, D.R., Lambert, D.L. 1992, *ApJ*, **387**, 673.
Gilmozzi, R., Cassatella, A., Clavel, J., Fransson, C., Gonzalez, R., Gry, C., Panagia, N., Talavera, A., Wamsteker, W. 1987, *Nature*, **328**, 318.
Goldreich, P., Schubert, G. 1967, *ApJ*, **150**, 571.
Gough, D.O., Ostriker, J.P., Stobie, R.S. 1965, *ApJ*, **142**, 1649.
Grevesse, N., Noels, A. 1993, in *Origin and Evolution of the Elements*, ed. N. Prantzo, E. Vangioni-Flam, M. Casse, Cambridge Univ. Press, Cambridge, p. 13.
Groenewegen, M.A.T., Whitelock, P.A. 1996, *MNRAS*, **281**, 1347.
Gummersbach, C.A., Zickgraf, F.-J., Wolf, B. 1995, *A&A*, **302**, 409.
Halbedel, E. 1996, *PASP*, **108**, 833.
Harkness, R.P., Wheeler, J.C. 1990, in *Supernovae*, ed. A.G. Petschek, Springer-Verlag, New York, p. 1.
Heger, A., Jeannin, L., Langer, N., Baraffe, I. 1997, *A&A*, **327**, 224.
Heger, A., Langer 1996, *A&A*, **315**, 421.
Heger, A., Langer 1998, *A&A*, **334**, 210.
Heger, A., Langer, N., Woosley, S. 1998, in *Proceedings of the 9$^{\rm th}$ Workshop on Nuclear Astrophysics*, ed. W. Hillebrandt, E. Müller, MPA/P10, p. 14.
Herrero, A. 1994, *Space Sci. Rev.*, **66**, 137.

Herrero, A., Kudritzki, R.P., Vilchez, J.M., Kunze, D., Butler, K., Haser, S. 1992, *A&A*, **261**, 209.
Herrero, A., Villamariz, M.R., Martín, E.L. 1998, in *Proceedings of the 2nd Boulder-Munich Workshop on Hot Stars*, ed. I. Howarth et al., PASPC, **131**, p. 159.
Hoffman, R.D., Woosley, S.E., Weaver, T.A. 1998, *ApJ*, in preparation.
Höflich, P., Langer, N., Duschinger, M. 1993, *A&A*, **275**, L29.
Hofmeister, E., Kippenhahn, R., Weigert, A. 1964, *ZfAp*, **59**, 242.
Hoppe, P., Amari, S., Zinner, E., Ireland, T., Lewis, R.S. 1994, *ApJ*, **430**, 870.
Howarth, I.D., Siebert, K.W., Hussain, G.A.J., Prinja, R.K. 1997, *MNRAS*, **284**, 265.
Hoyle, F., Fowler, W.A. 1960, *ApJ*, **132**, 565.
Huebener, W.F., Merts, A.L., Magee, N.H., Argo, M. F., J. 1964, *Astrophys. Opacity Library*, **LA-6760-M**.
Iben, I., J. 1974, *ARA&A*, **12**, 215.
Iglesias, C.A., Rogers, F.J. 1996, *ApJ*, **464**, 943.
Ignace, R., Cassinelli, J.P., Bjorkman, J.E. 1996, *ApJ*, **459**, 671.
Imshennik, V.S. 1995, *Space Sci. Rev.*, **74**, 325.
Itoh, N., Kohyama, Y., Takeuchi, H. 1987, *ApJ*, **317**, 733.
Itoh, N., Kuwashima, F., Munakata, H. 1990, *ApJ*, **362**, 620.
James, R.A., Kahn, F.D. 1970, *A&A*, **5**, 232.
James, R.A., Kahn, F.D. 1971, *A&A*, **12**, 332.
Jeannin, L., Fokin, A., Gillet, D., Baraffe, I. 1996, *A&A*, **314**, L1.
Jones, T.J., McGregor, P.J., Gehrz, R.D., Lawrence, G.F. 1994, *AJ*, **107**, 111.
Jorison, A., Arnould, M. 1989, *A&A*, **221**, 161.
Kato, S. 1966, *PASJ*, **18**, 374.
Kippenhahn, R. 1969, *A&A*, **2**, 309.
Kippenhahn, R. 1974, in *Late Stages of Stellar Evolution*, ed. R.J. Taylor, J.E. Hesser, IAU Symp. 66, Reidel, Dortrecht, p. 20.
Kippenhahn, R. 1977, *A&A*, **58**, 267.
Kippenhahn, R., Meyer-Hofmeister, E., Thomas, H.C. 1970, *ApJ*, **5**, 155.
Kippenhahn, R., Thomas, H.-C. 1970, in *Stellar Rotation*, ed. A. Slettebak, IAU Coll. 4, Reidel, Dortrecht, p. 20.
Kippenhahn, R., Weigert, A. 1991, *Stellar Structure and Evolution*, Springer–Verlag, Berlin, 2nd edition.
Knobloch, E., Spruit, H.C. 1983, *A&A*, **125**, 59.
Koerner, W.D., Sargent, A.I. 1995, *AJ*, **109**, 2138.
Krishnamurthi, A., Pinsonneault, M.H., Barnes, S., Sofia, S. 1997, *ApJ*, **480**, 303.
Kumar, P., Narayan, R., Loeb, A. 1995, *ApJ*, **453**, 480.
Kwok, S. 1993, *ARA&A*, **31**, 63.
Lamers, H.J.G.M.L. 1993, in *Massive Stars: Their Lives in the Interstellar Medium*, ed. J.P. Cassinelli, E.B. Churchwell, ASPC, **35**, p. 517.
Lang, K.R. 1991, *Astrophysical Data*, Springer–Verlag, New York.
Langer, G.E. 1971, *MNRAS*, **155**, 199.
Langer, N. 1989a, *A&A*, **210**, 93.
Langer, N. 1989b, *A&A*, **220**, 135.

Langer, N. 1989c, *Sterne und Weltraum*, **2**, 80.
Langer, N. 1991a, *A&A*, **252**, 669.
Langer, N. 1991b, *A&A*, **243**, 155.
Langer, N. 1992, *A&A*, **265**, L17.
Langer, N. 1997, in *Luminous Blue Variables: Massive Stars in Transition*, ed. A. Nota, H.J.G.L.M. Lamers, ASPC, **120**, p. 83.
Langer, N. 1998, *A&A*, **329**, 551.
Langer, N., Arcoragi, J.-P., Arnould, M. 1989, *A&A*, **210**, 187.
Langer, N., Braun, H., Wellstein, S. 1998a, in *Proceedings of the 9th Workshop on Nuclear Astrophysics*, ed. W. Hillebrandt, E. Müller, MPA/P10, p. 18.
Langer, N., Fliegner, J., Heger, A., Woosley, S.E. 1997a, in *Nuclei in the Cosmos IV*, ed. J. Görres, G. Mathews, M. Wiescher, S. Shore, Nuc. Phys. A, **621**, Elsevier Science BV, Amsterdam, p. 457c.
Langer, N., García-Segura, G., Mac Low, M.-M. 1998b, *ApJ*, submitted.
Langer, N., Heger, A. 1997, in *Proceedings of the 2nd Boulder-Munich Workshop on Hot Stars*, ed. I. Howarth et al., PASPC, **131**, p. 76.
Langer, N., Heger, A. 1998, in *Proceedings of Worshop on B[e] stars*, ed. C. Jaschek, A.M. Hubert, Kluwer, in press.
Langer, N., Heger, A., Fliegner, J. 1997b, in *Fundamental Stellar Properties: The Interaction between Observation and Theory*, ed. T.R. Bedding, A.J. Booth, J. Davis, IAU Symp., **189**, Kluwer, Dordrecht, p. 343.
Langer, N., Heger, A., García-Segura, G. 1998c, *Rev. Modern Astron.*, **11**, in press.
Langer, N., Kiriakidis, M., El Eid, M.F., Frick, K.J., Weiss, A. 1988, *A&A*, **192**, 177.
Langer, N., Maeder, A. 1995, *A&A*, **295**, 685.
Langer, N., Sugimoto, D., Fricke, K.J. 1983, *A&A*, **126**, 207.
Langer, N., Woosley, S.E. 1996, in *From Stars to Galaxies, The Impact of Stellar Physics on Galaxy Evolution*, ed. C. Leitherer et al., ASPC, **98**, p. 220.
Le Bertre, T. 1991, *A&A*, **250**, 351.
Le Bertre, T. 1993, *A&AS*, **97**, 729.
Leibundgut, B. 1995, in *The lives of the neutron stars*, ed. M.A. Alpar, Ü. Kızıloğlu, J. van Paradijs, Kluwer, Dordrecht, p. 3.
Leibundgut, B. 1996, in *Supernova and supernovae remnants*, ed. R. McCray, Z. Wang, IAU Coll. 145, CUP, Cambridge, p. 11.
Li, Y., Gong, Z.G. 1994, *A&A*, **289**, 449.
Lindblom, L., Owen, B.J., Morsink, S.M. 1998, *Phys. Rev. Lett.*, **80**, 4843.
MacFadyen, A., Woosely, S.E. 1998, *ApJ*, in preparation.
Maeder, A. 1987, *A&A*, **178**, 159.
Maeder, A. 1995, *A&A*, **299**, 84.
Maeder, A. 1997a, *A&A*, **321**, 134.
Maeder, A. 1997b, in *Proceedings of the 2nd Boulder-Munich Workshop on Hot Stars*, ed. I. Howarth et al., PASPC 131, p. 85.
Maeder, A., Meynet, G. 1996, *A&A*, **313**, 140.
Maeder, A., Zahn, J.-P. 1998, *A&A*, **334**, 1000.
Marti, J., Rodriguez, L.F., Reipurth, B. 1993, *ApJ*, **416**, 208.

Martin, C.L., Arnett, D. 1995, *ApJ*, **447**, 378.
Mashall, F.E., Gotthelf, E.V., Zhang, W., Middleditch, J., Wang, Q.D. 1998, astro-ph/9803214.
Mathews, G.J., Ward, R.A. 1985, *Rev. Prog. Phys.*, **48**, 1371.
Mestel, L. 1952, *MNRAS*, **112**, 598.
Mestel, L. 1953, *MNRAS*, **113**, 716.
Meyer, F. 1997, *MNRAS*, **285**, L11.
Meynet, G. 1997, in *Proceedings of the 2nd Boulder-Munich Workshop on Hot Stars*, ed. I. Howarth et al., PASPC 131, p. 96.
Meynet, G., Maeder, A. 1997, *A&A*, **321**, 465.
Meynet, G., Maeder, A., Schaller, G., Schaerer, D., Charbonnel, C. 1994, *A&AS*, **103**, 97.
Minkowski, R. 1941, *PASP*, **53**, 224.
Munakata, H., Kohyama, Y., Itoh, N. 1985, *ApJ*, **296**, 197.
Murdin, P. 1994, *MNRAS*, **269**, 89.
Nieuwenhuijzen, H., de Jager, C. 1990, *A&A*, **231**, 134.
Nomoto, K., Hashimoto, M. 1988, *Physics Reports*, **163**, 13.
Nomoto, K., Suzuki, T., Shigeyama, T., Kumahai, S., Yamaoka, H., Saio, H. 1993, *Nature*, **364**, 507.
Nomoto, K., Thielemann, F.-K., Yoki, K. 1984, *ApJ*, **286**, 644.
Nota, A., Livio, M., Clampin, M., Schulte-Ladbeck, R. 1995, *ApJ*, **448**, 788.
Nota, A., Smith, L., Pasquali, A., Clampin, M., Stroud, M. 1997, *ApJ*, **486**, 338.
Novikov, I. 1997, in *Stellar Remnants*, ed. G. Meynet, D. Schaerer, Saas Fee Advanced Course 25, Springer–Verlag, Berlin, p. 237.
Oberlack, U., Bennett, K., Bloemen, H., Diehl, R. et al. 1996, *A&AS*, **120**, C311.
Ostlie, D.A., Cox, A.N. 1986, *ApJ*, **311**, 864.
Ostriker, J.P., Bodenheimer, P. 1973, *ApJ*, **180**, 171.
Ostriker, J.P., Tassuol, J.L. 1969, *ApJ*, **155**, 987.
Oudmaijer, R.D., Geballe, T.R., Waters, L.B.F.M., Sahu, K.C. 1994, *A&A*, **281**, L33.
Owen, B.J., Lindblom, L., Cutler, C., Schutz, B.F., Vecchio, A., Andersson, N. 1998, *Phys. Rev. D*, in press.
Owocki, S.P., Cranmer, S.R., Gayley, K.G. 1996, *ApJ*, **472**, L151.
Owocki, S.P., Gayley, K.G. 1997, in *Luminous Blue Variables: Massive Stars in Transition*, ed. A. Nota, H.J.G.L.M. Lamers, ASPC, **120**, p. 121.
Palla, F., Stahler, S.W. 1991, *A&A*, **375**, 288.
Penny, L.R. 1996, *ApJ*, **463**, 737.
Pinsonneault, M.H., Deliyannis, C.P., Demarque, P. 1991, *ApJ*, **367**, 239.
Pinsonneault, M.H., Kawaler, S.D., Sofia, S., Demarque, P. 1989, *ApJ*, **338**, 424.
Plait, P.C., Lundquist, P., Chevalier, R.A., Kirshner, R.P. 1995, *ApJ*, **439**, 730.
Podsiadlowski, P. 1998, in *SN 1987A: Ten years after*, ed. M.M. Phillips, N.B. Suntzeff, Fifth CTIO/ESO/LCO Workshop, in press.
Popham, R., Woosley, S.E., Fryer, C. 1998, *ApJ*, submitted.
Prantl, L. 1925, *Z. Angew. Math. Mech.*, **5**, 136.
Prantzos, N., Diehl, R. 1996, *Physics Reports*, **267**, 1.

Rampp, M., Müller, E., Ruffert, M. 1998, *A&A*, **332**, 969.
Salasnich, B., Bressan, A., Chiosi, C. 1997, astro-ph/9711141.
Schaller, G., Schaerer, D., Meynet, G., Maeder, A. 1992, *A&AS*, **96**, 269.
Schwarz, H.E., Corradi, R.L.M., Melnick, J. 1992, *A&AS*, **96**, 23.
Shapiro, S.L., Teukolski, S.A. 1983, *Black Holes, White Dwarfs, and Neutron stars*, John Wiley, New York.
Slettebak, A. 1970, in *Stellar Rotation*, ed. A. Slettebak, Reidel, Dortrecht, p. 3.
Slettebak, A., Collins, G.W., Boyce, P.B., White, N.M., Parkinson, T.D. 1975, *ApJS*, **29**, 137.
Slettebak, A., Howard, R.F. 1955, *ApJ*, **121**, 102.
Smoliński, J., Climenhaga, J.L., Fletcher, J.M. 1989, in *Physics of Luminous Blue Variables*, ed. K. Davidson et al., Kluwer, Dortrecht, p. 131.
Soker, N. 1996, *ApJ*, **460**, L53.
Spitzer, L., J. 1962, *Physics of fully Ionized Gases*, Interscience Publ., New York.
Spruit, H.C. 1997, private communication.
Spruit, H.C. 1998, *A&A*, **333**, 603.
Spruit, H.C., Knobloch, E., Roxburgh, I.W. 1984, *Nature*, **304**, 520.
Spruit, H.C., Phinney, E.S. 1998, *Nature*, **393**, 139.
Stanghellini, L., Corradi, R.L.M., Schwarz, H.E. 1993, *A&A*, **276**, 463.
Stothers, R.B., Chin, C.-W. 1992, *ApJ*, **390**, 136.
Talon, S., Charbonnel, C. 1998, *A&A*, **335**, 959.
Talon, S., Zahn, J.-P. 1997, *A&A*, **317**, 749.
Talon, S., Zahn, J.-P., Maeder, A., Meynet, G. 1997, *A&A*, **322**, 209.
Tassoul, J.-L. 1978, *Theory of Rotating Stars*, Princeton Univ. Press, Princeton.
Thielemann, F.-K., Nomoto, K., Hashimoto, M. 1996, *ApJ*, **460**, 408.
Thompson, M.J. et al. 1996, *Sci.*, **272**, 1300.
Timmes, F.X., Woosley, S.E., Weaver, T.A. 1995, *ApJS*, **98**, 617.
Townsend, A.A. 1958, *J. Fluid Mech.*, **5**, 361.
Tsiopa, O.A. 1995, in *Wolf-Rayet stars: binaries, colliding winds, evolution*, ed. K.A. van der Hucht, P.M. Williams, IAU Symp. 163, p. 425.
Tsujimoto, T., Nomoto, K., Yoshi, Y., Hashimoto, M., Yanagida, S., Thielemann, F.-K. 1995, *MNRAS*, **227**, 954.
Urpin, V.A., Shalybkov, D.A., Spruit, H.C. 1996, *A&A*, **306**, 455.
Ushomirsky, G., Bildsten, L. 1998, *ApJ*, **497**, L101.
Vassiliadis, E., Wood, P. 1993, *ApJ*, **413**, 641.
Venn, K.A., Lambert, D.L., Lemke, M. 1996, *A&A*, **307**, 894.
Vitense, E. 1953, *ZfAp*, **32**, 135.
Vogt, H. 1925, *Astr. Nachr.*, **223**, 229.
von Zeipel, H. 1924a, *MNRAS*, **84**, 665.
von Zeipel, H. 1924b, *MNRAS*, **84**, 684.
Vrancken, M., Lennon, D.J., Dufton, P.L., Lambert, D.L. 1998, *A&A*, in preparation.
Wasiutyński, J. 1946, *Ap. Norveg.*, **4**, 1.
Waelkens, C. 1987, in *Lecture Notes in Physics 274, Stellar Pulsations*, ed. A.N. Cox, W.M. Spark, S.G. Starrfield, Springer, Berlin.

Waelkens, C. 1991, *A&A*, **246**, 453.
Waelkens, C., Aerts, C., Kestens, E., Grenon, M., Eyer, L. 1998, *A&A*, **330**, 215.
Walker, M.F. 1990, *PASP*, **102**, 726.
Walter, R., Maeder, A. 1989, *A&A*, **218**, 123.
Weaver, T.A., Woosley, S.E. 1993, *Physics Reports*, **227**, 65.
Weaver, T.A., Woosley, S.E. 1995, unpublished.
Weaver, T.A., Woosley, S.E., Fuller, G.M. 1984, in *Numerical Astrophysics*, ed. J. Centrella, J. LeBlanc, R. Bowers, Jones and Bartlett, Boston, p. 374.
Weaver, T.A., Zimmerman, G.B., Woosley, S.E. 1978, *ApJ*, **225**, 1021.
Weiler, K.W., van Dyk, S.D., Pringle, J.E., Panagia, N. 1992, *ApJ*, **399**, 672.
Weis, K., Duschl, W.J., Monas, D.J., Chu, Y.-H., Joner, M.D. 1997, *A&A*, **320**, 568.
Whitelock, P., Feast, M., Catchpole, R. 1991, *MNRAS*, **248**, 276.
Whitelock, P., Menzies, J., Feast, M., Marang, F., Carter, B., Roberts, G., Catchpole, R., Chapman, J. 1994, *MNRAS*, **267**, 711.
Wood, P.R., Bessell, M.S., Fox, M.W. 1983, *ApJ*, **272**, 99.
Wood, P.R., Whiteoak, J.B., Hughes, S.M.G., Bessell, M.S., Gardener, F.F., Hyland, A.R. 1992, *ApJ*, **397**, 552.
Woosley, S.E. 1986, in *Nucleosynthesis and chemical evolution*, Saas Fee Advanced Course 15, Geneva Observatoty, Sauverny-Versoix.
Woosley, S.E. 1990, in *Supernovae*, ed. A.G. Petschek, Springer-Verlag, New York, p. 182.
Woosley, S.E. 1993, *ApJ*, **405**, 273.
Woosley, S.E. 1997, private communication.
Woosley, S.E., Eastman, R.G., Weaver, T.A., Pinto, P.A. 1994, *ApJ*, **429**, 300.
Woosley, S.E., Heger, A., Weaver, T.A., Langer, N. 1998, in *SN 1987A: Ten years after*, ed. M.M. Phillips, N.B. Suntzeff, Fifth CTIO/ESO/LCO Workshop, in press.
Woosley, S.E., Langer, N., Weaver, T.A. 1993, *ApJ*, **411**, 823.
Woosley, S.E., Weaver, T.A. 1986, *ARA&A*, **24**, 205.
Woosley, S.E., Weaver, T.A. 1988, *Physics Reports*, **163**, 79.
Woosley, S.E., Weaver, T.A. 1995, *ApJS*, **101**, 181.
Zahn, J.-P. 1974, in *Stellar Instability and Evolution*, ed. P. Ledoux, A. Noels, A.W. Rogers, IAU Symp. 59, Reidel, Dortrecht, p. 185.
Zahn, J.-P. 1975, *Mem. Soc. Roy. Sci. Liège*, **8**, 31.
Zahn, J.-P. 1983, in *Processes in the Upper MS Stars*, ed. B. Hauck, A. Maeder, Saas-Fee Advanced Course 13, p. 253.
Zahn, J.-P. 1992, *A&A*, **265**, 115.
Zahn, J.-P. 1994, in *Evolution of Massive Stars: A Confrontation between Theory and Observation*, ed. D. Vanbeveren, W. van Rensbergen, C.W.H. de Loore, Space Sci. Rev., **66**, Kluwer, Dortrecht, p. 285.
Zickgraf, F.J., Humphreys, R.M., Lamers, H.J.G.L.M., Smolinski, J., Wolf, B., Stahl, O. 1996, *A&A*, **315**, 510.
Zwerger, T., Müller, E. 1997, *A&A*, **320**, 209.

Acknowledgements

At the very first, I want to thank Prof. Norbert Langer who supervised this work. I am indebted to him. He always found time to talk with me about new results and help with the various scientific and non-scientific problems that arose during the last years. I sincerely appreciated the many rewarding discussions. He contributed substantially to the genesis of this work. I learned a lot from him about all aspects of stellar evolution and nucleosynthesis, theoretical as well as observational.

I want to thank Prof. Stanford E. Woosley for his great interest in my work, his continuous encouragement, the many discussions on the evolution of rotating massive stars, in general, and on SN 1987A in particular, and his help with the KEPLER code. I am grateful to him for his invitations to visit the University of California at Santa Cruz and for the hospitality during my stays. Without him this work could not have been that successful.

I am very grateful to Prof. Wolfgang Hillebrandt who made it possible for me to do both my diploma and Ph.D. thesis at the Max-Planck-Institut für Astrophysik, and for his and the Institute's continuous support — for schools, conferences, and visits to other institutes. I also thank him for his splendid lectures on diverse special topics in astrophysics. I enjoyed them a lot. They certainly contributed significantly to my understanding of science and I learned much about many fascinating research fields in astrophysics.

I thank Dr. Henk Spruit for the often controversial, but alway fruitful, discussions on the physical effects of magnetic fields, turbulence, and rotation inside stars, and the different processes that might occur due to their interaction. I also want to thank Dr. Friedrich Meyer for the discussions on the triple-ring nebula around SN 1987A and his great analytic model for their formation, and Prof. Philipp Podsiadlowski for the discussions of his binary models for SN 1987A and other questions of stellar evolution theory.

I want to thank Jens Fliegner for supplying his stellar evolution code and helping me with its implementation; and Dr. Hartmut Braun for many discussions on computing-related topics and his help with IDL. Thanks to both Jens Fliegner and Dr. Hartmut Braun for many discussions on stellar evolution and numerics, as well as their help in learning about the details and their bearing of my many questions during my diploma and the beginning of the Ph.D. thesis.

I am grateful to Dr. Tomasz Plewa for the scientific discussions related to different numerical and hydrodynamic problems, supplying me with his hydrodynamic adaptive mesh code, and patiently teaching me the workings of the code, and also for the nice time and fun we had as office mates.

I want to thank Dr. Ulrich Kolb for the interesting discussions about low-mass X-ray binaries and their evolutionary paths. To Klaus Dolag, I am grateful for our entertaining discussions on computers and the good time we had as office mates, and to Konstantinos Kifonidis for our many discussions on computing, hydrodynamics and supernovae. I also want to thank all my other colleagues at MPA for the friendly atmosphere in the institute.

For our collaboration on the pulsation in red supergiants, I am grateful to Dr. Isabelle Baraffe and Dr. Laurent Jeannin from the CNRS in Lyon, France.

During my visit at the University of California at Santa Cruz, Andrew MacFadyen helped me a lot with the difficulties of life in a (for me) foreign country when I arrived. We also had may interesting discussions on hydrodynamics and the collapsar model for γ-ray bursts. I also thank Dr. Chris Fryer for the discussions we had at the MPA on γ-ray bursts and on low-mass X-ray binaries.

I want to thank Prof. Lars Bildsten for his interest in my work, the invitation to the the University of California at Berkeley and the really well organized scientific meetings with people at the UCB Astronomy department.

I'm grateful to the DAAD for the two grants that allowed me to visit Prof. Woosley and his group at the University of California at Santa Cruz during 1996/1997 and in April 1998. This certainly was a valuable experience and contributed a lot to the success of this work.

Thanks especially to my parents for all their help and support during my study.

Curriculum vitae

personal data:		Alexander Heger born on 20. January 1970 at Erding German nationality
school:	1976 – 1980	Volksschule München, Turnerstraße
	1980 – 1989	Michaeli-Gymnasium München
	26. June 1989	Abitur (senior grade)
study:	1989 – 1995	Allgemeine Physik (general physics) at the Technische Universität München
thesis work:		*Stationäre Modelle für Wolf-Rayet Sterne mit optisch dicken Winden*
diploma:	9. Aug. 1995	in physics
	1995 – 1998	graduate student at the Max-Planck-Institut für Astrophysik